Aus dem Max-Planck-Institut für Kolloid- und Grenzflächenforschung

Nichtwässrige Synthese und Bildungsmechanismus von Übergangsmetalloxid-Nanopartikeln

Nonaqueous Synthesis of Transition-Metal Oxide Nanoparticles and Their Formation Mechanism

Dissertation

zur Erlangung des akademischen Grades
"doctor rerum naturalium"
(Dr. rer. nat.)
in der Wissenschaftsdisziplin Kolloidchemie

eingereicht an der
Mathematisch-Naturwissenschaftlichen Fakultät
der Universität Potsdam

von

Georg Garnweitner

Potsdam, im Mai 2005

Die hier vorliegende Arbeit wurde in der Zeit von April 2003 bis Mai 2005 am Max-Planck-Institut für Kolloid- und Grenzflächenforschung in Potsdam/Golm angefertigt.

Gutachter: Prof. Dr. Markus Antonietti
Prof. Dr. Nicola Hüsing
Dr. habil. Helmut Cölfen

Tag der mündlichen Disputation: 24. 08. 2005

To my Family

Abstract

In this work, the nonaqueous synthesis of binary and ternary metal oxide nanoparticles is investigated for a number of technologically important materials. A strong focus was put on studying the reaction mechanisms leading to particle formation upon solvothermal treatment of the precursors, as an understanding of the formation processes is expected to be crucial for a better control of the systems, offering the potential to tailor particle size and morphology.

The synthesis of $BaTiO_3$ was achieved by solvothermal reaction of metallic barium and titanium isopropoxide in organic solvents. Phase-pure, highly crystalline particles about 6 nm in size resulted in benzyl alcohol, whereas larger particles could be obtained in ketones such as acetone or acetophenone. In benzyl alcohol, a novel mechanism was found to lead to $BaTiO_3$, involving a C–C coupling step between the isopropoxide ligand and the benzylic carbon of the solvent. The resulting coupling product, 4-phenyl-2-butanol, is found in almost stoichiometric yield. The particle formation in ketones proceeds via a Ti-mediated aldol condensation of the solvent, involving formal elimination of water which induces formation of the oxide. These processes also occurred when reacting solely the titanium alkoxide with ketones or aldehydes, leading to highly crystalline anatase nanoparticles for all tested solvents. In ketones, also the synthesis of nanopowders of lead zirconate titanate (PZT) was achieved, which were initially amorphous but could be crystallized by calcination at moderate temperatures. Additionally, PZT films were prepared by simply casting a suspension of the powder onto Si substrates followed by calcination.

Solvothermal synthesis however is not restricted to alkoxides as precursors but is also achieved from metal acetylacetonates. The use of benzylamine as solvent proved particularly versatile, making possible the synthesis of nanocrystalline In_2O_3, Ga_2O_3, ZnO and iron oxide from the respective acetylacetonates. During the synthesis, the acetylacetonate ligand undergoes a solvolysis under C–C cleavage, resulting in metal-bound enolate ligands which, in analogy to the synthesis in ketones, induce ketimine and aldol condensation reactions.

In the last section of this work, surface functionalization of anatase nanoparticles is explored. The particles were first capped with various organic ligands via a facile in situ route, which resulted in altered properties such as enhanced dispersibility in various solvents. In a second step, short functional oligopeptide segments were attached to the particles by means of a catechol linker to achieve advanced self-assembly properties.

Abstract

Die vorliegende Arbeit befasst sich mit der nichtwässrigen Synthese binärer und ternärer Metalloxid-Nanopartikel durch solvothermale Behandlung von Metalloxid-Vorstufen in organischen Lösungsmitteln. Dabei wurde besonderes Augenmerk auf die Reaktionsmechanismen gelegt, da eine genaue Kenntnis des Bildungsmechanismus eine bessere Kontrolle über das Partikelwachstum erwarten lässt, woraus sich die Möglichkeit der genauen Steuerung von Partikelgröße und –form ableitet.

Bariumtitanat ($BaTiO_3$) konnte durch solvothermale Reaktion von metallischem Barium und Titanisopropoxid in organischen Lösungsmitteln hergestellt werden. Hochkristalline, phasenreine Partikel von etwa 6 nm Durchmesser wurden in Benzylalkohol erhalten, während in Ketonen wie Aceton oder Acetophenon größere Partikel entstanden. In Benzylalkohol läuft ein neuartiger Reaktionsmechanismus ab, der eine C–C-Kupplungsreaktion zwischen dem Isopropoxid und dem benzylischen Kohlenstoffatom des Lösungsmittels umfasst. Das Kupplungsprodukt 4-Phenyl-2-butanol wird in praktisch stöchiometrischer Ausbeute erhalten. In Ketonen verläuft die Partikelbildung über eine titankatalysierte Aldolkondensation des Lösungsmittels, die formell die Eliminierung von Wasser einschließt, was zur Bildung des Oxids führt. Diese Prozesse liefen auch bei Umsetzung von reinem Titanisopropoxid in Ketonen oder Aldehyden ab, wobei hier hochkristalline Anatas-Nanopartikel entstanden. Auch die Synthese von Bleizirkonat-titanat-Nanopulvern war in Ketonen möglich; die zunächst amorphen Pulver konnten durch Kalzinierung bei relativ geringen Temperaturen in kristalline Nanopartikel überführt werden. Zusätzlich wurden Filme durch Auftragen einer Suspension der Pulver auf Siliziumwafer und anschließende Kalzinierung hergestellt.

Die solvothermale Synthese kann allerdings auch ausgehend von Metallacetylacetonaten durchgeführt werden. Benzylamin erwies sich hier als ein sehr vielseitiges Lösungsmittel und ermöglichte die Synthese von nanokristallinem In_2O_3, Ga_2O_3, ZnO und Eisenoxid ausgehend von den jeweiligen Acetylacetonaten. Im Verlauf der Synthese wird der Acetylacetonatligand unter C–C-Bindungsspaltung solvolysiert. Die entstehenden Enolatliganden reagieren dann unter Ketimin- und Aldolkondensation analog der Solvothermalsynthese in Ketonen weiter.

Der letzte Teil dieser Arbeit beschäftigt sich mit der Funktionalisierung der Partikel. Zunächst wurden TiO_2-Partikel durch verschiedene organische Liganden „in situ“ funktionalisiert, wodurch Eigenschaften wie etwa die Dispergierbarkeit in unterschiedlichen Lösungsmitteln beeinflusst werden konnten. In einem zweiten Schritt wurden kurze Oligopeptidketten über eine Katecholbrücke an die Partikel geknüpft, um anspruchsvolle Selbstanordnungseigenschaften zu erzielen.

Table of Contents

Acknowledgments

List of Publications

1 Introduction

While the words nanoscience and nanotechnology are relatively new, the existence of functional devices and structures of nanometer dimensions is not, and in fact such structures have existed on Earth as long as life itself.[1] One common definition regards nanoscience as "*the ability to do things – measure, see, predict and make – on the scale of atoms and molecules and exploit the novel properties found at that scale*".[2] Usually, this scale is being defined as between 1 and 100 nanometer, with 1 nm being one billionth of a meter.[3] At this scale, novel material properties are found, due to what is commonly referred to as *size effects*.[4] Nanoscale materials frequently show behavior which is intermediate between that of a macroscopic solid and that of an atomic or molecular system.[5] An inorganic crystal composed of few atoms, for instance, will have a significant fraction of its atoms sitting on the surface, therefore having a large influence on the overall properties of the crystal. One can easily imagine that this crystal might have a higher chemical reactivity than the corresponding bulk solid and that it will probably melt at lower temperature. In addition, quantum mechanics come into play, leading to the appearance of many additional properties which cannot easily be grasped by simple reasoning.[4-6] Phase transition pressures, melting points, optical, optoelectronic, catalytic, magnetic, and electric properties of nanomaterials differ both from those of the bulk solid and of the molecular species of which they consist – one could speak of a new state of matter.[7] Consequently, there is a multitude of potential applications for nano-engineered materials in very diverse fields, some of which being illustrated in Figure 1.1.

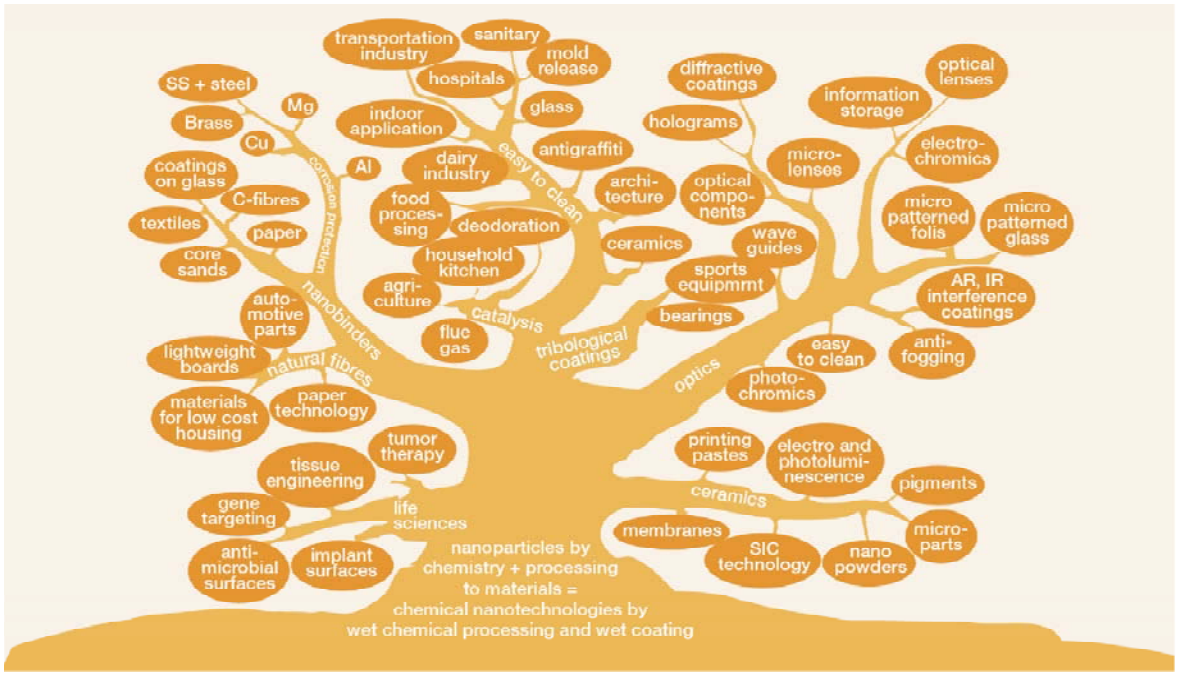

Figure 1.1. Potential applications for nanotechnologically manufactured materials.[2]

There has been an explosive growth of nanoscience and technology in the last decade, primarily because of the availability of new methods of synthesizing nanomaterials, as well as tools for characterization and manipulation.[8] For the synthesis of nanoscale materials, two basic approaches can be distinguished. The *Top-down* approach tries to enhance the methods from microtechnology to achieve structure sizes in the medium and also lower nanometer range.[9] This more physical approach makes use of lithography methods, with improved techniques such as particle-, ion-, electron-beam or scanning-probe-based lithography today being able to manufacture materials at the 50 nm-level.[10] On the other hand, the *Bottom-up* approach, influenced by chemical principles, involves assembly of atomic or molecular units to molecular structures ranging from atomic dimensions up to supramolecular structures in the nanometer range.[9] Even though bottom-up techniques are still in their infancy, recently a movement away from top-down techniques towards bottom-up strategies was observed within the international research community.[2]

One highly explored field of nanotechnology is the synthesis, characterization and application of small particles, usually referred to as nanoparticles or, being only a few nm in size in all three dimensions, quantum dots.[5] Whilst noble metal nanoparticles have been used by Roman glassmakers as early as in the fourth century A. D. to fabricate colored glasses,[1] and their scientific investigation started in the mid-nineteenth century by Faraday,[11] the synthesis of nanoparticles of metal oxides or chalcogenides has only been studied within the last decades, triggered by reports for instance on the outstanding behavior of titania colloids towards photocatalysis,[12,13] however experiencing an enormous development since. Metal oxides constitute an especially important class of materials, their unique characteristics making them the most diverse class of materials, with properties covering almost all aspects of materials science and solid state physics.[14] In particular, perovskite-phase mixed-metal oxides exhibit outstanding chemical and physical properties, including catalytic, oxygen transport, ferroelectric, pyroelectric, piezoelectric and dielectric behavior.[15-17] Consequently, metal oxides are used in the fabrication of microelectronic circuits, sensors, piezoelectric devices, fuel cells, coatings for the passivation of surfaces against corrosion, and as catalysts. As an example, almost all catalysts used in industrial applications involve an oxide as active phase, promoter, or support. In the chemical and petrochemical industries, products worth billions of dollars are generated every year through processes that use oxide and metal/oxide catalysts.[18]

The development of facile and inexpensive fabrication routes to metal oxide nanoparticles is of high importance for several reasons. First, powders consisting of particles in the nano-size regime are highly suitable for the fabrication of thin films, which are needed e.g. for applications in electronics. Compared to conventional powders with particle sizes in the micron regime, nanoparticulates possess the advantage of enhanced sintering properties, resulting in higher densification rates at lower temperatures.[17,19] Also, a more homogeneous product can be obtained, the small grain sizes in the final ceramic resulting in increased flexibility, less brittleness and greater strength.[3,20] Second, the general trend to further miniaturization of functional devices in emerging technologies such as sensing, pigmentation, energy storage and conversion and especially electroceramics demands for the production of materials in particle sizes already approaching the lower nanoscale.[5] As mentioned above, metal oxide nanoparticles furthermore can exhibit unique chemical and physical properties.[18]

Nowadays, a variety of methods is known to generate metal oxide nanoparticles with a reasonable control of the particle size. Physical strategies include gas/vapor condensation, spray pyrolysis, and thermochemical methods, also referred to as chemical vapor deposition. Whereas these methods are industrially used due to their low cost, control of particle size and morphology is difficult, and usually a broad size distribution is obtained.[18] Chemical methods, on the other hand, offer potential routes to obtain better materials in terms of chemical homogeneity, especially for mixed oxides, and morphological control. Within these, sol-gel processes are becoming the standard method for the synthesis of oxides, being based on the inorganic polymerization reaction of a metal precursor such as an alkoxide or halide.[21]

The research on the sol-gel synthesis of metal oxide nanoparticles was long focused on aqueous techniques, where the precursor is hydrolyzed. In an initiation step, the metal oxide or metal chloride (halide) is hydroxylated according to

$$\equiv M\text{–}OR + H_2O \longrightarrow \equiv M\text{–}OH + ROH \qquad \text{(Eq. 1.1)}$$

or

$$\equiv M\text{–}Cl + H_2O \longrightarrow \equiv M\text{–}OH + HCl \qquad \text{(Eq. 1.2).}$$

As soon as hydroxy groups are generated, propagation occurs through a polycondensation process.[22] Oxygen bridges form through the elimination of H_2O, ROH or HCl:

$$\equiv M\text{–}OH + \equiv M\text{–}OX \longrightarrow \equiv M\text{–}O\text{–}M\equiv + XOH \qquad \text{(Eq. 1.3, X being H or R)}$$

or

$$\equiv M\text{–}OH + \equiv M\text{–}Cl \longrightarrow \equiv M\text{–}O\text{–}M\equiv + HCl \qquad \text{(Eq. 1.4)}$$

Aqueous synthesis techniques have several disadvantages, which basically all result from the high reactivity of the precursor towards hydrolysis.[22] Usually, the obtained particles are amorphous and need to be crystallized in a subsequent calcination treatment. This additional step however may change the particle morphology, usually by particle growth, and rules out the possibility of preparing inorganic-organic hybrid materials, for example surface-modified particles. For the production of ternary metal oxides, the large differences in hydrolysis rates of different precursors can lead to undesirable inhomogeneities in the products, especially when using d^0 transition metals such as Ti or Zr.[23] Moreover, the synthesis conditions, such as temperature, method of mixing, pH and especially the nature and concentration of anions need to be controlled precisely.[24] In many cases, organic surfactants were used to control the growth of inorganic nanocrystals, however many of these commonly used surfactants are toxic, such as TOPO (trioctylphosphine oxide), lead to impurities in the final material, and are detrimental with respect to application of these materials in electronic and sensing devices.

Therefore, several strategies have been developed to achieve a more controlled synthesis. The metal precursor can be modified by stable ligands such as acetate or acetylacetonate, thereby decreasing its reactivity.[25-27] On the other hand, chemical or physical processes can be utilized that release H_2O very slowly and therefore promote the slow, controlled hydrolysis of alkoxide precursors. For example, the esterification of acetic acid by alcohols, or the formation of acetals from an aldehyde and an alcohol, gives slow, in situ water generation, which has allowed the formation of mixed oxide gels.[28] Also the synthesis of nanocrystalline titania has been achieved via esterification reactions.[29,30]

Another possibility is the complete avoidance of water in the reaction medium, i.e. the nonaqueous synthesis of metal oxides. First reports on the formation of silica in the absence of water were already published in the 1950s, when Gerrard et al. studied the reaction of various alcohols with silicon tetrachloride, resulting in the formation of hydrated silica and alkyl chlorides.[31,32] Many years later, Vioux et al. started systematic studies on the nonaqueous formation of monolithic silica[33] and metal oxide gels[34-41] by reacting the metal halides with alcohols, ethers or metal alkoxides, leading to metal-oxygen-metal bonds according to

$$\equiv M\text{–}Cl + ROX \longrightarrow \equiv M\text{–}OR + XCl \qquad \text{(Eq. 1.5, X being H or R)}$$

and/or

$$\equiv M\text{–}OR + \equiv M\text{–}Cl \longrightarrow \equiv M\text{–}O\text{–}M\equiv + RCl \qquad \text{(Eq. 1.6),}$$

the latter reaction being termed *alkyl halide elimination*. These approaches were subsequently extended by using catalysts such as iron(III) chloride.[23,42] Mixed metal oxide gels were also obtained by reacting metal acetates with metal alkoxides, ester elimination processes resulting in the formation of M–O–M bonds.[28,43-45] A few years later, also the synthesis of nanocrystalline materials, in particular TiO_2, was achieved via nonhydrolytic processes.[46] A slightly different, but highly interesting strategy was employed by Goel et al., who reacted a Zn alkoxide with acetone to form zincite nanocrystals under aldol condensation of acetone.[47] This process was later utilized for the room-temperature synthesis of $BaTiO_3$ nanocrystals by stirring a bimetallic alkoxide in acetone.[48]

Today, nonaqueous synthesis approaches are being employed as valuable alternatives to aqueous systems, and the family of metal oxide nanoparticles synthesized by nonhydrolytic reaction routes is rapidly growing.[49] Several nonaqueous methods have been reported leading to nanocrystalline binary metal oxides, especially titania,[50-56] zirconia,[57] and iron oxide.[58-62] Furthermore, mixed metal oxides like ferrites[63,64] have been prepared. Some of these procedures can be straightforwardly scaled-up to yield tens of gram quantities.[65] Most of these procedures still rely on the use of surfactants, especially TOPO, to control the crystal growth and to provide solubility. More advanced processes make use of solvents which act as reactant as well as control agent for particle growth, and thus allow the synthesis of high-purity nanomaterials.

In this work, the synthesis of binary and ternary transition metal oxide nanoparticles is investigated, with an emphasis on perovskite-phase materials due to their exceptional material properties. In the most cases, benzyl alcohol is used as solvent, as it has been found to be a versatile medium allowing the synthesis of high-purity nanocrystalline metal oxides.[66,67] Also the approach developed by Goel et al.[47] is further investigated and extended, for it appears a facile and inexpensive alternative route to metal oxide nanoparticles, taking place in a non-reductive environment, which appears advantageous in some cases. Usually, alkoxides and acetylacetonates were used as precursors, as they possess significant advantages over metal halides, leading to higher purity of the final materials. Moreover, the formation of hydrochloric or hydrobromic acid is avoided which would constitute a potential hazard and rule out the possibility to work in an ultra-pure, closed environment, such as in a glove box. Also, alkoxides and acetylacetonates are usually less reactive, facilitating handling and storage.

Due to the lower reactivity of metal alkoxides, however, the synthesis had to be performed under solvothermal conditions. The solvothermal method is a powerful route for preparing materials. It is similar to the hydrothermal method except that organic solvents are used instead of water.[55] The reaction mixture is transferred into a vessel which is sealed and heated in an oven, thereby leading to pressure buildup. Even though this autogenous pressure was calculated to be minute in the most cases, analogous treatment in open vessels did not result in nanocrystalline species.

Beside the detailed characterization of the obtained precipitates, a strong focus is put on investigating the reaction mechanisms leading to formation of the inorganic particles. Whereas the nonhydrolytic reaction of metal halides has been thoroughly investigated by Vioux and co-workers[34,39,41] even though it can be regarded as rather straightforward, the reaction mechanisms of alkoxides or acetylacetonates in organic solvents such as alcohols and ketones, especially under solvothermal conditions, are hardly known. They are often simply termed as decomposition processes[54,68] but in fact turn out to be rather complex, involving unexpected condensation processes with the solvent.

In the last section of this work, the functionalization of metal oxide nanoparticles is investigated, with TiO_2 particles as an example. Thus, not only properties such as the solubility are altered, but also the self-assembly behavior of the particles can be tailored. By using standard organic ligands, indeed the solubility of the nanoparticles in various solvents is enhanced significantly. In a second, more sophisticated step, functional oligopeptide units were covalently attached to the particle surface and the assembly behavior of these bioconjugates was investigated.

References

[1] C. P. Poole Jr., F. J. Owens, *Introduction to Nanotechnology*, J. Wiley & Sons, Weinheim, **2003**.

[2] J. M. Taylor, *New Dimensions for Manufacturing: UK Strategy for Nanotechnology*, Report for the UK Advisory Group for Nanotechnology Applications, London, **2002**: http://www.dti.gov.uk/innovation/nanotechnologyreport.pdf.

[3] A. Arora, *Adv. Eng. Mater.* **2004**, *6*, 244.

[4] C. N. R. Rao, A. Müller, A. K. Cheetham, *The Chemistry of Nanomaterials: Synthesis, Properties and Applications, Vol. 1*, Wiley-VCH, Weinheim, **2004**.

[5] W. J. Parak, L. Manna, F. C. Simmel, D. Gerion, A. P. Alivisatos in: *Nanoparticles: From Theory to Application (Ed.: G. Schmid)*, Wiley-VCH, Weinheim, **2004**.

[6] A. P. Alivisatos, *J. Phys. Chem.* **1996**, *100*, 13226.

[7] A. Eychmüller, *J. Phys. Chem. B* **2000**, *104*, 6514.

[8] C. N. R. Rao, A. K. Cheetham, *J. Mater. Chem.* **2001**, *11*, 2887.

[9] M. Kohler, W. Fritzsche, *Nanotechnology*, Wiley-VCH, Weinheim, **2004**.

[10] U. S. Schubert, D. Wouters, *Angew. Chem. Int. Ed.* **2004**, *43*, 2480.

[11] M. Faraday, *Philos. Trans. R. Soc. London* **1857**, *147*, 145.

[12] D. Duonghong, E. Borgarello, M. Gratzel, *J. Am. Chem. Soc.* **1981**, *103*, 4685.

[13] A. Henglein, *Ber. Bunsenges. Phys. Chem.* **1982**, *86*, 241.

[14] C. N. R. Rao, B. Raveau, *Transition metal oxides*, VCH, New York, **1995**.

[15] C. D. Chandler, C. Roger, M. J. Hampden-Smith, *Chem. Rev.* **1993**, *93*, 1205.

[16] M. A. Pena, J. L. G. Fierro, *Chem. Rev.* **2001**, *101*, 1981.

[17] A. S. Bhalla, R. Guo, R. Roy, *Mat. Res. Innovat.* **2000**, *4*, 3.

[18] M. Fernández-García, A. Martínez-Arias, J. C. Hanson, J. A. Rodriguez, *Chem. Rev.* **2004**, *104*, 4063.

[19] D. Hennings, M. Klee, R. Waser, *Adv. Mater.* **1991**, *3*, 334.

[20] N. Setter, R. Waser, *Acta Mater.* **2000**, *48*, 151.

[21] B. L. Cushing, V. L. Kolesnichenko, C. J. O'Connor, *Chem. Rev.* **2004**, *104*, 3893.

[22] C. Sanchez, J. Livage, *New J. Chem.* **1990**, *14*, 513.

[23] J. N. Hay, H. M. Raval, *J. Mater. Chem.* **1998**, *8*, 1233.

[24] E. Matijević, *Chem. Mater.* **1993**, *5*, 412.

[25] S. Doeuff, M. Henry, C. Sanchez, F. Babonneau, *J. Non-Cryst. Solids* **1987**, *89*, 206.

[26] C. Sanchez, J. Livage, M. Henry, F. Babonneau, *J. Non-Cryst. Solids* **1988**, *100*, 65.

[27] J. C. Debsikdar, *J. Non-Cryst. Solids* **1986**, *86*, 231.

[28] M. Jansen, E. Guenther, *Chem. Mater.* **1995**, *7*, 2110.

[29] M. Ivanda, S. Musić, S. Popović, M. Gotić, *J. Mol. Struct.* **1999**, *481*, 645.

[30] P. D. Cozzoli, A. Kornowski, H. Weller, *J. Am. Chem. Soc.* **2003**, *125*, 14539.

[31] W. Gerrard, A. H. Woodhead, *J. Chem. Soc.* **1951**, 519.

[32] W. Gerrard, K. D. Kilburn, *J. Chem. Soc.* **1956**, 1536.

[33] R. J. P. Corriu, D. Leclercq, P. Lefevre, P. H. Mutin, A. Vioux, *J. Non-Cryst. Solids* **1992**, *146*, 301.

[34] R. J. P. Corriu, D. Leclercq, P. Lefevre, P. H. Mutin, A. Vioux, *J. Mater. Chem.* **1992**, *2*, 673.

[35] P. Arnal, R. J. P. Corriu, D. Leclercq, P. H. Mutin, A. Vioux, *Mater. Res. Soc. Symp. Proc.* **1994**, *346*, 339.

[36] S. Acosta, R. J. P. Corriu, D. Leclercq, P. Lefevre, P. H. Mutin, A. Vioux, *J. Non-Cryst. Solids* **1994**, *170*, 234.

[37] M. Andrianainarivelo, R. J. P. Corriu, D. Leclercq, P. H. Mutin, A. Vioux, *J. Mater. Chem.* **1996**, *6*, 1665.

[38] P. Arnal, R. J. P. Corriu, D. Leclercq, P. H. Mutin, A. Vioux, *J. Mater. Chem.* **1996**, *6*, 1925.

[39] P. Arnal, R. J. P. Corriu, D. Leclercq, P. H. Mutin, A. Vioux, *Chem. Mater.* **1997**, *9*, 694.

[40] M. Andrianainarivelo, R. J. P. Corriu, D. Leclercq, P. H. Mutin, A. Vioux, *Chem. Mater.* **1997**, *9*, 1098.

[41] A. Vioux, *Chem. Mater.* **1997**, *9*, 2292.

[42] J. N. Hay, H. M. Raval, *J. Sol-Gel Sci. Technol.* **1998**, *13*, 109.

[43] J. Caruso, M. J. Hampden-Smith, A. L. Rheingold, G. Yap, *J. Chem. Soc. Chem. Commun.* **1995**, 157.

[44] J. Caruso, M. J. Hampden-Smith, E. N. Duesler, *J. Chem. Soc. Chem. Commun.* **1995**, 1041.

[45] M. Iwasaki, A. Yasumori, S. Shibata, M. Yamane, *J. Sol-Gel Sci. Technol.* **1994**, *2*, 387.

[46] T. J. Trentler, T. E. Denler, J. F. Bertone, A. Agrawal, V. L. Colvin, *J. Am. Chem. Soc.* **1999**, *121*, 1613.

[47] S. C. Goel, M. Y. Chiang, P. C. Gibbons, W. E. Buhro, *Mater. Res. Soc. Symp. Proc.* **1992**, *271*, 3.

[48] B. C. Gaskins, J. J. Lannutti, *J. Mater. Res.* **1996**, *11*, 1953.

[49] T. Hyeon, *Chem. Commun.* **2003**, 927.

[50] C. Wang, Z. Deng, Y. Li, *Inorg. Chem.* **2001**, *40*, 5210.

[51] H. Parala, A. Devi, R. Bhakta, R. A. Fischer, *J. Mater. Chem.* **2002**, *12*, 1625.

[52] C. Wang, Z. X. Deng, G. H. Zhang, S. S. Fan, Y. D. Li, *Powder Technol.* **2002**, *125*, 39.

[53] C. S. Kim, B. K. Moon, J.-H. Park, B. C. Choi, H. J. Seo, *J. Cryst. Growth* **2003**, *257*, 309.

[54] C. S. Kim, B. K. Moon, J.-H. Park, S. T. Chung, S.-M. Son, *J. Cryst. Growth* **2003**, *254*, 405.

[55] W. S. Nam, G. Y. Han, *Korean J. Chem. Eng.* **2003**, *20*, 1149.

[56] Y. W. Jun, M. F. Casula, J. H. Sim, S. Y. Kim, J. Cheon, A. P. Alivisatos, *J. Am. Chem. Soc.* **2003**, *125*, 15981.

[57] J. Joo, T. Yu, Y. W. Kim, H. M. Park, F. X. Wu, J. Z. Zhang, T. Hyeon, *J. Am. Chem. Soc.* **2003**, *125*, 6553.

[58] J. Rockenberger, E. C. Scher, A. P. Alivisatos, *J. Am. Chem. Soc.* **1999**, *121*, 11596.

[59] T. Hyeon, S. S. Lee, J. Park, Y. Chung, H. B. Na, *J. Am. Chem. Soc.* **2001**, *123*, 12798.

[60] S. Sun, H. Zeng, *J. Am. Chem. Soc.* **2002**, *124*, 8204.

[61] Z. Li, H. Chen, H. B. Bao, M. Y. Gao, *Chem. Mater.* **2004**, *16*, 1391.

[62] F. X. Redl, C. T. Black, G. C. Papaefthymiou, R. L. Sandstrom, M. Yin, H. Zeng, C. B. Murray, S. P. O'Brian, *J. Am. Chem. Soc.* **2004**, *126*, 14583.

[63] S. H. Sun, H. Zeng, D. B. Robinson, S. Raoux, P. M. Rice, S. X. Wang, G. X. Li, *J. Am. Chem. Soc.* **2004**, *126*, 273.

[64] Q. Song, Z. J. Zhang, *J. Am. Chem. Soc.* **2004**, *126*, 6164.

[65] J. Park, K. An, Y. Hwang, J.-G. Park, H.-J. Noh, J.-Y. Kim, J.-H. Park, N.-M. Hwang, T. Hyeon, *Nat. Mater.* **2004**, *3*, 891.

[66] M. Niederberger, M. H. Bartl, G. D. Stucky, *J. Am. Chem. Soc.* **2002**, *124*, 13642.

[67] M. Niederberger, M. H. Bartl, G. D. Stucky, *Chem. Mater.* **2002**, *14*, 4364.

[68] W. S. Seo, H. H. Jo, K. Lee, J. T. Park, *Adv. Mater.* **2003**, *15*, 795.

2 Analytical Methods

2.1 X-ray Diffraction (XRD)

An ideal inorganic crystal is constructed by the infinite repetition of identical structural units in space. In the simplest crystals, the structural unit is a single atom, such as in copper, silver or gold, but usually the smallest structural unit comprises many atoms or molecules.[1]

When a regular array of objects is irradiated with light of a suitable wavelength, the light undergoes diffraction, leading to a characteristic pattern in dependence of the angle of incidence. When irradiating inorganic crystals with visible light, however, the crystal appears as homogeneous matter, as the wavelength of visible light is far greater than the distance of the repeat units in the crystal. X-rays, with a wavelength λ in the Å regime, "see" and interact with the very inhomogeneous, but periodical, electron density distribution $\rho(\vec{x})$ within the crystal, leading to a characteristic diffraction pattern.[2]

From the electron density $\rho(\vec{x})$, $\vec{x}$ denoting the position, the complex amplitude of the diffracted wave can be directly calculated according to

$$F(\vec{s}) = \int_V \rho(\vec{x}) \exp(2\pi i\, \vec{s} \cdot \vec{x})\, dV = \mathcal{F}(\rho(\vec{x})) \qquad \text{(Eq. 2.1)},$$

$\vec{s}$ being the scattering vector.[3]

In a diffraction experiment, however, not the complex amplitude but the intensity distribution $I(\vec{s})$ of this diffracted wave is measured, with $I(\vec{s}) = |F(\vec{s})|^2$. As a consequence, it is not possible to directly calculate the electron density $\rho(\vec{x})$ of a sample from the measured diffraction data as the phase information is lost in the intensity distribution.

A simple formula was developed by W. L. Bragg, reducing diffraction to reflection of X-rays on one set of crystal planes (Fig. 2.1).[4] Positive interference only occurs if the phase shift of the two rays is a multiple of λ. As the phase shift calculates to 2 d sin θ (determined by simple geometry), the Bragg equation is

$$n\lambda = 2\, d\, \sin\theta \qquad \text{(Eq. 2.2)}.$$

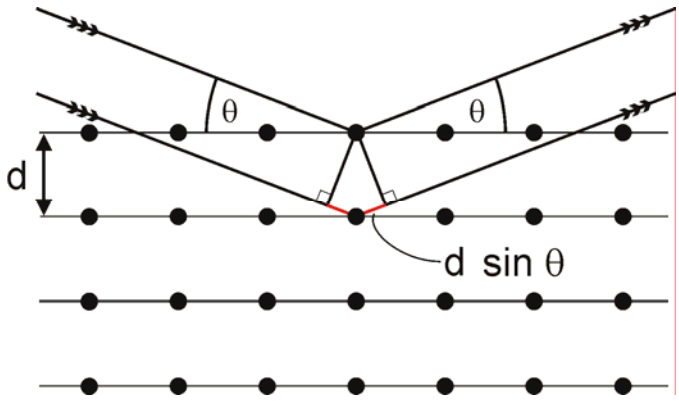

Figure 2.1. Diffraction on one set of lattice planes, according to W. L. Bragg.[4]

Hence, each reflection in the XRD pattern is caused by scattering of X-rays on one particular set of crystal planes. The position of a reflection results from the respective distance of the repeat units, the *d* spacing, which depends solely on the geometry of the crystal's unit cell. The relative intensity of the signals depends on the type of atoms in the crystal and their location in the unit cell.[5] Each crystalline material has, within limits, a unique diffraction pattern as its "fingerprint". Today, the XRD patterns for all known crystalline materials are recorded in databases for convenient assignment of spectra (e.g., the JCPDS catalog).

When measuring nanometer-sized objects, the number of lattice planes within one crystallite is no longer practically infinite, as in large crystals. This results in a significant broadening of all reflections. In turn, there is a possibility to determine the crystallite size from the XRD pattern. Even though nowadays detailed and complex analysis techniques exist to evaluate XRD patterns with respect to crystallite size and strain effects within the crystals,[6] in this work only a very basic approach is used. The *integral breadth* of a single reflection, defined as the width of a rectangle having the same area A and height I_0 of the observed line profile, or

$$\beta = A / I_0 \qquad \text{(Eq. 2.3)}$$

can be used as a measure of dispersion of the reflection. With *b* as the instrumental line broadening which can be determined by measuring a reference material of high crystallinity and large crystallite size, the line broadening caused by the sample is, in first approximation, calculated as $\beta' = \beta - b$. The size of the crystallites τ can then be calculated using the Scherrer equation:[7]

$$\tau = \frac{K\lambda}{\beta' \cos\theta} \qquad \text{(Eq. 2.4)},$$

K being the shape factor which usually is assumed as 0.9.[2]

The setup for the measurement of powders is rather straightforward. The X-rays are produced in a vacuum X-ray tube, using a tungsten filament as electron source. The electrons are accelerated onto a copper anode where they induce the emission of X-ray irradiation. Due to they small wavelength, X-rays cannot be focused by lenses but only using slits (causing a great loss in intensity). Soller slits lead to irradiation with minimized lateral (axial) divergence. The scattered irradiation is again narrowed by slits and eventually enters the detector.

Two different diffractometers were used, showing differences regarding the geometry and setup. One device featured a one-dimensional curved position sensitive detector spanning the whole angular range 2θ = 10-110°. Such detectors are basically proportionation counters, airtight chambers filled with a gas such as Ar. As X-ray irradiation enters the chamber (usually through a beryllium window) and hits a gas atom, the atom loses an electron which is accelerated onto an anode wire and registered there as a voltage pulse. The electrons are collected at the two ends of the wire and amplified to result in the output signal. If a bad conductor material is used as anode wire, the signal reaches the ends of the wire at different points of time, depending on the position where the signal was initiated.

The second device featured a scintillation counter as detector, which can only detect one angular position at one time. To record the whole diffractogram, step-scaning must be performed, where both the X-ray source and the detector are moved simultaneously (but in opposite direction) along a circle (the goniometer circle) around the sample. Thereby, the angle of incindence (towards the horizontal sample) equals the scattering angle (θ-θ geometry). The sample itself remains in a horizontal position. A scintillation counter features a scintillation crystal (typically Tl-doped NaI) which absorbs X-ray irradiation and emits lower-energy light, which is detected in a subsequent photomultiplier.

2.2 Microscopy

Since the first microscope was built some 380 years ago by Dutch glassmakers, the possibility to observe minuscule objects has become an indispensable means of all areas of pure and applied natural sciences. Great improvements have been achieved, especially by A. van Leeuwenhoek, E. K. Abbe, C. Zeiss and R. A. Zsigmondy, opening up the possibility to visualize smaller and smaller objects.[8] However, there is a fundamental limit to the resolution of light microscopy of about 200 nm. To directly depict smaller objects, one has to use different kinds of radiation. Electron microscopy has become a widespread characterization

tool, by which objects in the Angström-size regime can be visualized (as in the case of HR-TEM).

2.2.1 Transmission Electron Microscopy (TEM)

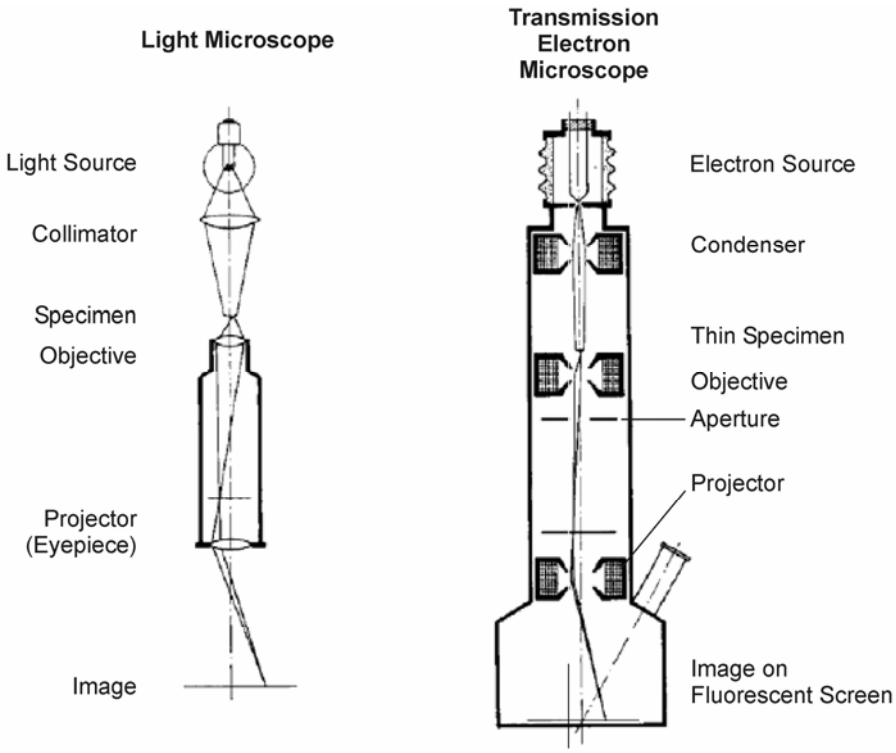

Figure 2.2. Major components of a light microscope (left), and of a TEM device (right).

The general setup of a TEM device is comparable to a light microscope, as illustrated in Figure 2.2. Electrons are produced either by thermoionic emission using a heated filament (e.g., LaB_6) or in a field emission gun from a fine tungsten tip, and are accelerated towards an anode.[9] The resulting electron beam is focused using electromagnetic lenses. Its divergence and beam width is minimized by a condenser slit before hitting the sample, which is located under high vacuum on a copper grid as sample holder. The electrons have to pass through the sample, however the penetration depth of electrons into solid materials is very limited (ca. 100 nm). Therefore, only very thin samples can be used. The electrons may undergo several kinds of interaction with the solid material, namely absorption, diffraction, and elastic or inelastic scattering. Scattering processes result from interaction of the electrons with nuclei of the sample. Heavy elements therefore lead to higher scattering, which results in fewer electrons reaching the image plate. Hence, sample regions containing these elements appear dark. Conversely, areas only containing light elements, such as in organic compounds, result in limited scattering of electrons and appear bright. The contrast between these areas is

improved by removing inelastically scattered electrons from the beam after sample penetration, using an aperture. The electron beam then passes further magnetic lenses for magnification and finally hits a fluorescent screen coated with CdS and ZnS. The resulting irradiation is recorded by a CCD camera.

As the kinetic energy of a charged species being accelerated in an electric field is equal to its charge multiplied by the acceleration voltage *U*, the electrons hitting the specimen in the TEM device possess a velocity v according to

$$v = \sqrt{\frac{2Ue}{m_e}} \qquad \text{(Eq. 2.4).}$$

Therefore, the used acceleration voltage of 120 kV leads to electrons traveling at $2 \cdot 10^8$ m s^{-1}, with the electron mass $m_e = 9.1 \cdot 10^{-31}$ kg and its charge $e = 1.6 \cdot 10^{-19}$ C.

The de Broglie equation relates the wave properties to the particle properties through

$$\lambda = \frac{h}{mv} \qquad \text{(Eq. 2.5).}$$

The wavelength of the electron beam can thus be calculated to $3.5 \cdot 10^{-12}$ m = $3.5 \cdot 10^{-3}$ nm.

The resolution *g* of a microscope is related to the wavelength of the used irradiation, employing Abbé's law,

$$g = 0.61 \frac{\lambda}{n \sin \alpha} \qquad \text{(Eq. 2.6).}$$

Whilst *n* is the refractive index, and α the aperture angle, the product $n \sin \alpha$ is referred to as the numeric aperture of the microscope. For the used microscope, the numeric aperture was 0.014, resulting in a theoretical resolution of 0.15 nm.

2.2.2 Scanning Electron Microscopy (SEM)

SEM is probably the most widely used technique for surface analysis. The specimen, which is often coated with a metal such as gold prior to the measurement to achieve better contrast, is placed in a vacuum chamber. A focused electron beam is then scanned across its surface in synchronism with the spot of a display cathode ray tube. A detector monitors the intensity of a

chosen secondary signal from the specimen (usually, secondary electrons are used), and the brightness of the spot on the display is determined by an amplified version of the detected signal. If the intensity of the emitted secondary signal changes across the specimen, then contrast will be seen in the image on the cathode ray tube. The resulting image reflects the surface topography of the specimen and can be readily interpreted because it contains light and shade in much the same way as everyday images which are familiar to our eye.[10]

2.2.3 Atomic Force Microscopy (AFM)

The AFM technique, after its invention in 1986 by Binnig, Quate and Gerber,[11] has quickly become a widespread tool for the analysis of surfaces on atomic and molecular scale. It makes use of a fine tip which mechanically scans the sample surface. Silicon is the most common material for AFM tips, featuring a tip radius of 10-20 nm. The tip is pressed on the specimen via a cantilever. As the specimen is moved by piezoelectric actuation devices, the tip remains horizontally steady but vertically follows the surface topography of the sample. On the back side of the cantilever, a laser beam is reflected. A position sensitive photodiode detects the reflected beam and thus the vertical deviation of the tip is determined at an accuracy of as low as 0.1 nm.[12]

The interaction between the tip and the sample can be approximated with the Lennard-Jones potential (α and β being constants)

$$V = \frac{\alpha}{r^{12}} - \frac{\beta}{r^{6}} \qquad \text{(Eq. 2.7).}$$

As the tip approaches the surface, first a attractive van-der-Waals interactions come into effect (dependent on r^{-6}). Upon touching, the electron shells are compressed resulting in strongly repulsive forces (r^{-12}).

Several measurement modes have been established. Whereas in contact mode almost atomic resolution is achieved, only small regions with a relatively plain surface can be measured. Soft surfaces can even be altered or destroyed by the measurement. Therefore, a tapping mode measurement was established.[11,13] In this case, the tip is held in oscillation in a distance of 2-20 nm to the sample surface. The frequency of this oscillation is close to its eigenfrequency ω_0. Van-der-Waals interactions occur between the sample and the tip at this lengthscale and cause the resonating frequency to slightly differ by $\delta\omega = \omega - \omega_0$ and hence the amplitude to

decrease. The distance between tip and surface can then be calculated from the amplitude deviation.

2.3 Analytical Ultracentrifugation (AUC)

AUC was first used for the analysis of small particles as early as in 1923 by T. Svedberg,[14] however soon becoming a widespread method for the analysis of polymeric systems. Its application for the analysis of colloidal systems became more or less forgotten for decades, even though it constitutes a suitable technique, with significant advantages over microscopic techniques, such as detection of the whole sample, eliminating statistical problems, and the absence of a drying step that might cause artifacts.[15] Furthermore, AUC has been shown to possess almost atomic resolution.[16]

An analytical ultracentrifuge features several optical detection systems, usually employing UV-Vis absorption optics and/or Rayleigh interference optics. To obtain a particle size distribution by AUC, a so-called sedimentation velocity experiment is performed, where a homogeneous solution/dispersion of the particles is subjected to high centrifugal fields.[15] Here, the particles sediment according to their mass and size, density and shape, without significant back diffusion. The radial concentration profile is observed over time and can be transformed into a sedimentation coefficient distribution according to

$$s_i = \frac{\ln(r_i / r_m)}{\omega^2 t} \qquad \text{(Eq. 2.8)},$$

where ω is the angular velocity of the rotor, t the time, r_i the radial distance to the center of rotation for a particle fraction i, and r_m the radial distance of the meniscus.[16]

Assuming the validity of Stoke's law (i.e., the particles are spherical), an absolute particle size distribution can be obtained by

$$d_i = \sqrt{\frac{18\eta s_i}{\rho_p - \rho}} \qquad \text{(Eq. 2.9)},$$

with η as the solvent viscosity, ρ_p the density of the particles, and ρ the density of the solvent.[16] Even though the accurate determination of the particle size distribution thus highly relies on the knowledge of the density of the sedimenting particles, including species adhering to the particle surface, which for small nanoparticles is a severe problem, and the obtained

size distributions are widened by diffusive peak broadening, AUC is a valuable, straightforward technique for obtaining statistical information on the size and aggregation state of inorganic nanoparticles. Nanoparticulate powders which cannot be dispersed in an adequate solvent due to their too high aggregation tendency, however, are not suitable for analysis by AUC.

2.4 References

[1] C. Kittel, *Introduction to Solid State Physics*, J. Wiley & Sons, New York, **1986**.

[2] R. Allmann, *Röntgenpulverdiffraktometrie*, Verlag Sven von Loga, Köln, **1994**.

[3] E. Zobetz, *Lecture Notes: Kristallographie II*, Vienna University of Technology, Vienna, **2001**.

[4] W. L. Bragg, *Nature* **1912**, *90*, 410.

[5] J. A. Dean, *Analytical Chemistry Handbook*, McGraw-Hill, New York, **1995**.

[6] R. Delhez, T. H. de Keijser, E. J. Mittemeijer, *Fresenius Z. Anal. Chem.* **1982**, *312*, 1.

[7] P. Scherrer, *Nachr. Ges. Wiss. Göttingen* **1918**, 96.

[8] J. Falbe, M. E. Regitz, *Römpp Chemie Lexikon*, 9th Ed., Georg Thieme Verlag, Stuttgart, **1991**.

[9] L. Reimer, *Scanning Electron Microscopy*, Springer Verlag, Berlin, **1985**.

[10] D. Chescoe, P. J. Goodhew, *The Operation of Transmission and Scanning Electron Microscopes*, Oxford University Press, Oxford, **1990**.

[11] G. Binnig, C. F. Quate, C. Gerber, *Phys. Rev. Lett.* **1986**, *56*, 930.

[12] D. A. E. Bonnell, *Scanning Tunnelling Microscopy and Spectroscopy*, VCH, New York, **1993**.

[13] Q. Zhong, D. Inniss, K. Kjoller, V. B. Elings, *Surf. Sci. Lett.* **1993**, *290*, L688.

[14] T. Svedberg, J. B. Nichols, *J. Am. Chem. Soc.* **1923**, *45*, 2910.

[15] H. Cölfen, *ACS Symp. Ser.* **2004**, *881*, 119.

[16] H. Cölfen, T. Pauck, *Colloid Polym. Sci.* **1997**, *275*, 175.

3 Nonaqueous Synthesis of $BaTiO_3$ Nanoparticles

3.1 Introduction to Ferroelectric Materials

$BaTiO_3$ is probably the best-known ferroelectric oxide.[1] The ferroelectricity is based on its perovskite crystal structure. Other materials which will be presented later in this work also possess the perovskite structure, e.g. $PbTiO_3$ (cf. Chapter 7) or $KNbO_3$ (Chapter 8), and also exhibit ferroelectric properties. Therefore, a short introduction to the phenomenon of ferroelectricity is given here with the example of $BaTiO_3$.

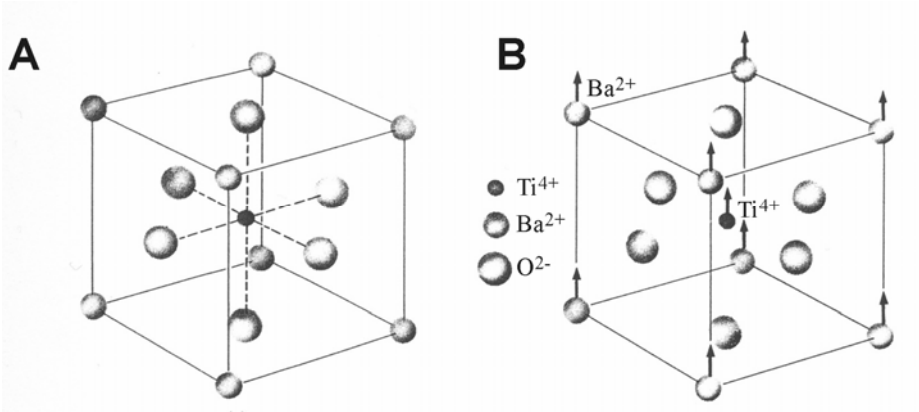

Figure 3.1. The crystal structure of barium titanate. Above T_c, the structure is cubic (**A**), whereas below, the structure is deformed, leading to spontaneous polarization (**B**).[2]

The crystal structure of barium titanate is illustrated in Figure 3.1. At temperatures above the so-called Curie temperature, T_c, of 135 °C, the structure is perfectly cubic, with the Ti^{4+} ion in the center of the cube, the Ba^{2+} ions on the corners, and O^{2-} in the face centers (Fig. 3.1 **A**), and the material is paraelectric. At lower temperatures (Fig. 3.1 **B**), the Ba^{2+} and Ti^{4+} ions are shifted with respect to the O^{2-} ions, thereby developing a polarization (net dipole moment) of 26 μC cm^{-2}.[3] This shift breaks the cubic symmetry, resulting in six symmetry-equivalent variants with polarizations along the x, y, or z directions.[4] For bulk systems, the polarization is usually not uniformly aligned along the same direction throughout the whole crystal but only within a region which is called a ferroelectric domain. The various domains within one crystal are separated by domain walls.[5] An example for a 90° domain wall is given in Figure 3.2 **A**. Initially, the domains within one crystal are randomly oriented, resulting in a net polarization P_R of zero (Fig. 3.2 **B**, left, P_R refers to remanent polarization, i.e. after removal of any external field). The ferroelectric domains can be oriented by a so-called poling process, where a high electric field is applied at elevated temperature. This causes the molecular dipoles in the material to align more or less in the field direction. As the material is cooled

whilst maintaining the strong field, the dipoles are fixed into the aligned orientation.[1] After the poling process, still many domain walls are present, P_R however differs from zero (Fig. 3.2 **B**, right).[5]

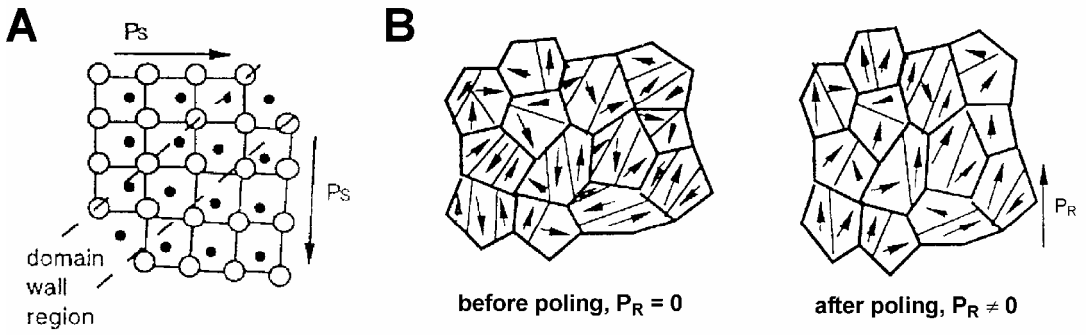

Figure 3.2. Schematic view of a 90° domain wall (**A**, P_s…spontaneous polarization), and illustration of the effect of poling on a polycrystalline ferroelectric with random orientation of domains (**B**).[5]

The most important characteristic of ferroelectrics is polarization switching by an external field. The direction of the polarization is stable when the field is removed. This renders ferroelectrics interesting materials for electro-optical devices and for memory storage. Enormous storage densities could be achieved using ferroelectrics, however the potential of this device was not fully realized for several reasons, including fatigue phenomena.[3] In view of the current strong trend towards miniaturization, the fascinating potential of ferroelectric oxides is that in principle, they can be made to operate on atomic scales.[4]

3.2 Synthesis in Benzyl Alcohol

3.2.1 Introduction

In view of the importance of $BaTiO_3$, it is not surprising that a variety of methods for its synthesis have been developed, e.g. coprecipitation processes,[6,7] thermal decomposition of metal-organic precursors,[8,9] and sol-gel procedures using titanium alkoxides and barium salts or alkoxides.[10-12] Another intensively studied synthesis pathway is the hydrothermal treatment of a titania source, such as titanium alkoxide, titanium oxide, or titanium oxide gels in the presence of barium salts such as barium halides, acetate, nitrate or hydroxide in strongly alkaline solutions.[13-15]

All these preparation methods resulted in the formation of particles being a few hundreds to a few tens of nanometers in size. However, $BaTiO_3$ particles smaller than 10 nm and nearly

spherical in shape are of particular interest for several reasons. First of all, polycrystalline $BaTiO_3$ with grain sizes < 100 nm is, in contrast to the bulk material, nonferroelectric and stabilized in the cubic structure at room temperature resulting in stable dielectric properties.[16-18] This so-called size effect is still not clearly understood,[19] but has been suggested to be mostly caused by strain effects induced by grain boundaries and cracks or pores, often as a result of the preparation process and to a large extent not being intrinsic.[20-23] A simple synthesis route to nanocrystalline $BaTiO_3$ in gram quantities would facilitate further investigations on the precise nature of ferroelectricity in dependence of the particle size. Another important reason for having $BaTiO_3$ in a nanocrystalline form is the current trend to miniaturization in the fabrication of nanodevices with improved properties and high reliability. For all these applications, it is a key requirement that the $BaTiO_3$ powder is easily processed into defect free thin films.[24] Furthermore, powders with uniform and fine particle sizes provide good sinterability, an essential property for the formation of advanced ceramic materials.[25] A powder in the nanometer size regime, non-aggregated, possessing high purity and compositional homogeneity, would constitute a "perfect" precursor, e.g. for the fabrication of multi-layer ceramic capacitors, but is still not commercially available.[26]

In this chapter, a novel nonaqueous synthesis approach to $BaTiO_3$ nanoparticles is presented by a solvothermal reaction in benzyl alcohol, which has already shown to be a versatile reaction medium for the synthesis of transition metal oxide nanoparticles with good control over particle size, shape and crystallinity.[27,28] Without the use of any additional ligands or templates, the crystal growth is highly controlled. To investigate the role of the solvent during the formation and growth of the oxide, the reaction mechanism was studied in detail.

3.2.2 Results and Discussion

All synthesis steps were carried out in a glovebox to rule out the possibility of influence of oxygen or moisture. In a first step, metallic barium was reacted with anhydrous benzyl alcohol at elevated temperature (70-100 °C), to form barium benzyl alcoholate under release of hydrogen, which was clearly visible by the formation of H_2 bubbles. Although many bivalent alkoxides are reported as insoluble in alcohols, in the case discussed here, a clear yellowish, homogeneous solution was obtained. The solution was transferred into an autoclave, which was sealed, taken out of the glovebox and heated in an oven at 200 °C for 2 d. Note that 200 °C is still below the boiling point of benzyl alcohol (205 °C). Therefore, the reaction actually takes place under subsolvothermal conditions. However, if the reaction is performed

in an open reaction vessel at 200 °C under ambient pressure, only a white precipitate mainly amorphous in nature is formed instead of crystalline perovskite nanoparticles.

The crystallinity of the resulting particles was analyzed by XRD. A typical powder diffractogram of as-synthesized $BaTiO_3$ particles is given in Figure 3.3, **A**. All diffraction peaks can be assigned to the $BaTiO_3$ phase (JCPDS No. 31-174) without any indication of crystalline byproducts such as $BaCO_3$ or TiO_2. The powder pattern in the region $2\theta = 40\text{-}50°$ is usually characteristic for the presence of either the cubic or the tetragonal $BaTiO_3$ structure.[29] However, in the present case the reflections are too broad to discriminate between the two crystal modifications due to the small particle size.[30]

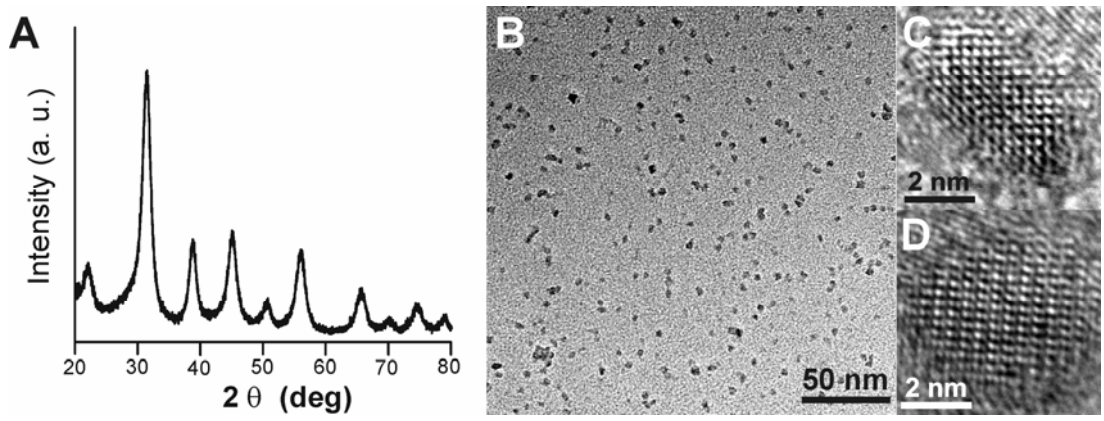

Figure 3.3. Analysis of as-prepared $BaTiO_3$ particles obtained by solvothermal treatment in benzyl alcohol: powder XRD pattern (**A**) overview TEM image (**B**), and HRTEM micrographs (**C** and **D**).

The $BaTiO_3$ powder was further characterized by TEM. A representative overview image (Fig. 3.3 **B**) at low magnification illustrates that the sample entirely consists of nanosized individual barium titanate particles without the presence of larger particles or agglomerates. Images at higher magnification of isolated nanocrystals (Fig. 3.3 **C** and **D**) show sets of lattice fringes, giving additional evidence that the particles are highly crystalline. The particles are quite uniform in size and shape and mostly spherical. Typically, the particle diameter ranges from 4 to 8 nm.

Most non-hydrolytic pathways to titania reported so far involve the reaction of titanium tetrachloride with either a metal alkoxide or an organic oxygen donor such as diisopropyl ether.[31] In these routes, the formation of the Ti–O–Ti bonds results from the condensation between Ti–Cl and M–OR functions, where M is either a titanium atom[32,33] or an organic

alkyl group.[31,34] However, in our reaction system there are no halides present. A possible reaction pathway for halide-free systems involves an aprotic condensation reaction, where the formation of an oxo bridge is provided by eliminating an organic ether:[34]

$$\equiv M\text{–}OR \; + \; RO\text{–}M\equiv \; \rightarrow \; \equiv M\text{–}O\text{–}M\equiv \; + \; R\text{–}O\text{–}R.$$

This ether elimination route was suggested as possible pathway for the formation of metal oxides by reacting metal alkoxides with each other.[34] However, it was never reported for the formation of transition metal oxides, as this process was much less employed as compared to the ester and alkyl halide elimination routes.

In order to elucidate the reaction mechanism of the $BaTiO_3$ nanoparticle formation, a synthesis was performed with a particularly small amount of benzyl alcohol (ratio of benzyl alcohol to Ba of 7) to facilitate the identification of the formed organic compounds. The reaction mixture was centrifuged to remove the $BaTiO_3$ precipitate, the supernatant liquid additionally filtered and then analyzed by ^1H and ^{13}C-NMR spectroscopy and by coupled gas chromatography – mass spectrometry (GC–MS). We thank Dr. I. Starke, Chemisches Institut der Universität Potsdam, for carrying out all GC–MS measurements.

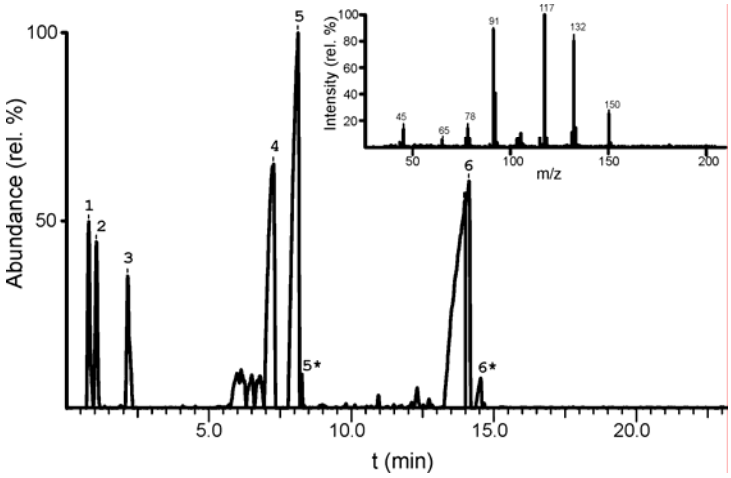

Figure 3.4. Gas chromatogram of the final reaction solution; ***inset***: mass spectrum of peak **5** (see text for assignment).

Figure 3.4 shows the results of the gas chromatography measurements for the filtered reaction mixture. The individual signals were identified by evaluation of the respective mass spectra. Signal **1** corresponds to isopropanol, and **2** stems from hexane used as solvent for the chromatography (the main hexane peak was blinded out). The mass spectrum of peak **3** can be clearly assigned to toluene, peak **4** to benzyl alcohol. The assignment of signal **5**, representing the main product, is discussed below. Peak **6** is identified as 1,5-diphenyl-3-pentanol. The signals **5*** and **6*** correspond to the ketones 4-phenyl-2-butanone and 1,5-diphenyl-3-pentanone, respectively. It is interesting to note that the initially expected organic ethers such as benzyl ether, isopropyl ether and benzyl isopropyl ether are found only in small quantities.

The recorded mass spectrum of peak **5** is shown in Fig. 3.4, inset. The spectrum matches well with 4-phenyl-2-butanol. The M^+ peak appears at m/z 150, whereas the peak at m/z 132 corresponds to the dehydrated fragment $[M - H_2O]^+$. Cleavage of the α'-methyl group and additional dehydration leads to m/z 117. The m/z 91 signal can be assigned to the stabilized benzyl fragment $[C_7H_7]^+$. The less favored α-cleavage leads to the peaks at m/z 105 and m/z 45, whereas m/z 78 corresponds to the phenyl fragment. The spectrum is in excellent accordance to reference spectra for 4-phenyl-2-butanol found in the Integrated Spectral Data Base System for Organic Compounds.[35]

The reaction mixture was also analyzed by ^{13}C-NMR spectroscopy (Figure 3.5 **A**). Benzyl alcohol is present in excess, therefore the corresponding peaks (labeled **BA**) are dominant. The unsubstituted aromatic carbon atoms appear at 126.9-128.3 ppm, whereas the aliphatic peak is visible at 64.8 ppm. Isopropanol causes the prominent peak at 25.3 ppm; the signal of the secondary carbon (expected at 64.0 ppm) is superimposed by the benzyl alcohol peak, but it is still visible as a shoulder. All peaks of the main reaction product, 4-phenyl-2-butanol, can be seen in the spectrum. However, the aromatic carbon atoms labeled **6** appear at positions very close to the BA peaks, leading to the signal at 125.5-128.5 ppm. The substituted aromatic position (peak **5**) appears now at 142.6 ppm, which constitutes further deshielding (compared to 141.5 ppm for the corresponding position in benzyl alcohol) caused by the larger alkyl moiety bound to the aromatic system. The aliphatic peaks are nicely visible at 23.6, 32.3, 41.0 and 67.3 ppm (peaks **1** – **4**). The peaks marked **D** are caused by the di-substituted product 1,5-diphenyl-3-pentanol, as verified in NMR simulations, whereas the peak marked **T** at 21.4 ppm can be clearly attributed to toluene. The ketone products identified by GC–MS could not be detected in the NMR spectrum due to their small amount present in the reaction solution.

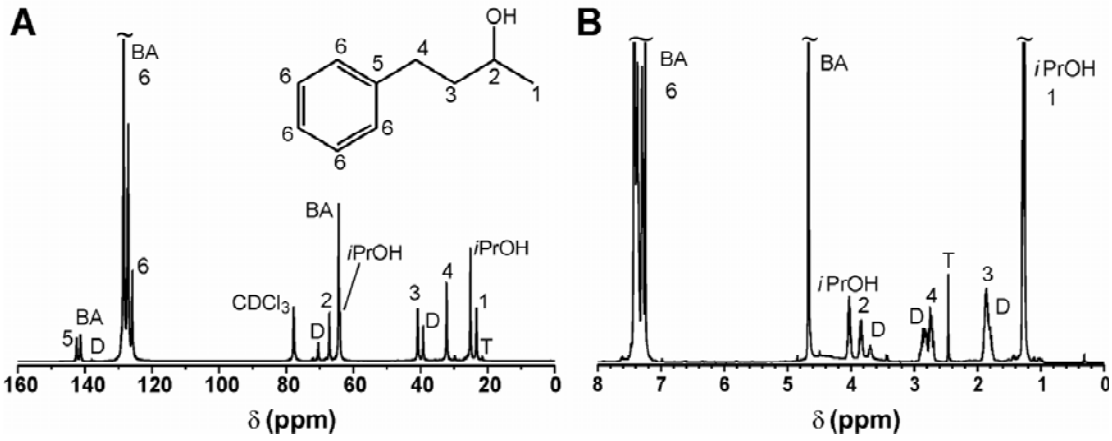

Figure 3.5. ^{1}H-BB-decoupled ^{13}C-NMR (**A**) and ^{1}H NMR spectrum (**B**) of the filtered reaction solution measured in $CDCl_3$.

The ^1H NMR spectrum confirms these results (Fig. 3.5 **B**). The labeling is according to the assignments in the ^{13}C spectrum. Whereas the aromatic hydrogen signals of 4-phenyl-2-butanol are superimposed with the benzyl alcohol signals in the region 7.1-7.8 ppm, the aliphatic CH and CH_2 signals are clearly visible at 3.83, 2.75 and 1.86 ppm, respectively. The shoulders are caused by the disubstituted product. The $–CH_3$ group is superimposed by the isopropanol signal at 1.23 ppm, however calculation of the product ratios is easily possible by subtracting the isopropanol contribution as determined from the second *i*PrOH signal at 4.01 ppm. The product ratio hence was calculated to 1.0 isopropanol : 0.75 4-phenyl-2-butanol : 0.15 1,5-diphenyl-3-pentanol : 0.13 toluene.

These results are surprising, since it was expected that nonaqueous condensation reactions between metal alkoxides and alcohols should occur via an ether elimination pathway.[34] Furthermore, to the best of our knowledge, up to now there is no reaction known in metal-organic chemistry leading to the formation of an alkyl C–C bond between an alcohol and the β-position of a simple metal alkoxide. However, it is known for years that C–H bonds can be activated by the coordination of organic molecules to metal centers,[36] and a great deal of research has been carried out to study these activations.[37] Aldol addition, one of the most prominent reactions to form C–C bonds, can be catalyzed and even stereochemically controlled by using titanium alkoxides.[38-40] The direct formation of aryl C–C bonds via activation with transition metals has been shown for *tert*-butyl groups using palladium.[41] Only recently, there has been one report of the direct reaction of $Ti(O\mathit{t}Bu)_4$ with aldehydes leading to the formation of diols and triols under the influence of lithium salts, and barium salts were reported to react similarly;[42] however, these results were corrected later.[43] The formed products actually were not diols or triols but substituted tetrahydropyranols, and were assumed to be formed via an elimination–addition mechanism, interestingly occurring only in the presence of $LiClO_4$.[44] In our case, as benzyl alcohol was used as solvent, not a diol but a simple alcohol is formed, which cannot condensate to form pyranolic structures. Moreover, the presence of such structures would have been clearly detected by GC–MS.

We propose a reaction mechanism according to Scheme 3.1. The resulting C–C bond can conceivably only be formed via a nucleophilic attack of a β-carbon atom of the isopropoxide onto the benzyl group which is activated by an interaction of the alcohol –OH group with Ti. Hence, in a first step, benzyl alcohol is assumed to coordinate to a Ti atom forming a five-fold coordination complex. Upon coordination, the C–O bond of the benzyl alcohol is weakened, and the resulting benzylic carbon atom is highly electrophilic and activated toward

nucleophilic attack. In a next step, one of the two β-carbon atoms of the isopropoxy group is formally deprotonated (**1**). The role of the base is most probably played by the benzyl alcoholate, which was produced from the reaction between metallic Ba and benzyl alcohol. This is supported by the fact that the formation of 4-phenyl-2-butanol occurs only in the presence of Ba. Furthermore, it is a notable feature of this reaction that deprotonation does not occur on the α-carbon atom, but on the β-sites, only. This means that this deprotonation is supported by a stabilizing effect of the C–Ti interaction, as indicated by the dashed line (**2**). This interaction, similar to an agostic bond,[36] leads to a fully, six-fold coordinated Ti center. Due to the sterical proximity of the benzyl group and the formal carbanion at two neighboring sites of the intermediate titania octahedron, the nucleophilic attack is expected to occur quite fast, resulting in the formation of a titania complex with coordinated 4-phenyl-2-butoxide (**3**) and an –OH group. This –OH group later on promotes further condensation of the titanium monomer to Ti–O–Ti species via alcohol elimination, finally leading to the oxidic nanoparticles. To the same degree as the inorganic crystal formation, this process leads to the release of the alcohol (**4**). The presence of smaller amounts of 1,5-diphenyl-3-propanol in the reaction mixture shows that the other methyl group of the isopropoxide ligand can react with another benzyl group in analogous manner, however, due to the sterical hindrance this reaction proceeds at lower reaction rates.

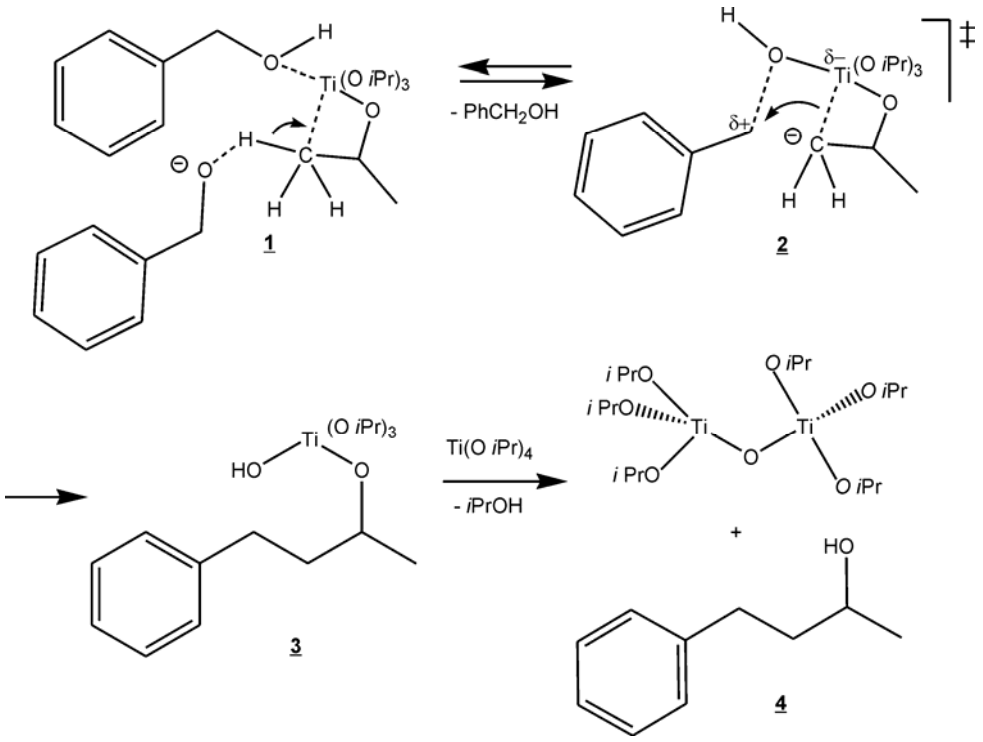

Scheme 3.1. Proposed reaction mechanism for the simultaneous formation of $BaTiO_3$ nanoparticles and 4-phenyl-2-butanol.

In principle, it is also conceivable that the mechanism for this coupling reaction proceeds via different pathways, for example an elimination–addition mechanism, involving the transient formation of propene, or a radical mechanism. Other theoretical possibilities include the formation of barium and titanium-containing clusters which catalyze the C–C coupling reaction. These mechanisms are however rather improbable, as additional experiments indicated which are discussed in detail in Chapter 9.

As stated above, the final molar ratio of *i*PrOH to 4-phenyl-2-butanol is approximately 1 to 0.75, whereas the postulated mechanism would lead to a ratio of 1. This speaks for the high efficiency of this reaction pathway and the high coupling yields; the differences are presumably due to the existence of another, also novel side reaction. The presence of toluene in the final solution gives evidence that this side reaction most probably involves a hydride transfer, similar to the Meerwein-Ponndorf-Verley (MPV) reaction. The absence of acetone in the system shows that oxidation of an isopropoxide group does not occur, i.e., the medium is essentially reductive. However, higher ketones such as 4-phenyl-2-butanone and 1,5-diphenyl-3-pentanone have been detected in the system by GC–MS.

Scheme 3.2 gives a possible mechanism of this side reaction of toluene and ketone formation starting with complex **3** from Scheme 3.1. In a first step, another benzyl alcohol molecule coordinates to the titanium, once again creating a strongly electrophilic benzylic carbon atom. The next reaction step (**4***) involves a hydride transfer from the α-carbon atom, similar to the MPV reduction. The main difference to an MPV reaction, however, is that no aldehyde or ketone was used. Here, the reduction of an alcohol, namely benzyl alcohol, by oxidation of another, the 4-phenyl-2-butanol, resulted in the formation of toluene and 4-phenyl-2-butanone (**5***). Of course, also for this reaction a mediating influence of Ba^{2+} ions is possible. On the other hand, one must take into account that the synthesis is performed at, in terms of organic chemistry, high temperatures of 200 °C, and in the presence of active titania clusters or nanoparticles, being able to catalyze various kinds of organic reactions. The disproportionation of benzyl alcohol, for example, is known to occur at 300 °C on alumina surfaces.[45]

1,5-Diphenyl-3-pentanone is assumed to form in a similar way starting from Ti-coordinated 1,5-diphenyl-3-pentanol. The obtained ratio of the diphenylketone to the monophenylketone was much higher than the ratio of 1,5-diphenyl-3-pentanol to 4-phenyl-2-butanol, suggesting that the hydride transfer is preferred for those species through stabilization effects of the benzyl substitution, i.e., 1,5-diphenyl-3-pentanol is the better reducing agent. This view also

explains the strict absence of acetone in the system. The molar ratio of toluene to 4-phenyl-2-butanol in the final solution was calculated from ^{1}H-NMR to be about 1 : 6. This finding explains half of the missing yield of 4-phenyl-2-butanol.

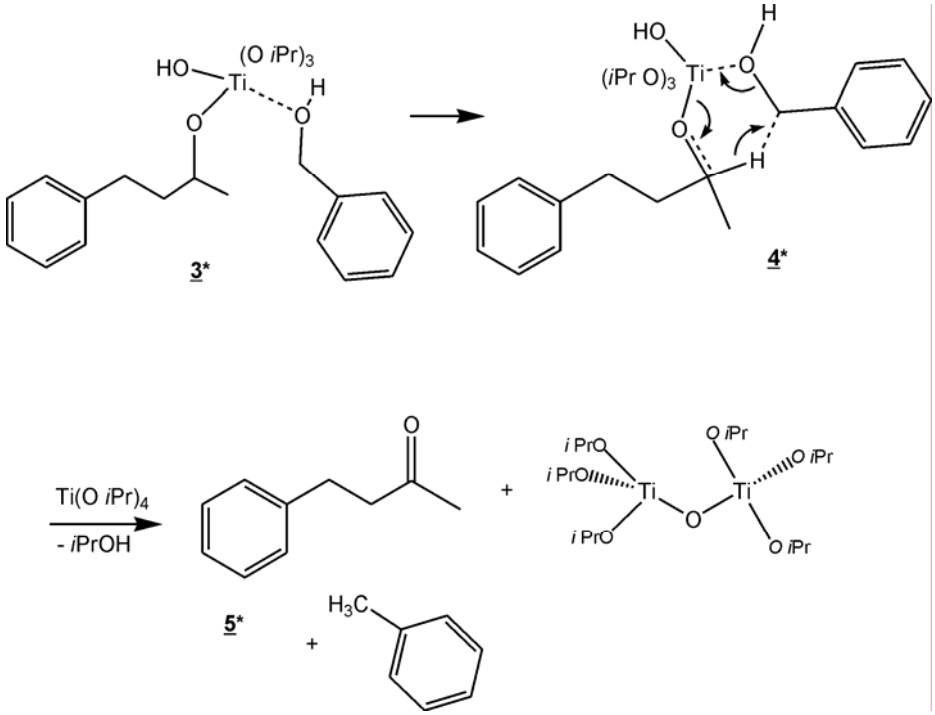

Scheme 3.2. Suggestion of a side reaction mechanism, somewhat similar to the Meerwein-Ponndorf-Verley reaction, leading to the simultaneous formation of toluene and 4-phenyl-2-butanone.

Vice versa, the strong but reversible binding of titanium to the different aromatic alcohols also explains the extraordinary quality and high colloidal stability of the final oxidic nanoparticles. It is to be assumed that their surface is tightly covered with these alcohols, presumably via unhydrolyzed Ti–O–R groups.

3.3 Synthesis in Ketones

3.3.1 Introduction

The results shown above are rather surprising, as they indicate that also other mechanisms than the expected ether elimination can lead to the formation of metal oxides in the absence of water. Based on these findings, also the synthesis in organic media other than alcohols or ethers becomes conceivable, which offers a host of new possibilities for the controlled nonaqueous synthesis of oxides in the nano-size regime.

Even though the benzyl alcohol route to $BaTiO_3$ nanoparticles presented above is versatile and well-suited for the large-scale production of particles in the size regime of 4-6 nm, it is difficult to control the particle size using this approach. Neither changing the concentration of the reactants nor varying the temperature of the solvothermal treatment influenced the size of the nanoparticles considerably.

Therefore, it appeared promising to investigate the possibilities of solvothermal synthesis in organic solvents others than alcohols. Ketones, for example, represent an interesting class of organic reaction media, as they are cheap and almost nontoxic. Due to their aprotic character, the reaction with metal alkoxides is slower than for alcohols, opening up the possibility for better control over particle nucleation and growth processes. The formation of oxides, however, requires the supplementation of oxygen from the solvent, which is therefore termed "oxygen-supplying agent". These processes have hardly been explored. Alternatively, also a decomposition of the alkoxide ligand is theoretically possible and has been suggested for TiO_2 syntheses in solvents like toluene, however it was never proven or studied in detail.[46,47] A few examples of the formation of metal oxide species in ketones have been reported, such as the formation of ZnO gels[48] and $BaTiO_3$ powders[49] in acetone.

3.3.2 Results and Discussion

As in the benzyl alcohol system, metallic barium was used as precursor, and was dissolved in the reaction medium in a first step. Using anhydrous ketones, the dissolution process was slower than in the alcohol, and had to be performed at elevated temperatures. In acetophenone, a red-brown solution was obtained, whereas a turbid white liquid formed when reacting Ba with acetone. Hydrogen bubbles were observed in both cases, indicating that the Ba reacted with the enol tautomer of the solvent to give barium enolate.

Only the acetone and acetophenone systems will be discussed here as they led to the best results. A range of temperatures was explored for acetone, but in each case impurities, in particular crystalline $BaCO_3$, were present in the XRD patterns of the samples after washing. Figure 3.6 **a** shows the pattern of a sample prepared at 130 °C. The reflections corresponding to $BaTiO_3$ are marked *. In addition, small barium carbonate (*C*) reflections are present. The other signals are caused by organic side products (*O*). It is clearly visible that the crystallites are larger here than for $BaTiO_3$ obtained in benzyl alcohol (cf. Fig. 3.3). Using the Scherrer equation, the particle size was calculated to 10.5 nm from the (111) reflection at $2\theta = 38.9°$. The sample obtained in acetophenone at 180 °C gave optimum results in terms of phase-purity

of $BaTiO_3$ (Fig. 3.6 **b**). Aside from a small $BaCO_3$ peak, all other impurities are absent. The signals are slightly broader here than in the acetone system, indicating smaller crystallites. The cubic and tetragonal $BaTiO_3$ structure can be discriminated in the region 2θ = 40-50°. The cubic 200 signal is split into 200 and 002 reflections in the tetragonal modification.[50] In the case of acetophenone, the presence of a single peak points to cubic $BaTiO_3$, however the peaks still may be too broad to allow an unambiguous assignment.

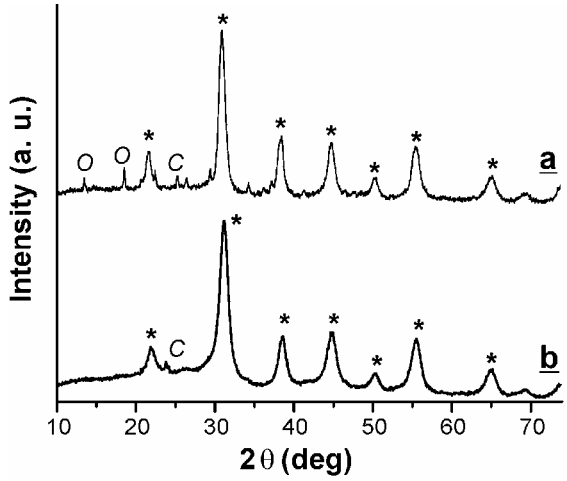

Figure 3.6. XRD patterns of $BaTiO_3$ nanocrystals obtained by solvo-thermal treatment in acetone (**a**) and acetophenone (**b**). Peaks marked * correspond to $BaTiO_3$, whereas *C* denotes $BaCO_3$, and *O* organic byproducts.

TEM images of the particles prepared in acetone and acetophenone are presented in Figure 3.7. **A** shows that the particles are somewhat aggregated but otherwise quite uniform in size and shape, their diameter being about 10 nm. A small fraction of the sample however featured larger particles, as illustrated in Fig. 3.7 **B**. They are ca. 20 nm in diameter and indicate that the sample is inhomogeneous, respectively contains impurities, as was also visible in the XRD pattern. The sample prepared in acetophenone does not contain any larger species but consists entirely of spherical or slightly ellipsoidal particles about 10 nm in size (Figure 3.7 **C**)

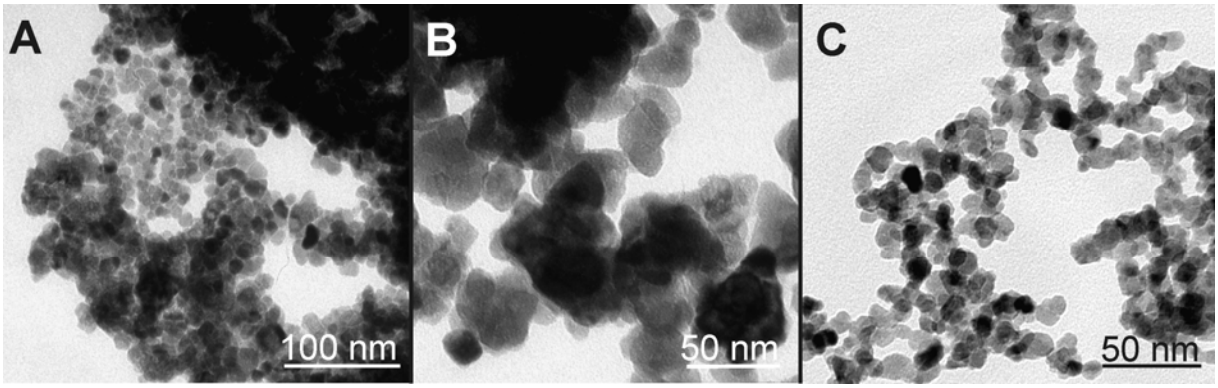

Figure 3.7. TEM pictures of $BaTiO_3$ particles prepared in acetone, (**A** and **B**, presented in two magnifications from different portions of the sample), and in acetophenone (**C**).

Only the formation mechanism leading to $BaTiO_3$ in acetophenone will be briefly treated here, as the reaction of titanium alkoxides and ketones is discussed in detail in Chapter 4, and

the additional presence of Ba and subsequently enolates seems only to enhance but not significantly change the condensation mechanism.

In order to evaluate the formation mechanism, the final acetophenone reaction solution was filtered to remove the precipitated nanoparticles and subsequently analyzed by ^1H and ^{13}C NMR. The ^1H-BB decoupled ^{13}C spectrum is shown in Figure 3.8. Apart from the solvent acetophenone (**A**), 1-phenylethanol (**1**), acetone (**2**), isopropanol (**3**) and 1,3-diphenyl-2-buten-1-one (**4**) were detected. Mesityl oxide and 1-phenyl-3-methyl-2-buten-1-one were found in traces.

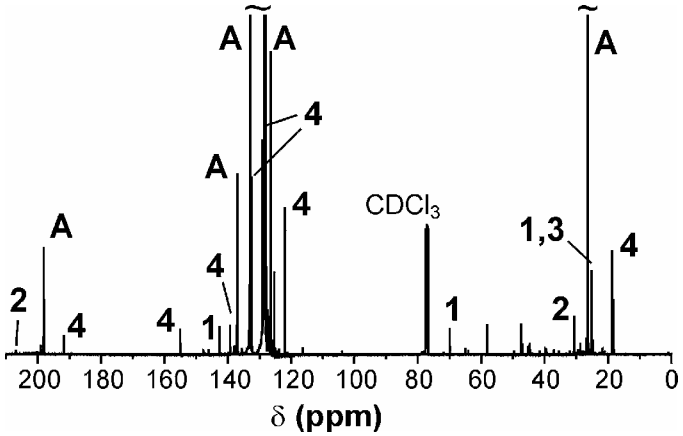

Figure 3.8. $^{13}C\{^1H\}$ NMR spectrum of the final reaction solution for the acetophenone system. See text for assignment.

The main product, 1,3-diphenyl-2-buten-1-one, is the aldol coupling product of acetophenone with itself. In Chapter 4, it is shown than the solvothermal reaction of metal alkoxides in ketones generally leads to aldol coupling reactions of the solvent, catalyzed by the metal centers, which in turn cause the elimination of formal water that promotes the formation of metal-oxygen-metal bonds. The main mechanism is therefore proposed as illustrated in Scheme 3.3. The first step (**A**) involves the reaction of metallic barium with the ketone to form barium enolates (**1**). As titanium isopropoxide is added (**B**), the ketone, respectively the aldolate, coordinates to the metal center (**2**). Upon heating in the autoclave, it attacks a second acetophenone similar to an aldol coupling mechanism (**3**), mediated by the Ti center. Formal elimination of water (**4**) leads to the formation of 1,3-diphenyl-2-buten-1-one (**5**). This is the key step in the mechanism, because it provides the oxygen necessary for the formation of crystalline $BaTiO_3$. The resulting Ti–OH groups can react with another titanium isopropoxide under release of isopropanol to form Ti–O–Ti bonds, which are the basic units of oxidic particles. The barium ions are presumably incorporated in the crystal lattice in the subsequent crystal growth process to yield crystalline barium titanate. As side reactions, analogous aldol condensations occur, e.g. the attack of acetophenone on acetone, leading to 1-phenyl-3-methyl-2-buten-1-one, or condensation of two acetone molecules yielding mesityl oxide, which however are only found in very small quantities.

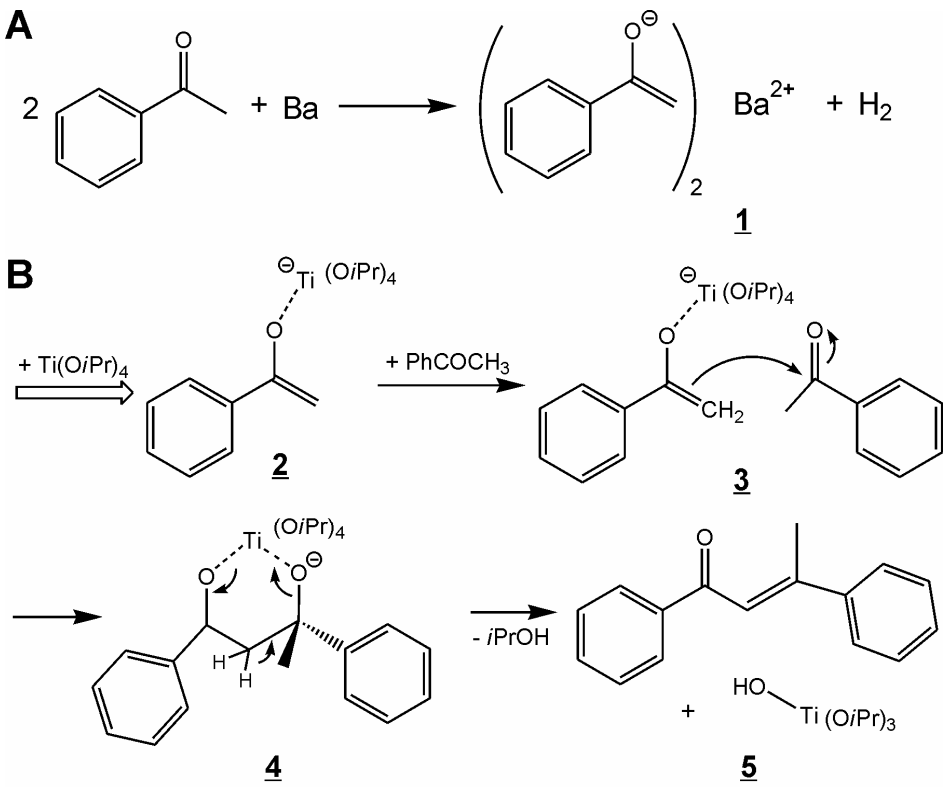

Scheme 3.3. Proposed mechanism for the formation of $BaTiO_3$ in acetophenone.

3.4 Summary and Conclusions

In this chapter, two pathways have been presented for the nonaqueous synthesis of $BaTiO_3$ nanoparticles. Solvothermal treatment in benzyl alcohol leads to highly crystalline, phase pure particles about 4-8 nm in diameter. By TEM, the particles were found hardly aggregated and practically spherical in shape. A very unusual and novel coupling reaction was found as the mechanism leading to particle formation in the alcohol. This C–C coupling reaction will be further investigated and discussed in subsequent sections of this work, especially in Chapter 9.

On the other hand, the solvothermal synthesis is also possible in aprotic media such as acetone or acetophenone. Good purity was achieved in acetophenone, with only a small amount of $BaCO_3$ being present. In both solvents, larger particles about 10 nm in size were formed. The reaction mechanism was found to involve aldol condensation processes of the solvent, resulting in the formal elimination of water which induces the formation of metal-oxygen-metal bonds as the starting point for nanoparticle formation.

3.5 Experimental Details

3.5.1 Synthesis in benzyl alcohol

Titanium(IV) isopropoxide (99.999%), barium metal (99.99%), and anhydrous benzyl alcohol (99.8%) were used as obtained from Aldrich Inc. without further purification but were stored in a glovebox. For the hydrothermal treatment, Parr acid digestion bombs were used, either large autoclaves equipped with 45 mL Teflon liners, or small ones with 23 mL Teflon cups.

The synthesis procedure was completely carried out in a glovebox. Typically, 2 mmol (274.7 mg) Ba was stirred in a vial with 25 mL benzyl alcohol at slightly elevated temperature until completely dissolved. 1 mol equivalent of $Ti(O\textit{i}Pr)_4$ was added slowly to the solution. The reaction mixture was stirred for another few minutes and then transferred into an autoclave. The autoclave was sealed, taken out of the glovebox and heated to 200 °C for about 48 hours. The resulting cloudy suspension was centrifuged, the precipitate thoroughly washed with ethanol and diethyl ether and subsequently dried at 60 °C overnight. The yield of the as-synthesized white perovskite powder was about 90 %.

3.5.2 Synthesis in ketones

The ketones were used as received in p.a./dry quality by Acros Organics or Aldrich, Inc. The synthesis procedure was very similar to the benzyl alcohol system. Usually 1.4 mmol of metallic Ba was stirred in a vial with 20 mL of the respective ketone at 75 °C for 1 h yielding a red-brown solution. After addition of 1 mol equivalent of $Ti(O\textit{i}Pr)_4$, the reaction mixture was stirred for another few minutes and then transferred into the autoclave, which was removed from the glovebox and heated at 180 °C for 3 days. The resulting suspension was centrifuged, the precipitate washed 3-5 × with ethanol and dried at 60 °C overnight.

3.5.3 Obtained NMR Data

The ^1H NMR measurements were carried out at 400 MHz, using $CDCl_3$ as solvent. All ^{13}C NMR measurements were performed under ^1H-BB decoupling at 100 MHz, also in $CDCl_3$. Only the relevant main reaction products are stated. Signals not visible because of superposition with solvent or other peaks are not mentioned.

a. Benzyl Alcohol System

4-Phenyl-2-butanol: ^1H NMR δ [ppm]: H_{Ph} superimposed, 3.77 (1H, H2), 2.75/2.67 (2H, H4), 1.80/1.73 (2H, H3), $-CH_3$ superimposed with *i*PrOH, -OH not visible; ^{13}C NMR δ [ppm]: 142.4 (Ph_{ipso}), 128.5-127.4 superimposed, 125.8 (Ph_{para}), 67.2 (C2), 40.8 (C3), 32.2 (C4), 23.3 (C1).

1,5-Diphenyl-3-pentanol: ^{1}H NMR H_{Ph} superimposed, 3.62 (1H, H3), 2.75/2.67 (4H, H1/5), 1.80/1.73 (4H, H2/4), -OH not visible; ^{13}C NMR: 70.4 (C3), 39.2 (C2/4), 32.1 (C1/5).

b. Acetophenone System

1-Phenylethanol: ^{13}C NMR: 146.1 (C1'), 128.4 (C3', C5'), 127.4 (C4'), 125.3 (C2', C6'), 70.0 (C1), 25.5 (C2).
1,3-diphenyl-2-buten-1-one: 191.7 (C1), 155.0 (C3), 142.6 (C1"), 139.2 (C1'), 132.5 (C4'), 129.1 (C2', C6'), 128.5 (C3', C5'), 128.4 (C3", C5", superimposed), 127.9 (C4"), 126.4 (C2", C6"), 121.9 (C2), 18.7 (C4).

3.6 References

[1] H. S. Tzou, H.-J. Lee, S. M. Arnold, *Mech. Adv. Mater. Struct.* **2004**, *11*, 367.

[2] C. Kittel, *Introduction to Solid State Physics*, J. Wiley & Sons, New York, **1986**.

[3] M. E. Lines, A. M. Glass, *Principles and Applications of Ferroelectrics and Related Materials*, Oxford University Press, London, **2001**.

[4] C. H. Ahn, K. M. Rabe, J.-M. Triscone, *Science* **2004**, *303*, 488.

[5] D. Damjanović, *Rep. Prog. Phys.* **1998**, *61*, 1267.

[6] P. Gherardi, E. Matijević, *Colloids Surf.* **1988**, *32*, 257.

[7] Y.-S. Her, E. Matijević, M. C. Chon, *J. Mater. Res.* **1995**, *10*, 3106.

[8] D. Hennings, W. Mayr, *J. Solid State Chem.* **1978**, *26*, 329.

[9] P. R. Arya, P. Jha, D. Ganguli, *J. Mater. Chem.* **2003**, *13*, 415.

[10] M. N. Kamalasanan, S. Chandra, P. C. Joshi, A. Mansingh, *Appl. Phys. Lett.* **1991**, *59*, 3547.

[11] M. H. Frey, D. A. Payne, *Chem. Mater.* **1995**, *7*, 123.

[12] R. N. Viswanath, S. Ramasamy, *Nanostruct. Mater.* **1997**, *8*, 155.

[13] A. N. Christensen, *Acta Chem. Scand.* **1970**, *24*, 2447.

[14] P. K. Dutta, R. Asiaie, S. A. Akbar, W. D. Zhu, *Chem. Mater.* **1994**, *6*, 1542.

[15] J. O. Eckert Jr., C. C. Hung-Houston, B. L. Gersten, M. M. Lencka, R. E. Riman, *J. Am. Ceram. Soc.* **1996**, *79*, 2929.

[16] M. H. Frey, D. A. Payne, *Appl. Phys. Lett.* **1993**, *63*, 2753.

[17] G. Arlt, D. Hennings, G. de With, *J. Appl. Phys.* **1985**, *58*, 1619.

[18] T. Takeuchi, M. Tabuchi, K. Ado, K. Honjo, O. Nakamura, H. Kageyama, Y. Suyama, N. Ohtori, M. Nagasawa, *J. Mater. Sci.* **1997**, *32*, 4053.

[19] I. J. Clark, T. Takeuchi, N. Ohtori, D. C. Sinclair, *J. Mater. Chem.* **1999**, *9*, 83.

[20] M. H. Frey, Z. Xu, P. Han, D. A. Payne, *Ferroelectrics* **1998**, *206*, 337.

[21] I. Rychetsky, J. Petzelt, T. Ostapchuk, *Appl. Phys. Lett.* **2002**, *81*, 4224.

[22] T. Ostapchuk, J. Petzelt, V. Zelezny, A. Pashkin, J. Pokorny, I. Drbohlav, *Phys. Rev. B* **2002**, *66*, 235406.

[23] T. M. Shaw, S. Trolier-McKinstry, P. C. McIntyre, *Annu. Rev. Mater. Sci.* **2000**, *30*, 263.

[24] M. C. Wang, F. Y. Hsiao, C. S. Hsi, N. C. Wu, *J. Cryst. Growth* **2002**, *246*, 78.

[25] G. H. Haertling, *J. Am. Ceram. Soc.* **1999**, *82*, 797.

[26] B. I. Lee, M. Wang, D. Yoon, M. Hu, *J. Ceram. Process. Res.* **2003**, *4*, 17.

[27] M. Niederberger, M. H. Bartl, G. D. Stucky, *J. Am. Chem. Soc.* **2002**, *124*, 13642.

[28] M. Niederberger, M. H. Bartl, G. D. Stucky, *Chem. Mater.* **2002**, *14*, 4364.

[29] M. H. Frey, D. A. Payne, *Phys. Rev. B* **1996**, *54*, 3158.

[30] M. Niederberger, N. Pinna, J. Polleux, M. Antonietti, *Angew. Chem. Int. Ed.* **2004**, *43*, 2270.

[31] P. Arnal, R. J. P. Corriu, D. Leclercq, P. H. Mutin, A. Vioux, *Chem. Mater.* **1997**, *9*, 694.

[32] T. J. Trentler, T. E. Denler, J. F. Bertone, A. Agrawal, V. L. Colvin, *J. Am. Chem. Soc.* **1999**, *121*, 1613.

[33] R. J. P. Corriu, D. Leclercq, P. Lefevre, P. H. Mutin, A. Vioux, *J. Mater. Chem.* **1992**, *2*, 673.

[34] A. Vioux, *Chem. Mater.* **1997**, *9*, 2292.

[35] Integrated Spectral Data Base System for Organic Compounds: http://www.aist.go.jp/RIODB/SDBS/.

[36] Z. Dawoodi, M. L. H. Green, V. S. B. Mtetwa, K. Prout, *J. Chem. Soc. Chem. Commun.* **1982**, 802.

[37] J. A. Labinger, Bercaw, J. E., *Nature* **2002**, *417*, 507.

[38] M. T. Reetz, R. Peter, *Tetrahedron Lett.* **1981**, *22*, 4691.

[39] R. Mahrwald, *Tetrahedron* **1995**, *51*, 9015.

[40] R. Mahrwald, *Org. Lett.* **2000**, *2*, 4011.

[41] G. Dyker, *Angew. Chem. Int. Ed.* **1994**, *33*, 103.

[42] R. Mahrwald, *Angew. Chem. Int. Ed.* **2002**, *41*, 1361.

[43] R. Mahrwald, *Angew. Chem. Int. Ed.* **2003**, *42*, 2443.

[44] M. Markert, I. Buchem, H. Krüger, R. Mahrwald, *Tetrahedron* **2004**, *60*, 993.

[45] R. Sreekumar, C. N. Pillai, *Catal. Lett.* **1993**, *19*, 281.

[46] C. S. Kim, B. K. Moon, J.-H. Park, B. C. Choi, H. J. Seo, *J. Cryst. Growth* **2003**, *257*, 309.

[47] C. S. Kim, B. K. Moon, J.-H. Park, S. T. Chung, S.-M. Son, *J. Cryst. Growth* **2003**, *254*, 405.

[48] S. C. Goel, M. Y. Chiang, P. C. Gibbons, W. E. Buhro, *Mater. Res. Soc. Symp. Proc.* **1992**, *271*, 3.

[49] B. C. Gaskins, J. J. Lannutti, *J. Mater. Res.* **1996**, *11*, 1953.

[50] R. Asiaie, W. D. Zhu, S. A. Akbar, P. K. Dutta, *Chem. Mater.* **1996**, *8*, 226.

4 Synthesis of Titania Nanoparticles in Aprotic Solvents

4.1 Introduction

Titanium dioxide is a material with outstanding chemical and physical properties which are of interest for a variety of different applications such as gas sensing,[1,2] optics,[3,4] photovoltaics[5] or as pigments.[6] It is cheap, abundant, nontoxic and biocompatible.[5] Above all, titanium dioxide is one of the most prominent catalyst materials.[7] A heavily researched field in this context is the photocatalytical degradation of organic pollutants on titania surfaces.[8,9]

TiO_2 exhibits two main modifications, namely anatase and rutile. The structure of both can be described in terms of chains of $[TiO_6]$ octahedra. The two structures differ by the distortion of each octahedron and by the assembly pattern of the chains.[9] The unit cells are illustrated in Figure 4.1. Each Ti^{4+} ion is surrounded by an octahedron of six O^{2-} ions. The octahedron in rutile is slightly distorted, whereas the distortion in anatase is higher, resulting in a lower symmetry and thus a larger unit cell. Synthesis processes under kinetic control result in anatase, whereas processes involving Ostwald ripening lead to rutile, the equilibrium phase.[10] Upon heating, anatase transforms into rutile between 600 °C and 1100 °C, the transformation rate being greatly influenced by particle size and the presence of impurities.[10] Comparing the two modifications, the photocatalytic activity of anatase is much higher than that of rutile.[11]

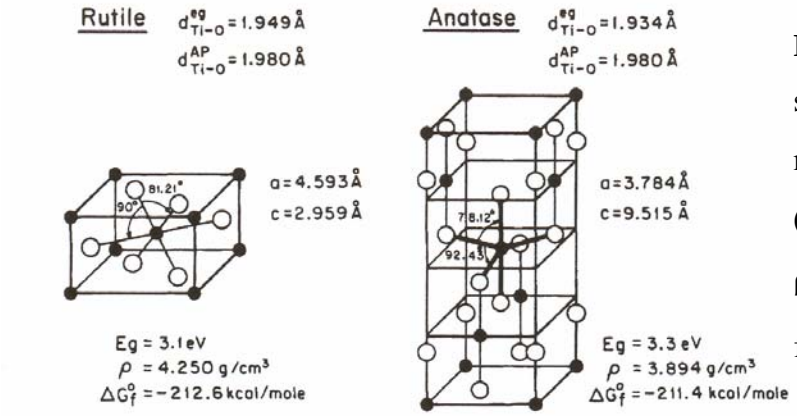

Figure 4.1. Comparison of the structure of rutile and anatase modifications of TiO_2. (●) Ti^{4+}, (○) O^{2-}, E_g electronic band gap, ρ density, ΔG_f^0 standard free formation energy, from Ref. 9.

The physical and chemical characteristics of TiO_2 are controlled not only by its crystalline phase but also by its particle size and morphology.[12] Nanostructured titania materials with ultrafine crystallite size (< 100 nm) and high surface areas have attracted significant interest, due to their unusual optical, electrical and catalytic properties.[4,13-16]

Therefore, the synthesis of titania nanoparticles is a well-established process. Pigmentary titania nanoparticles are fabricated on a commercial scale using flame processes.[17] Particles

< 10 nm in size have been prepared even by unusual techniques such as ultrasound irradiation[18] and from metallic Ti by an oxidation-hydrolysis combination.[19] Most groups, however, focused on aqueous sol-gel synthesis, where the sol of a titania precursor is prepared and then hydrolyzed to induce the condensation reaction.[12,20] The reactivity of the precursor can be decreased by adding chelating agents.[21]

Even the nonaqueous synthesis of titania has been explored to a substantial extent. The nonhydrolytic reaction of $TiCl_4$ and $Ti(OiPr)_4$ has been first described in 1992 to result in anatase, however requiring a calcination treatment at 400 °C.[22] The nucleophilic attack of the alkoxide oxygen on the Ti center of the chloride induces elimination of an alkyl chloride (in this case, isopropyl chloride), simultaneously resulting in a Ti–O–Ti bond which represents the starting point of oxide formation.[23] $TiCl_4$ was also reacted with ethers as oxygen donors (termed etherolysis), again leading to anatase after calcination of the resulting gel.[23,24] Etherolysis in isopropyl ether was reported to result in at least partially crystalline TiO_2 material after vacuum drying at 180 °C.[10] Later, the synthesis of nanocrystalline titania via the alkyl halide elimination route was achieved, however in the presence of TOPO (trioctylphosphine oxide) as surfactant.[25] Nanosized TiO_2 was also obtained by in situ generation of water.[26] The reaction of $TiCl_4$ in benzyl alcohol has proven as a particularly versatile route, making possible the synthesis of highly crystalline anatase nanoparticles at low temperatures (80 °C).[27,28]

As has been shown in Chapter 3.3, the solvothermal synthesis in aprotic solvents such as ketones can be a valuable alternative to the synthesis in alcohols. In order to gain further insight into the mechanisms and effects of solvothermal treatment in aprotic solvents, the synthesis of TiO_2 nanoparticles, representing a simpler system, in ketones as well as in other aprotic solvents such as aldehydes was explored and compared. Unlike the ketones, aldehydes have not been shown at all so far to react with metal alkoxides to form oxides. However, there are reports about the formation of gels upon reaction of benzaldehyde with silicon halides[29] and $TiCl_4$.[30] In addition, other aprotic solvents such as benzamide were investigated, and also the solvothermal reaction in benzylamine is briefly described here. Not $TiCl_4$ but titanium tetraisopropoxide was used as precursor, on the one hand to make the system comparable to the synthesis of $BaTiO_3$, but also as $TiCl_4$ would react more violently under partial formation of HCl which constitutes an unpredictable hazard when working under solvothermal conditions, not to mention corrosion problems.

4.2 Results and Discussion

Simple ketones such as acetone, 2-butanone, 3-pentanone, cyclohexanone, acetophenone and benzophenone as well as the aldehydes butyraldehyde and benzaldehyde were mixed with titanium tetraisopropoxide. The samples were prepared in a rather concentrated fashion in a molar ratio of 10:1. For all solvents, yellow to amber suspensions were obtained, which were separated by centrifugation. The precipitate became white to slightly yellow upon washing with chloroform and dichloromethane, and was dried in vacuo.

Figure 4.2 shows the XRD patterns measured for the TiO_2 particles prepared in acetone (**a**), 2-butanone (**b**), acetophenone (**c**) and benzophenone (**d**) as well as benzaldehyde (**e**). The patterns are very similar, all featuring reflections clearly corresponding to the anatase modification. The peaks are rather sharp, also compared to TiO_2 nanocrystals obtained from $TiCl_4$ in benzyl alcohol,[28] indicating a larger size of the particles when synthesized in ketones or aldehydes. The peak broadness however visibly differs between the systems. It clearly increases when going from aliphatic ketones (**a**, **b**) to aromatic ones (**c**, **d**) or aldehydes (**e**).

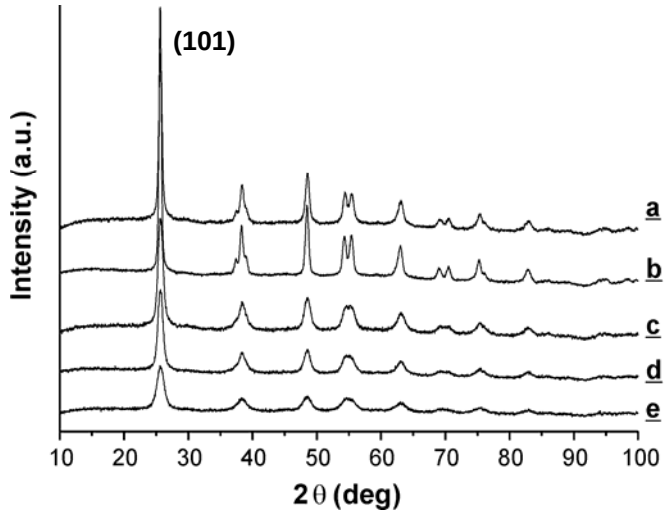

Figure 4.2. XRD patterns of anatase nanoparticles synthesized in acetone (**a**), 2-butanone (**b**), acetophenone (**c**), benzophenone (**d**) and benzaldehyde (**e**).

The particle size was calculated from the XRD patterns using the Scherrer equation. The size obtained from the (101) reflections as well as the respective yields are illustrated in Table 4.1. The data clearly confirms that indeed the particle size decreases when using cyclic or aromatic ketones, and also when switching to aldehydes as solvents.

solvent	reaction conditions	yield [%]	size [nm]
acetone	1 d, 130 °C	90	15.2
2-butanone	1 d, 180 °C	80	20.3
3-pentanone	1 d, 180 °C	79	20.3
cyclohexanone	3 d, 200 °C	84	15.1
acetophenone	3 d, 200 °C	85	10.8
benzophenone	3 d, 200 °C	48	7.0
butyraldehyde	3 d, 200 °C	90	10.5
benzaldehyde	1 d, 200 °C	100	6.9

Table 4.1. Synthesis details of TiO_2 particles prepared from $Ti(OiPr)_4$ in various ketones and aldehydes, and obtained respective yield and crystallite size at a constant Ti-to-solvent ratio of 1:10.

The purity of the samples was evaluated by TGA. The thermograms of samples prepared in ketones are shown in Figure 4.3 **A**. In general, the weight loss is rather low, amounting to less than 10 %. The first decrease below 150 °C is attributed to adsorbed solvents and molecularly adsorbed water, amounting to 1-4 wt %. At higher temperatures, surface-bound hydroxyl groups are removed, and organic species adsorbed to the particles decompose. For 2-butanone and cyclohexanone, the weight loss in this range is only about 1 %, whereas it is significantly higher for acetone and acetophenone. The thermograms of the particles obtained in aldehydes are presented in Fig. 4.3 **B**. Butyraldehyde shows a similar behavior as 2-butanone, whereas the weight loss observed for the particles prepared in benzaldehyde is more pronounced in the region 300-400 °C, amounting to ca. 5 %. Comparing the obtained plots, it can be clearly observed that the content of organic/volatile species is higher for aromatic solvents and for acetone compared to higher aliphatic ketones or aldehydes.

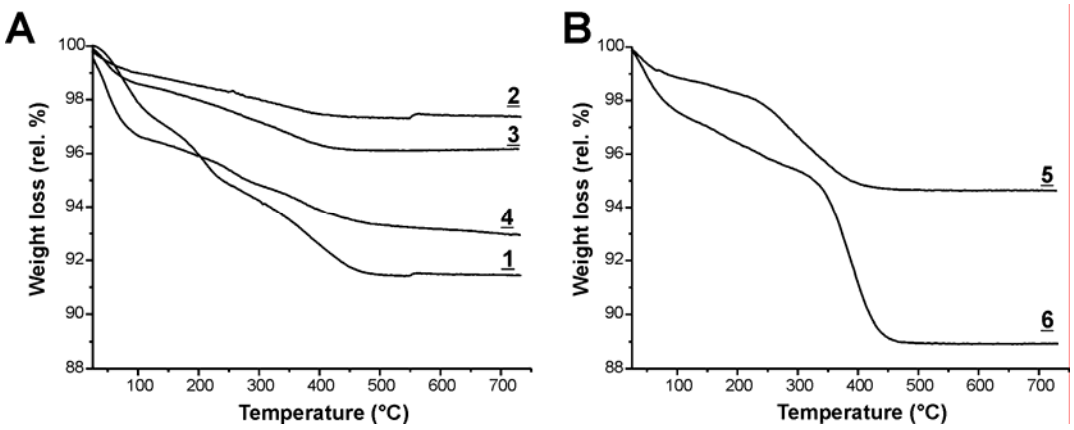

Figure 4.3. TGA curves of the obtained nanoparticles after washing and thorough drying in vacuo: acetone system (**1**), 2-butanone (**2**), cyclohexanone (**3**), acetophenone (**4**), and butyraldehyde (**5**) and benzaldehyde (**6**).

FT-IR measurements (data not shown) revealed the presence of unsaturated ligands, probably in the form of enolates or aldolates, on the surface of the particles prepared in acetone ($\nu_{C=C}$ = 1636 cm^{-1} found). Therefore, we infer that acetone and aromatic species ligate more strongly to the TiO_2 surface. Accordingly, the particle growth is restricted, resulting in a smaller particle size. Hence, the solvents, and their reaction products, control the particle morphology.

The particles were studied also by TEM. Figure 4.4 displays the obtained particles after washing, for the acetone system (Fig. 4.4 **A**), for acetophenone (**B**), 3-pentanone (**C**), benzophenone (**D**), benzaldehyde (**E**) and butyraldehyde (**F**). Although the particles are agglomerated to some extent, the individual nanoparticles can be clearly distinguished. The average diameter can be determined as about 15 nm for the particles prepared in acetone and acetophenone, ca. 25 nm for the ones prepared in 3-pentanone, 5-10 nm for the benzophenone system, 5 nm for benzaldehyde, and about 10-15 nm for butyraldehyde, which overall is in good consistency with the data calculated from XRD.

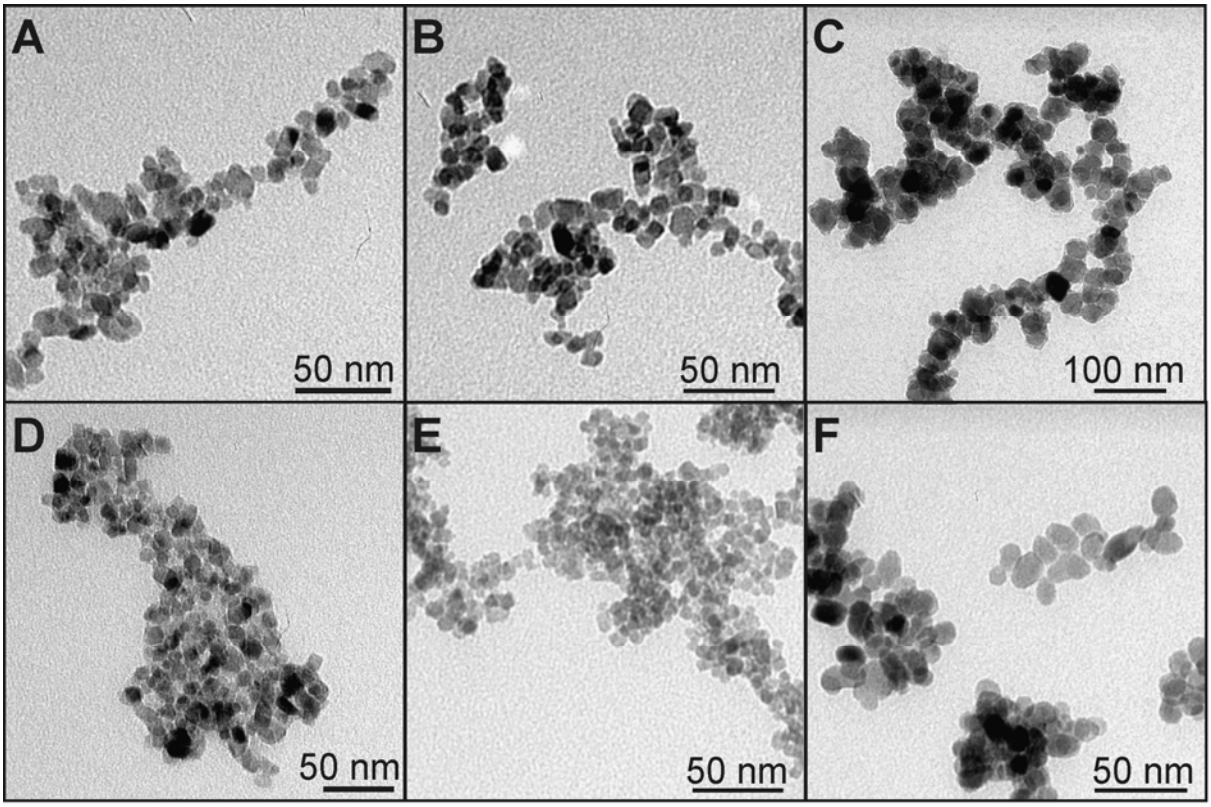

Figure 4.4. TEM micrographs of the nanoparticles prepared in acetone (**A**), acetophenone (**B**), 3-pentanone (**C**), benzophenone (**D**), benzaldehyde (**E**), and butyraldehyde (**F**).

In order to evaluate the formation mechanism, the obtained reaction solutions were filtered to remove any remaining particles and then subjected to ^{1}H and ^{1}H-BB decoupled ^{13}C liquid-

state NMR analysis to investigate the side products of the reactions. It turned out that the composition was generally rather complex. In Figure 4.5, the ^{1}H and $^{13}C\{^{1}H\}$ NMR spectra obtained for the acetone system are presented. Aside from acetone (labeled **1**) and isopropanol (**2**), several aldol condensation products of acetone are found, mainly mesityl oxide (4-methyl-3-penten-2-one, **3**) and mesitylene (1,3,5-trimethylbenzene, **4**), which lead to the yellow color of the solution. The intermediate of mesitylene condensation from acetone, phorone (2,6-dimethyl-2,5-heptadien-4-one, **5**), was only found in traces. From ^{1}H-NMR, the molar ratio was calculated to 3.0 isopropanol : 1.0 mesityl oxide : 0.07 mesitylene.

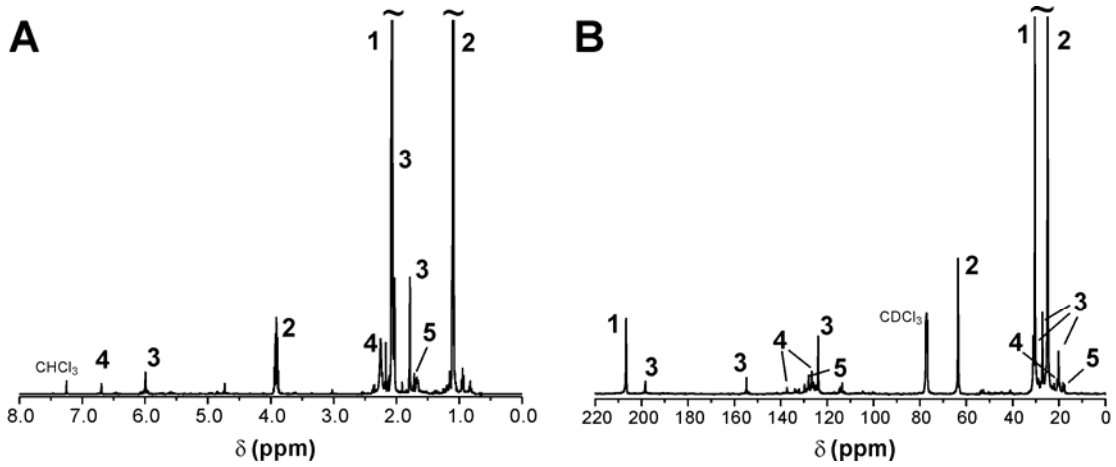

Figure 4.5. ^{1}H (**A**) and $^{13}C\{^{1}H\}$ NMR spectra of the reaction solution for the Ti(O*i*Pr)$_4$ – acetone system after removal of the particles by filtration.

Based on these side products, we propose a formation mechanism as depicted in Scheme 4.1, which is somehow related to the mechanism for ZnO gel formation described by Goel et al.:[31] First, acetone is coordinated to the titanium center, and deprotonation leads to the enolate complex under concurrent release of isopropanol (**1**). The enol ligand nucleophilically attacks a second acetone molecule to form a C–C bond (**2**). Now an aldolate ligand is coordinated to the Ti center. Analogously to the elimination of water, the ligand can react with another titanium center (**3**) to form a Ti–O–Ti bond, which represents the starting point of nanoparticle formation and crystallization. Isopropanol and mesityl oxide are released (**4**). Further condensation of mesityl oxide leads to phorone and mesitylene which are, however, only found in small quantities. The higher *i*PrOH : mesityl oxide ratio found (3:1 instead of 2:1) is explained by adsorption of acetone condensation products on the titania surface, as especially the aldolate ligand **3** can be expected to strongly bind to Ti.

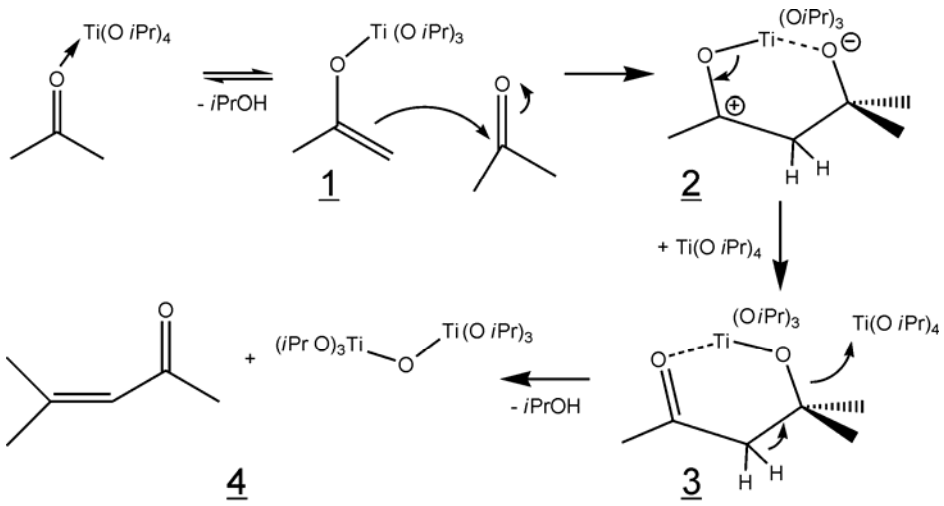

Scheme 4.1. Proposed formation mechanism of TiO_2 in acetone via aldol condensation of the solvent.

Even more complex compositions were found for the reaction solutions in the higher aliphatic ketones 2-butanone and 3-pentanone. In addition to the solvent and isopropanol, interestingly also acetone was found in large amounts, as well as the reduction product of the solvent (2-butanol and 3-pentanol, respectively). This is due to a reduction–oxidation mechanism between the isopropoxide ligand and the ketone solvent mediated by the Ti center, and is analog to a Meerwein-Ponndorf-Verley reaction commonly known to occur when heating aluminum alkoxides in acetone.[32-34] This mechanism has also been observed as side reaction in the formation of $BaTiO_3$ in cyclohexanone.[35] The mechanism for this hydride transfer reaction is presented in Scheme 4.2.

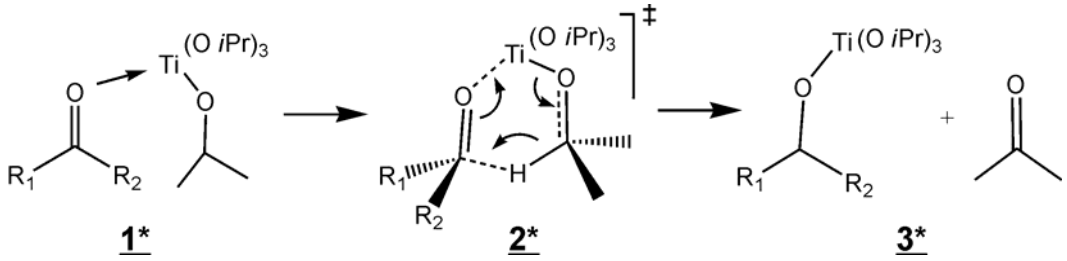

Scheme 4.2. Side reaction observed during the formation of TiO_2 in higher aliphatic and aromatic ketones, similar to the Meerwein-Ponndorf-Verley reaction.

Initially, the solvent again coordinates to the Ti center (**1***). In a next step, however, the isopropoxide ligand transfers the hydrogen from its α-position to the ketone via a hydride transfer in a six-membered cyclic transition state (**2***).[36] The reduced ketone solvent is then bound to Ti as an alkoxide, and acetone is released (**3***). Upon condensation, also the reduction product is released as secondary alcohol. By itself, however, this side reaction does

not contribute to the oxide formation process; therefore, aldol coupling reactions as described for the main mechanism are essential for nanoparticle formation. As the MPV-like reaction produces significant amounts of acetone, now two ketone species are present in the system, which can each add onto itself or the other species present, under such rigid solvothermal conditions theoretically leading to a mixture of four primary aldol addition products, not to mention any higher coupling products.

In the cyclohexanone system, an MPV-like reaction took place to a large extent as well, as substantial amounts of acetone and cyclohexanol in the final solution indicated. To facilitate identification of the main coupling product, more volatile components, especially acetone and cyclohexanol as well as a large fraction of the solvent, were removed from the reaction solution in vacuo before performing further NMR analysis. The resulting $^{13}C\{^1H\}$ NMR spectrum is illustrated in Figure 4.6, **A**. Clearly, 2-(1-cyclohexenyl)cyclohexanone can be identified, the individual signals being labeled according to the assignment in Fig. 4.6 **B**. Interestingly, the expected and favored Saytzew-type elimination, resulting in the double bond conjugated to the carbonyl function, did not take place here, as no 2-cyclohexylidenecyclohexanone was found, but the Hofmann-type elimination, resulting in 2-(1-cyclohexenyl)cyclohexanone. This is probably due to steric hindrance in the transition product which is assumed analogous to **3** in Scheme 4.1. Additionally, smaller unlabeled peaks are found in the NMR spectrum which correspond to aldol condensation products of cyclohexanone with acetone.

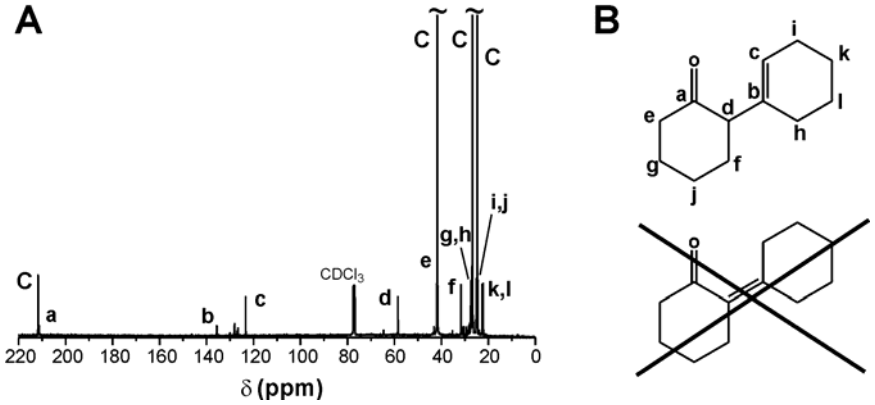

Figure 4.6. $^{13}C\{^1H\}$ NMR spectrum obtained after solvothermal synthesis of TiO_2 in cyclohexanone (**A**), chemical structures of possible coupling products (**B**).

The synthesis in acetophenone proceeds in a similar fashion, mainly yielding 1,3-diphenyl-2-buten-1-one as organic reaction product. This mechanism has already been discussed in Chapter 3.3 for the synthesis of $BaTiO_3$ in acetophenone.
In principle, the synthesis within benzophenone would not be possible via a simple aldol condensation mechanism, as benzophenone does not possess any α-H atoms, necessary for direct condensation between two ketone molecules. Taking into account the occurrence of MPV-like processes, however, aldol coupling of acetone on benzophenone is well possible. Indeed, the obtained NMR spectra (data not shown) suggest the presence of 4,4-diphenyl-3-buten-2-one, which is the condensation product of acetone with benzophenone. The presence of both benzhydrol (diphenylmethanol) and acetone supports the assumption that first benzophenone undergoes MPV reduction to benzhydrol. This leads to the release of acetone, which next condensates with another benzophenone and thus provides the formal oxygen needed for titania formation. Due to the steric hindrance of benzophenone, the system shows a lower reactivity, which is expressed in a lower yield (ca. 50 %).

The benzaldehyde system is discussed in detail to illustrate the reaction path when using aldehydes as solvents. ^{13}C-NMR analysis of the reaction solution (Figure 4.7) showed the presence of several species in addition to the aldehyde (labeled **1**). Substantial amounts of benzyl alcohol (**2**) as reduction product of benzaldehyde, and of benzyl benzoate (**3**), a disproportionation product of benzaldehyde, were detected. Interestingly, a significant amount of 4-phenyl-2-butanone (**4**) was found, being the analog to 4-phenyl-2-butanol which has been found in large amounts for the synthesis of $BaTiO_3$ in benzyl alcohol, see Chapter 3.2. There, the formation of 4-phenyl-2-butanol was proposed to proceed via a C–C coupling reaction from $Ti(OiPr)_4$ and benzyl alcohol in the presence of barium benzyl alcoholate during the oxide formation. Therefore, in the benzaldehyde system, one can assume intermediate formation of 4-phenyl-2-butanol which is then oxidized by the aldehyde to form the ketone. On the other hand, the aldol addition product of acetone to benzaldehyde, 4-phenyl-3-buten-2-one (**5**), could also be identified. A number of smaller peaks in the NMR spectrum are attributed to higher condensation products of the aldehyde.

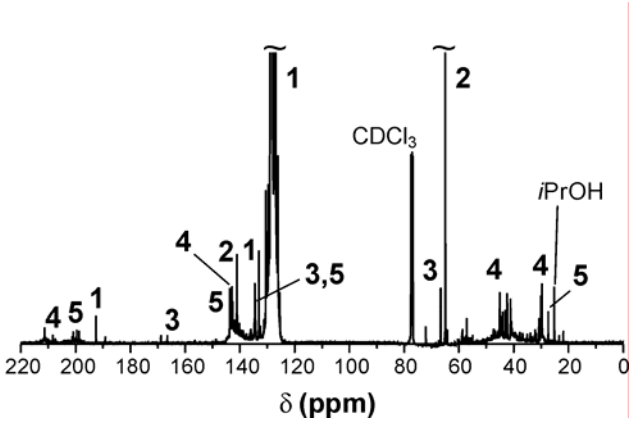

Figure 4.7. $^{13}C\{^1H\}$ NMR analysis of the obtained reaction solution obtained after the solvothermal synthesis of TiO_2 in benzaldehyde after particle removal.

Therefore, an even more complicated reaction sequence leading to the formation of TiO_2 is proposed as illustrated in Scheme 4.3: First (**A**), an MPV-like reaction of benzaldehyde with $Ti(OiPr)_4$ leads to acetone and benzyl alcohol (**1**). Then, there are two possible routes: the alcohol can react (**B**) with another isopropoxy ligand via the aforementioned C–C coupling reaction (**2**). Due to the surplus of benzaldehyde as oxidizing agent, the resulting 4-phenyl-2-butanol is readily oxidized to 4-phenyl-2-butanone (**3**). For the second pathway (**C**), aldol addition of acetone to the aldehyde (**4**,**5**) is proposed. In benzaldehyde, route **B** is favored as the intermediate carbo cation is stabilized (found product ratio 2.2 4-phenyl-2-butanone : 1.0 4-phenyl-3-buten-2-one), whilst it does not take place in butyraldehyde. Thus, aldol coupling reactions (route **C**) are the probable pathway to TiO_2 formation in aliphatic aldehydes.

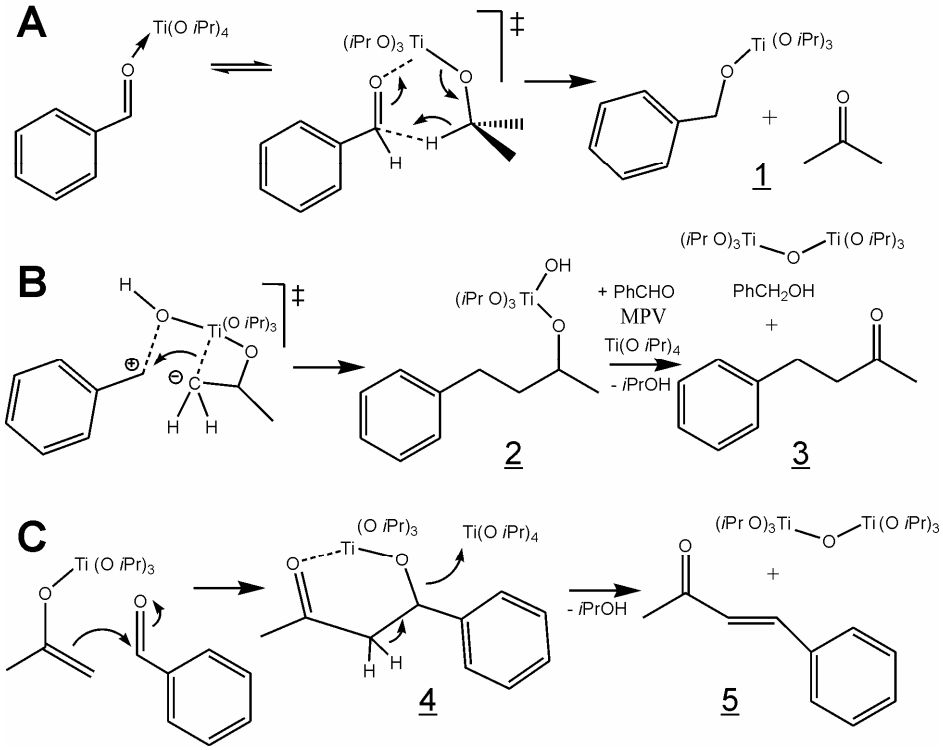

Scheme 4.3. Reaction pathways identified for the synthesis of TiO_2 particles in benzaldehyde.

Aprotic solvents other than ketones and aldehydes were investigated as well. Whereas the solvothermal treatment of Ti(O*i*Pr)$_4$ in anhydrous THF or 1,4-dioxane (150 °C) did not result in titania particles but in a clear solution, the reaction in benzamide at 200 °C yielded highly crystalline anatase particles ca. 5.2 nm in size, as calculated from the (101) reflection. NMR analysis of the final reaction solution (data see Chapter 4.4.2) suggests that isopropyl ether, N-isopropylbenzamide and isopropyl benzoate are present. Hence, the main reaction leading to particle formation is ether elimination. As side reaction, nucleophilic attack of the amide nitrogen on the α-carbon of the isopropoxide, followed by elimination of an –OH group, also results in the oxide. Such N-alkylation reactions of benzamide with alcohols are unusual but have been reported to occur under catalysis of transition metals.[37]

A more nucleophilic solvent such as an amine can be expected to primarily react via this mechanism. The reaction of the titanium isopropoxide in benzylamine is therefore briefly described here, even though benzylamine of course cannot be classified as an aprotic solvent. Interestingly, large aggregates of elongated nanoparticles were formed after treatment at 200 °C for 3 days. TEM images show that the nanoparticles in fact are stacked in a lamellar fashion (Figure 4.9 **A**). This stacking is very regular, which also can be seen in the XRD pattern (Fig. 4.9 **B**) by the dominant low-angle reflection at 2θ = 7.3° representing the 100 reflection of the lamellae, corresponding to a *d*-spacing of 1.2 nm. A second-order peak is visible at 14.1°. The signals at larger angles correspond to the crystal structure of the material. The anatase peaks are rather broad, indicating small crystallites, except for the 200 reflection found at 2θ = 48.3°. This indicates that the lamellae are parallel to the anatase 200 direction. The reflection marked * cannot be assigned to anatase and probably stems from a small amount of rutile present in the sample.

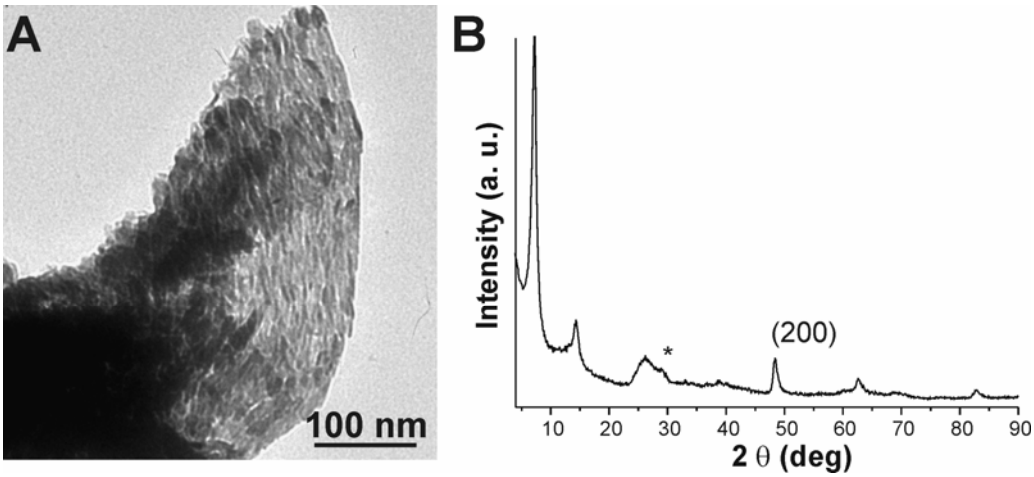

Figure 4.9. Characterization of the material obtained after solvothermal treatment of Ti(O*i*Pr)$_4$ in benzylamine: TEM image (**A**) and XRD pattern (**B**).

NMR analysis of the final reaction solution revealed that aside from the solvent benzylamine, dibenzylamine and *i*PrOH were present in larger quantities, and N-benzylidenebenzylamine and N-isopropylbenzylamine in traces. This indicates that condensation reactions of the amine take place, mainly with itself, as illustrated in Scheme 4.4, **A**. As dibenzylamine forms, ammonia is released, which escapes when opening the autoclave, and was even visible as "boiling" of the reaction solution. To a smaller extent, condensation with the isopropoxy ligands occurs (Scheme 4.4 **B**) via nucleophilic attack of the amine onto the secondary carbon position of an isopropoxy ligand. This leads to the (formal) release of water, producing a Ti–OH group which then induces formation of the oxide.

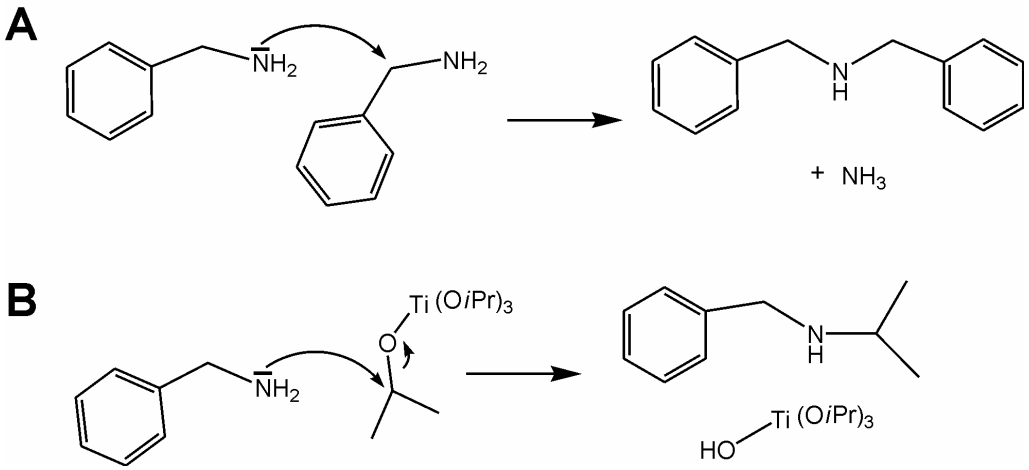

Scheme 4.4. Proposed reactions occurring during the solvothermal treatment of $Ti(OiPr)_4$ in benzylamine.

4.3 Conclusions

These results clearly prove that the nonaqueous sol-gel synthesis of highly crystalline nanoparticles can be extended to organic solvents other than alcohols or ethers, and proceeds via a variety of reactions providing the oxygen necessary to form Ti–O–Ti bridges. In all tested solvents, organic condensation reactions occur involving formal elimination of water which then induces condensation of the oxide. In this respect, the presented formation mechanisms could be seen as nonaquoeus processes providing water *in situ*. However, the difference to classical condensations (for example ester elimination processes) producing water *in situ* is that here, the metal center is actually required for the organic condensation to occur.

In ketones and aldehydes, the organic condensation processes are aldol coupling reactions. The resulting materials show high crystallinity, even though the synthesis is performed at low temperatures. A clear trend was observed: the particle size was significantly smaller for aromatic ketones and aldehydes than for higher aliphatic ones, which seems to go hand in hand with the ability of the solvent to bind to the particles and thus to the amount of organic material remaining on the particle surface after washing, as identified by TGA. Aromatic ketones and aldehydes can bind more strongly to the particles, due to the mesomeric effect of the aromatic substituent, which in turn prevents the growth of larger particles. The synthesis of anatase was also explored in organic solvents other than aldehydes and ketones. Whereas in ethers such as THF and 1,4-dioxane no particles formed, in benzamide, anatase particles resulted mainly from an ether elimination process. In benzylamine, highly ordered aggregates were obtained, the oxide mainly forming through condensation between the solvent and the isopropoxy ligands.

In general, the high concentration of the TiO_2 precursor in the reaction systems and the excellent yields are promising aspects with respect to practical applications, especially for the ketone systems. The approach described here also functions as a model system for the synthesis of other metal oxides, as will be shown for PZT materials (cf. Chapter 7).

4.4 Experimental Details

4.4.1 Synthesis

The ketones and aldehydes, benzamide and benzylamine were used as received in p.a./dry quality by Acros Organics and Aldrich. For a special experiment, acetone was dried over mole sieve 4 Å and distilled before use, however the results were similar when using the as-received chemical. Next, the solvents were mixed with titanium tetraisopropoxide, $Ti(O\mathit{i}Pr)_4$ (Aldrich, 99.999%), in a glove box under Ar. Yield and crystallinity were best when using a molar ratio of 10:1. Hydrothermal treatment was performed in acid digestion bombs with 23 mL Teflon cup holders, Parr Instruments, which were sealed, removed from the glove box and heated for 1-3 days at various temperatures as specified.

4.4.2 NMR data

All ^{13}C NMR measurements were performed under ^{1}H-BB decoupling at 100 MHz, using $CDCl_3$ as solvent. Only the relevant main reaction products are stated, peaks superimposed by other compounds are mostly not stated.

a. Acetone System
Mesityl oxide (4-methyl-3-penten-2-one): δ [ppm]: 198.6 (C2), 155.0 (C4), 124.1 (C3), 31.6 (C1), 27.5, 20.5 (CH3).
Phorone (2,6-dimethyl-2,5-heptadiene-4-one): 191.4 (C4), 154.2 (C2/6), 126.1 (C3/5), 27.7, 20.5 (CH_3, superimposed with mesityl oxide peaks).
Mesitylene: 137.6, 126.8 (Ph), 21.1 (CH_3).

b. Cyclohexanone System
Cyclohexanone and cyclohexanol and acetone are not discussed in detail.
2-(1-Cyclohexenyl)cyclohexanone: δ [ppm]: 211.6 ($C_{carbonyl}$), 135.7, 123.5 ($C_{C=C}$), 58.6 (CH), 42.1*, 31.7, 27.5, 27.2*, 25.4*, 24.8, 22.8, 22.3 (CH_2, *superimposed by cyclohexane/ cyclohexanol peaks).

c. Acetophenone System
1,3-Diphenyl-2-buten-1-one: δ [ppm]: 191.7 (C1), 155.0 (C3), 142.6 (C1"), 139.2 (C1'), 132.5 (C4'), 129.1 (C2', C6'), 128.5 (C3', C5'), 128.4 (C3", C5", superimposed), 127.9 (C4"), 126.4 (C2", C6"), 121.9 (C2), 18.7 (C4).

d. Benzophenone System
4,4-Diphenyl-3-buten-2-one: δ [ppm]: 200.0 (C2), 153.9 (C4), 141.1 (C_{Ph}, other aromatic signals superimposed by benzophenone), 115.7 (C3), 30.3 (CH_3).

e. Benzaldehyde System
4-Phenyl-2-butanone: δ [ppm]: 207.4 (C2), 141.1 (Ph_{ipso}), 45.1 (C4), 30.1 (C1), 29.7 (C3).
4-Phenyl-3-buten-2-one: 198.8 (C2), 143.5 (C3), 27.5 (C1).

f. Benzamide System
Isopropyl ether: δ [ppm]: 68.8 (CH), 22.1 (CH_3).
N-Isopropylbenzamide: 166.8 (CO), 135.6 (Ph_{ipso}), 131.8 (Ph_{para}), 42.3 (CH), 22.9 (CH_3).
Isopropyl benzoate: 166.1 (CO), 132.6 (Ph_{para}), 131.2 (Ph_{ipso}), 68.3 (CH), 21.8 (CH_3).

g. Benzylamine System
Dibenzylamine: δ [ppm]: 140.3 (Ph_{ipso}), other Ph superimposed by benzylamine, 53.1 (CH_2).
N-Benzylidenebenzylamine: 161.8 (C=N), 139.3/136.2 (Ph_{ipso}), 130.7 (Ph_{para}), 65.0 (CH_2).
N-Isopropylbenzylamine: 136.5 (Ph_{ipso}), 51.6 (CH_2), 48.0 (CH), 22.9 (CH_3).

4.5 References

[1] E. Traversa, M. L. Di Vona, S. Licoccia, M. Sacerdoti, M. C. Carotta, L. Crema, G. Martinelli, *J. Sol-Gel Sci. Technol.* **2001**, *22*, 167.

[2] V. Guidi, M. C. Carotta, M. Ferroni, G. Martinelli, L. Paglialonga, E. Comini, G. Sberveglieri, *Sens. Actuators, B* **1999**, *57*, 197.

[3] Q. B. Meng, C. H. Fu, Y. Einaga, Z. Z. Gu, A. Fujishima, O. Sato, *Chem. Mater.* **2002**, *14*, 83.

[4] K. L. Frindell, M. H. Bartl, A. Popitsch, G. D. Stucky, *Angew. Chem. Int. Ed.* **2002**, *41*, 959.

[5] A. Hagfeldt, M. Grätzel, *Acc. Chem. Res.* **2000**, *33*, 269.

[6] C. Feldmann, *Adv. Mater.* **2001**, *13*, 1301.

[7] M. Fernández-García, A. Martínez-Arias, J. C. Hanson, J. A. Rodriguez, *Chem. Rev.* **2004**, *104*, 4063.

[8] A. Mills, R. H. Davies, D. Worsley, *Chem. Soc. Rev.* **1993**, *22*, 417.

[9] A. L. Linsebigler, G. Lu, J. T. Yates Jr., *Chem. Rev.* **1995**, *95*, 735.

[10] P. Arnal, R. J. P. Corriu, D. Leclercq, P. H. Mutin, A. Vioux, *J. Mater. Chem.* **1996**, *6*, 1925.

[11] J. Augustynski, *Electrochim. Acta* **1993**, *38*, 43.

[12] C. C. Wang, J. Y. Ying, *Chem. Mater.* **1999**, *11*, 3113.

[13] B. Levy, *J. Electroceram.* **1997**, *1*, 239.

[14] A. Fuerte, M. D. Hernández-Alonso, A. J. Maira, A. Martínez-Arias, M. Fernández-García, J. C. Conesa, J. Soria, *Chem. Commun.* **2001**, 2718.

[15] M. Grätzel, *J. Sol-Gel Sci. Technol.* **2001**, *22*, 7.

[16] M. Grätzel, *Curr. Opin. Colloid Interface Sci.* **1999**, *4*, 314.

[17] H. K. Kammler, L. Maedler, S. E. Pratsinis, *Chem. Eng. Technol.* **2001**, *24*, 583.

[18] W. P. Huang, X. H. Tang, Y. Q. Wang, Y. Koltypin, A. Gedanken, *Chem. Commun.* **2000**, 1415.

[19] Q. Chen, Y. Qian, Z. Chen, G. Zhou, Y. Zhang, *Mater. Lett.* **1995**, *22*, 77.

[20] E. Matijević, M. Budnik, L. Meites, *J. Colloid Interface Sci.* **1977**, *61*, 302.

[21] E. Scolan, C. Sanchez, *Chem. Mater.* **1998**, *10*, 3217.

[22] R. J. P. Corriu, D. Leclercq, P. Lefevre, P. H. Mutin, A. Vioux, *J. Mater. Chem.* **1992**, *2*, 673.

[23] P. Arnal, R. J. P. Corriu, D. Leclercq, P. H. Mutin, A. Vioux, *Mater. Res. Soc. Symp. Proc.* **1994**, *346*, 339.

[24] R. J. P. Corriu, D. Leclercq, *Angew. Chem. Int. Ed.* **1996**, *35*, 1420.

[25] T. J. Trentler, T. E. Denler, J. F. Bertone, A. Agrawal, V. L. Colvin, *J. Am. Chem. Soc.* **1999**, *121*, 1613.

[26] M. Ivanda, S. Musić, M. Gotić, A. Turković, A. M. Tonejc, O. Gamulin, *J. Mol. Struct.* **1999**, *481*, 641.

[27] M. Niederberger, M. H. Bartl, G. D. Stucky, *J. Am. Chem. Soc.* **2002**, *124*, 13642.

[28] M. Niederberger, M. H. Bartl, G. D. Stucky, *Chem. Mater.* **2002**, *14*, 4364.

[29] R. J. P. Corriu, D. Leclercq, P. Lefevre, P. H. Mutin, A. Vioux, *J. Non-Cryst. Solids* **1992**, *146*, 301.

[30] J. N. Hay, H. M. Raval, *J. Sol-Gel Sci. Technol.* **1998**, *13*, 109.

[31] S. C. Goel, M. Y. Chiang, P. C. Gibbons, W. E. Buhro, *Mater. Res. Soc. Symp. Proc.* **1992**, *271*, 3.

[32] H. Meerwein, R. Schmidt, *Liebigs Ann. Chem.* **1925**, *444*, 221.

[33] A. Verley, *Bull. Soc. Chim. Fr.* **1925**, *37*, 537.

[34] W. Ponndorf, *Angew. Chem.* **1926**, *39*, 138.

[35] B. C. Gaskins, J. J. Lannutti, *J. Mater. Res.* **1996**, *11*, 1953.

[36] V. J. Shiner, D. Whittaker, *J. Am. Chem. Soc.* **1963**, *85*, 2337.

[37] J. Que, Y. Ishimura, M. Nagato, *Nippon Kagaku Kaishi* **1996**, 256.

5 Synthesis of Yttria-Based Nanostructures and their Formation Mechanism

5.1 Introduction

Like TiO_2, yttrium oxide is a promising semiconductor material. It has high thermal stability up to 2300 °C, and possesses a high dielectric constant and a bandgap of ca. 5.1 eV.[1] This makes Y_2O_3 films an excellent candidate for storage capacitors in dynamic random-access memory devices.[1,2] On the other hand, yttrium oxide, activated by doping with europium, is a well-known and widely used commercial red phosphor, its main applications being lighting and cathode ray tubes, display materials, tricolor fluorescent lamps, field emission displays and laser devices.[3] It is advantageous that the phosphor particles are as small as possible, as this potentially leads to higher screen resolution, lower screen loading and a higher screen density.[4]

Many attempts have been made to prepare nanocrystalline Y_2O_3, mainly in the form of thin films.[5,6] The combustion synthesis of (doped) yttrium oxide nanopowders has been investigated intensively.[7] The synthesis via soft chemical routes has also been reported. A method where nucleation of yttria is induced by decomposition of urea yielded particles about 70-100 nm in size, which however had to be subjected to a thermal treatment to induce crystallization.[4] Precipitation from an aqueous solution of yttrium nitrate by organic bases resulted in smaller particles ca. 10 nm in size,[8] whereas another group reported doped yttria particles 8-16 nm in size prepared in a nonionic reverse microemulsion,[9] both systems however still requiring subsequent calcination at 700 °C to obtain crystalline materials.

Hence, it appeared promising to explore the possibility of a nonaqueous synthesis of Y_2O_3 nanoparticles. In fact, however, it turned out that not inorganic nanoparticles but organic-inorganic hybrid structures were formed by solvothermal reaction of yttrium(III) isopropoxide in benzyl alcohol. These structures had high lamellar ordering, consisting of alternating layers of yttria and organic material, each only about 0.5 and 1.5 nm thick, respectively.

The controlled synthesis and characterization of such lamellar structures is still a challenge in nanochemistry. 2-Dimensional systems such as quantum wells and layered heterostructures are of high scientific and technological interest. Their electronic and optical properties make them promising for thermoelectric applications[10] and as components for optoelectronic devices.[11,12]

Confined structures, which includes not only 2D systems but also quantum dots (0D), nanowires and nanotubes (1D),[13] are usually prepared employing template-directed approaches to achieve size and shape control.[14,15] However, there are also much simpler systems, where the control over the dimensionality of the nanoparticles is exerted by the solvent. The solvent acts as monodentate ligand and shape controller, so that additional surfactants are not required. This has the big advantage that the concentration of impurities in the final product can be kept as low as possible. Using this approach, e.g. semiconductor chalcogenide nanorods were synthesized in n-butylamine.[16]

Therefore, the fact that a one-step nonaqueous chemical treatment resulted in the synthesis of an inorganic-organic nanocomposite being composed of two-dimensional crystalline layers and organic ligands, is of high technological importance, especially due to the facile synthesis. Hence, the reaction mechanism is studied in detail to gain insight into the formation processes resulting in such a highly ordered structure.

5.2 Results and Discussion

Yttrium(III) isopropoxide was subjected to a solvothermal treatment in benzyl alcohol by simply dispersing the alkoxide in the solvent and transferring the solution into an autoclave. After 2 days at 250 °C, and subsequent separation and washing of the precipitate, a white powder was obtained. Figure 5.1 **A** presents a TEM image of an as-prepared sample. Typically, nanostructures 20 nm in width and 40-50 nm in length were found, entirely consisting of equally spaced parallel lamellae with very different electron contrast. The dark layers arise from the presence of strong scatterers, indicating inorganic material, whereas the organic material stays practically invisible between those layers. The particles are stacked in one direction, forming rod-like nanostructures with corrugated sides. In addition, there is also some lateral aggregation, i.e., perpendicular to the yttrium oxide layers. Individual and isolated particles are scarcely found in this sample. It is a notable feature of these nanostructures that the high order of layers is preserved over several hundreds of nanometers. The Fourier transform of this image (Fig. 5.1 **B**) gives rise to a pair of sharp spots, which can be attributed to the 100 reflection of the lamellar structure. The interlayer distance measured from those pictures is 1.7 nm.

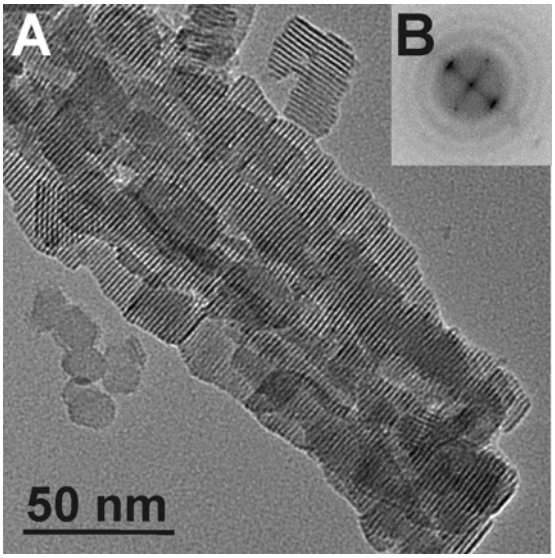

Figure 5.1. TEM image of the yttrium oxide nanocomposite (**A**) and its Fourier transform (**B**).

Both SAXS and WAXS were employed to further characterize the material and verify the TEM results. Figure 5.2 **A** shows the SAXS data obtained on a Kratky camera. The pattern of the as-prepared sample (**1**) exhibits a very sharp peak (the presented data are raw data still smeared with the applied slit collimation), which is characteristic of a lamellar structure. The reflection centered at 0.576 nm^{-1} corresponds to an interlamellar distance of 1.74 nm. After calcination at 550 °C, when the organic material can be expected to be vanished by degradation, the peak is no longer present (**2**).

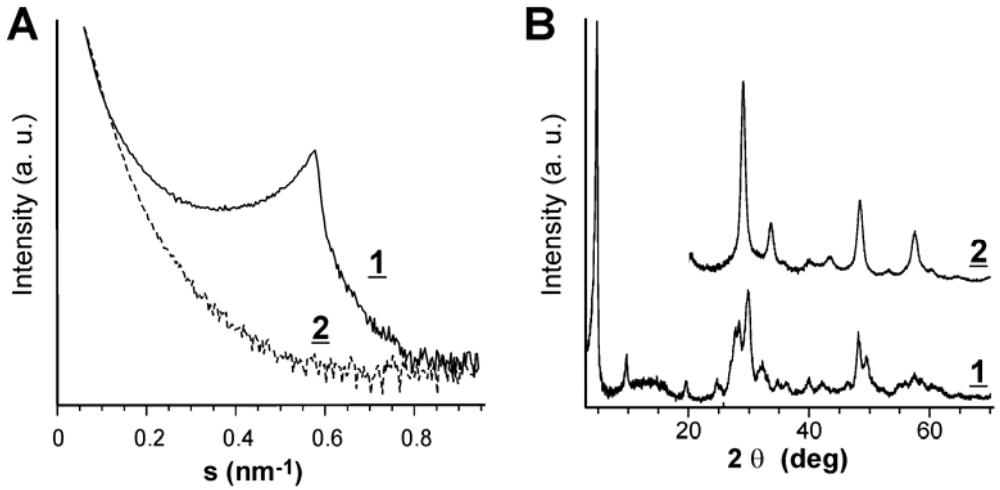

Figure 5.2. SAXS (**A**) and WAXS (**B**) data obtained for the yttrium oxide nanocomposite, each as-prepared (**1**) and after calcination at 550 °C (**2**).

The obtained WAXS data are presented in Fig. 5.2 **B**. The pattern of the as-prepared sample (**1**) exhibits the same feature in the low-angle region as the SAXS plot, being dominated by a signal at 2θ = 4.8°, corresponding to the 100 diffraction of the lamellar phase. The second, fourth and fifth order reflections can be clearly assigned at 2θ = 4.8°, 9.8°, 19.6° and 24.6°.

Quantitative analysis of the XRD data was performed following the approach of Ruland and Smarsly[17,18] by fitting the experimental data with analytical expressions for the one-dimensional density function. The so-called lattice model was used, assuming that the mean thickness of each layer, $\bar{d}_j$, is independent of the thickness of the previous one. Fitting parameters are *L*, the distance of the centers of two equal layers, also referred to as the long period, and its variance σ_L. Hence, the scattering intensity I_1, in dependence of the length *s* of the scattering vector, is calculated to

$$I_1(s) = \frac{1}{2\pi^2 s^2} \cdot \left\{ 1 - \mathrm{Re}\, H_1(s) + 4 \cdot \left[\mathrm{Im}\, H_1\left(\frac{s}{2}\right) \right]^2 \cdot \mathrm{Re}\left[\frac{H_L(s)}{1 - H_L(s)} \right] \right\} \qquad \text{(Eq. 5.1)}$$

with $H_1 = \exp(2\pi i \bar{d}_1 s - 2\pi^2 \sigma_1^2 s^2)$ (Eq. 5.2)

and $H_L = \exp(2\pi i \bar{L} s - 2\pi^2 \sigma_L^2 s^2)$ (Eq. 5.3).

The long period *L* deduced by this method is 1.75 nm, the thicknesses $\bar{d}_j$ of the two layers are about 1.2-1.25 nm and 0.55-0.6 nm, respectively, and their variation in thickness is smaller than 0.05 nm. The other wide angle reflections belong to the structure of nanocrystalline yttrium oxide. They are about to match with the peak positions of the monoclinic modification of yttrium oxide (JCPDS No. 44-399). However, the agreement is not perfect, and some of the peaks are slightly moved or even split. This can be explained by the fact that the yttrium oxide is essentially just present as a two-dimensional layer of yttrium oxide octahedra with reduced periodicity in all directions that are not in the plane.

The XRD pattern of the sample obtained after calcination at 550 °C for 5 h (Fig. 5.2 **B**, **2**) shows sharp reflections that can be attributed to the cubic structure of yttrium oxide (JCPDS No. 41-1105). The low angle peaks are no longer visible, proving the collapse of the lamellar structure, i.e. the nanohybrid has been destroyed.

The elemental composition of the nanohybrid was measured by CHN elemental analysis for the carbon and hydrogen content, and by ICP-OES to determine the yttrium content. According to these analyses, the composition of the yttria hybrid can be expressed by the general formula $Y_{1.95}O_{5.46}C_7H_{5.52}$ (oxygen providing the remaining mass of the sample). The large amount of oxygen, and low amount of hydrogen with respect to carbon, points to the possibility that the organic component of the hybrid is not benzyl alcohol but benzoic acid. This is confirmed by solid-state NMR measurements showing the exclusive presence of

benzoate molecules in the intercalated organic species. Aside from the anisotropic sidebands, peaks were observed only at δ = 126.8 ppm for the acid group, and a broader signal at δ = 133.3-127.6 ppm for the aromatic carbons. The position of the acid group is shifted compared to uncoordinated benzoic acid (172.8 ppm). This is indicative for the binding of the carboxylate group to the Lewis-acidic yttrium centers, leading to an electron flow from the carbon atom to the yttrium cations. Neither uncoordinated, protonated benzoic acid nor benzyl alcohol were detected in the sample. Hence, all carbon is assumed to be present as benzoate species coordinated to yttrium. The surplus of hydrogen with respect to benzoate gives a hint to the presence of surface-adsorbed water, leading to the composition of the nanocomposite as $Y_2O_{2.5}(C_7H_5OO)(H_2O)_x$ with $0.5 < x < 1$.

Raman spectroscopy was carried out to investigate the binding of benzoate to the yttrium centers.[19] The results indicated that most probably, benzoate is coordinated in a bridging fashion as depicted in Figure 5.3.

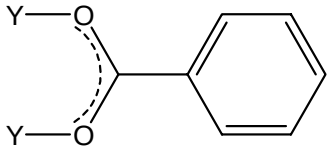

Figure 5.3. Proposed coordination of the benzoate to two yttrium atoms.

Considering the simplicity of the starting reaction mixture (yttrium isopropoxide and benzyl alcohol only) and the complexity of the resulting product, it is clear that the formation must proceed via a number of parallel or consecutive reactions. For analysis of the synthesis mechanism, the formed nanohybrid precipitate was removed by centrifugation and filtration and the resulting solution carefully analyzed by ^{1}H-BB decoupled ^{13}C and by ^{1}H NMR measurements (Figure 5.4 **A** and **B**) in order to detect the side products of the synthesis. In addition to the solvent benzyl alcohol (labeled BA), isopropanol (**1**) as well as 4-phenyl-2-butanol (**2**) were found in significant quantities. Toluene (**3**) and small amounts of benzyl ether (**4**), benzaldehyde (**5**) and 1,5-diphenyl-3-pentanol (**6**) could also be identified from the ^{13}C-NMR spectrum. From the ^{1}H spectrum, a molar ratio of 1.00 4-phenyl-2-butanol : 0.71 isopropanol : 1.42 toluene : 0.26 benzyl ether : 0.25 1,5-diphenyl-3-pentanol : 0.38 benzaldehyde was calculated. The amount of benzyl ether, however, can only be roughly estimated, as its signals are very similar to the dominant benzyl alcohol peaks and had to be calculated by deconvolution.

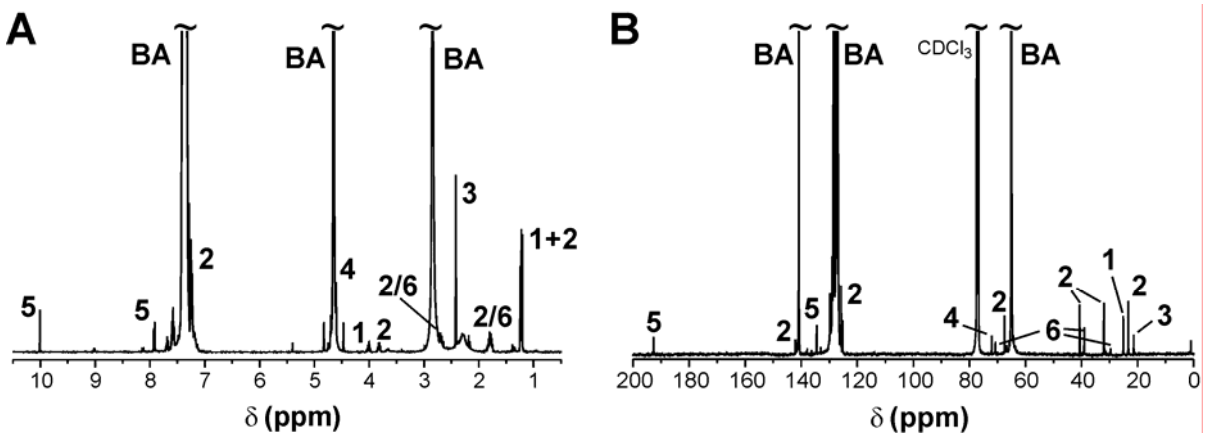

Figure 5.4. ^{1}H (**A**) and ^{1}H-BB decoupled ^{13}C (**B**) NMR spectra of the final reaction solution after removal of the solid material by centrifugation and filtration (see text for labels).

These results prove that ether formation, which would be expected for a conventional nonhydrolytic sol-gel mechanism,[20] is almost negligible (diisopropyl ether or isopropyl benzyl ether could not be detected at all). The formation of the yttria nanocomposite material however obviously proceeds via the novel C–C coupling route as observed for the synthesis of $BaTiO_3$ nanoparticles in benzyl alcohol (cf. Chapter 3.2).

In the $BaTiO_3$ system, a major role in the formation mechanism was attributed to the deprotonation of the isopropoxy ligand due to the very alkaline conditions in the reaction mixture. These alkaline conditions are however not present in the system discussed here. On the contrary, yttrium(III) complexes are hard Lewis acids. Potentially, the absence of a formal base could be compensated by the Lewis-acidity of the metal complex, as the formation of an agostic bond on the metal complex is expected to be greatly enhanced by the attraction of electrons to the yttrium center. Based on these findings, the mechanism is proposed as shown in Scheme 5.1. First, the oxygen atom of benzyl alcohol is coordinated to an yttrium center, strongly enhanced by the Lewis-acidity of the metal. This Lewis-acidity also supports the deprotonation of a $–CH_3$ group of the isopropoxy ligand (**1**). The carbanion is stabilized via an agostic bond to the yttrium, which is now in a pentacoordinated transition state. The carbanion instantly reacts with the benzyl fragment to form a C–C bond (**2** and **3**). Upon condensation, 4-phenyl-2-butanol is released (**4**). Deprotonation of the second $–CH_3$ group, followed by another coupling step, leads to the disubstituted product 1,5-diphenyl-3-pentanol, which is found to a lower but significant extent.

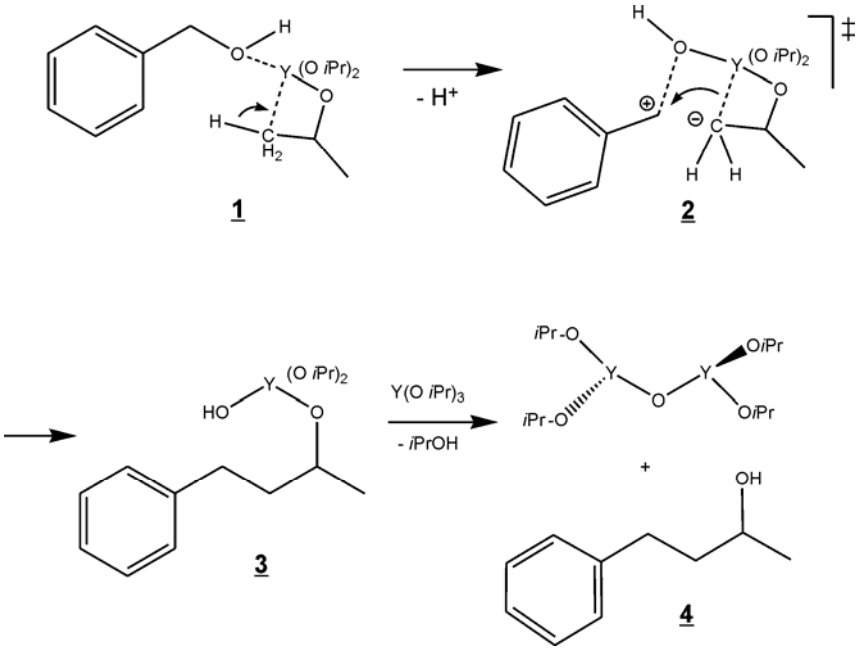

Scheme 5.1. Reaction of $Y(OiPr)_3$ with benzyl alcohol, leading to the simultaneous formation of yttria clusters and 4-phenyl-2-butanol.

Throughout the synthesis of $BaTiO_3$, a simultaneous side reaction was observed, similar to the Meerwein-Ponndorf-Verley (MPV) reaction, leading to the formation of toluene and ketones. It is interesting to note that the amount of toluene in the reaction solution is much higher for the yttria system, as even more toluene then C–C coupling product was found. No 4-phenyl-2-butanone was present in the solution, but a significant amount of benzaldehyde. Therefore, we infer that yttrium catalyzes a slightly different reaction involving two benzyl alcohol species (Scheme 5.2). This mechanism is analogous to the disproportionation of benzyl alcohol observed on alumina surfaces at 300°C.[21] It is an open question whether the reaction is actually catalyzed by just an individual yttrium alkoxide or, more probably, on the surface of the already formed yttrium oxide nanostructures. As both reactions would proceed in a quite similar fashion, for simplicity of presentation the former case is discussed. Ligand exchange is often observed for sol-gel reactions performed in alcohols.[20] Due to the large excess of benzyl alcohol, it is likely that an exchange of isopropoxy against benzyl alcohol ligands occurs to a large extent. As another benzyl alcohol molecule coordinates to the metal center (**1***), a hydride transfer can take place between the CH_2 group of the coordinated benzyl alcohol ligand and the CH_2 group of the second ligand (**2***) via a cyclic transition state. The next step involves the release of toluene and benzaldehyde. At the same time a hydroxy group is formed on the yttrium species, promoting the condensation with another yttrium isopropoxide (**3***).

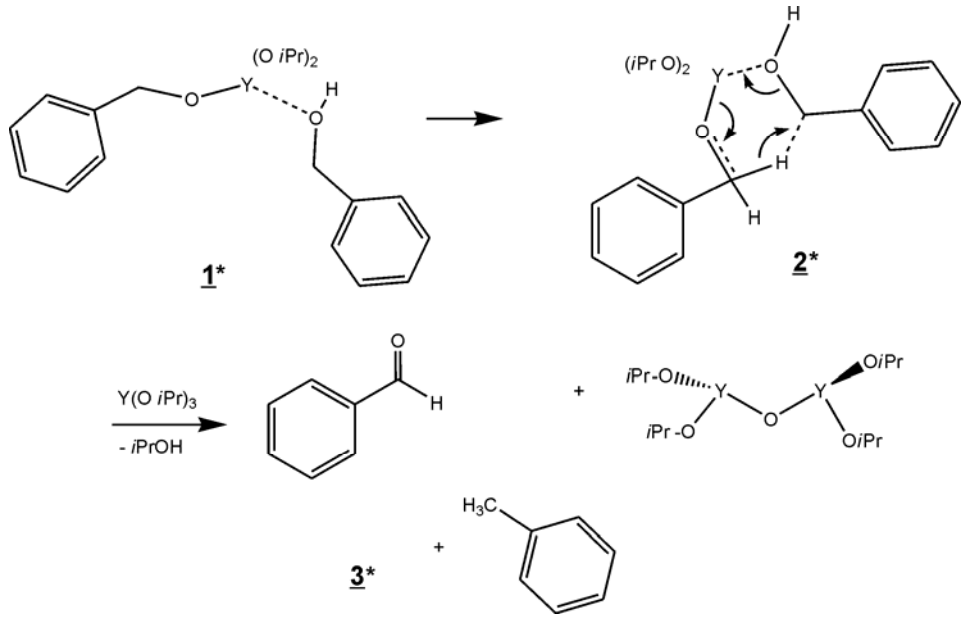

Scheme 5.2. Side reaction in the system, a hydride transfer similar as in an MPV reaction leading to the disproportionation of benzyl alcohol to toluene and benzaldehyde.

As benzaldehyde is found in much lower proportion than toluene (about 1 : 4), but the nanocomposite contains larger amounts of benzoic acid, it appears probable that the yttrium oxide nanostructure catalyzes another hydride-transfer reaction. Note that oxygen was excluded during the synthesis so that simple oxidation cannot take place. The formation of benzoic acid via a Cannizzaro-like reaction on various metal oxides is known, and even the simultaneous formation of metal-coordinated benzoic acid and toluene from benzyl alcohol and benzaldehyde has been suggested.[22]

The proposed mechanism is displayed in Scheme 5.3. First, benzaldehyde coordinates to an yttrium center via the carbonyl oxygen, producing a highly electrophilic carbon atom (**1**$^{\pm}$). In a next step, the oxygen atom of a benzyl alcohol molecule, which is coordinated to a vicinal yttrium center, attacks the electrophilic carbon. Simultaneously, hydride transfer takes place to form toluene (**2**$^{\pm}$). As the resulting benzoic acid is coordinated to the yttrium oxide surface in a stable fashion (**3**$^{\pm}$), it blocks further 3D growth of the nanocrystal. Both reaction and structure formation are therefore self-confining: the generated surface-bound acid stops further structural growth and defines the geometry of a lamellar nanostructure of alternating yttria/benzoic acid layers, whereas no further benzoic acid is generated when the surface is saturated. This self-confinement also speaks for the fact that the presence of a minute yttria surface is a prerequisite for the side reaction to form benzoic acid. This proposed mechanism was verified by reacting the yttrium alkoxide directly with benzaldehyde instead of benzyl alcohol. To a great extent, benzyl benzoate $C_6H_5CH_2OCOC_6H_5$, which is the expected product

of two benzaldehyde molecules reacting via the proposed mechanism, was found in the reaction solution. This proves the occurrence of hydride transfer reactions under these reaction conditions.

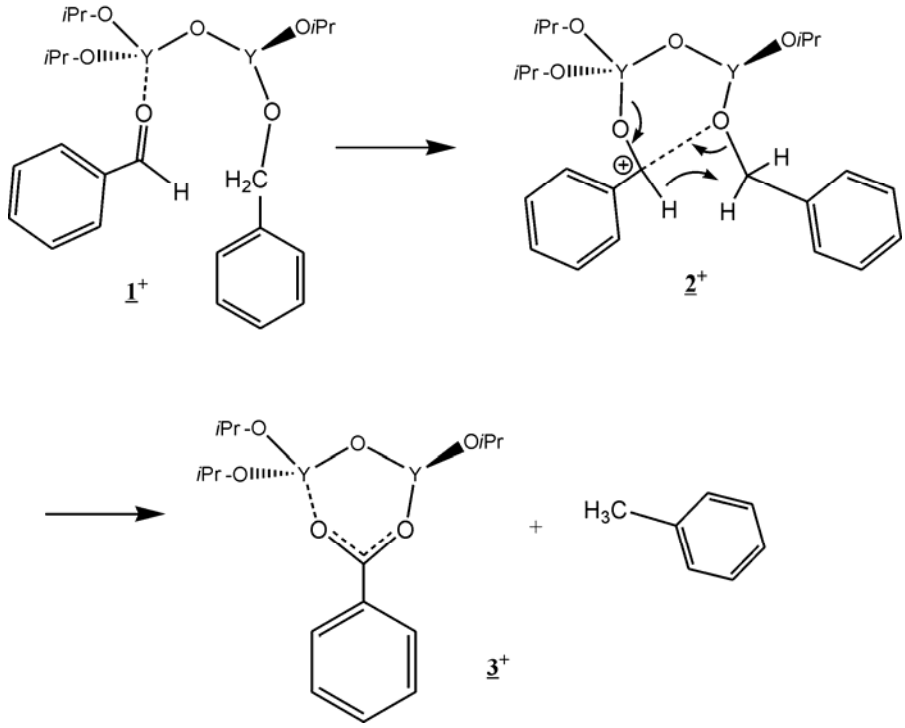

Scheme 5.3. Proposed formation mechanism of the yttria-benzoate nanocomposite via the disproportionation of benzyl alcohol.

5.3 Summary and Conclusions

The reaction of yttrium(III) isopropoxide in benzyl alcohol did not result in inorganic nanocrystals, as for other systems, but led to the formation of a lamellar nanocomposite. The layers are arranged in a very regular manner, as has been shown by TEM and SAXS. In fact, the nanocomposite consists of alternating layers of yttria and benzoic acid. It is quite surprising that such a simple system leads to highly organized nanostructures.

The reaction mechanism was studied, and it was found that the C–C coupling reaction observed for $BaTiO_3$ indeed also takes place in the yttrium-containing system. Interestingly, strongly alkaline conditions, which were believed essential for deprotonation and hence activation of the isopropoxide ligand in the $BaTiO_3$ system, are absent here, but are probably compensated by the strong Lewis-acidity of Y^{3+} centers. Further studies on the coupling reaction are discussed in Chapter 9. In addition, MPV-like oxidation/reduction processes were

found to take place to a large extent, eventually resulting in benzoate species which strongly ligate to the yttria surface, hence causing a confinement effect which controls the growth of the crystals to form the observed nanolayers.

5.4 Experimental Section

5.4.1 Synthesis

The synthesis was carried out in a glovebox (O_2 and H_2O < 0.1 ppm). In a typical synthesis of yttria nanohybrids, 500 mg of yttrium(III) isopropoxide was added to 20 mL of benzyl alcohol. The reaction mixture was transferred into a Teflon cup of 45 ml inner volume, slid into a steel autoclave (Parr Instruments) and carefully sealed. The autoclave was taken out of the glovebox and heated in a furnace at 250 °C for 2 days. The resulting milky suspension was centrifuged, the precipitate thoroughly washed with ethanol and dichloromethane and subsequently dried in air at 60 °C. The powder was further dried in vacuo for 2 days to remove adsorbed solvent molecules. For special characterization experiments, the dry powder was calcined at 550 °C for 5 hours in air.

5.4.2 NMR Data

^{13}C NMR measurements were performed under ^{1}H-BB decoupling at 100 MHz, ^{1}H NMR measurements at 400 MHz, all in $CDCl_3$. Only the main reaction products are given.

4-phenyl-2-butanol: ^{1}H NMR δ[ppm]: 7.25-7.15 (5H, H_{Ph}), 3.77 (1H, H2), 2.72/2.65 (2H, H4), 1.75/1.72 (2H, H3), 1.17 (3H, $–CH_3$), –OH not visible; ^{13}C NMR δ[ppm]: 142.2, 128.5-127.4, 125.9 (C_{Ph}), 67.4, 40.7, 32.1 (C2,3,4), 23.3 (C1).
1,5-diphenyl-3-pentanol: ^{1}H NMR 7.25-7.15 (5H, H_{Ph}), 3.66 (1H, H3), 2.72/2.65 (4H, H1/5), 1.75/1.72 (4H, H2/4), -OH not visible; ^{13}C NMR 142.2, 128.5-127.4, 125.9 (C_{Ph}), 70.7, 39.1, 32.0 (C3, C2/4, C1/5).
Benzaldehyde: ^{1}H NMR 9.95 (1H, –CHO), CH_{Ph} superimposed with other aromatic species present in the mixture; ^{13}C NMR 192.4 (–CHO), 136.2, 134.4 (C_{Ph}, other aromatic carbons superimposed).
Toluene: ^{1}H NMR 2.32 (3H, $–CH_3$), CH_{Ph} superimposed; ^{13}C NMR 21.5 ($–CH_3$), C_{Ph} superimposed with other aromatic species.
Benzyl ether: ^{1}H NMR 4.55 (2H, $–CH_2–$, integral calculated by deconvolution), CH_{Ph} superimposed; ^{13}C NMR 137.8 (C_{Ph}, other aromatic carbons superimposed), 72.0 ppm ($–CH_2–$).

5.5 References

[1] M.-H. Cho, D.-H. Ko, J. G. Seo, S. W. Whangbo, K. Jeong, I. W. Lyo, C. N. Whang, D. Y. Noh, H. J. Kim, *Thin Solid Films* **2001**, *382*, 288.

[2] A. C. Rastogi, R. N. Sharma, *J. Appl. Phys.* **1992**, *71*, 5041.

[3] M. V. Nazarov, J. H. Kang, D. Y. Jeon, E.-J. Popovici, L. Muresan, B. S. Tsukerblat, *Solid State Commun.* **2005**, *133*, 183.

[4] G. Wakefield, E. Holland, P. J. Dobson, J. L. Hutchison, *Adv. Mater.* **2001**, *13*, 1557.

[5] R. J. Gaboriaud, F. Pailloux, P. Guerin, F. Paumier, *J. Phys. D: Appl. Phys.* **2000**, *33*, 2884.

[6] R. P. Rao, *Solid State Commun.* **1996**, *99*, 439.

[7] G. Tessari, M. Bettinelli, A. Speghini, D. Ajò, G. Pozza, L. E. Depero, B. Allieri, L. Sangaletti, *Appl. Surf. Sci.* **1999**, *144-145*, 686.

[8] M. D. Fokema, E. Chiu, J. Y. Ying, *Langmuir* **2000**, *16*, 3154.

[9] M.-H. Lee, S. J. Oh, S.-C. Yi, *J. Colloid Interface Sci.* **2000**, *226*, 65.

[10] M. S. Dresselhaus, G. Dresselhaus, X. Sun, Z. Zhang, S. B. Cronin, T. Koga, *Phys. Solid State* **1999**, *41*, 679.

[11] L. Eldada, *Rev. Sci. Instrum.* **2004**, *75*, 575.

[12] F. Bassani, G. C. La Rocca, D. M. Basko, V. Agranovich, *Phys. Solid State* **1999**, *41*, 701.

[13] G. C. Papavassiliou, *Prog. Solid State Chem.* **1997**, *25*, 125.

[14] R. A. Caruso, *Top. Curr. Chem.* **2003**, *226*, 91.

[15] S. H. Yu, M. Antonietti, H. Cölfen, M. Giersig, *Angew. Chem. Int. Ed.* **2002**, *41*, 2356.

[16] J. Yang, C. Xue, S. H. Yu, J. H. Zeng, Y. T. Qian, *Angew. Chem. Int. Ed.* **2002**, *41*, 4697.

[17] W. Ruland, B. Smarsly, *J. Appl. Cryst.* **2004**, *37*, 575.

[18] G. Garnweitner, B. Smarsly, R. Assink, D. R. Dunphy, C. Scullin, C. J. Brinker, *Langmuir* **2004**, *20*, 9811.

[19] N. Pinna, G. Garnweitner, P. Beato, M. Niederberger, M. Antonietti, *Small* **2005**, *1*, 113.

[20] A. Vioux, *Chem. Mater.* **1997**, *9*, 2292.

[21] R. Sreekumar, C. N. Pillai, *Catal. Lett.* **1993**, *19*, 281.

[22] D. Haffad, U. Kameswari, M. M. Bettahar, A. Chambellan, J. C. Lavalley, *J. Catal.* **1997**, *172*, 85.

6 Synthesis of Binary Metal Oxide Nanoparticles from Metal Acetylacetonates

6.1 Introduction

Metal acetylacetonates, or generally metal β-diketonates, are interesting precursor materials for the synthesis of metal oxides. The acetylacetonates are commercially available in good quality for most transition metals, as well as for group III and IV metals such as Pb and Sn. These acetylacetonates are cheap compared to metal alkoxides and, most importantly, they are chemically more stable, facilitating handling and storage procedures.

Thanks to these properties, already for more than a decade metal acetylacetonates are being used as source materials for chemical vapor deposition[1] and as precursor materials for aerogels.[2,3] Also the synthesis of nanoparticles by sol-gel routes involving the use of acetylacetonates and especially acetylacetonate (acac)-modified precursors has been widely explored. In many cases, the reactivity of metal alkoxides or chlorides towards hydrolysis is too high to allow control of hydrolysis – condensation rates, and can be decreased by modification with β-diketones such as acetylacetone, which has become a popular strategy, leading to a more controlled reaction and more uniform products.[4] For example, whilst the hydrolysis of $Ti(O\textit{i}Pr)_4$ produced polydispersed TiO_2 particles 10-25 nm in size, the same treatment of $Ti(O\textit{i}Pr)_3(acac)$ resulted in a colloidal sol of 5-10 nm-sized particles.[5] Using acac-complexed $Ti(O\textit{n}Bu)_4$, the size of the resulting particles could even be adjusted in the 1-2 nm range.[6] However, a too high acetylacetone/metal ratio may decrease the yield of nanoparticles as the resulting acac chelate ligand is too stable against hydrolysis, as found for the synthesis of SnO_2 nanoparticles.[7]

Recently, several reports on the nonaqueous conversion of metal acetylacetonates to oxides were published, most of them not mentioning the formation mechanism at all, or claiming a thermal decomposition of the acac precursor during the synthesis, however without studying the mechanism in detail.[8-11] Under vacuum, metal acetylacetonates indeed start to decompose to acetylacetone and acetone around 200 °C,[12] however their behavior during solvothermal treatments at temperatures above 100 °C has not been described so far. Few investigations dealt with the fate of the acetylacetonate ligands upon formation of the oxidic material. The synthesis of Si-O-Al bonds from $Al(acac)_3$ by heating the acetylacetonate with polycarbosilane under N_2 was found to leave organic condensation products such as 3-penten-2-one and 2,3-dihydro-1,4-dioxine,[13] whereas the reaction of $Zn(acac)_2$ in boiling ethanol was

reported to result in nanocrystalline ZnO particles whilst the acetylacetonate is reacted to acetone and sodium acetate.[14]

In this chapter, the nonaqueous synthesis of metal oxides by solvothermal treatment of metal acetylacetonates is described and investigated in detail. Whereas phase-pure magnetite (Fe_3O_4) particles were obtained upon reaction in benzyl alcohol, benzylamine showed to be a very versatile reaction medium, making possible the synthesis of various binary oxides such as γ-Ga_2O_3, zincite ZnO, and cubic In_2O_3 as well as iron oxide. The technological importance of these oxides is huge. Submicrometric iron oxides are important materials for magnetic and pigment applications. Acicular maghemite (γ-Fe_2O_3), for example, is the magnetic powder most often used for recording information.[15] Magnetic particles, especially of Fe_3O_4, are also exploited in the form of thin films in a range of protective or sensitive coatings.[16,17] Indium oxide and zinc oxide both show a wide band gap (3.65 and 3.37 eV, respectively), making them promising materials for transparent conductive coatings and gas sensors.[18-22]

6.2 Synthesis in benzylamine

Benzylamine, like other amines, is basic and corrosive. Due to its high boiling point of 184 °C, on the other hand, it possesses low volatility and can be stored and handled in a glove box. The synthesis was performed simply by mixing a metal acetylacetonate with benzylamine followed by solvothermal treatment in the autoclave. In all cases, powders were obtained which were separated by centrifugation and washed several times.

The powder XRD patterns of the as-synthesized metal oxide samples are shown in Figure 6.1. All diffraction peaks can be assigned to the respective phases without indication of other crystalline byproducts. The reflections of the In_2O_3 nanoparticles are sharp and correspond to the cubic structure (Fig. 6.1, **2**, JCPDS No. 6-416). Gallium oxide (Fig. 6.1, **3**) exhibits broader peaks characteristic for small crystallite sizes with the γ-Ga_2O_3 structure (JCPDS No. 20-426). The sharp reflections of the XRD pattern of zinc oxide (Fig. 6.1, **4**) can be attributed to the zincite structure ZnO (JCPDS No. 36-1451). The pattern of the iron oxide exhibits broad peaks (Fig. 6.1, **1**) matching with both the magnetite Fe_3O_4 (JCPDS No. 19-629) and maghemite γ-Fe_2O_3 (JCPDS No. 39-1346) structure. The XRD pattern of magnetite and maghemite just differ in a few low intensity reflections (< 5 %) present at $2\theta = 23.8$ and 26.1° and therefore, Raman measurements have to be consulted to unambiguously assign the crystal phase.[23]

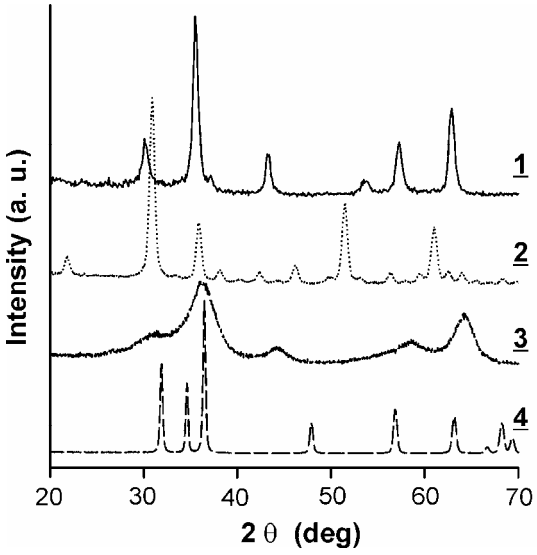

Figure 6.1. XRD patterns of the iron oxide (**1**, solid line), indium oxide (**2**, dotted line), gallium oxide (**3**, dashed line), and zinc oxide (**4**, long dashed line) samples.

Figure 6.2 presents the Raman spectrum of the iron oxide nanoparticles. There is a main band at 672 cm^{-1}, which is characteristic for magnetite. The broad structures around 700, 500 and 350 cm^{-1}, respectively, are typical for maghemite[23] and give evidence that as a matter of fact the iron oxide sample consists of both phases.

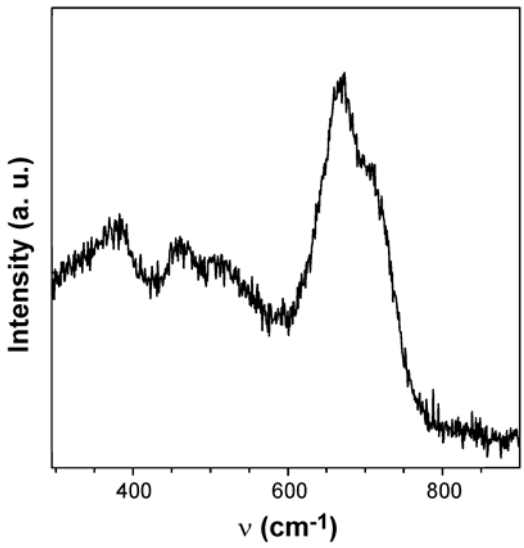

Figure 6.2. Raman spectrum of the iron oxide nanoparticles.

Transmission electron microscopy (TEM) measurements of the as-synthesized particles are presented in Figure 6.3. The overview TEM image of the iron oxide particles (Fig. 6.3 **A**) shows that their size ranges from 15 to 20 nm. The maghemite phase as part of the iron oxide sample is further proved by the presence of the corresponding diffraction rings, as indicated by the arrows in Fig. 6.3 **B**. The indium oxide nanoparticles exhibit a cubic shape with sizes of 10-15 nm (Fig. 6.3 **C**), similar to In_2O_3 synthesized from indium(III) isopropoxide in benzyl alcohol.[19]

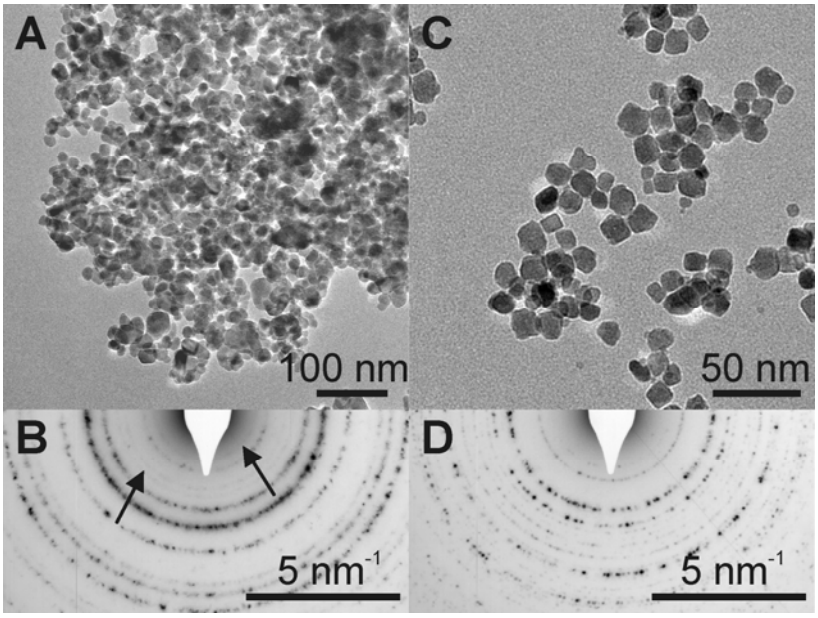

Figure 6.3. TEM overview images of iron oxide (**A**), indium oxide (**C**), gallium oxide (**E**) and zinc oxide nanoparticles (**G** and **H**, scale bar 100 nm) and their respective SAED patterns (**B**, **D, F** and **I**).

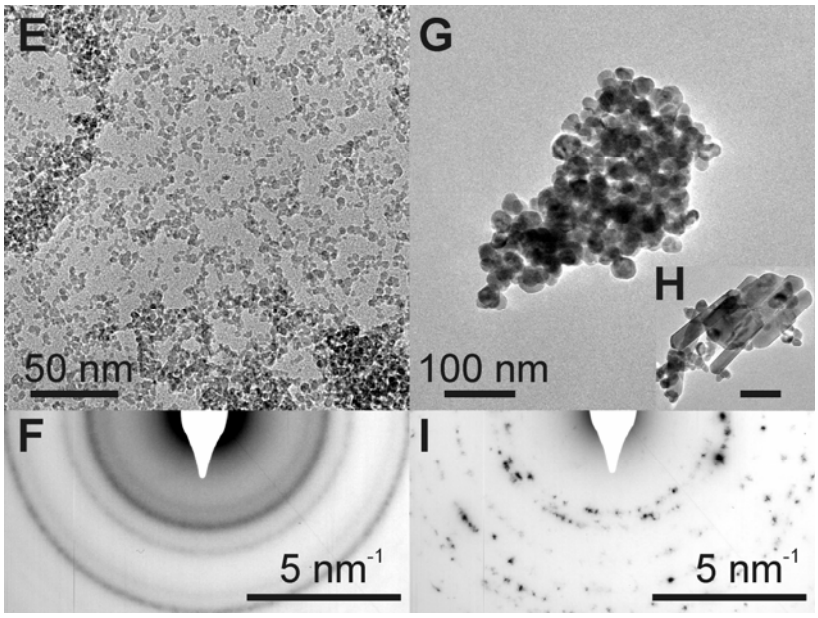

As already expected from the XRD measurements, the gallium oxide nanoparticles are particularly small (Fig. 6.3 **E**), with sizes ranging from 2.5 to 3.5 nm. The zinc oxide displays less uniform particle morphology. In addition to spherical nanoparticles typically of 20 nm in diameter (Fig. 6.3 **G**), also nanorods were frequently found, generally about 200 nm long and 30 nm wide (Fig. 6.3 **H**). The crystal structure of these nanoparticles was additionally studied by selected area electron diffraction (SAED) as depicted in Fig. 6.3 **B**, **D**, **F** and **I,** respectively. In all cases, the patterns coincide well with the XRD data.

It is amazing that equal experimental conditions (i.e., the reaction of a metal acetylacetonate in benzylamine at 200 °C) lead to the formation of nicely crystalline nanopowders of different families of metal oxides. In order to investigate the formation mechanism for these systems, the composition of the obtained reaction solution was studied for each metal oxide after removal of the particles by centrifugation. The mixtures of organic reaction products found, however, turned out to be very similar for all systems. Therefore only the iron oxide system will be discussed in detail.

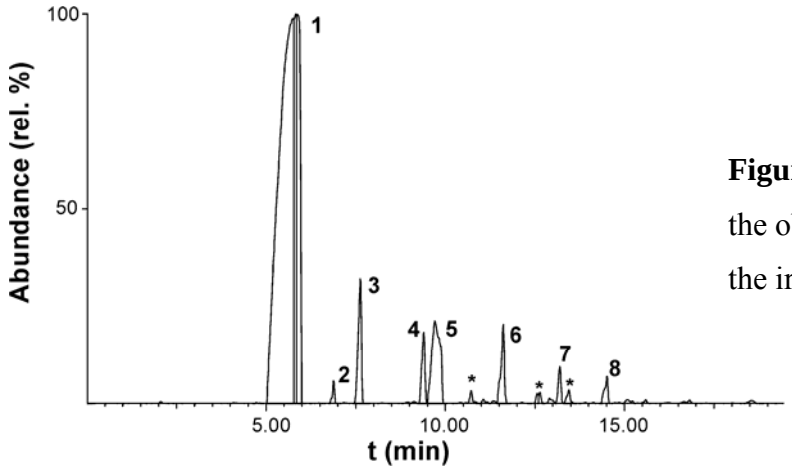

Figure 6.4. Gas chromatogram of the obtained reaction solution for the iron oxide system.

GC–MS analysis was performed to identify the components of the mixture, which was rather complex. Figure 6.4 shows the obtained chromatogram with individual peaks analyzed by MS (data not shown). $CHCl_3$ and other substances with low retention time are not shown in this plot. The largest peak (**1**) corresponds to the solvent benzylamine. A small amount of N-isopropylbenzylamine was also found (**2**), whereas the amount of N-isopropylidenebenzylamine was quite significant (**3**). Peak **4** is attributed to 4-benzylamino-3-penten-2-one, whilst **5** stems from N-benzylacetamide. Peak **6** is assigned to N-benzylidenebenzylamine, whereas peaks **7** and **8** are assumed to stem from N-(4-phenylbutan-2-ylidene)benzylamine and 5-benzylamino-1-phenyl-4-hexen-3-one, respectively. The small peaks (marked *) are attributed to other condensation products and are not discussed in detail due to their low quantity. The chemical structures of the identified compounds are illustrated in Figure 6.5.

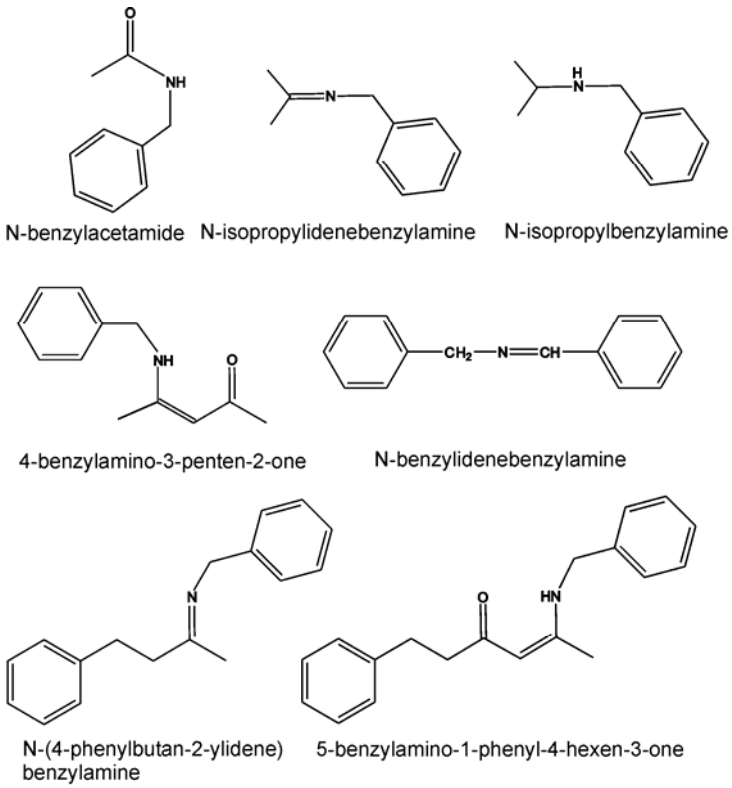

Figure 6.5. Chemical structures of the organic species found in the final reaction mixture in the iron oxide system.

To verify these results, ^{1}H and $^{13}C\{^{1}H\}$ NMR spectra were recorded. The ^{13}C spectrum in Figure 6.6 shows, in addition to the excess of the solvent benzylamine (labeled S), the presence of substantial amounts of N-benzylacetamide (**A**) and, to a smaller extent, N-benzylidenebenzylamine (**B**). Significant amounts of acetone were also found in the mixture (**C**). N-isopropylidenebenzylamine and N-isopropylbenzylamine were detected in small quantities, and N-(4-phenylbutan-2-ylidene)benzylamine as well as 5-benzylamino-1-phenyl-4-hexen-3-one in traces (unlabeled as only identified in higher magnification of appropriate regions of the spectrum).

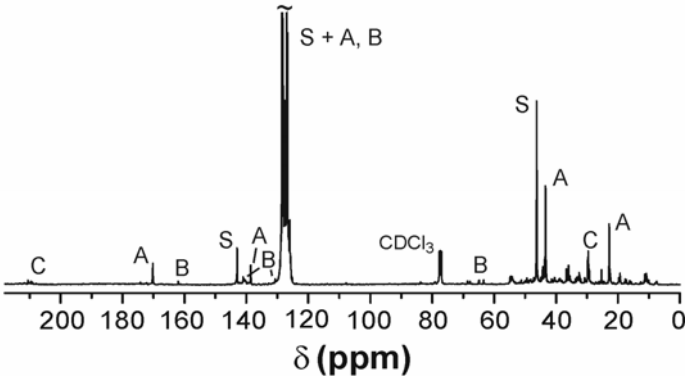

Figure 6.6. $^{13}C\{^{1}H\}$ NMR spectrum of the final iron oxide reaction solution.

Catalysts such as hydrochloric acid are able to promote the alcoholysis of acetylacetone in alcohol to form acetone and acetic esters.[24] Under the influence of active metal centers such

as yttrium, acetylacetone is cleaved even at room temperature.[25] The formation of acetic acid and acetone has also been found to occur during the formation of ZnO particles from Zn(II) acetylacetonate in a NaOH/EtOH mixture.[14] To the best of our knowledge, the analogous reaction of acetylacetone in amine solvents to form simple amides has not been described so far. However, the synthesis of N-benzylacetamide from 3-nitro-2,4-pentanedione has been reported.[26] As a reference experiment, we heated acetylacetone with benzylamine in an autoclave at 200 °C. No acetylacetonate was left after this treatment, but substantial amounts of N-benzylacetamide. Therefore, the fact that the amide is present in the iron oxide reaction mixture in quite large amounts is seen as a solvolysis ("aminolysis") of acetylacetone, and is not attributed to the formation of oxidic nanoparticles. During this process no formal oxygen is released, which would be a requirement for the formation of Fe–O–Fe bonds. In the final reaction mixture, however, acetone is present to a far lower amount than N-benzylacetamide (molar ratio 0.2 acetone : 1.0 amide, calculated from ^{1}H NMR measurements), although pro forma generated in stoichiometric amounts. This observation is attributed to further condensation of acetone, which has already been shown to constitute the key step in a novel nonaqueous pathway to metal oxides,[27] making possible the synthesis of TiO_2 and $BaTiO_3$ in aprotic solvents (see Chapters 3.3 and 4).

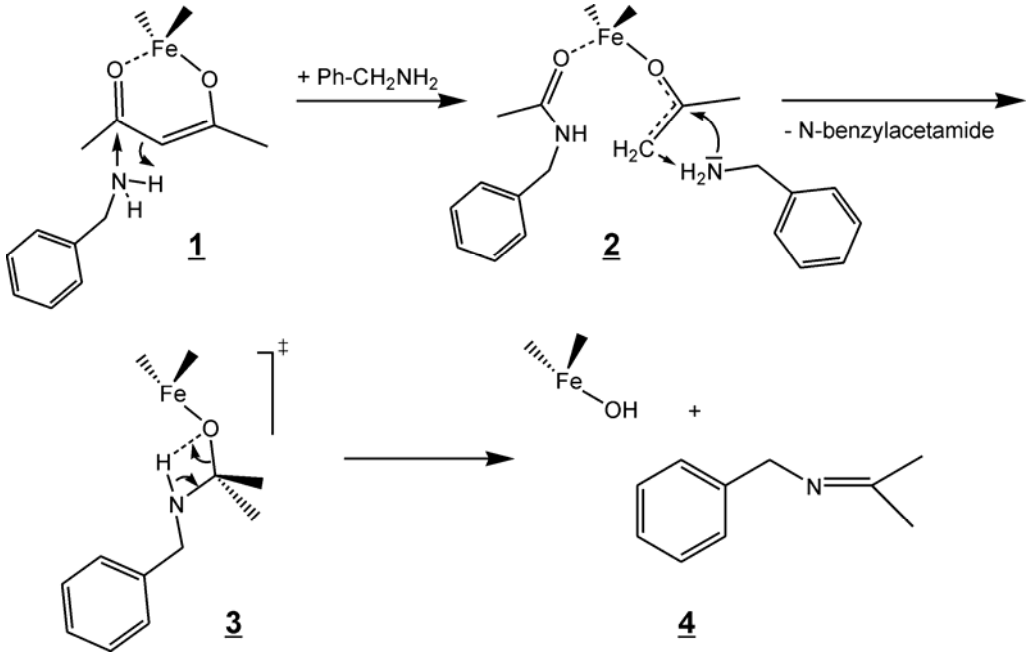

Scheme 6.1. Proposed pathway of the reaction of Fe(III) acetylacetonate in benzylamine leading to a transfer of oxygen to iron to enable nanoparticle formation.

For the system discussed here, we propose a combined solvolysis – condensation mechanism as illustrated in Scheme 6.1. Benzylamine nucleophilically attacks one carbonyl group of the acetylacetonate ligand (**1**). Aminolysis leads to N-benzylacetamide and an acetonate/enolate

ligand coordinated to the iron center (**2**). Condensation between the acetonate and another benzylamine occurs via nucleophilic attack of the amine onto the electrophilic carbonyl center, leading to the release of a hydroxyl group (**3**) and the formation of an imine (**4**). The hydroxyl group bound to the Fe atom then induces condensation by attacking another iron center, resulting in the formation of a Fe-O-Fe bond. This step represents the starting point of crystallization. In principle, condensation of two hydroxyl groups would imply the concomitant elimination of water. Since the number of Fe-OH groups is small compared to the amount of iron acetylacetonate, it is more probable that the condensation process takes place under elimination of acetylacetone via a nucleophilic attack of the OH oxygen to the monomeric iron species, and a proton transfer to the acetylacetone. This would render a truly nonhydrolytic formation process.

Although this mechanism is proposed as the main route, several other condensation products of acetone and benzylamine are observed. N-benzylidenebenzylamine is formed by dehydrogenative oxidation of benzylamine and thus explains the formation of magnetite. Upon condensation of two benzylamine molecules under concurrent release of NH_3 (which is found when opening the autoclave), formally one mol of hydrogen is released, responsible for the reduction of the iron centers to Fe(II). As maghemite was also observed as a side product, it was not possible to relate the amount of N-benzylidenebenzylamine formed to the quantity of Fe(II) in the product.

The presence of 4-benzylamino-3-penten-2-one, on the other hand, proves that not all acetylacetone is cleaved to form the amide. Instead, it can also directly undergo condensation (Scheme 6.2). The reaction starts with the nucleophilic attack of benzylamine on one carbonyl center of the acetylacetonate (**1***). In contrast to the aminolysis, the C–C bond is not broken (**2***). The oxygen is released in the form of a hydroxyl group, **3***, concurrently leading to 4-benzylamino-3-penten-2-one.

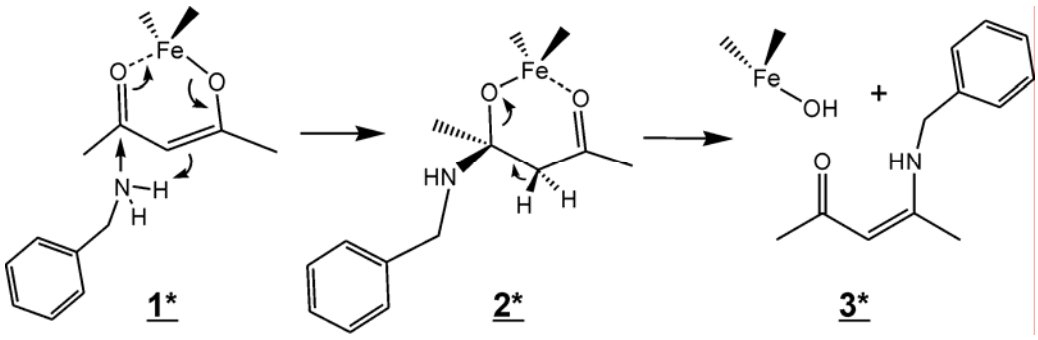

Scheme 6.2. Side route involving ketimine condensation without the cleavage of acetylacetone.

N-(4-Phenylbutan-2-ylidene)benzylamine and 5-benzylamino-1-phenyl-4-hexen-3-one are formed in an analogous fashion. The difference lies in a previous, additional coupling step of the enolate ligand with benzylamine, quite analogous to the Aldol condensation steps described for the nanoparticle formation in ketones (cf. Chapter 4). The suggested mechanism for this step is shown in Scheme 6.3. The enolate ligand (formed during the main reaction, see Figure 4) now acts as nucleophile. As benzylamine is a good nucleophile itself, an attack of the amine is rather improbable. It is more likely that an amide is attacked (**1**$^{\pm}$), as the cleavage of benzyl groups from amide nitrogen is known to proceed under reasonably mild conditions.[28] This reaction would lead to the release of acetamide. However, acetamide was not found in the ^{13}C NMR spectrum, due to its low solubility in $CHCl_3$. An NMR measurement in D_2O (data not shown) revealed the presence of small amounts of acetamide, which supports this side mechanism. Since no water/hydroxide is formed in this step, the alkoxide is not released as the free ketone (**2**$^{\pm}$), but undergoes further condensation with benzylamine to form N-(4-phenylbutan-2-ylidene)benzylamine (**3**$^{\pm}$ and **4**$^{\pm}$). Analogous reactions with uncleaved acetylacetonate would lead to 5-benzylamino-1-phenyl-4-hexen-3-one. It needs to be mentioned, however, that these side processes only take place to a small extent and therefore could not be thoroughly explored.

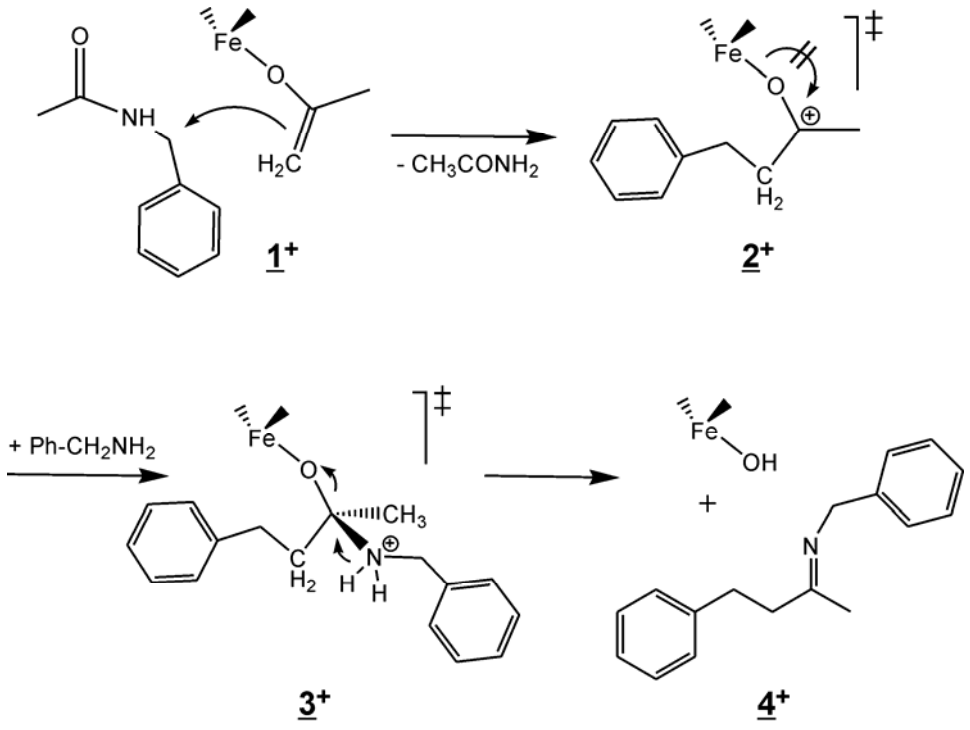

Scheme 6.3. Proposed second side route involving an addition reaction under cleavage of N-benzylacetamide, followed by ketimine condensation.

6.3 Synthesis in benzyl alcohol

Analogously, the reaction of iron(III) acetylacetonate in benzyl alcohol was explored. Again, highly crystalline iron oxide was obtained. The XRD pattern of particles synthesized at 175 °C is presented in Figure 6.7 **A**. The pattern exhibits broad peaks and looks like the pattern obtained in benzylamine (cf. Fig. 6.1), proving the presence of magnetite (Fe_3O_4) and/or maghemite (γ-Fe_2O_3). The particle size was estimated from the peak broadening using the Scherrer equation to about 10.5 nm. The TEM picture of these particles (Fig. 6.7, **B**) indicates the presence of non-aggregated particles quite uniform in shape and size. The average size of ca. 10 nm confirms the results obtained from XRD. Electron diffraction and HR-TEM images confirm the high crystallinity of the particles.[29] In addition, Raman and ^{57}Fe Mössbauer spectroscopy studies were carried out, and prove the presence of pure magnetite. These analyses shall not be discussed here in detail and are found in Ref. 29.

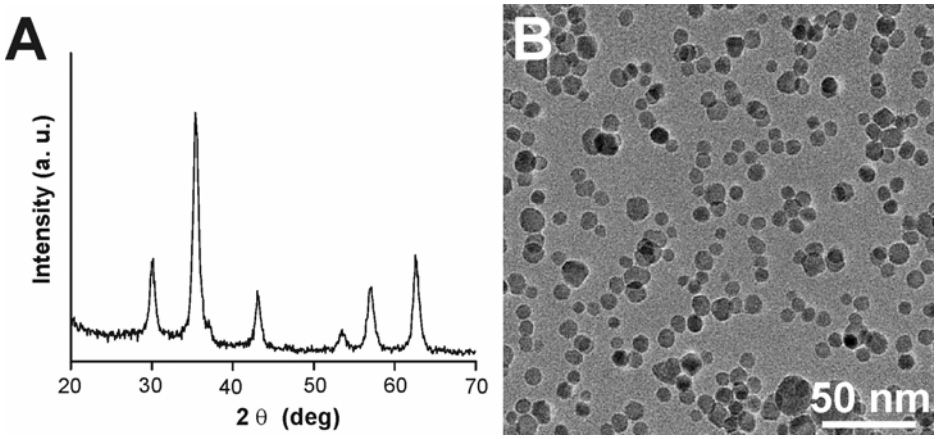

Figure 6.7. XRD pattern (**A**) and TEM image (**B**) of iron oxide nanoparticles obtained in benzyl alcohol at 175 °C.

The mechanism leading to the formation of such highly crystalline Fe_3O_4 particles was studied by analyzing the reaction solution after removal of the particles. A more concentrated mixture (molar ratio of 1 $Fe(acac)_3$: 40 solvent) was additionally prepared (using the same reaction conditions) to simplify analysis. GC–MS measurements were performed to identify the components of the mixture. Figure 6.8 shows the chromatogram obtained; the individual mass spectra used for identification of the peaks are not presented here. The solvent $CHCl_3$ and other substances with low retention time are not shown in this plot. Peak **1** is clearly attributable to benzaldehyde, whilst the large peak **2** corresponds to the solvent benzyl alcohol. **3** was identified as benzyl acetate, whereas peaks **4** and **5** stem from 4-phenyl-2-butanone and 4-phenyl-3-buten-2-one, respectively. The signal **6** is attributed to benzyl ether,

and **7** is assumed to correspond to 3-phenylmethyl-4-phenyl-2-butanone. Smaller peaks marked with an asterisk are attributed to other condensation products and are not discussed in detail due to their small quantity.

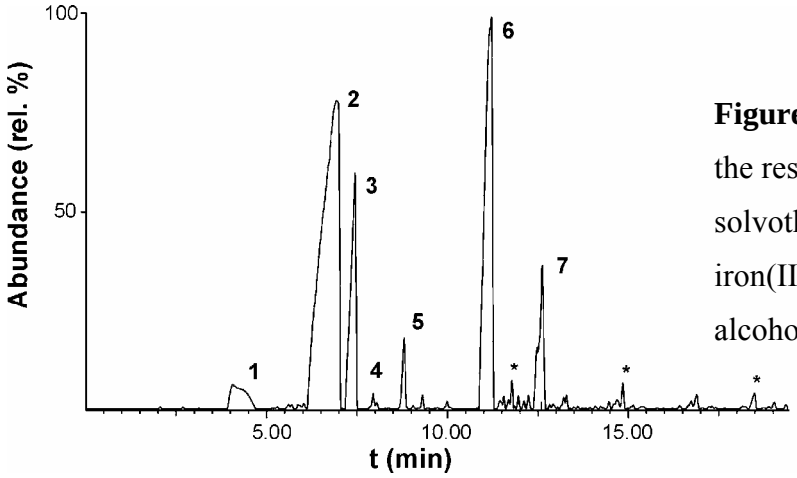

Figure 6.8. Gas chromatogram of the resulting solution after solvothermal treatment of iron(III) acetylacetonate in benzyl alcohol.

^{1}H and ^{13}C{^{1}H} NMR spectra confirm these results by and large. The ^{13}C spectrum (Figure 6.9) shows, in addition to the solvent (marked BA), the presence of substantial amounts of benzyl acetate (**1**), isopropanol (**2**) and benzaldehyde (**3**). 3-Phenylmethyl-4-phenyl-2-butanone (**4**) and 4-phenyl-2-butanone (**5**) were found in small quantities. Benzyl ether (**6**), stemming from condensation of benzyl alcohol, was also present, however in a much lower quantity than found in the GC–MS measurement, which is attributed to the fact that a more concentrated reaction approach was used for the GC–MS (the respective solution was also subjected to NMR measurements and a much higher amount of benzyl ether was found). Also 4-phenyl-3-buten-2-one was found in smaller amounts than expected from GC–MS but is still clearly visible in the ^{13}C NMR spectrum in higher magnification. The product ratio was calculated from ^{1}H NMR (not shown) to 1.0 benzaldehyde : 5.1 benzyl acetate : 1.0 *i*PrOH : 0.6 benzyl ether : 1.0 4-phenyl-2-butanone : 0.60 3-phenylmethyl-4-phenyl-2-butanone.

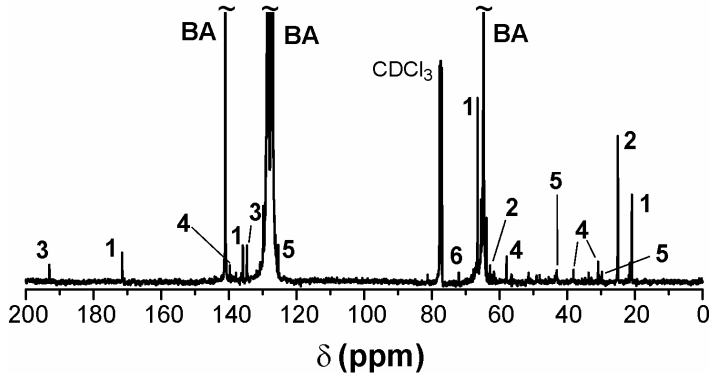

Figure 6.9. ^{13}C{^{1}H}NMR spectrum of the obtained reaction solution for the synthesis of Fe_3O_4 particles in benzyl alcohol.

These results clearly indicate that, in an analogous manner as in benzylamine, the acetylacetonate ligand is cleaved to a large extent during the course of the reaction. Most probably, this occurs as an alcoholysis of acetylacetone, which is known for a long time, leading to equimolar amounts of the corresponding acetic ester and acetone.[24] Like the aminolysis, this reaction even occurs in the absence of the iron precursor, as was verified in a reference experiment. Acetone, however, is not present in the analyzed iron oxide reaction solution; this is partly attributed to a Meerwein-Ponndorf-Verley reaction, which occurs during solvothermal treatment of metal alkoxides to a large extent (cf. Chapter 4), resulting in conversion of acetone and benzyl alcohol to isopropanol and benzaldehyde, which are both found in almost equimolar amounts. On the other hand, acetone can undergo aldol condensations which would imply the formal release of water which contributes to the oxide formation.

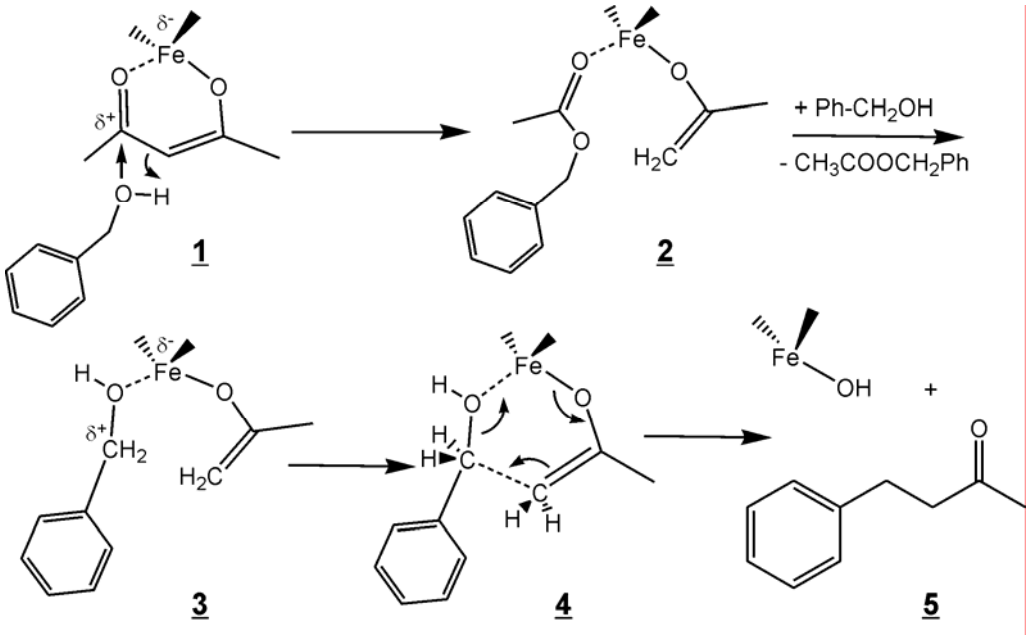

Scheme 6.4. Main reaction occurring upon solvothermal treatment of $Fe(acac)_3$ in benzyl alcohol involving solvolysis of the acetylacetonate, followed by condensation reactions.

Combining these reactions, we propose an alcoholysis–condensation mechanism as illustrated in Scheme 6.4. Benzyl alcohol nucleophilically attacks one carbonyl group of the acetylacetonate ligand (**1**). Alcoholysis leads to benzyl acetate and an enolate ligand coordinated to the iron center (**2**). In a next step, benzyl alcohol coordinates to the Fe center, releasing benzyl acetate in a ligand exchange reaction. Then, the enolate attacks the coordinated benzyl alcohol (**3**, **4**), and free 4-phenyl-2-butanone is released (**5**). The Fe-bound hydroxyl group can attack another Fe center, hence representing the starting point of nanoparticle formation.

As is visible from GC–MS, also a substantial amount of 4-phenyl-3-buten-2-one is present in the system. In principle, 4-phenyl-3-buten-2-one could be formed via a nucleophilic attack of the enolate on coordinated benzaldehyde, just as observed for the synthesis of TiO_2 in benzaldehyde (cf. Chapter 4). However, this is rather improbable, as the amount of benzaldehyde is low compared to benzyl alcohol, and also the alcohol is more prone to ligate to the iron than a carbonyl function. Moreover, it is contradicted by the fact that benzylamine and isopropanol are present in the final solution in equimolar amounts, just as they would be formed by an MPV-like reaction. 4-Phenyl-3-buten-2-one on the other hand is an oxidation product of 4-phenyl-2-butanone. As in the benzylamine system, one third of the iron must be reduced to Fe^{2+} to obtain phase-pure magnetite. Therefore, 4-phenyl-3-buten-2-one is proposed to form from 4-phenyl-2-butanone via dehydrogenative oxidation, concurrently reducing two iron centers. Unfortunately, the ^1H NMR signals of 4-phenyl-3-buten-2-one could not be distinguished and integrated as they are completely superimposed with signals of the solvent and other byproducts.

The disubstituted product 3-methylphenyl-4-phenyl-2-butanone is formed to a large extent. Interestingly, the second coupling step does not occur on the free CH_3 group but on the benzyl-substituted α-CH_2 group, possibly under the influence of the aromatic group even though no conjugated double bond is formed during this step. The monosubstituted product probably does not even desorb from the iron center but, under elimination of a proton, keeps coordinated, as illustrated in Scheme 6.5, **1***. The resulting enolate couples to previously ligated benzyl alcohol (**2***, **3***), subsequently leading to the release of free 3-methylphenyl-4-phenyl-2-butanone (**4***) and another iron-bound hydroxyl group.

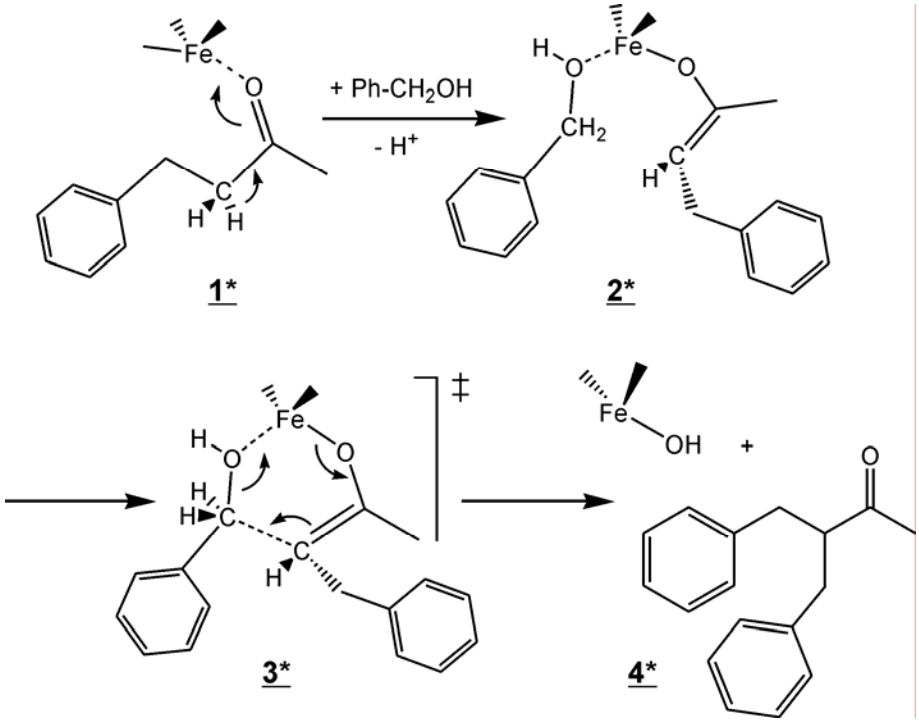

Scheme 6.5. Side reaction leading to the disubstituted coupling product, 3-phenylmethyl-4-phenyl-2-butanone.

6.4 Summary and Conclusions

This chapter has shown that metal acetylacetonates as monomeric precursor species are also well suited for the nonaqueous synthesis of metal oxide nanoparticles. The solvothermal treatment of metal acetylacetonates in benzylamine has proven particularly versatile, enabling the synthesis of highly crystalline, phase pure Ga_2O_3, In_2O_3, ZnO, and of iron oxide particles consisting of magnetite and maghemite. Phase-pure magnetite was observed when treating the Fe(III) acetylacetonate in benzyl alcohol. Interestingly, in no case free acetylacetone was present in the final reaction solution. Solvolysis of acetylacetone involving a C–C bond cleavage takes place to a large extent, resulting in the formation of N-benzylacetamide or benzyl acetate. On the other hand, enolate ligands are formed which undergo ketimine/aldol condensation reactions. Formally, water is released in the course of these reactions, which finally induces the formation of the metal oxide nanoparticles. Reduction of Fe(III) to Fe^{2+} which is essential for formation of magnetite takes place via a dehydrogenative oxidation of either the solvent itself, as in the case of benzylamine, or of a coupling product, as in benzyl alcohol.

6.5 Experimental Section

6.5.1 Synthesis

All synthesis procedures were carried out in a glovebox (O_2 and H_2O < 0.1 ppm). In a typical synthesis of nanoparticles in benzylamine, 1.0 g $Fe(acac)_3$ (2.81 mmol), 0.5 g $In(acac)_3$ (1.21 mmol), 0.5 g $Ga(acac)_3$ (1.36 mmol), or 0.5 g $Zn(acac)_2 \cdot$ x H_2O (1.90 mmol), respectively, was added to 20 mL of benzylamine. For the synthesis of iron oxide in benzyl alcohol, 1.0 g of $Fe(acac)_3$ (2.81 mmol) was added to 20 ml of benzyl alcohol. The reaction mixture was transferred into a Teflon cup of 45 mL inner volume, slid into a steel autoclave and carefully sealed. The autoclave was taken out of the glovebox and heated in a furnace at 200 °C (or 175 °C for the benzyl alcohol system) for 2 days. The resulting turbid suspensions were centrifuged, the precipitates thoroughly washed with ethanol and dichloromethane and subsequently dried in air at 60 °C.

6.5.2 NMR data

All samples were measured in $CDCl_3$. Only the relevant main reaction products are given. Most aromatic signals of benzyl derivatives are completely superimposed by the large aromatic solvent peaks and are therefore not stated.

a. Benzylamine System
N-Benzylacetamide: δ [ppm]: 170.0 (CO), 138.7 (Ph_{ipso}), 43.38 (CH_2), 22.8 (CH_3).
N-Benzylidenebenzylamine: 161.9 (C=N), 139.3/136.1 (Ph_{ipso}), 130.7 (Ph_{para}), 64.9 (CH_2).

b. Benzyl Alcohol System
Benzyl acetate: δ [ppm]: 171.1 (CO), 135.5 (Ph_{ipso}), 66.1 (CH_2), 20.6 (CH_3).
Benzaldehyde: 192.7 (CHO), 135.9 (Ph_{ipso}), 134.3 (Ph_{para}).
3-Phenylmethyl-4-phenyl-2-butanone: 211.9 (CO, only visible in higher enlargement), 137.6 (Ph_{ipso}), 56.4 (CH), 38.1 (CH_2), 30.5 (CH_3).
4-Phenyl-2-butanone: 207.5 (CO, only visible in higher enlargement), 139.6 (Ph_{ipso}), 43.1 (C4), 30.0 (C3), 29.7 (C1).
(trans-)4-Phenyl-3-buten-2-one: peaks only visible in higher enlargement. 195.8 (CO), 142.5 (C4), 134.9 (Ph_{ipso}), 129.2 (C3), 28.0 (C1).

6.6 References

[1] M. Leskelä, H. Mölsä, L. Niinistö, *Supercond. Sci. Tech.* **1993**, *6*, 627.

[2] D. C. M. Dutoit, M. Schneider, A. Baiker, *J. Catal.* **1995**, *153*, 165.

[3] R. J. Willey, N. P., G. Busca, *Chem. Eng. Comm.* **1993**, *123*, 1.

[4] C. Sanchez, J. Livage, M. Henry, F. Babonneau, *J. Non-Cryst. Solids* **1988**, *100*, 65.

[5] M. J. Hampden-Smith, T. A. Wark, C. J. Brinker, *Coord. Chem. Rev.* **1992**, *112*, 81.

[6] E. Scolan, C. Sanchez, *Chem. Mater.* **1998**, *10*, 3217.

[7] V. Brisois, S. Belin, M. Zucolotto Chalaça, R. H. A. Santos, C. V. Santilli, S. H. Pulcinelli, *Chem. Mater.* **2004**, *16*, 3885.

[8] Y. Hou, S. Gao, T. Ohta, H. Kondoh, *Eur. J. Inorg. Chem.* **2004**, 1169.

[9] F. X. Redl, C. T. Black, G. C. Papaefthymiou, R. L. Sandstrom, M. Yin, H. Zeng, C. B. Murray, S. P. O'Brian, *J. Am. Chem. Soc.* **2004**, *126*, 14583.

[10] W. S. Seo, H. H. Jo, K. Lee, J. T. Park, *Adv. Mater.* **2003**, *15*, 795.

[11] W. S. Seo, H. H. Jo, K. Lee, B. Kim, S. J. Oh, J. T. Park, *Angew. Chem. Int. Ed.* **2004**, *43*, 1115.

[12] J. Von Hoene, R. G. Charles, W. M. Hickam, *J. Phys. Chem.* **1958**, *62*, 1098.

[13] F. Cao, D.-P. Kim, X.-D. Li, C.-X. Feng, Y.-C. Song, *J. Appl. Polym. Sci.* **2001**, *85*, 2787.

[14] Y. Inubushi, R. Takami, M. Iwasaki, H. Tada, S. Ito, *J. Colloid Interface Sci.* **1998**, *200*, 220.

[15] C. Domingo, R. Rodríguez-Clemente, M. Blesa, *J. Colloid Interface Sci.* **1994**, *165*, 244.

[16] J. J. Krebs, D. M. Lind, S. D. Berry, *J. Appl. Phys.* **1993**, *73*, 6457.

[17] F. C. Meldrum, N. A. Kotov, J. H. Fendler, *J. Phys. Chem.* **1994**, *98*, 4506.

[18] A. Murali, A. Barve, V. J. Leppert, S. H. Risbus, *Nano Lett.* **2001**, *1*, 287.

[19] N. Pinna, G. Neri, M. Antonietti, M. Niederberger, *Angew. Chem. Int. Ed.* **2004**, *43*, 4345.

[20] B. Cheng, E. T. Samulski, *Chem. Commun.* **2004**, 986.

[21] K.-S. Weißenrieder, J. Müller, *Thin Solid Films* **1997**, *300*, 30.

[22] S. Shukla, S. Seal, L. Ludwig, C. Parish, *Sens. Actuators B* **2004**, *97*, 256.

[23] D. L. A. de Faria, S. Venâncio Silva, M. T. de Oliveira, *J. Raman Spectrosc.* **1997**, *28*, 873.

[24] H. Adkins, W. Kutz, D. D. Coffman, *J. Am. Chem. Soc.* **1930**, *52*, 3212.

[25] O. Poncelet, L. G. Hubert-Pfalzgraf, *Polyhedron* **1990**, *9*, 1305.

[26] T. Tokumitsu, T. Hayashi, *Nippon Kagaku Kaishi* **1983**, *1*, 88.

[27] S. C. Goel, M. Y. Chiang, P. C. Gibbons, W. E. Buhro, *Mater. Res. Soc. Symp. Proc.* **1992**, *271*, 3.

[28] C.-Y. Chern, Y.-P. Huang, W. M. Kan, *Tetrahedron Lett.* **2003**, *44*, 1039.

[29] N. Pinna, S. Grancharov, P. Beato, P. Bonville, M. Antonietti, M. Niederberger, *Chem. Mater.* **2005**, *17*, 3044.

7 Synthesis of Lead Zirconate Titanate Nanoparticles

7.1 Introduction to Piezoelectric Materials

Lead zirconate titanate (PZT) materials with the general formula $PbZr_{1-x}Ti_xO_3$ possess the perovskite structure, like $BaTiO_3$. Whilst pure $PbZrO_3$ is antiferroelectric, compositions with $x > 0.1$ are ferroelectric.[1] At high temperatures, the cubic perovskite structure is realized, as illustrated in Figure 7.1 **A**. As the temperature is lowered, PZT undergoes a phase transition, and the cubic unit cell is distorted due to the parallel ferroelectric shift of the cations with respect to the oxygen octahedra, like $BaTiO_3$, resulting in a tetragonal phase (Fig. 7.1 **B**, see also Chapter 3.1).[2,3]

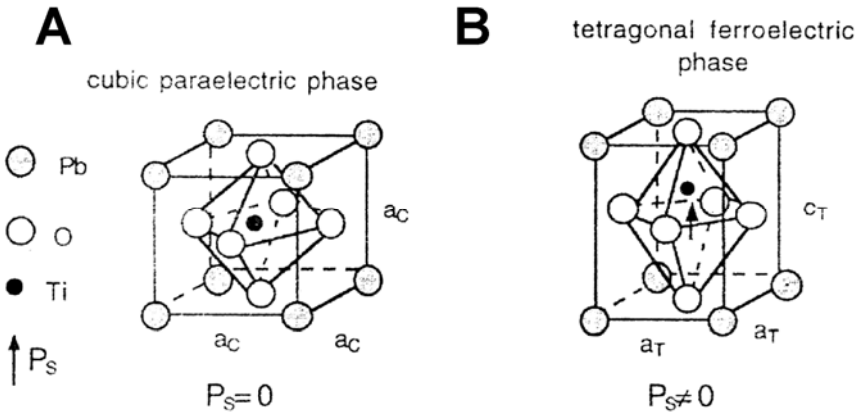

Figure 7.1. The $PbTiO_3$ perovskite structure, being cubic above the Curie temperature (**A**), and tetragonal below T_C (**B**), in the latter case a spontaneous polarization P_s is found.[4]

What makes PZT materials technologically highly important is their large piezoelectric constant. A piezoelectric material responds to mechanical forces/pressures and generates electric charges/voltages, which is referred to as the direct piezoelectric effect. The applied stress causes a dislocation of the cations, resulting in a change in polarization and hence the generation of electric charges. Conversely, electric charges/fields applied to the material can induce mechanical stresses or strains, which is called the converse piezoelectric effect.[5] Raw synthetic piezoceramics, however, are usually isotropic and nonpiezoelectric. They become anisotropic and piezoelectric only after a poling process (cf. Chapter 3.1).

For the direct dielectric effect, the resulting elastic strain *e* produced by an electric field E is linear in the field and can be calculated in one-dimensional notation according to

$$e = Z \cdot s + d \cdot E \qquad \text{(Eq. 7.1)},$$

where *d* is the piezoelectric strain constant, Z the stress, s the elastic compliance constant. The converse dielectric effect is described by

$$P = Z \cdot d + E \cdot \chi \qquad \text{(Eq. 7.2)},$$

P being the polarization and χ the dielectric susceptibility.[6,7] The piezoelectric strain constant, or piezoelectric coefficient, *d* is generally defined by

$$d = \frac{\partial e}{\partial E} \qquad \text{(Eq. 7.3)}.$$

Quartz is the most widely used piezoelectric material (but is not ferroelectric) and exhibits a piezoelectric coefficient of $d \approx 3 \cdot 10^{-12}$ m V^{-1}, whilst for $BaTiO_3$ it is about $3 \cdot 10^{-10}$ m V^{-1}.[7] PZT materials in contrast possess a piezoelectric coefficient of as high as $6 \cdot 10^{-10}$ m V^{-1}.[2]

Pure lead titanate has a strong lattice distortion (c/a = 1.04) and exhibits a comparably high Curie temperature of about 490 °C.[8] With increasing zirconium content, the tetragonal lattice distortion decreases and poling becomes easier. A phase boundary, called the morphotropic phase boundary as it stays practically constant with temperature,[4] is found at x = 0.45. Whereas Zr-rich PZT is rhombohedral, the Ti-rich phase possesses a tetragonal structure.[1] The phase diagram of $Pb(Zr,Ti)O_3$ solid solutions is presented in Figure 7.2. The piezoelectric coefficients of PZT materials are highest near the morphotropic phase boundary.[1]

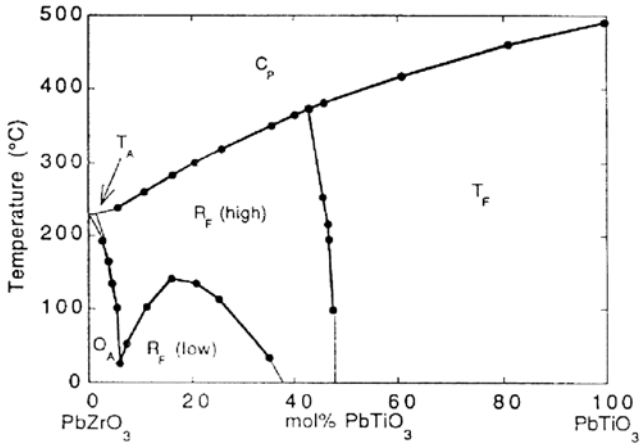

Figure 7.2. Phase diagram of $PbTi_xZr_{1-x}O_3$ solid solutions, according to Ref. 4.

The first applications of the piezoelectric effect were already developed during the First World War by Langevin as depth-sounding devices.[3,5] Today, PZT ceramics show a broad range of technical applications as piezoelectric sensors or actuators, mainly due to their optimum electromechanical coupling properties.[9,10] The needs of automotive and aero space industry as well as other industrial areas in high precision positioning systems have further increased the interest in these materials.[11,12] Because of their high piezoelectric anisotropy, they are particularly well suited for applications in medical diagnostic devices.[13] Moreover,

PZT materials have the advantage of high Curie temperatures, can easily be poled, possess a wide range of dielectric constants, are easy to sinter and form solid-solution compositions with many different constituents.[14]

7.2 Synthesis of PZT Nanoparticles

The traditional route to PZT materials involves solid state reactions between the individual metal oxide or carbonate powders at temperatures between 600 and 1100 °C. However, this processing technique suffers from a number of uncertainties and drawbacks. One major flaw is that the volatility of certain compounds like PbO during the preparation leads to deviation of stoichiometry, the use of excess PbO however causes further complications such as composition fluctuations.[15] Impurities in the raw materials, lack of homogeneity due to poor mixing and large particle sizes, which require intensive milling, are some other major problems that resulted in the development of a large number of alternative synthesis techniques.

Wet-chemical procedures, in general, offer good control from the molecular precursor to the final material, providing high purity, small crystallite sizes, well-defined particle morphologies and small particle size distributions. Hence, there are many reports of soft-chemistry routes to PZT materials involving the transformation of soluble precursors, in most cases lead alkoxides or salts and titanium and zirconium alkoxides or oxychlorides, into the metal oxide framework.[16-19] Also heterometallic, single-source precursors were used.[20,21] Often, hydrothermal processes in a strongly alkaline (KOH) environment were performed.[16,18]

Reports about particles with sizes smaller than 100 nm, however, are rather scarce. By far the most synthesis procedures are either based on aqueous sol-gel chemistry, mainly involving hydrothermal processes[22-25] and co-precipitation,[26,27] or on thermal decomposition of polymeric precursors.[28-31] No reports on the preparation of PZT materials by solvothermal treatment in an organic solvent were found, even though a nonaqueous synthesis may be a valuable alternative, eliminating the need for a strongly alkaline solution as necessary for hydrothermal synthesis routes, and possibly providing better control over particle growth and thus the particle size and shape. By concept, high purity precursor powders would be obtained in good yields without contamination with other inorganics such as halides or alkali metals.

As reported in Chapter 3.2, $BaTiO_3$ nanoparticles could be conveniently synthesized by dissolving metallic barium in benzyl alcohol, followed by addition of titanium isopropoxide

and solvothermal treatment in an autoclave. For lead-containing materials, however, it was found that when using benzyl alcohol as solvent, in the standard preparations lead cations were always reduced to metallic lead by the alcohol. This could be prevented by using non-reductive organic solvents. The synthesis of TiO_2 and $BaTiO_3$ in anhydrous ketones and aldehydes has been introduced in Chapters 3.3 and 4. As ketones, in contrast to alcohols, are practically non-reductive, it appeared promising to extend this strategy also to PZT materials.

7.3 Results and Discussion

The reaction between lead(II) acetylacetonate or acetate and titanium and/or zirconium isopropoxide in 2-butanone resulted in the formation of an amorphous white precipitate after solvothermal treatment. Acetone and higher ketones such as 3-pentanone led to similar results, whereas aromatic ketones such as acetophenone produced very viscous liquids which were hard to separate and wash to obtain the inorganic material.

The as-prepared, washed precipitates were analyzed by X-ray diffraction (XRD). Figure 7.3 shows the obtained patterns for samples prepared with lead(II) acetylacetonate in 2-butanone. All diffractograms feature a broad peak centered around $2\theta = 30°$. A second, broad peak is visible at about 48° in the $PbTiO_3$ system (Fig. 7.3 **a**) and also for the mixed oxide (Fig. 7.3 **b**), whereas in the $PbZrO_3$ system (Fig. 7.3 **c**), another signal is found centered at about 58°. The broadness of these peaks indicates a low crystallinity with very short ranged order of the samples. Such patterns have been observed for sol-gel derived lead titanate, and were suggested to correspond to amorphous materials locally ordered in the cubic pyrochlore $Pb_2Ti_2O_6$ structure. This structure is kinetically favored but transforms irreversibly to tetragonal $PbTiO_3$ upon heat treatment.[32]

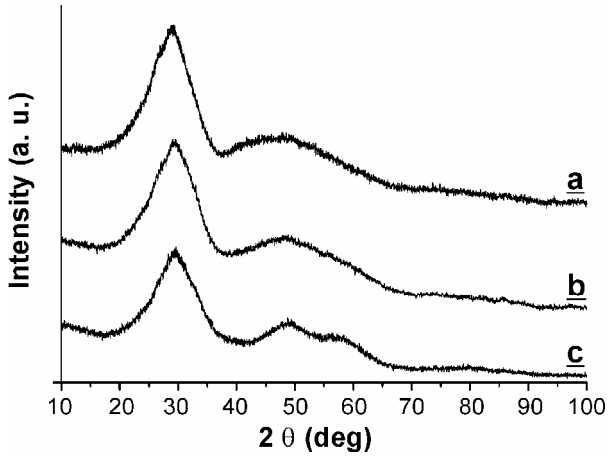

Figure 7.3. XRD patterns of the as-prepared powders of $PbTiO_3$ (**a**), $Pb(Zr_{0.52}Ti_{0.48})O_3$ (**b**), $PbZrO_3$ (**c**).

Hence, a subsequent calcination treatment was performed to induce crystallization and the resulting XRD plots are shown in Figure 7.4. The powders were prepared from lead(II) acetylacetonate, however samples obtained from lead(II) acetate gave similar results. For a given calcination time and temperature, samples prepared in 2-butanone clearly showed the highest crystallinity. Therefore, it was regarded as the solvent of choice and was used for all samples presented in this chapter.

A calcination temperature of 400 °C was sufficient to obtain highly crystalline, phase-pure $PbTiO_3$ (Fig. 7.4 **a**). All reflections can be assigned to the tetragonal modification (JCPDS No. 6-452). For the PZT system, the temperature had to be raised to 450 °C (Fig. 7.4 **b**). The peaks are significantly broader, indicating smaller crystallite size. They clearly correspond to $Pb(Zr_{0.52}Ti_{0.48})O_3$ (JCPDS No. 33-784), except for the small signals marked with asterisks, which are attributed to remaining amorphous material. $PbZrO_3$ had to be treated at higher temperatures to induce crystallization. After treatment at 600 °C, a pattern with much sharper reflections is obtained (Fig. 7.4 **c**). This observation points to larger crystallites, which is expected due to enhanced crystal growth at higher temperature. The reflections match the orthorhombic lead zirconate structure (JCPDS No. 35-739). From the obtained XRD patterns, the crystallite sizes were calculated using the Scherrer equation. For $PbTiO_3$, the crystallite size was determined to 19.5 nm, using the (111) reflection, whereas for the PZT system, a significantly smaller size of about 10 nm was obtained (calculated from the same reflection). The (240) reflection was employed for calculating the crystal size of $PbZrO_3$, which amounted to 26 nm. Consequently, calcination at relatively moderate temperatures resulted in highly crystalline materials for all three systems. The crystallite size for PZT was much smaller compared to the pure titanate and zirconate systems. With increasing Zr content, the samples

need to be treated at higher temperatures to induce crystallization. This trend reflects the general shift to higher temperature necessary for formation of crystalline PZT materials with increasing Zr/Ti ratio.[21]

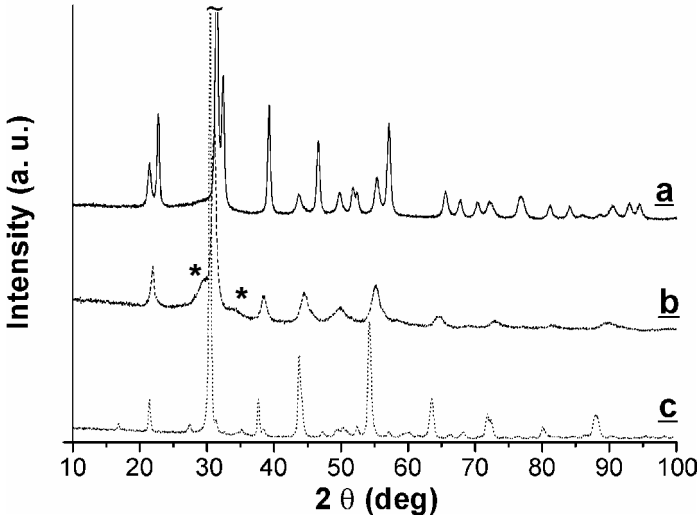

Figure 7.4. XRD patterns of the calcined powders: $PbTiO_3$ after calcination at 400 °C (**a**), $Pb(Zr_{0.53}Ti_{0.48})O_3$ at 450 °C (**b**), and $PbZrO_3$ calcined at 600 °C (**c**).

The obtained nanopowders were also investigated by transmission electron microscopy (TEM). Figure 7.5 displays the micrographs of samples after calcination, $PbTiO_3$ after heat treatment for 4 h at 400 °C (Fig. 7.5 **A**), $Pb(Ti,Zr)O_3$ after 6 h at 450 °C (Fig. 7.5 **B**), and $PbZrO_3$ after 6 h at 600 °C (Fig. 7.5 **C**). All micrographs show almost spherical or slightly ellipsoidal nanoparticles with a narrow size distribution within the same system. Although the particles are somewhat aggregated, it is clearly visible that the lead titanate and lead zirconate particles are significantly larger compared to the PZT sample. The particle sizes lie in the range of 25-35 nm for lead titanate and 20-30 nm for lead zirconate, whereas the PZT material consists of particles with an average diameter of about 10 nm. These results coincide well with the crystallite sizes calculated from XRD data.

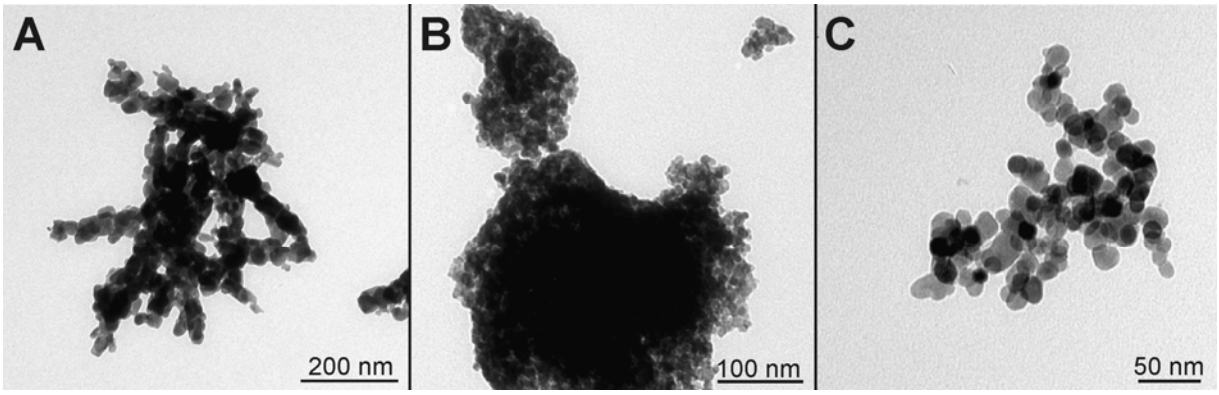

Figure 7.5. TEM images of the samples after calcination. $PbTiO_3$ after heat treatment at 400 °C (**A**), PZT particles treated at 450 °C (**B**), $PbZrO_3$ calcined at 600 °C (**C**).

Thermogravimetric analysis (TGA) was performed to investigate the thermal behavior of the as-prepared samples (Figure 7.6). In all cases, only a slight, steady decrease in weight by about 1.8-3.1 % is observed up to 200 °C, which is attributed to desorption of water and ethanol from the washing process. Between 200 and 330 °C, a strong weight loss is visible, additionally featuring a small shoulder at about 320-360 °C. The height of this step ranges from 9.7 wt % in the case of $PbTiO_3$ to 11.8 wt % for $PbZrO_3$. The weight loss is clearly attributed to the removal of organic species adsorbed to the as-prepared particles (see below). At higher temperatures, no significant weight loss was observed for any sample. This result gives evidence for the absence of carbon above this temperature and proves the stability of the obtained particles at high temperatures, especially regarding the commonly observed PbO loss through evaporation at temperatures above 500 °C. This is further confirmed by analogous TGA experiments with calcined, crystalline samples showing practically no weight decrease (< 0.9 %) in the range of 100-900 °C (data not shown). Consequently, this behavior eliminates one of the big problems in the synthesis of crystalline PZT materials, namely the compensation for any lead loss.[15]

The adsorbed organic species can be easily characterized by IR spectroscopy. Figure 7.6, inset, shows the FT-IR spectrum observed for as-prepared PZT samples. Strong stretching vibration bands in the range ν=1280-1520 cm^{-1} are characteristic for metal-bound β-diketonates. These bands were not found in the IR spectra of calcined samples. Therefore, we infer that the as-prepared particles are covered with acetylacetonate stemming from the lead precursor, which during the synthesis process is bound to the particle surface and thus acts as a stabilizer. Due to the strong binding, desorption/decomposition does not occur at temperatures below 200 °C.

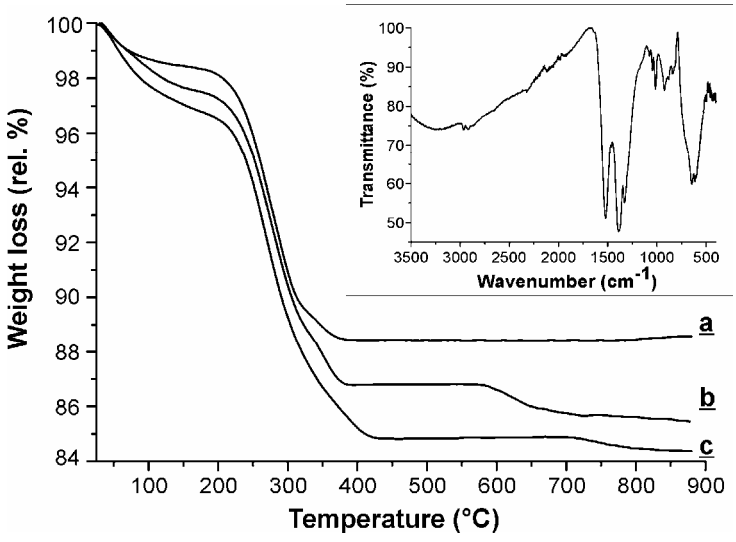

Figure 7.6. TGA plots of as-prepared samples: $PbTiO_3$ (**a**), $Pb(Zr_{0.53}Ti_{0.48})O_3$ (**b**), and $PbZrO_3$ (**c**). Inset: FT-IR spectrum of an as-prepared PZT sample.

The mechanism leading to the formation of lead zirconate titanate particles in 2-butanone can be elucidated by studying the composition of the final reaction solution after removal of the inorganic material. Figure 7.7 shows the $^{13}C\{^{1}H\}$ NMR spectrum of the filtered solution. The system discussed here is more complicated in comparison to the reaction of titanium tetraisopropoxide in common ketones to form TiO_2, as described in Chapter 4, due to the additional presence of the Pb(II) acetylacetonate species. The NMR spectrum however looks similar to the Ti(O*i*Pr)$_4$ – 2-butanone system. Both spectra feature a large number of peaks. The presence of 2-butanol and acetone (marked **1** and **2**, respectively) proves the occurrance of a MPV-like oxidation-reduction mechanism, where the isopropanolate ligand is oxidized to acetone whilst reducing the solvent (**S**) to the secondary alcohol. The spectrum also indicates the presence of 5-methyl-4-heptene-3-one (**3**) and 5-methyl-4-hexene-3-one (**4**, only some peaks are labeled as the others coincide with the peaks of **3**), the aldol coupling product of 2-butanone with itself and acetone, respectively. Therefore, the formation mechanism is expected to occur via aldol condensations of the solvent. Due to the large amount of byproducts formed, it was not possible to investigate the fate of lead(II) acetylacetonate during the reaction. No acetylacetone was identified in the final solution, therefore a decomposition/solvolysis is proposed, possibly in a similar manner as for Fe(III) acetylacetonate in benzyl alcohol or benzylamine (cf. Chapters 6.2 and 6.3); benzyl acetate however was not found in the reaction solution in significant quantities.

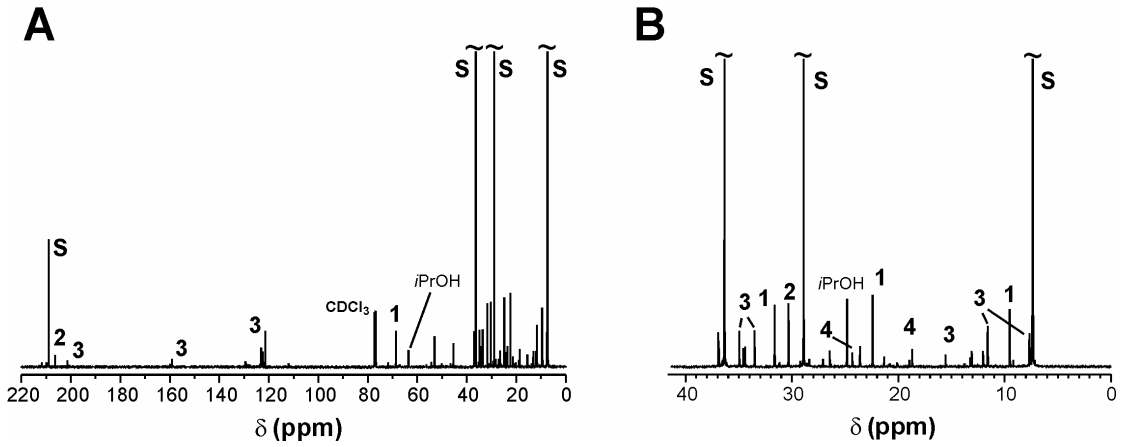

Figure 7.7. $^{13}C\{^{1}H\}$ NMR spectrum of the obtained reaction solution (after filtering) for a standard $PbTiO_3$ sample prepared by reacting Pb(acac)$_2$ and Ti(O*i*Pr)$_4$ in 2-butanone.

To investigate the elemental composition of the amorphous precursor particles, elemental analysis was performed by ICP-OES analysis with the samples previously digested in acids. The molar Pb : Ti : Zr ratio found was 1 : 0.97 : 0 for $PbTiO_3$, 1 : 0.45 : 0.55 for $Pb(Ti_{0.47}Zr_{0.53})O_3$, and 1 : 0 : 1.05 in the case of $PbZrO_3$, which within the experimental error

is in good agreement with the target composition. Combustion analysis was performed in order to measure the carbon and hydrogen content. For all samples, the prepared precursor particulates contained about 6-7 wt % carbon and about 0.6 wt % hydrogen. Assuming that all ligands are acetylacetonate, this would result in an organic content of 9.9-11.6 wt %, which agrees well with the data obtained by TGA.

Films were prepared by simply casting a dispersion of the as-prepared particles on Si wafers. After annealing at 500 °C, the surface featured very uniform, spherical particles about 2-3 µm in size, as seen in an overview scanning electron microscopy (SEM) image of a sample prepared using PZT particles (Figure 7.8 **A**, **B**). An image at higher magnification shows that these large balls consist of smaller particles (Fig. 7.8 **B**, inset). However, one can clearly distinguish between spheres featuring a defined edge and spheres with an apparently blurred edge, pointing to the fact that some beads are just attached loosely to the surface of the underlying smooth PZT film, whereas the other ones are partially incorporated in the film. From SEM images of a scratched sample (data not shown), the film thickness was estimated to be about 0.5 µm. Based on the fact that the particles are not stabilized by surface complexants other than the acetylacetonate from the synthesis, it is reasonable to assume that the spheres are already formed in solution, before the film coating process. Hence, there must be both large aggregates in the form of the spheres and smaller, isolated particles present in solution. The smaller particles get into contact with the substrate, and based on their higher activity they form a homogeneous film. The large sphere-like aggregates retain their shape and are found sitting on or partially inside the film. It is fascinating, though, that the large aggregates show such a uniform shape and size.

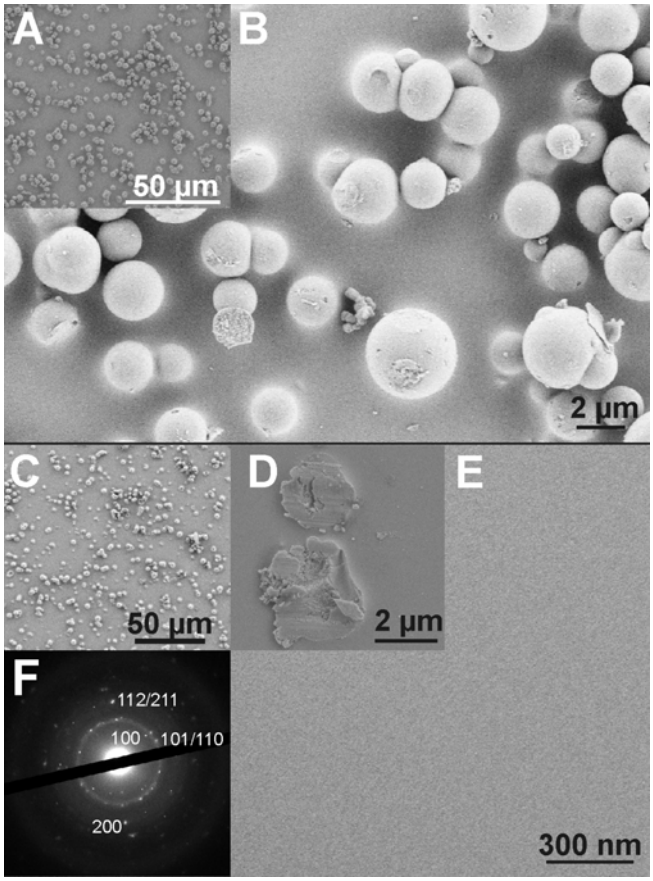

Figure 7.8. SEM images of films prepared from a dispersion of PZT particles after calcination: overview picture (**A**) and detailed image of spheres before washing (**B**); overview (**C**), fractured spheres (**D**) and homogeneous film after washing (**E**). Electron diffraction pattern of the scratched-off film

In order to remove the spheres not connected to the film, thorough washing was performed by rinsing the films with distilled water and ethanol. A great deal of the micron-sized balls can be removed by this treatment, as is evident on the overview SEM image (Fig. 7.8 **C**). Even more interesting, spheres previously embedded in the underlying film are fractured upon extensive washing (Fig. 7.8 **D**). A region only featuring the film is shown at higher magnification (Fig. 7.8 **E**). It can be clearly seen that the film is highly homogeneous in an area several μm^2 large and has a smooth surface. Parts of the film were scratched off and measured in a TEM instrument. The electron diffraction image of such a section is presented and proves that the material is crystalline, with all visible reflections corresponding to the tetragonal lead zirconate titanate phase (Fig. 7.8 **F**).

An analogously treated sample was analyzed by atomic force microscopy, again after thorough washing with water and ethanol. An area without any spheres is presented in Figure 7.9 **A**. Section analysis gave evidence that the film is crack-free and rather smooth with a low mean surface roughness of 0.13 nm (Fig. 7.9 **B**). Also the side view (Fig. 7.9 **C**) proves that the film is rough only on a small nanometer scale. This is remarkable considering the particle size of about 10 nm observed for the calcined powder and this indicates that the thermal treatment is very efficient for thin film formation.

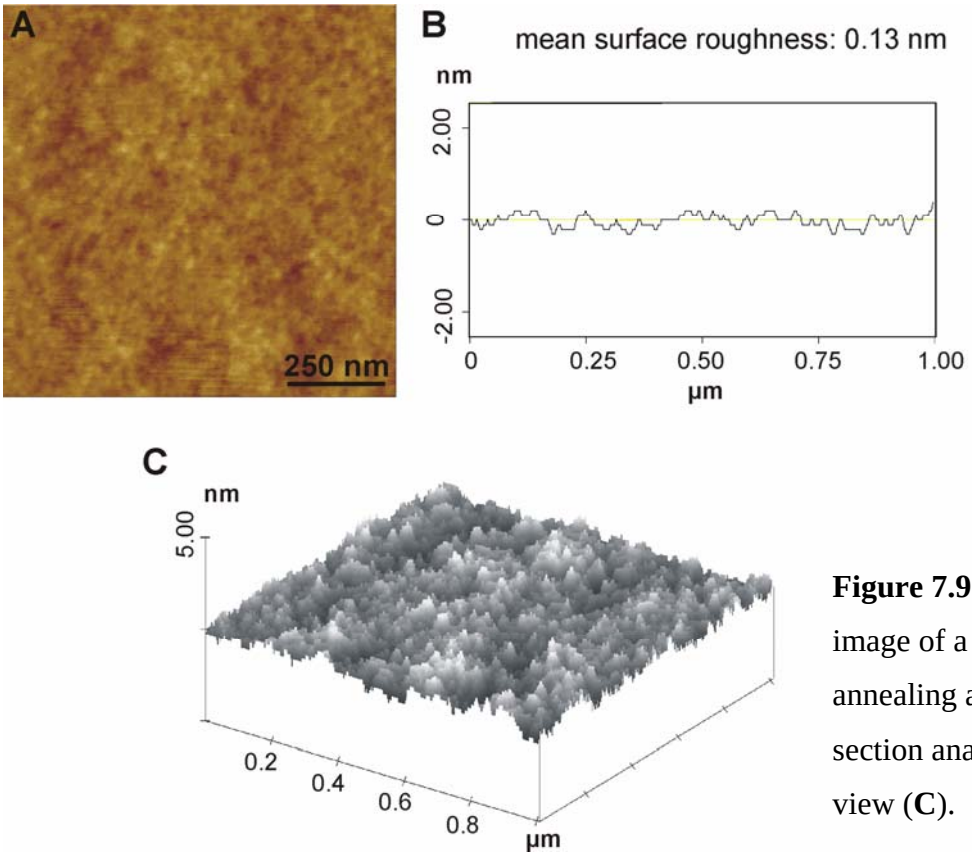

Figure 7.9. AFM height image of a PZT film after annealing at 500 °C (**A**), section analysis (**B**), in side view (**C**).

By optimization of the film preparation procedure, the homogeneity of the films could be further improved. On the one hand, the particle dispersion in EtOH was subjected to an extended ultrasonication treatment, using a W-450 D Digital Sonifier, Banson Ultrasonics Corp. The subsequent film casting was performed as usual, however after calcination, the films were cleaned by ultrasonication in EtOH for 1 h. A SEM overview image of a such treated sample (Figure 7.10 **A**) reveals that the homogeneous domains now extend over dozens of microns, however still some spheres are visible. A micrograph at higher magnification (Fig. 7.10 **B**) indicates that now almost all spheres are incorporated in the film, suggesting that removal of loosely attached aggregates via ultrasonication of the prepared film is rather efficient.

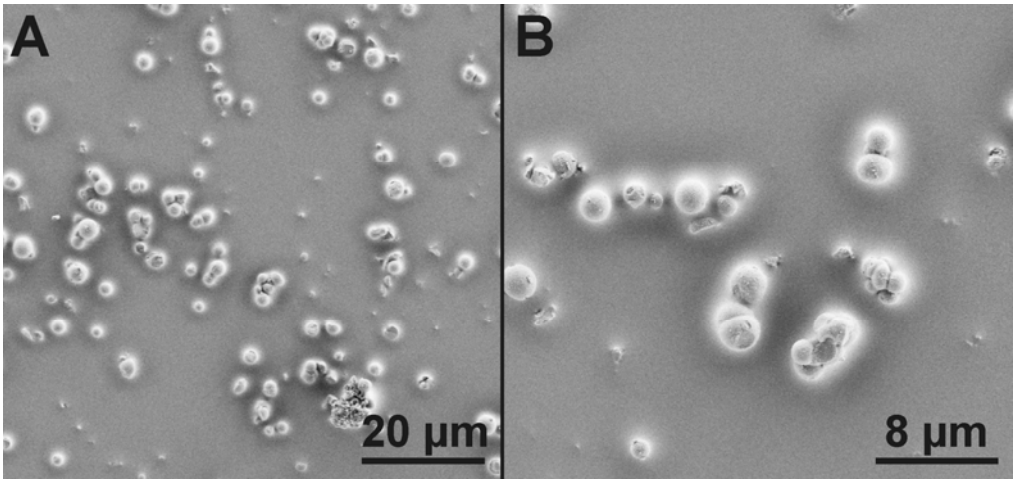

Figure 7.10. SEM images of a film prepared under extended ultrasonication, showing a significantly reduced number of aggregates on the homogeneous film.

7.4 Summary and Conclusions

In this chapter, a simple and facile route to crystalline PZT nanopowders has been presented. Starting from commercially available metal compounds such as lead(II) acetylacetonate and titanium/zirconium alkoxides, the synthesis of amorphous precursor powders is achieved under nonaqueous and nonalkaline conditions by solvothermal treatment in 2-butanone. The synthesis reaction was found to proceed via aldol-like condensation of the solvent, providing the formal water needed for formation of the oxide. The as-synthesized powders are perfect precursors for PZT materials, since they contain the metals in the correct and targeted ratio. Subsequent calcination at moderate temperatures of 400-600 °C led to highly crystalline, phase-pure nanoparticles with crystallite sizes in the range of about 20 nm for $PbTiO_3$ and $PbZrO_3$ particles, and about 10 nm for the PZT system. The moderate calcination conditions circumvent the problem of PbO evaporation and the consequent change in stoichiometry. The processing temperature is also a crucial factor because ferroelectric thin films are usually deposited on silicon substrates, which are seriously damaged by treatments above 500 °C.[33]

Another big advantage of powder precursors lies in the possibility of film formation by simply casting suspensions of the as-prepared particles on silicon wafers. Homogeneous and crack-free PZT films were obtained over an area of several microns. Without the use of any surface complexants, however, larger spherical aggregates were obtained on top of the film, which could be mainly removed by thorough washing. Improved treatment via extended ultrasonication both of the suspension before casting and of the final film resulted in significantly larger areas of homogeneous, aggregate-free film.

7.5 Experimental Section

7.5.1 Synthesis

Lead(II) acetylacetonate (technical grade), lead(II) acetate trihydrate (99.99%) as well as titanium isopropoxide Ti(O*i*Pr)$_4$ (99.999%), zirconium isopropoxide Zr(O*i*Pr)$_4$·*i*PrOH (99.99%) and 2-butanone (HPLC grade, 99.5+%) were used as-received from Aldrich. In a typical synthesis, 1.23 mmol of titanium tetraisopropoxide or zirconium tetraisopropoxide isopropanol complex were mixed with 2-butanone in a molar ratio of 1 : 50. For the mixed oxide, 0.58 mmol Ti(O*i*Pr)$_4$ and 0.65 mmol Zr(O*i*Pr)$_4$·*i*PrOH were used. After stirring for 10 min, 1.23 mmol lead(II) acetylacetonate or lead(II) acetate trihydrate was added, and further stirred for 1 h. An orange to yellow, slightly turbid liquid was obtained, which was transferred into an autoclave equipped with a Teflon liner. The autoclave was sealed and heated in an oven to 200 °C for 24 h. In all cases, white to yellow suspensions were obtained, which were centrifuged and the precipitates washed with ethanol and dried in vacuo. Calcination was carried out in air applying a heating rate of 100 °C/h and holding the calcination temperature of 400-600 °C for 4-6 h.

Films were prepared by casting several drops of a suspension of the as-prepared nanoparticles in EtOH (about 1 %wt) on a silicon wafer previously treated with an SPM ("piranha") solution (1 H_2O_2 : 2 H_2SO_4) at 120 °C for 30 min to remove organic contaminants. After preliminary drying, the films were heated to 100 °C, held for 2 h for drying the film, and then rapidly heated to 500 °C, which was held for 2 h.

7.5.2 NMR data

The ^{13}C NMR measurements were performed using $CDCl_3$ as solvent, under ^{1}H-BB decoupling at 100 MHz. Peaks which were completely superimposed by the solvent are not mentioned.

2-Butanol: δ [ppm]: 69.2 (C2), 32.1 (C3), 22.9 (C1), 9.9 (C4).
5-Methyl-4-heptene-3-one: 201.7 (C3), 159.2 (C5), 123.1 (C4), 35.0 (C2), 33.5 (C6), 16.0 (C6'), 11.6 (C7), 7.8 (C1).
5-Methyl-4-hexene-3-one: 201.1 (C3), 159.9 (C5), 122.3 (C4), 35.0 (C2), 19.1 (C6').

7.6 References

[1] B. Jaffe, R. S. Roth, S. Marzullo, *J. Appl. Phys.* **1954**, *25*, 809.

[2] B. Noheda, *Curr. Opin. Solid State Mater. Sci.* **2002**, *6*, 27.

[3] A. J. Pointon, *IEE Proc.* **1982**, *129*, 285.

[4] D. Damjanovic, *Rep. Prog. Phys.* **1998**, *61*, 1267.

[5] H. S. Tzou, H.-J. Lee, S. M. Arnold, *Mech. Adv. Mater. Struct.* **2004**, *11*, 367.

[6] W. Heywang, H. Thomann, *Annu. Rev. Mater. Sci.* **1984**, *14*, 27.

[7] C. Kittel, *Introduction to Solid State Physics*, J. Wiley & Sons, New York, **1986**.

[8] D. Richter, S. Trolier-McKinstry in *Nanoelectronics and Information Technology* (Ed.: R. Waser), Wiley-VCH, Weinheim**, 2005**.

[9] M. Kamlah, *Continuum Mech. Thermodyn.* **2001**, *13*, 219.

[10] D. L. Polla, F. F. Lorraine, *Annu. Rev. Mater. Sci.* **1998**, *28*, 563.

[11] M. J. Hoffmann, H. Kungl, *Curr. Opin. Solid State Mater. Sci.* **2004**, *8*, 51.

[12] G. G. Guilbault, J. M. Jordan, *CRC Crit. Rev. Anal. Chem.* **1988**, *19*, 1.

[13] A. V. Turik, V. Y. Topolov, *J. Phys. D: Appl. Phys.* **1997**, *30*, 1541.

[14] G. H. Haertling, *J. Am. Ceram. Soc.* **1999**, *82*, 797.

[15] K. Kakegawa, O. Matsunaga, T. Kato, Y. Sasaki, *J. Am. Ceram. Soc.* **1995**, *78*, 1071.

[16] N. T. Mandoki, C. Courtois, P. Champagne, A. Leriche, *Mater. Lett.* **2004**, *58*, 2489.

[17] H. Hirashima, E. Onishi, M. Nakagawa, *J. Non-Cryst. Solids* **1990**, *121*, 404.

[18] H. Cheng, J. Ma, B. Zhu, Y. Cui, *J. Am. Ceram. Soc.* **1993**, *76*, 625.

[19] M. Murata, K. Wakino, *Mater. Res. Bull.* **1976**, *11*, 323.

[20] E. Suvaci, A. Dogan, J. Anderson, J. H. Adair, *Chem. Eng. Comm.* **2003**, *190*, 843.

[21] T. R. N. Kutty, R. Balachandran, *Mater. Res. Bull.* **1984**, *19*, 1479.

[22] J. Moon, J. A. Kerchner, H. Krarup, J. H. Adair, *J. Mater. Res.* **1999**, *14*, 425.

[23] R. N. Das, R. K. Pati, P. Pramanik, *Mater. Lett.* **2000**, *45*, 350.

[24] Y. Deng, L. Liu, Y. Cheng, C. W. Nan, S. J. Zhao, *Mater. Lett.* **2003**, *57*, 1675.

[25] S. B. Cho, J. S. Noh, M. M. Lencka, R. E. Riman, *J. Eur. Ceram. Soc.* **2003**, *23*, 2323.

[26] C. Liu, B. Zou, A. J. Rondinone, Z. J. Zhang, *J. Am. Chem. Soc.* **2001**, *123*, 4344.

[27] E. R. Camargo, M. Popa, J. Frantti, M. Kakihana, *Chem. Mater.* **2001**, *13*, 3943.

[28] T. K. Mandal, S. Ram, *Mater. Lett.* **2003**, *57*, 2432.

[29] P. R. Arya, P. Jha, G. N. Subbanna, A. K. Ganguli, *Mater. Res. Bull.* **2003**, *38*, 617.

[30] S. Bose, A. Banerjee, *J. Am. Ceram. Soc.* **2004**, *87*, 487.

[31] A. Banerjee, S. Bose, *Chem. Mater.* **2004**, *16*, 5610.

[32] E. R. Camargo, E. Longo, E. R. Leite, V. R. Mastelaro, *J. Solid State Chem.* **2004**, *177*, 1994.

[33] M. L. Calzada, I. Bretos, R. Jiménez, H. Guillon, L. Pardo, *Adv. Mater.* **2004**, *16*, 1620.

8 Synthesis of Niobates by Solvothermal Treatment in Benzyl Alcohol

8.1 Introduction

Despite their excellent piezoelectric properties, there is a strong tendency to replace PZT ceramics with other materials owing to concerns regarding the toxicity of lead, their main component.[1,2] Although significant research efforts were devoted to the development of suitable substitutes,[3,4] no effective alternative to PZT was found, until recently the synthesis of a material called "LF4T" was developed which exhibits an electric-field induced strain comparable to PZT. This material, with the complicated formula $(K_{0.55}Na_{0.52}Li_{0.04})(Nb_{0.84}Ta_{0.10}Sb_{0.06})O_3$, is an alkaline niobate-based perovskite solid solution, and was prepared via a complicated route involving sintering at 1135 °C.[2]

These new findings emphasize the technological importance of sodium and potassium niobates as piezoelectric materials. Their ferroelectricity has been discovered in 1949.[5] Both materials undergo a phase transformation from orthorhombic to tetragonal to cubic upon increase of the temperature – the phase changes are hence analogous to $BaTiO_3$.[6] T_c was found at about 420 °C for the mixed $K_{0.5}Na_{0.5}NbO_3$.[7]

$KNbO_3$ has several other promising properties, for example the frequency doubling of laser irradiation.[8] Also the possibility of data storage by thermal hologram fixing in pure and doped $KNbO_3$ has been investigated.[9] On the other hand, potassium hexaniobate ($K_4Nb_6O_{17}$) is a promising semiconductor photocatalyst for the decomposition of water.[10]

Conventional solid-state reactions above 900 °C lead to potassium and sodium niobates with high crystallinity but very large crystal sizes and low surface areas.[11] Densified potassium-sodium niobate ceramics were prepared by spark-plasma sintering at 1100 °C, however also exhibiting grain sizes in the micron regime.[12] Therefore, alternative synthesis techniques were developed. A soft chemical method involving selective dissolution of the layered perovskite K_2NbO_3F as precursor material resulted in $KNbO_3$ particles about 100-300 nm in size.[13] Smaller and more uniform particles of 10-20 nm were achieved via hydrothermal treatment of K_2CO_3 and Nb_2O_5 in a strongly alkaline (KOH) environment, however the reaction temperature had to be increased to 400 °C to achieve a crystalline material.[11] Using very high KOH concentrations, crystalline particles were obtained already at 200 °C, however being several µm large. The formation of rod-like particles, again several µm in length, was reported

for hydrothermal treatment at lower temperatures.[14] $NaNbO_3$ nanoparticles of about 25 nm in size were prepared using a polymeric precursor route, however, decomposition had to be carried out at temperatures above 450 °C to obtain crystalline materials.[15]

In analogy with the $BaTiO_3$ system, a solvothermal treatment seems promising to achieve both a crystalline material at rather moderate temperatures and small crystal/particle sizes, due to stabilization effects by adsorption of benzyl alcohol on the particle surface. Again, we used the elemental form of the alkali metal, and an alkoxide for the transition metal species, i.e. sodium or potassium and niobium(V) ethoxide. However, treatment in benzyl alcohol at 200 °C resulted in a completely transparent solution. The reaction temperature had to be increased to 220 °C to obtain particulate materials.

8.2 Results and Discussion

The alkali metals were found to dissolve rapidly in benzyl alcohol at room temperature. Titanium isopropoxide was added to the resulting clear solution, and solvothermal treatment was carried out at 220 °C for 2 days. In all cases, white suspensions were obtained, which were centrifuged and the precipitate washed with EtOH and dried to yield a white powder.

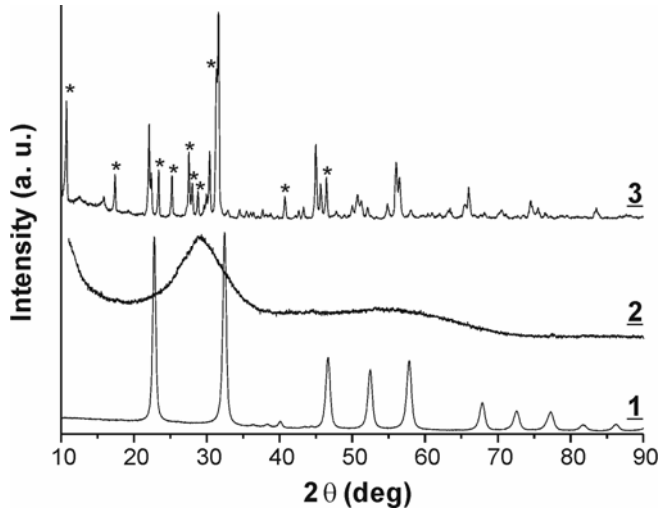

Figure 8.1. XRD diffraction pattern observed for $NaNbO_3$ particles (**1**) and $KNbO_3$, as-prepared (**2**) and after calcination at 700 °C (**3**).

The XRD patterns of the obtained powders are shown in Figure 8.1. The $NaNbO_3$ sample (Fig. 8.1, **1**) is highly crystalline, with all obtained reflections corresponding to cubic $NaNbO_3$ (Lueshite, JCPDS No. 19-1221). From the (110) reflection at $2\theta = 32.4°$, the particle size was calculated to 10 nm, using the Scherrer equation. Potassium niobate (Fig. 8.1, **2**), as well as the mixed $Na_{0.5}K_{0.5}NbO_3$ (not shown), were however not crystalline directly after the

synthesis. Broad signals were found at 2θ = 29° and 55° which could not be correlated with any potassium niobate phase. After calcination at 700 °C, the powder becomes crystalline (Fig. 8.1, **3**). The pattern matches best with orthorhombic $KNbO_3$ (JCPDS No. 32-822), however the presence of cubic $KNbO_3$ (JCPDS No. 8-212) cannot be excluded. The additional peaks marked * are attributed to potassium hexaniobate $K_4Nb_6O_{17}$ (JCPDS No. 21-1295).

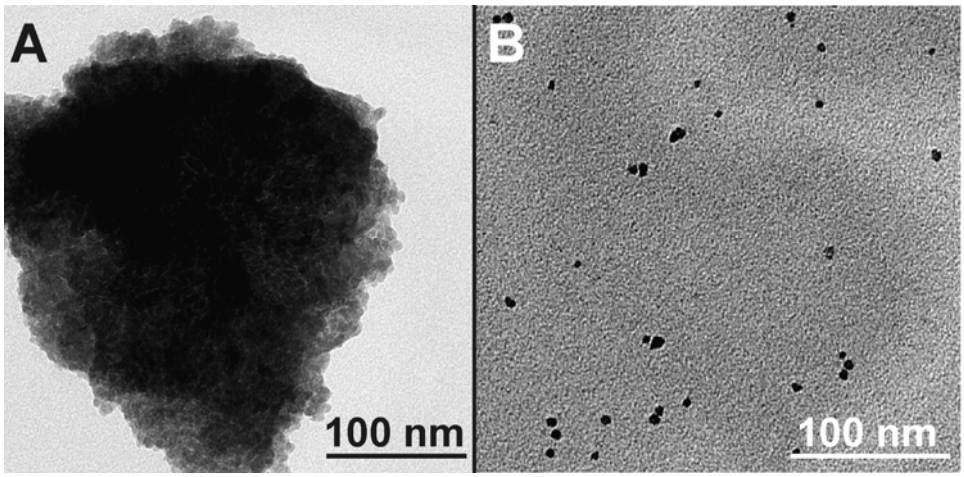

Figure 8.2. TEM images of as-prepared $NaNbO_3$ particles, using a suspension in EtOH (**A**) and after ultrasonic treatment and removal of larger aggregates (**B**).

TEM analysis of the $NaNbO_3$ powders revealed the presence of large aggregates, several hundred nm in size (Figure 8.1 **A**). The individual particles can only be distinguished at the edges of the aggregate to be about 5-10 nm in size. However, after long ultrasonic treatment of a dispersion of the particles in EtOH, followed by removal of larger aggregates by centrifugation at 4000 rpm, solely individual particles can be seen (Fig. 8.2 **B**). Such a size selection technique is quite commonly employed, usually not only to remove aggregates but to obtain monodisperse fractions of particles,[16,17] however it naturally goes hand in hand with a dramatic decrease in yield. The fraction of nonaggregated particles, as visible in Fig. 8.2 **B**, shows a size of about 5 nm, which is slightly smaller than calculated from the XRD. Most particles are spherical in shape, some show a slight ellipsoidal elongation.

As the reaction system can be considered very similar to the $BaTiO_3$ system discussed in Chapter 3.2, either ether elimination or the novel C–C coupling reaction was expected as the mechanism leading to particle formation. The $^{13}C\{^1H\}$carbon NMR spectrum for a $NaNbO_3$ sample prepared in a more concentrated approach is presented in Figure 8.3. Beside the solvent peaks of $CDCl_3$ and benzyl alcohol (marked BA), strong ethanol peaks are observed

(marked EtOH). 3-Phenylpropanol can clearly be identified (**1**), as well as 1,2-diphenylethanol (**2**). 2-Benzyl-3-phenylpropanol (**3**) and benzyl ether (**4**) are present in lower quantities, as are toluene (**5**) and benzaldehyde (the low-field region is not shown). The small signals in the high-field region marked * presumably stem from ethoxy species (see below). Due to the presence of a high number of coupling products and coupling byproducts, it was however not possible to assign all peaks in the spectrum.

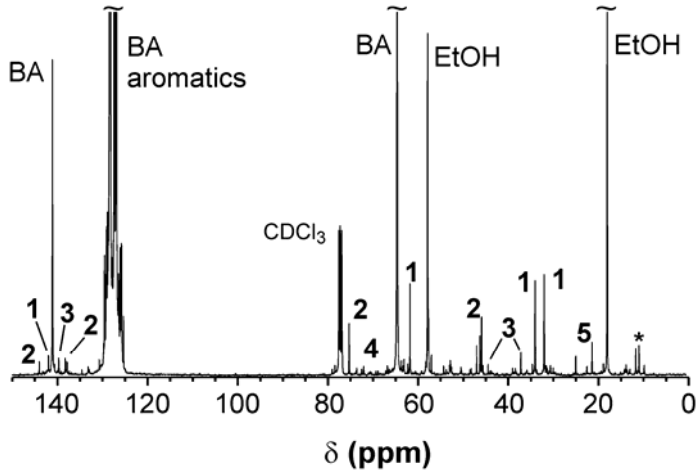

Figure 8.3. ^{13}H-BB-decoupled ^{13}C NMR spectrum of the reaction solution for the $NaNbO_3$ system.

The obtained reaction solution was therefore analyzed by GC–MS to determine the composition of the solution in detail. The gas chromatogram is shown in Figure 8.4. It can be clearly seen that the solution is a very complex mixture, containing over 20 different species (the ethanol peak was blinded out from this measurement, as well as the hexane signal). The signals were identified from the obtained respective mass spectra (data not shown); for the sake of conciseness, only the more significant components will be discussed. The peak labeled **1** is assigned to toluene, **2** to benzaldehyde, and **3** to allylbenzene (stemming from dehydration of **8**). The large signal **4** is, as expected, the reaction solvent benzyl alcohol. The small peaks **5** and **6** are attributed to benzyl ethyl ether and benzyl acetate, respectively, whereas **7** stems from a coupling product of benzyl alcohol with two ethyl species, most probably being 3-phenyl-1,5-pentanediol. Peak **8** resembles a main reaction product, 3-phenylpropanol. Peaks **9** and **10** are attributed to cinnamyl alcohol and 5-phenylpentanol, respectively, whereas peak **11** clearly can be assigned to benzyl ether. Signal **12**, being 1,2-diphenylethanol, and peak **13**, a coupling product of two benzylic and one ethoxy species, probably 1-ethoxy-1,2-diphenylmethane, are found in larger quantities. Peak **14** was assigned to 2-benzyl-3-phenylpropanol. The smaller signals at higher retention times stem from even higher condensation products, eg. signal **15** possibly being 1-benzoxy-1,2-diphenylethane. The chemical structures of the more complex organic reaction products are presented in Figure 8.5.

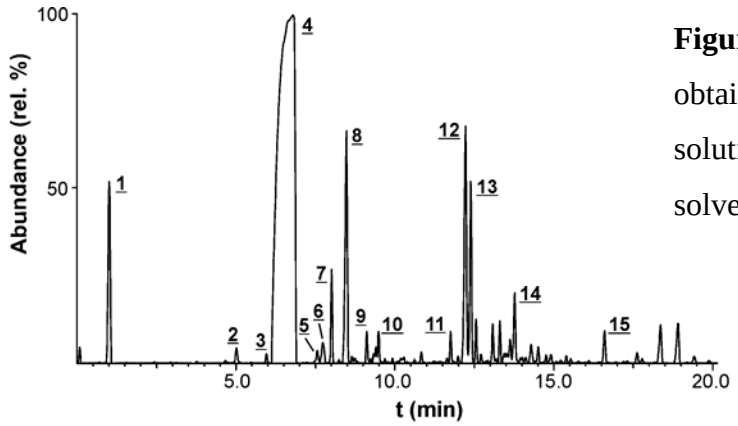

Figure 8.4. Gas chromatogram obtained for the filtered reaction solution in hexane (EtOH and solvent peaks blinded out).

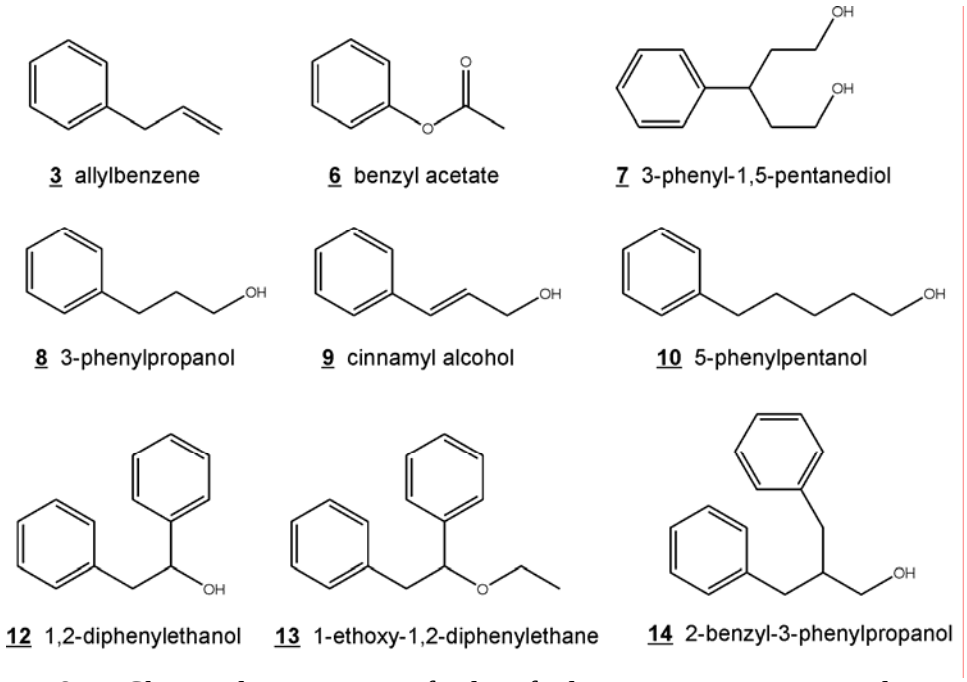

Figure 8.5. Chemical structures of identified organic reaction products, the respective labels corresponding to the assignment of the GC–MS results.

It is astonishing that a simple reaction approach (only the metal, niobium ethoxide and benzyl alcohol present) yields such a variety of organic species. The main reaction product is 3-phenylpropanol, which can only be formed via a C–C coupling mechanism, most probably in an analog fashion as in the $BaTiO_3$ system (Scheme 8.1). In a first step, benzyl alcohol coordinates to the Nb center (**1**). Due to the strongly alkaline environment after dissolution of sodium metal, an ethoxy ligand is deprotonated in the β-position, and attacks the electrophilic benzyl carbocation (**2**). This position is preferred, as the negative charge is stabilized via an agostic bond with the metal center, as has been reported before for the case of titanium.[18] A C–C bond is formed (**3**), concurrently leading to a metal-bound hydroxyl group. Subsequent condensation leads to 3-phenylpropanol and Nb–O–Nb bonds. Alternatively, the β-position can be attacked by another benzyl alcohol, finally leading to 2-benzyl-3-phenylpropanol.

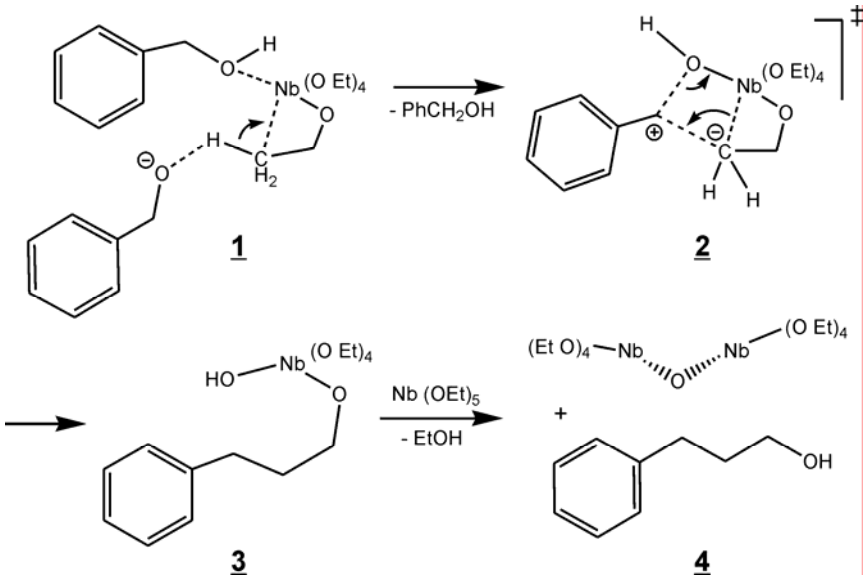

Scheme 8.1. Proposed main mechanism leading to the concurrent formation of Nb–O–Nb bonds and 3-phenylpropanol.

In view of such an abundance of side products, it is clear that not all mechanisms can be discussed here in detail. As in most other systems investigated, MPV-like reduction/oxidation reactions take place on the niobium centers between two benzylic species to form benzaldehyde and toluene. The presence of allylbenzene and cinnamyl alcohol is noteworthy even though they were only formed in small quantities, as theoretically they might constitute intermediates in the formation of 3-phenylpropanol via an elimination process, which would contradict the reaction pathway proposed here. This is discussed in detail in Chapter 9.

On the other hand, quite large amounts of 1,2-diphenylethanol and 1-ethoxy-1,2-diphenylethane were present in the reaction mixture. We have not found these compounds for any other system investigated before. Basically, they must be formed via a C–C coupling reaction between two benzyl moieties, and their existence can be explained due to the high amount of deprotonated benzoxy species. In this context, one must also keep in mind that the solvothermal treatment is performed at 220 °C, at a higher temperature than the synthesis of $BaTiO_3$, and that benzyl alcohol already starts to undergo thermolysis reactions in an inert solvent such as cyclohexane at 250 °C, resulting in dibenzyl ether by dehydration, in disproportionation products such as toluene and benzaldehyde, but also, to a lesser extent, in coupling products such as dibenzyl (0.2 % yield), without any catalyzing metals present.[19]

We suggest the formation mechanism as presented in Scheme 8.2. Benzyl alcohol is coordinated in large amounts due to ligand exchange reactions.[20] The coordinated benzoxy species (**1**) can also be deprotonated, the difference to the ethoxy species however is that

deprotonation must occur on the α site (due to the lack of any β-hydrogens). The deprotonated benzoxy species is stabilized via an inductive effect of the electrophilic niobium center, but also via charge delocalization in the aromatic system (**2**). Similar to the main mechanism, next another benzyl alcohol coordinates with the Nb center, and an attack of the negatively charged ligand onto the electrophilic second benzyl group (**3**) results in C–C bond formation (**4**). The simultaneously formed –OH groups lead to formation of Nb-O-Nb bridges under release of EtOH and 1,2-diphenylethanol (**5**). Alternatively, condensation of an ethoxy group with the ligated 1,2-diphenylethoxy species yields 1-ethoxy-1,2-diphenylethane.

Also the finding of 5-phenylpentanol is very interesting, as it indicates that a second coupling step can occur to a small extent. The intermediate 3-phenyl-butoxide (**3** in Scheme 8.1) hence can also act as a nucleophile (which was originally expected) to be attacked by another β-deprotonated ethoxy species (as in step **1**), C–C bond formation and condensation occurring analogously as in Scheme 8.1 producing the 5-phenylpentanol species.

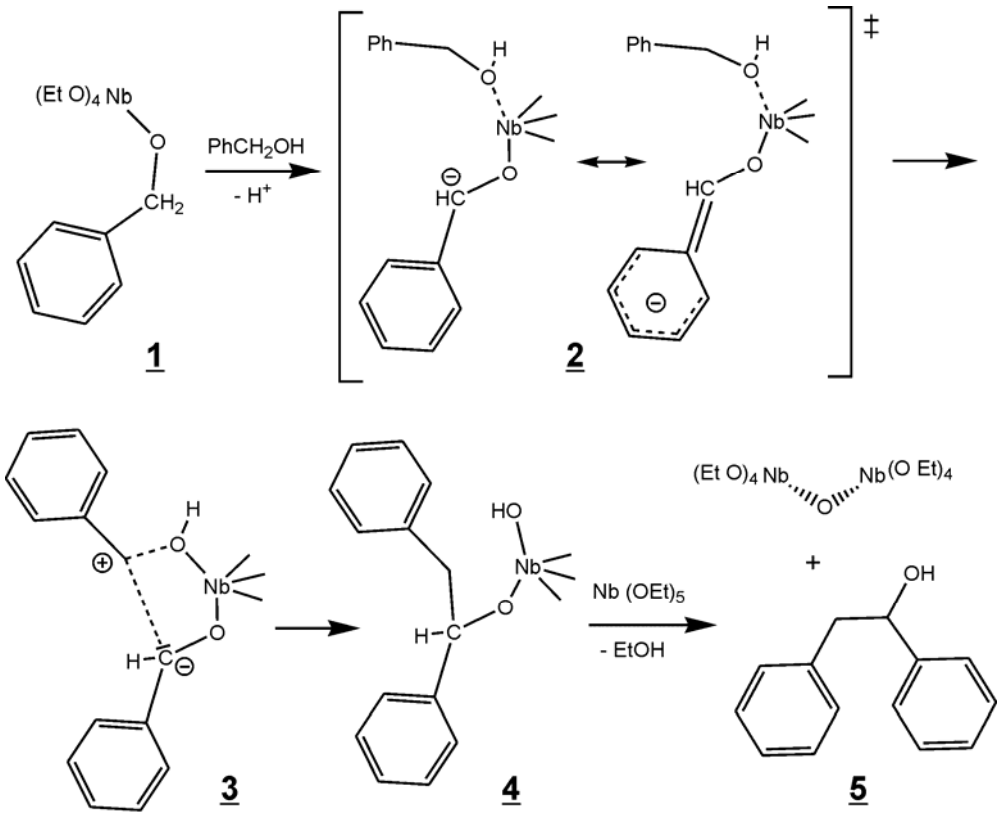

Scheme 8.2. Proposed side reaction involving a C–C bond formation of two benzylic species to form 1,2-diphenylethanol.

Comparing to the $BaTiO_3$ system, it becomes clear that the coupling reaction is much less favored with the ethoxy species, leading to a lower yield of the primary coupling product

(3-phenylpropanol), and, to a high degree, to side reactions, in particular coupling reactions between two benzylic species, which were not observed at all in the $BaTiO_3$ system (cf. Chapter 3.2). Another possible explanation for such coupling products is the higher reaction temperature which had to be used to obtain a solid material.

8.3 Summary and Conclusions

The synthesis of highly crystalline $NaNbO_3$ nanoparticles can be conveniently realized by the solvothermal route with benzyl alcohol as solvent. By using the alkali metals as precursors, high purity is achieved. The as-prepared particles are highly crystalline and about 5-10 nm in size. Interestingly, the synthesis of highly crystalline $KNbO_3$ or $Na_{0.5}K_{0.5}NbO_3$ was not possible in benzyl alcohol. Amorphous particles were obtained which had to be subjected to calcination at 700 °C to induce crystallization, however yielding a mixture of phases.

The reaction mechanism is similar as observed in the $BaTiO_3$ – benzyl alcohol system. The β-carbon position of the ligand is deprotonated and nucleophilically attacks the benzylic carbon atom to form a C–C bond. In the niobate system, however, side reactions occur to a much higher extent. Surprisingly, even C–C coupling between two benzylic species takes place, which is attributed to the lower stabilization of the ethoxy ligand but may also be due to the higher reaction temperature.

8.4 Experimental Section

8.4.1 Synthesis

Sodium niobate, potassium niobate, and mixed sodium potassium niobate samples were prepared by dissolving metallic sodium or potassium (3.0 mmol total amount of metal) in 25 mL benzyl alcohol (anhydrous, 99.8%). For analysis of the reaction solution, a more concentrated approach was employed, by only using 5 mL benzyl alcohol. After ca. 30 min stirring, a clear solution was obtained, to which niobium(V) ethoxide (0.955 g, 3.0 mmol) was added. The mixture was stirred for further 10 min, and then solvothermal treatment was performed in an autoclave at 220 °C for 3 days. After cooling, the resulting white to slightly yellow suspension was separated by centrifugation. The precipitate was washed 3 × with EtOH and dried to yield a white powder, whereas the reaction solution was filtered and subjected to NMR and GC–MS analysis for determination of the reaction mechanisms.

8.4.2 NMR Data

The ^{13}C NMR measurements were performed under ^{1}H-BB decoupling at 100 MHz, using $CDCl_3$ as solvent. Only the main reaction products are given, and signals superimposed by the sovent are not stated.

3-Phenylpropanol: δ [ppm]: 142.0 (Ph_{ipso}), 61.8 (C1), 34.1 (C3), 32.0 (C2).
1,2-Diphenylethanol: 144.0 ($Ph_{ipso,1}$), 139.7 ($Ph_{ipso,2}$), 75.3 (C1), 45.9 (C2).
Benzyl ether: 137.9 (C_{ipso}), 72.1 (CH_2).
2-Benzyl-3-phenylpropanol: 139.4 (Ph_{ipso}), 66.9 (C1), 44.2 (C2), 37.0 (C3).

8.5 References

[1] E. Cross, *Nature* **2004**, *432*, 24.

[2] Y. Saito, H. Takao, T. Tani, T. Nonoyama, K. Takatori, T. Homma, T. Nagaya, M. Nakamura, *Nature* **2004**, *432*, 84.

[3] G. H. Haertling, *J. Am. Ceram. Soc.* **1999**, *82*, 797.

[4] T. Takenaka, H. Nagata, *Key Eng. Mater.* **1999**, *157-158*, 57.

[5] B. T. Matthias, *Phys. Rev.* **1949**, *75*, 1771.

[6] T. M. Shaw, S. Trolier-McKinstry, P. C. McIntyre, *Annu. Rev. Mater. Sci.* **2000**, *30*, 263.

[7] G. Shirane, H. Danner, A. Pavlovic, R. Pepinsky, *Phys. Rev.* **1954**, *93*, 672.

[8] H. Tsuchida, *Opt. Rev.* **1996**, *3*, 309.

[9] G. Montemezzani, P. Gunter, *J. Opt. Soc. Am. B* **1990**, *7*, 2323.

[10] A. Kudo, A. Tanaka, K. Domen, K.-I. Maruya, T. Onishi, *J. Catal.* **1988**, *111*, 67.

[11] H. Hayashi, Y. Hakuta, Y. Kurata, *J. Mater. Chem.* **2004**, *14*, 2046.

[12] R. Wang, R. Xie, T. Sekiya, Y. Shimojo, *Mater. Res. Bull.* **2004**, *39*, 1709.

[13] K. Toda, N. Ohtake, M. Kawakami, S. Tokuoka, K. Uematsu, M. Sato, *Jpn. J. Appl. Phys.* **2002**, *41*, 7021.

[14] G. Suyal, E. Colla, R. Gysel, M. Cantoni, N. Setter, *Nano Lett.* **2004**, *4*, 1339.

[15] J. M. Calderon-Moreno, E. R. Camargo, *Catal. Today* **2003**, *78*, 539.

[16] D. Gasser, A. Baiker, *J. Catal.* **1988**, *113*, 325.

[17] J. F. Bertone, J. Cizeron, R. K. Wahi, J. K. Bosworth, V. L. Colvin, *Nano Lett.* **2003**, *3*, 655.

[18] Z. Dawoodi, M. L. H. Green, V. S. B. Mtetwa, K. Prout, *J. Chem. Soc. Chem. Commun.* **1982**, 802.

[19] A. R. Katritzky, M. Balasubramanian, *Energy Fuels* **1990**, *4*, 499.

[20] A. Vioux, *Chem. Mater.* **1997**, *9*, 2292.

9 Discussion of the Novel C – C Coupling Reaction

9.1 Introduction

In the previous chapters, novel pathways to transition metal oxides have been presented, showing than indeed the solvothermal synthesis of metal oxides can proceed not only following the conventional nonaqueous routes such as ether or ester elimination.[1] Moreover, simple "thermolysis" of the precursors, which is suggested frequently in the literature,[2] was not observed, at least not in its classical meaning, which would solely imply the occurrence of elimination processes, producing e.g. propene from titanium isopropoxide.

Basically, three nonaqueous processes leading to the formation of oxidic materials from metal alkoxides or acetylacetonates by solvothermal reaction in organic media can be distinguished. One is the conventional ether elimination, which is not discussed in this work. It has been suggested already a decade ago[1] and was observed by us recently upon the solvothermal reaction of hafnium(IV) ethoxide and tantalum(V) ethoxide in benzyl alcohol to form HfO_2 and Ta_2O_5 nanopowders.[3]

The second observed mechanism is based on organic condensation reactions, especially aldol and ketimine coupling. A C–C bond formation occurs in the course of this reaction, but the key step is the elimination of water, which in our case leads to a hydroxyl group bound to the metal center which can then react with another metal alkoxide to form metal-oxygen-metal bonds, constituting the first step to build up the inorganic crystal. This mechanism is observed when reacting metal alkoxides in ketones or aldehydes but also upon reaction of metal acetylacetonates in benzyl alcohol or benzylamine, even though in the latter case there are side reactions occurring to a substantial extent. The prerequisite for this type of mechanism is the presence of enolates ligating the metal center, which are formed either through attack of the metal by the ketone/aldehyde solvent, or through cleavage of the acetylacetonate ligand. In principle, aldol and ketimine reactions are well-known and widely used in organic chemistry. One could argue that they are merely another pathway for the in situ generation of water which then induces the inorganic condensation, comparable to ester elimination or acetal formation processes, where reaction of the alkoxide with the solvent leads to water which then promotes oxide formation.[4,5] There is, however, a significant difference to these reactions, as in our case the metal center is proposed to play a significant role in the organic condensation process itself and molecular water is not expected to form in the course of the condensation reaction.

The third pathway is unique as there is no known equivalent in organic chemistry. Surprisingly, it is not restricted to a specific system but seems to be induced and catalyzed by a variety of transition metals, as it was observed leading to $BaTiO_3$, $NaNbO_3$ and Y_2O_3. It also involves a C–C coupling step, however in this case it is the alkoxide itself which is deprotonated, consequently possessing a negative charge on its β-position. At first, we expected this deprotonation to be caused by the very alkaline reaction medium present after dissolution of alkali and alkaline earth metals in alcohols. As this novel mechanism however is also observed for the formation of an Y_2O_3 nanocomposite, where only yttrium(III) isopropoxide and benzyl alcohol are present in the reaction solution, also Lewis-acidic metal centers such as Y^{3+} apparently catalyze this reaction. When comparing to the aldol coupling mechanism, especially as it is observed in the $Fe(acac)_3$ – benzyl alcohol system (cf. Chapter 8.3, Scheme 8.4), one notes that the only difference is the oxidation state of the nucleophile. Whereas the attack of the double bond constitutes an addition reaction well-known to organic chemists, the appearance of a transient negative charge on the β-carbon of alkoxides, and their subsequent nucleophilic attack on an alcohol has, to the best of our knowledge, not been observed so far. This chapter is aimed at a more detailed investigation of this reaction, exploring the role of alkaline ions present and the possibility of its extension to other alkoxides, as well as investigating the probability of other mechanisms than the proposed one to lead to the observed results.

9.2 Results and Discussion

9.2.1 Investigations on the Influence of Metal Ions

Aside from the Y_2O_3 system, the C–C coupling reaction was only observed in the presence of alkaline species after dissolving an alkali metal or an alkaline earth metal in a benzylic alcohol. Hence an influence of these ions might be significant.

The $BaTiO_3$ system shows the highest yield in the monosubstituted coupling product, 4-phenyl-2-butanol. Therefore, analysis of the reaction efficiency is easiest emanating from this system. In order to investigate the role of the Ba^{2+} ions in the course of the reaction, Ba was replaced by an alkali metal such as sodium. After equal treatment, the sodium system showed a comparable yield of C–C coupling products, the only difference being that the ratio of monosubstituted to disubstituted product was decreased from about 4:1 to 1.4:1. This ratio was however found to also greatly depend on the concentration of the alkoxide in the solvent within one system: Whereas high concentrations resulted only in a negligible amount of the

disubstituted species compared to 4-phenyl-2-butanol, diluted systems yielded di- and monosubstituted product in practically equimolar amounts.

The solvothermal treatment of titanium isopropoxide was therefore also performed without adding barium or sodium. Highly crystalline anatase particles were formed (as verified by XRD, not discussed here). The reaction solution was again analyzed by NMR spectroscopy. In the $^{13}C\{^{1}H\}$ NMR spectrum (Figure 9.1 **A**), the presence of ethers is detected in addition to the alcohols. Especially dibenzyl ether (**1**) was formed, but also diisopropyl ether (**2**), and, to a smaller extent, mixed benzyl isopropyl ether (**3**) is found. Hence, in nonalkaline conditions the formation of oxide particles follows the initially expected ether elimination route.

In the presence of strong organic bases such as sodium ethoxide (NaOEt), however, the ethers are no longer present in the final solution. The NMR spectrum of a system with the initial composition 1 Ti(O*i*Pr)$_4$ – 5 benzyl alcohol – 2 NaOEt is shown in Fig. 9.1 **B**. In fact, 4-phenyl-2-butanol (**4**) is formed in large quantities, as well as 1,5-diphenyl-2-pentanol (**5**). The peaks labeled **6** correspond to ethanol stemming from the base. The ratio of **4** to **5** is 2.6:1.

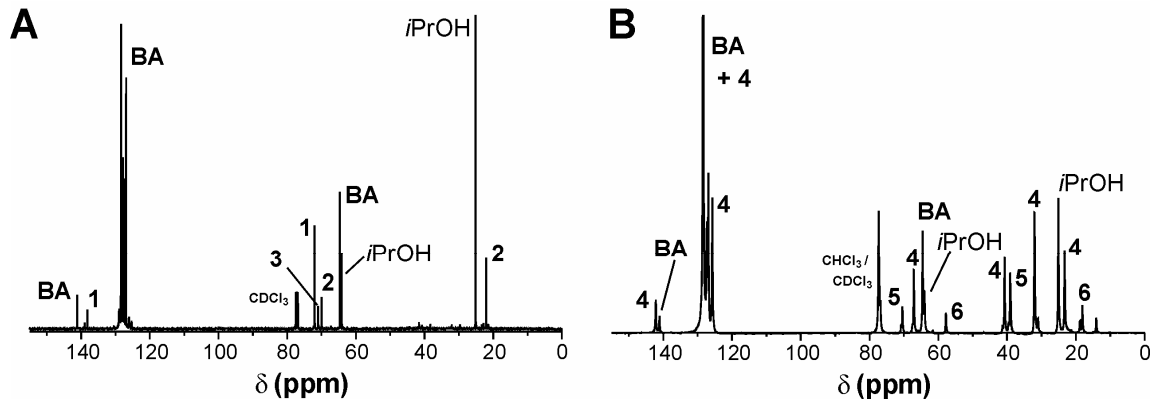

Figure 9.1. ^{1}H-BB decoupled ^{13}C NMR spectra of the solutions obtained via solvothermal reaction of Ti(O*i*Pr)$_4$ in benzyl alcohol in the absence of any base (**A**), and in the presence of NaOEt (**B**).

Also the niobate system was explored in terms of influence of basic conditions on the reaction mechanism. The treatment of niobium(V) ethoxide in benzyl alcohol, without the presence of the alkali metal, resulted in formation of highly crystalline Nb_2O_5 (the XRD best matching JCPDS No. 28-317, hexagonal Nb_2O_5). The ^{13}C NMR of the reaction solution (not shown) indicates the presence of benzyl ether and diethyl ether. 3-Phenylpropanol and 1,2-

diphenylethanol, the main products found for $NaNbO_3$, are completely absent. Interestingly, a quite large amount of diphenylmethane, a reported thermolysis product of benzyl alcohol,[6] is found. When adding NaOEt to the system prior to solvothermal treatment, crystalline $NaNbO_3$ was obtained, showing similar crystallinity and particle size as the sodium metal system. Even the composition of the final reaction solution was identical, apart from a higher content in EtOH. Therefore, NaOEt can be used as a substitute for metallic sodium in this system.

These results clearly prove that the presence of organic bases, which can also generated in situ by the reaction of metals with the alcohol solvent, is necessary for the Ti- or Nb-catalyzed C–C coupling reaction to occur. The yttrium oxide system is the only case where the coupling procedure occurred without presence of an alkaline species. This can be explained by the very Lewis-acidic character of the Y^{3+} center, facilitating deprotonation of the $–CH_3$ group on the ligand and stabilization of the negative charge.

9.2.2 Experiments with Other Alcohols / Other Alkoxides

When using isopropoxide or ethoxide ligands, always the β-carbon atom underwent deprotonation and subsequent electrophilic attack by the benzylic carbon. This is reasonable, since the negative charge can be best stabilized by agostic bonding.[7]

On the other hand, γ- and higher carbons are not present in these ligands. Although stabilization of the β position is best, in principle also higher positions may undergo coupling reactions. Therefore, experiments involving various titanium alkoxides were performed, not only to investigate the occurrence of further coupling reactions but also to probe the possibility of applying the coupling reaction to other organic systems, especially in view of the yield achieved. As a second step, the selectivity of the reaction for the benzylic carbon atom is tested by using solvents other than benzyl alcohol, such as 1-phenylethanol.

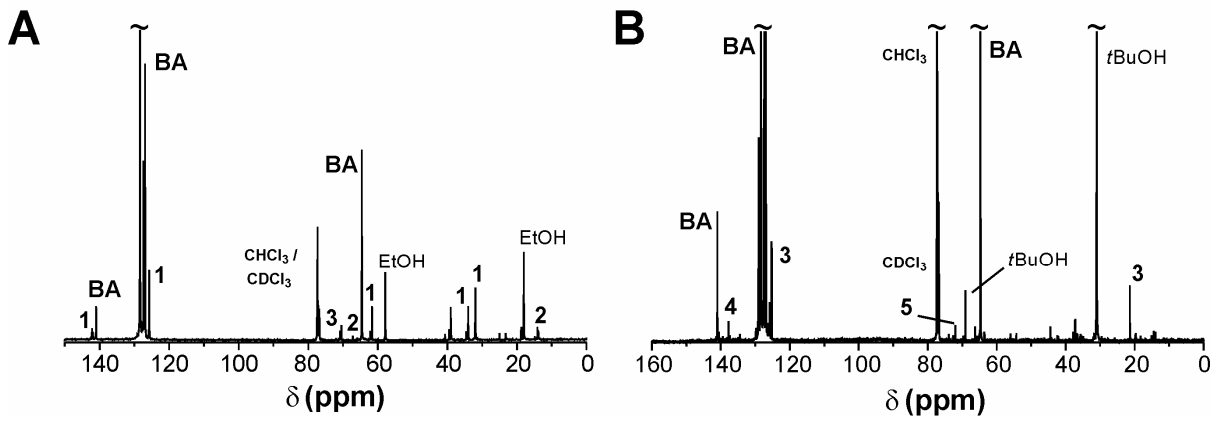

Figure 9.2. $^{13}C\{^1H\}$ NMR spectra of the obtained reaction solutions for the systems $Ti(OEt)_4$ / NaOEt / benzyl alcohol (**A**) and $Ti(O\mathit{t}Bu)_4$ / KO*t*Bu / benzyl alcohol (**B**).

A variety of coupling products has been found upon treatment of $Nb(OEt)_5$ in benzyl alcohol at 220 °C. However, one cannot directly conclude that ethoxy ligands are less suitable to undergo the coupling reaction, due to the higher temperature used for this system and the presence of Nb centers with possibly different catalytic properties than the Ti. To make the results comparable, experiments were performed treating titanium ethoxide, $Ti(OEt)_4$, in benzyl alcohol at 200 °C. NaOEt was added to the system as organic base (molar ratio 1 alkoxide : 2 base : 5 alcohol). After treatment for 1 day at 200 °C, a white to yellowish suspension was obtained. The precipitate, which was characterized as $NaTiO_3$ by XRD measurements (data not shown), was removed and the reaction solution analyzed by NMR. Figure 9.2 **A** presents the obtained ^{13}C NMR spectrum, which aside from benzyl alcohol and ethanol peaks clearly proves the presence of substantial amounts of 3-phenylpropanol (**1**). In addition, small ether signals are visible (**2** corresponding to diethyl ether and **3** to benzyl ether).

Interestingly, titanium *tert*-butoxide does not undergo the C–C coupling reaction, at least not in the yields as found for ethoxide or isopropoxide. The ^{13}C NMR spectrum (Fig. 9.2 **B**) of a solution obtained after solvothermal treatment of $Ti(O\mathit{t}Bu)_4$ in the presence of KO*t*Bu in benzyl alcohol results in fairly crystalline $KTiO_3$ particles (XRD data not shown here), but apart from the alcohols and the MPV products of benzyl alcohol (**3** corresponding to toluene and **4** to benzaldehyde), only benzyl ether (**5**) was found as potential side product of oxide formation, however in low yield. The absence of the carbon coupling reaction in this case is explained by steric hindrance by the bulky *tert*-butyl group, not allowing nucleophilic attack of the benzylic carbon center.

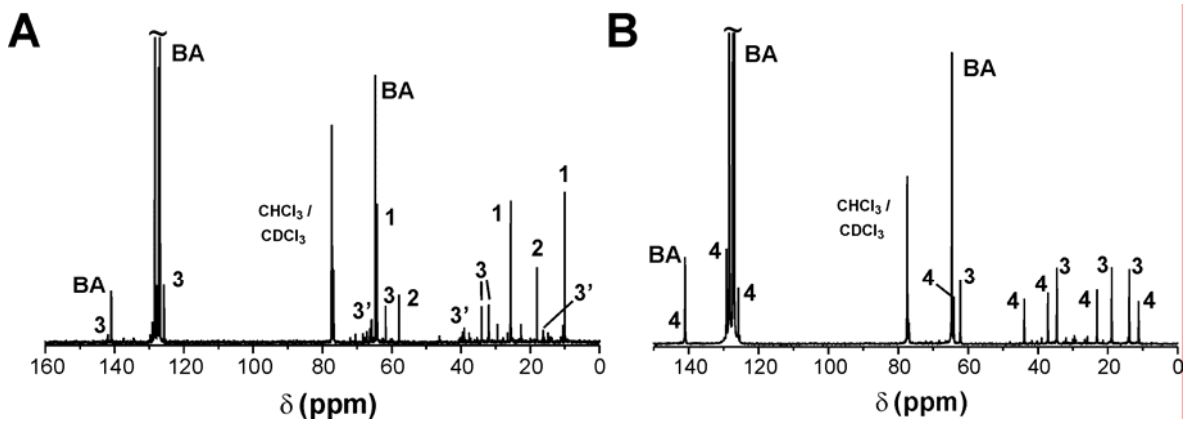

Figure 9.3. $^{13}C\{^1H\}$ NMR spectra of the obtained reaction solutions for the systems $Ti(O\mathit{n}Pr)_4$ / NaOEt / benzyl alcohol (**A**) and $Ti(O\mathit{n}Bu)_4$ / Ba / benzyl alcohol (**B**).

To probe the possibility of coupling reactions on γ- or higher carbon atoms, unbranched alkoxides were used as titania precursors. In a first step, titanium tetra-*n*-propoxide $Ti(OnPr)_4$, was reacted in an analogous fashion as described above for $Ti(OEt)_4$, again using NaOEt to as the alkaline species. The resulting ^{13}C NMR spectrum is shown in Figure 9.3 **A**. The results obtained here at first sight are surprising. Besides the alcohols (**1** denoting *n*-propanol and **2** ethanol), only a small amount of the expected 3-phenyl-2-methyl-1-propanol (**3´**) was obtained, but, in much larger quantities, 3-phenylpropanol (**3**). The latter of course cannot result from C–C coupling of the propoxide but its formation emanates from an ethoxide. Ligand exchange is expected to occur to a large extent, leading to an equilibrium of ethoxide and *n*-propoxide ligands. Probably, the inductive effect of the additional $–CH_3$ group of the *n*-propoxide makes deprotonation less favorable than for the ethoxide, leading to 3-phenylpropanol in much higher quantity. Coupling of the γ-position of the *n*-propoxide was not observed.

In principle, however, longer alkyl ligands undergo C–C coupling in similarly high yields as the ethoxide or isopropoxide. As an example, the reaction solution when using titanium tetra-*n*-butoxide is presented in Fig. 9.3 **B**. Here, however, metallic barium was used to prevent the presence of ethanol. In addition to *n*-butanol (marked **3**), the expected coupling product 2-benzylbutanol (**4**) is found in practically stoichiometric yields (as compared to the free alcohol). Again, no other coupling products were found, especially no 3-benzylbutanol or 5-phenylpentanol which would result from coupling on higher carbon positions.

Additionally, higher aliphatic titanium alkoxides were explored. Symmetric alkoxides were prepared to obtain a smaller number of products, simplifying their identification. Titanium tetra-3-pentoxide and titanium tetra-4-heptoxide were then added to barium dissolved in benzyl alcohol, and reacted in an autoclave at 200 °C for 1 d. The resulting milky suspensions were centrifuged, and the solution analyzed. The obtained NMR spectra are presented in Figure 9.4. For the 3-pentoxide (**A**), the free alcohol was found in the solution (labeled **1**), but no di-3-pentyl ether or benzyl ether. Instead, 1-phenyl-2-methyl-3-pentanol (**2**) and 1,5-diphenyl-2,4-dimethyl-3-pentanol (**3**) were formed in substantial amounts. Due to superposition in the ^1H NMR spectrum (data not shown), the obtained product ratio can only be roughly calculated to ca. 1.08 3-pentanol : 1.00 1-phenyl-2-methyl-3-pentanol : 0.54 1,5-diphenyl-2,4-dimethyl-3-pentanol. In the 4-heptoxide system (**B**), the free alcohol (**3**) as well as 3-benzyl-4-heptanol were observed, but the disubstituted product was not observed in significant quantities.

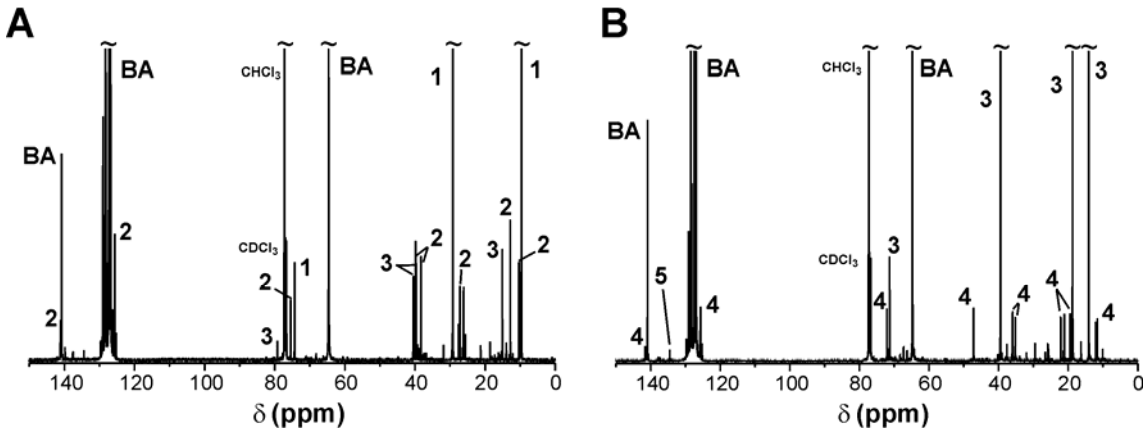

Figure 9.4. $^{13}C\{^{1}H\}$ NMR spectra of the obtained reaction solutions for the systems Ti(O–3-pentyl)$_4$ (**A**) and Ti(O–4-heptyl)$_4$ (**B**), both subjected to solvothermal treatment in benzyl alcohol after dissolution of metallic barium.

These results prove that also higher alkoxides undergo the C–C coupling reaction in high yields. Exclusively the β-position undergoes deprotonation and coupling. Any unsaturated products however were not found in significant amounts (see below).

The occurrence of the coupling reaction was also investigated in solvents other than benzyl alcohol. Figure 9.5 presents the NMR spectra of solutions obtained by solvothermal treatment of Ti(O*i*Pr)$_4$ in 1-phenylethanol (**A**) and 2-phenylethanol (**B**), after dissolving Ba in the respective solvent to obtain the respective barium alcoholate. The solvents are marked **S** in both cases. In 1-phenylethanol, the expected coupling product, 2-phenyl-4-pentanol, was achieved in high yield. Some ether (bis(α-methylbenzyl) ether) was also found. 2-Phenylethanol, with the –OH group not bound to the benzylic carbon but to the vicinal carbon, obviously does not undergo nucleophilic attack. In this case, no crystalline material but an amorphous gel was obtained. In the spectrum (Fig. 9.5 **B**), large *i*PrOH peaks are seen in addition to the solvent, the condensation mechanism however could not be elucidated. On the one hand, small diisopropyl ether signals were detected (labeled **3**), which would point to ether formation leading to partial condensation and thus gel formation. On the other hand, the signals marked * might indicate the presence of small quantities of styrene, which is the dehydration product of 2-phenylpropanol. Any water released by such a dehydration would cause the release of isopropanol under simultaneous formation of Ti–O–Ti bridges.

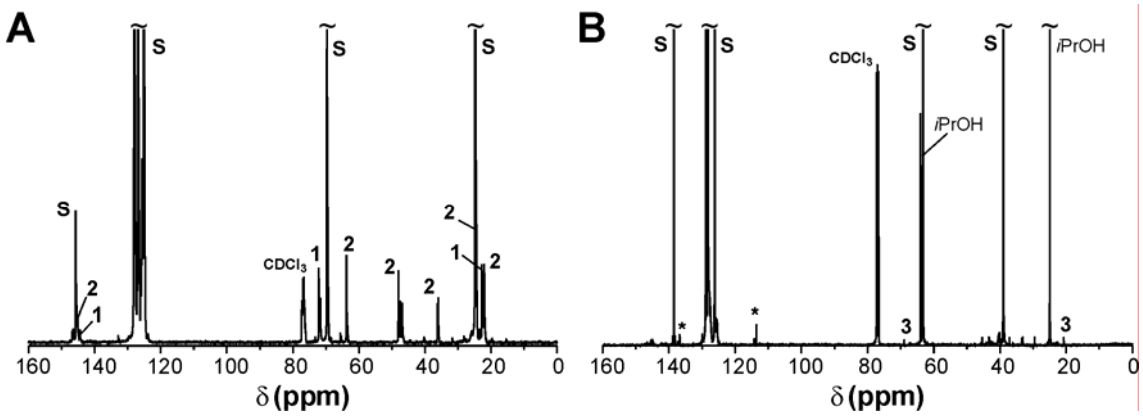

Figure 9.5. $^{13}C\{^{1}H\}$ NMR spectra of the reaction solutions resulting from solvothermal treatment of a $Ti(OiPr)_4$ in 1-phenylethanol (**A**) and 2-phenylethanol (**B**), after dissolution of barium in the respective solvent.

9.2.3 Discussion of Alternative Reaction Pathways

A variety of other reaction mechanisms is conceivable leading to C–C coupling, such as a radical mechanism or an elimination–addition mechanism. The latter mechanism is illustrated in Scheme 9.1. The ligand first eliminates an –OH group, equal to a thermolysis (**1**). The hydroxyl group is then bound to the Ti center and can induce condensation with another titanium. For simple and small ligands, as used here in all cases, the elimination product is gaseous, eg. propene when emanating from an isopropoxide (**2**). Formation of these products is expected to considerably increase the pressure in the autoclave. Hence, they can be expected to undergo further reactions, above all addition with the rather electrophilic benzylic carbon (most probably from a Ti-coordinated benzyl alcohol, **3**). The intermediate **4** features a carbocation, which will react either by elimination of a proton or by addition. Experiments were performed to investigate the possibility and probability of these mechanisms. (Saytzew) elimination (**a**) would be the more probable pathway here, leading to 4-phenyl-2-butene, which however was not found in any analyzed titanium isopropoxide – benzyl alcohol system, although its low volatility would render it stable (and the analyses of ketone systems and of the niobate have shown that indeed unsaturated species are stable under the applied solvothermal conditions). To obtain the alcohol, however, addition of either water or a hydroxy species (**6**, R = H) would have to occur (**b**). Considering the water-deficient and water-consuming reaction regime, the first possibility can be excluded. There are hydroxy groups present which are coordinated to the metal, although their stability before coupling with the next Ti center is unknown. If one of these hydroxy species would attack the carbocation, release of the free alcohol could then only be achieved via cleavage of the Ti–O

bond, which is improbable due to the strong electrophilicity of the Ti centers – in fact the *formation* of Ti–O bonds is the driving force behind the coupling mechanism. Therefore, the occurrence of an elimination–addition mechanism is considered improbable.

Interestingly, in the $NaNbO_3$ system several unsaturated products were found, namely allylbenzene and cinnamyl alcohol. Both were, however, found in much lower quantities than 3-phenylpropanol. What is more, cinnamyl alcohol cannot be an intermediate or side product of a possible elimination but merely is the oxidation product of 3-phenylpropanol. Thus, the trace of allylbenzene is the only fact possibly pointing to an elimination–addition mechanism. On the other hand, it could just as well have formed by dehydration of 3-phenylpropanol. In this system, one must also consider the second main reaction product, 1,2-diphenylethanol. Its formation *cannot* occur via an elimination–addition mechanism, as benzyl alcohol cannot formally undergo elimination of water or –OH due to the lack of β-hydrogen atoms. It is rather improbable that various C–C coupling reactions take place within one system via completely different mechanisms.

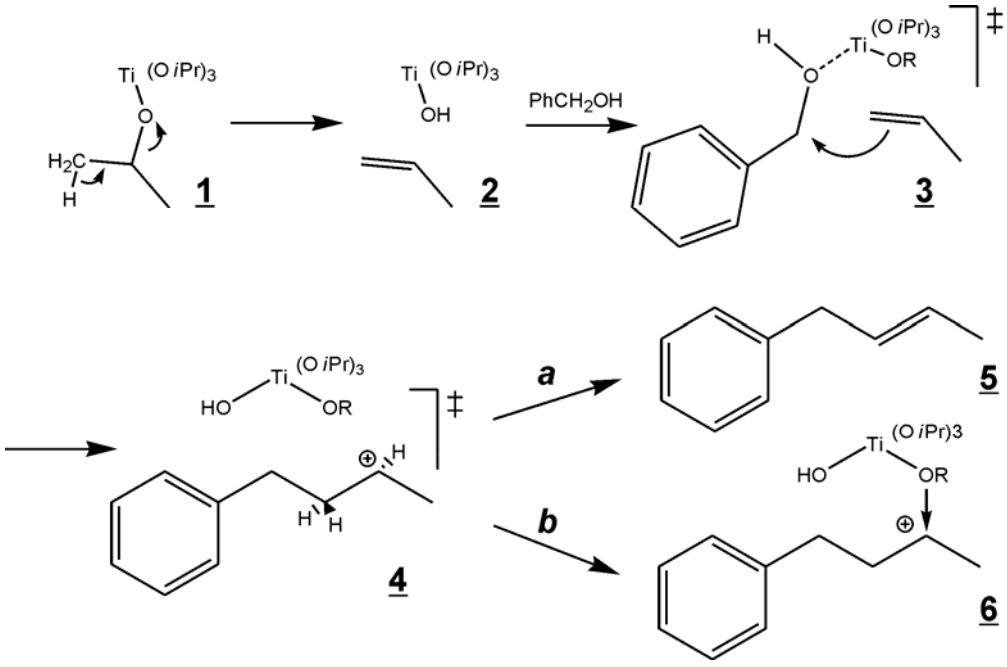

Scheme 9.1. Conceivable elimination–addition pathway which in principle cannot be ruled out to induce the formation of C–C coupling products.

The observation of the C–C coupling reaction after reacting metallic Ba in benzyl alcohol initially led us to the assumption of radical processes occurring in the course of this reaction, possibly mediated by Ba^{+}/Ba^{2+} ions. As shown in Chapter 9.2.1, however, the reaction proceeds just as well when using a strong organic base, which contradicts the influence of radical processes catalyzed by heavy metal ions. Nevertheless, experiments were performed

using 2,2,6,6-tetramethyl-piperidine-1-oxyl (TEMPO), which is a stable radical well-known in organic chemistry.[8] This radical is also used in order to scavenge other radicals in the system, blocking further reaction. However, we found the usual reaction products, in amounts comparable to standard reaction mixtures (Figure 9.6).

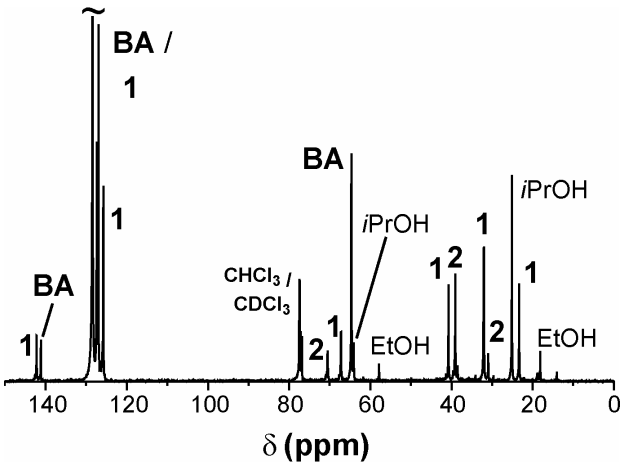

Figure 9.6. $^{13}C\{^{1}H\}$ NMR spectrum of the reaction solutions obtained from solvothermal reaction of $Ti(OiPr)_4$ and NaOEt in benzyl alcohol in the presence of TEMPO.

In principle, also aldol-coupling processes are conceivable pathways leading to C–C bond formation and hence the observed coupling products. The direct α-alkylation of ketones with primary alcohols has recently been suggested for ruthenium and iridium-catalyzed systems[9,10] An alcohol is reacted with a ketone, and the α-alkylated ketone and its reduction product, a secondary alcohol, are the products.[10] This step would however imply a very complicated cascade of reactions, as *all* the reaction products would have to be oxidized first, which would mean the necessity for simultaneous reduction, probably of benzyl alcohol to toluene, and later the reduction of a β-unsaturated ketone to the alcohol. Also, these reported catalyzed coupling reactions only worked if the ketone form was initially used for at least one of the reactants, and they never resulted in more than 25 % yield in alcohol.[10] Therefore, it can be ruled out that aldol processes cause the formation of the observed coupling products during solvothermal treatment in benzylic alcohols.

9.3 Conclusions

The C–C coupling mechanism discovered to lead to the synthesis of various metal oxides indeed most probably proceeds via deprotonation of an isopropoxide ligand, followed by a nucleophilic attack of the benzylic carbon. Radical mechanisms as well as aldol coupling steps can be excluded, and an elimination–addition mechanism is highly improbable.

Moreover, the coupling reaction was explored when changing both the alkali/alkaline earth precursor and the titania precursor. In fact, the coupling was found to take place to an equal

extent when using strong organic bases such as NaOEt or KO*t*Bu instead of the metal, but not in the absence of alkaline species. Titanium *tert*-butoxide did not undergo the coupling reaction, probably due to steric hindrance, but both unbranched longer alkoxides, such as Ti(O*n*Bu), and secondary alkoxides such as titanium tetra-4-heptoxide.

Basically, the reaction presented here has no direct equivalent in organic chemistry. The direct coupling of two alcohols may provide an interesting and economically advantageous new pathway to organic products, especially with respect to the observed high yields of the coupling products, with strong side reactions being absent in most systems, and the found selectivity for the β-carbon position, also when using higher aliphatic alkoxides.

9.4 Experimental Section

9.4.1 Synthesis

Titanium tetra-3-pentoxide and titanium tetra-4-heptoxide were prepared by stirring $Ti(O\textit{i}Pr)_4$ with dry 3-pentanol or 4-heptanol (molar ratio of 1 : 10) in a glovebox overnight. The resulting *i*PrOH as well as the surplus of the respective higher alcohol were then removed by distillation in vacuo. NMR analysis indicated that neither *i*PrOH nor isopropoxide ligands were present in both cases. Therefore, the obtained clear solutions were transferred into the glovebox and added to barium previously dissolved in benzyl alcohol (molar ratio 1 Ba : 1 titanium alkoxide : 20 benzyl alcohol). After mixing, solvothermal treatment was carried out as usual (2 days, 200 °C). Experiments involving organic bases, such as NaOEt, were carried out by first dissolving the base in benzyl alcohol, resulting in clear but colored solutions (eg., amber when using NaOEt). The titanium alkoxide was added next, and the mixture was transferred into an autoclave after stirring shortly. The experiments in 1-phenylethanol and 2-phenylethanol were also performed in a glovebox. The solvents used as received in anhydrous quality by Aldrich, Inc., but were thoroughly degassed by bubbling with Ar and then transferred into the glovebox. In both solvents, the Ba did not dissolve unless the mixture was heated to 100 °C, resulting in clear but viscous solutions. After addition of $Ti(O\textit{i}Pr)_4$, the mixtures were transferred into autoclaves and treated as usual (200 °C, 2-3 d).

Unless noted otherwise, milky suspensions were obtained in all cases. The inorganic particles were removed by centrifugation and additionally filtration before analyzing the reaction solution. Analysis of the particles was performed after washing 2 × with EtOH and drying in vacuo.

9.4.2 NMR data

All samples were measured in $CDCl_3$. Only the relevant main reaction products are given. Most aromatic signals of benzyl derivatives are completely superimposed by the large aromatic solvent peaks and are therefore not stated. The identity of aliphatic signals in more complex systems was clarified by additional APT measurements.

a. pure Ti(O*i*Pr)$_4$ – Benzyl Alcohol System (no base)
Benzyl ether: δ [ppm]: 138.2 (Ph_{ipso}), 72.0 (CH_2).
Diisopropyl ether: 70.0 (CH), 22.1 (CH_3).
Benzyl isopropyl ether: 71.0 (CH), other peaks superimposed by the other ethers and *i*PrOH.

b. NaOEt – Ti(O*i*Pr)$_4$ – Benzyl Alcohol System
4-Phenyl-2-butanol: 142.2 (Ph_{ipso}), 125.7 (Ph_{para}), 67.1 (C2), 40.7 (C3), 32.0 (C4), 23.3 (C1).
1,5-Diphenyl-3-pentanol: 142.2 (Phipso), 70.4 (C3), 39.1 (C2/4), 32.0 (C1/5).

c. NaOEt – Ti(OEt)$_4$ – Benzyl Alcohol System
3-Phenylpropanol: 142.0 (Phipso), 125.6 (Phpara), 61.5 (C1), 33.9 (C3), 31.8 (C2).
Diethyl ether: 66.0 (CH_2), 15.1 (CH_3).
Benzyl ether: 138.0 (Ph_{ipso}), 72.0 (CH_2).

d. KO*t*Bu – Ti(O*t*Bu)$_4$ – Benzyl Alcohol System
tert-Butanol: 69.1 (C_q), 31.0 (CH_3).
Benzyl ether: 138.3 (Ph_{ipso}), 72.0 (CH_2).

e. NaOEt – Ti(O*n*Pr)$_4$ – Benzyl Alcohol System
3-Phenylpropanol: 142.0 (Ph_{ipso}), 125.7 (Ph_{para}), 61.8 (C1), 34.0 (C3), 32.0 (C2).
3-Phenyl-2-methyl-1-propanol: Ph_{ipso}, Ph_{para} superimposed, 65.8 (C1), 39.0 (C3), 37.7 (C2), 16.6 (CH_3).

f. Barium – Ti(O*n*Bu)$_4$ – Benzyl Alcohol System
2-Benzylbutanol: 142.2 (Ph_{ipso}), 125.8 (Ph_{para}), 64.1 (C1), 43.9 (C2), 37.1 (C_{Benzyl}), 23.1 (C3), 11.2 (C4).

g. Ba – Ti(O*i*Pr)$_4$ – 1-Phenylethanol System
1-Phenylethanol (α-methylbenzyl alcohol): 145.8 (Ph_{ipso}), 128.0 (Ph_{meta}), 126.9 (Ph_{para}), 125.2 (Ph_{ortho}), 69.7 (C1), 24.9 (C2).
Bis(α-methylbenzyl) ether: 144.5 (Ph_{ipso}), 72.4 (CH_2), 22.7/22.8 (CH_3).
4-Phenyl-2-propanol: 145.1 (Phipso), 65.6 (C2), 48.1/47.5 (C3), 36.3/36.1 (C4), 24.4 (C1), 22.0 (C5).

h. Ba – Ti(O*i*Pr)$_4$ – 2-Phenylethanol System
2-Phenylethanol: 138.5 (Ph_{ipso}), 128.8 (Ph_{ortho}), 128.3 (Ph_{meta}), 126.1 (Ph_{para}), 63.3 (C1), 39.0 (C2).
Diisopropyl ether: 70.0 (CH_2), 21.8 (CH_3).
Styrene: 137.4 (Ph_{ipso}), 136.7 (CH), other aromatic signals superimposed, 113.6 (CH_2).

i. Barium – Ti(O–3-pentyl)$_4$ – Benzyl Alcohol System

3-Pentanol: 74.4 (C3), 29.3 (C2), 9.7 (C1).
1-Phenyl-2-methyl-3-pentanol: 141.1 (Ph_{ipso}), 125.6 (Ph_{para}), 74.4 (C3), 39.7 (C2), 38.3 (C1), 27.2 (C4), 12.9 (CH_3), 10.1 (C5).
1,5-Diphenyl-2,4-dimethyl-3-pentanol: 141.1 (Ph_{ipso}), 125.6 (Ph_{para}), 79.2 (C3), 40.4 (C1/5), 39.8 (C2/4), 15.1 (CH_3).

j. Barium – Ti(O–4-heptyl)$_4$ – Benzyl Alcohol System
4-Heptanol: 71.3 (C4), 39.5 (C3), 19.4 (C2), 14.1 (C1).
3-Benzyl-4-heptanol: 141.6 (Ph_{ipso}), 125.7 (Ph_{para}), 72.1 (C4), 47.2 (C3), 36.1 (C5), 35.2 (C_{Benzyl}), 22.1 (C2), 19.4 (C6), 14.4 (superimposed, C7), 12.1 (C1).

k. NaOEt – Ti(O–*i*Pr)$_4$ – Benzyl Alcohol – TEMPO System
4-Phenyl-2-butanol: 142.2 (Ph_{ipso}), 125.8 (Ph_{para}), 67.2 (C2), 40.7 (C3), 32.1 (C4), 23.3 (C1).
1,5-Diphenyl-3-pentanol: 142.2 (Phipso), 70.5 (C3), 39.1 (C2/4), 32.1 (C1/5).

9.5 References

[1] A. Vioux, *Chem. Mater.* **1997**, *9*, 2292.

[2] C. S. Kim, B. K. Moon, J.-H. Park, S. T. Chung, S.-M. Son, *J. Cryst. Growth* **2003**, *254*, 405.

[3] N. Pinna, G. Garnweitner, M. Antonietti, M. Niederberger, *Adv. Mater.* **2004**, *16*, 2196.

[4] M. Iwasaki, A. Yasumori, S. Shibata, M. Yamane, *J. Sol-Gel Sci. Technol.* **1994**, *2*, 387.

[5] M. Jansen, E. Guenther, *Chem. Mater.* **1995**, *7*, 2110.

[6] A. R. Katritzky, M. Balasubramanian, *Energy Fuels* **1990**, *4*, 499.

[7] Z. Dawoodi, M. L. H. Green, V. S. B. Mtetwa, K. Prout, *J. Chem. Soc. Chem. Commun.* **1982**, 802.

[8] H. G. O. Becker, *Organikum*, J. A. Barth Verlag, Heidelberg, **1996**.

[9] C. S. Cho, B. T. Kim, H.-S. Kim, T.-J. Kim, S. C. Shim, *Organometallics* **2003**, *22*, 3608.

[10] K. Taguchi, H. Nakagawa, T. Hirabayashi, S. Sakaguchi, Y. Ishii, *J. Am. Chem. Soc.* **2004**, *126*, 72.

10 Surface Functionalization of TiO_2 Nanoparticles

10.1 Introduction

One ambitious goal of nanotechnology is the controlled arrangement of individual nanoparticles, or nanobuilding blocks, into hierarchically ordered superstructures.[1] This can be achieved through self-assembly, which is one of the few practical strategies for making ensembles of nanostructures.[2] The driving forces leading to self-assembly are abounding, on the molecular scale including, among others, van-der-Waals interactions and electrostatic forces.[3,4] Because of its simplicity and versatility, self-assembly is expected to play a major role in nanotechnology in the future.[5]

The proper design of the individual components that organize themselves into desired patterns and functions is the key to applications of self-assembly.[6] In most cases, self-assembly requires that the building units are mobile, and therefore takes place in fluid phases or on smooth surfaces. Adequate tailoring of the surface properties of the building blocks is undoubtedly the key parameter for an optimized assembly behavior. Especially for small building blocks, such as nanoparticles only a few nanometers in size, the surface properties tend to predominate over those of the bulk,[7] and thus determine their suitability towards self-assembly.[8]

The surface of inorganic nanoparticles can be conveniently altered by the grafting of functional organic ligands. This is achieved via the attachment of reactive organic groups through strong covalent or ionic interactions. Whilst for metal particles, eg., a gold surface, the covalent, selective and stable attachment of ligands is achieved using thiol functions, for oxidic surfaces no such general yet selective route has been established, however substantial research activities have been carried out employing ligands such as alkane thiols, alcohols, amines, and phosphonic and sulfonic acids.[9]

There are two general surface modification methods, either grafting the organic groups to a preformed nanoparticle (*post synthesis* modification) or introducing the organic ligands during the nanoparticle synthesis (*in situ* approach).[10] The advantage of in situ functionalization lies in the self-limiting organization process of the inorganic and organic building blocks, where on the one hand the organic ligand controls the growth of the nanoparticle, and on the other hand also the attachment of the organic ligand on the nanoparticle surface is governed by the chemical reactions that result in the formation of the nanoparticles.[10] Surface modification is easiest accomplished in solution.[11-14]

As a first step, investigations were carried out using functional organic ligands to probe their binding ability and stability to the TiO_2 nanoparticles. Both in situ and post-synthesis modification steps were employed in order to tailor the surface properties of the TiO_2 nanoparticles. Four ligands were investigated which appeared to be suitable. Enediol systems (referred to as catechols) such as ascorbic acid, catechol, dopamine and alizarin seem most appropriate to form stable conjugates. The are long known to strongly bind to transition metal ions,[15] and have also been reported to bind to transition metal oxide surfaces via covalent linkage.[16-18] By using substituted catechols, specific functions can be attached to the surface, such as amine/ammonium functions, in the case of dopamine, or hydrophobic groups, as for 4-*tert*-butyl catechol (TBC). These were both used to explore the properties of the particles after surface modification with such different functionalities. Other ligands such as carboxylic acids bind much less strongly to a titania surface and, under certain conditions, can be leached by nucleophilic attack of the solvent.[19] Thus, two other possible ligands, glycine and serinol, are investigated for comparison. Figure 10.1 shows the chemical structure of all used ligands.

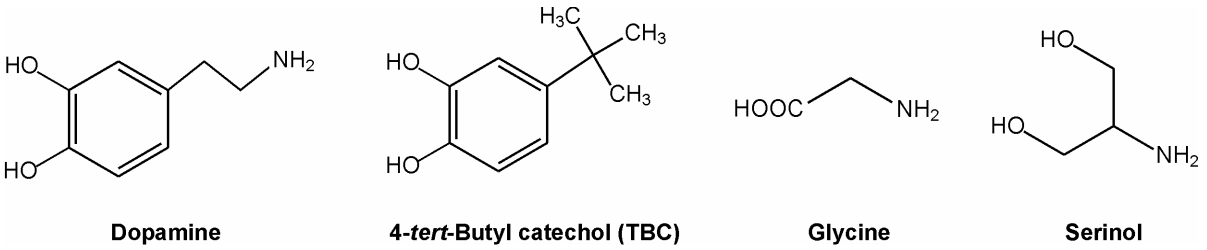

Figure 10.1. Chemical structure of the investigated ligands.

The second part of this chapter is focused on surface modification with more sophisticated ligands. Using the knowledge gained by investigating the binding behavior of the four abovementioned ligands, biofunctionalization of the particles is targeted with the aim of inducing controlled self-assembly by binding short functional oligopeptides on the anatase nanoparticles. Such an approach has been reported to lead to complex structures with protein-like properties.[20]

In the last years, substantial research on biofunctionalization of gold nanoparticles has been performed, involving capping with oligonucleotides and grafting of helical peptides to the nanoparticles.[21-23] Conjugates of gold particles and functional proteins have shown to be a versatile and powerful tool to achieve controlled particle assembly, especially using biotin–avidin coupling.[24-27] Belt-and-braces-like systems have been presented, featuring isolated oligopeptide-capped particles which aggregate upon addition of a functional peptide strand, the “belt”.[28] This system has even shown to be reversible.[29]

There are, however, much less reports on the biological functionalization of nano-sized oxides. Peptide bonds could be formed in a controlled fashion onto polyoxotungstates equipped with an alkyltin group,[30] and onto alumina surfaces by means of a siloxane linker.[31] Several strategies have been suggested to bind biological functions onto titanium oxide surfaces. Silanization of titanium surfaces was reported using aminoalkylsilanes, which covalently bind to the oxide layer, the free terminal amine then being accessible to biological molecules.[32,33] On the other hand, also catechol groups form covalent bonds to titanium centers on TiO_2 surfaces, as mentioned above. Hence, acting as coupling agents they open up a promising pathway for linking organic or biological molecules to oxidic nanoparticles.[34] The formation of TiO_2-oligonucleotide nanocomposites[35] and TiO_2-biotin conjugates[36] using this pathway have been reported. Therefore, catecholic binding seems the most suitable way to obtain covalent attachment of peptides and proteins to oxidic nanoparticles.

10.2 Modification with Functional Organic Groups

10.2.1 In Situ Functionalization

The titania nanoparticles were synthesized following a convenient nonaqueous method reported recently.[37,38] Titanium tetrachloride is added dropwise to benzyl alcohol and aged for 3 days at temperatures below 100 °C, leading to a white suspension. The product, anatase nanoparticles about 4-8 nm in size, is retrieved by centrifugation, followed by washing and drying. In situ modification of the titania particle surface was achieved simply by dissolving/dispersing the respective ligand in benzyl alcohol prior to addition of $TiCl_4$. The mixtures were aged at room temperature for about 2 hours and then at 70-80 °C for 3 days. Dark red reaction mixtures were obtained for catecholic ligands, whereas the Gly and serinol systems were white. The products were retrieved by centrifugation, washing with chloroform or methylene chloride, and drying.

For all four tested ligands, resoluble precipitates were obtained. Depending on the nature and concentration of the used ligand, the as-synthesized titania particles were soluble either in water or in organic solvents such as THF, DMF, and DMSO. Figure 10.2 shows dopamine- and glycine-functionalized particles and their solutions in distilled water. The dried powders of dopamine- (Fig. 10.2 **a**) and Gly-functionalized (Fig. 10.2 **c**) titania can be redissolved in water, which results in a red, completely transparent solution for dopamine (Fig. 10.2 **b**), and

a white, only slightly turbid solution in the case of glycine (Fig. 10.2 **d**). The deep red color of the solution of dopamine-capped particles stems from the ligand-to-metal charge transfer interaction between the ligand and surface metal atoms, and is found for all catecholic systems.[16,18] Additionally, the dopamine ligands have positively charged terminal ammonium groups resulting in particle-particle repulsion, which leads to a stable aqueous colloidal solution.[16] The particles functionalized with glycine are obviously also well stabilized but slightly more aggregated. Amino acids have been suggested to bind to TiO_2 predominantly via the carboxylic acid function.[39] Therefore, we assume that also for Gly and serinol, protonated amine groups cause particle-particle repulsion and thus stabilization in water, however less efficiently than for dopamine. Serinol-covered particles showed similar behavior as the glycine system, forming a stable dispersion in water which however is also slightly turbid. The still wet and freshly prepared TBC-functionalized sample could be directly redissolved in THF, DMSO and DMF after removal of benzyl alcohol to result in red transparent solutions. The washed and dried powder, however, was less soluble, which is attributed to the fact of enhanced particle-particle interaction, as surface charges are eliminated by surface functionalization with uncharged catechols.[16]

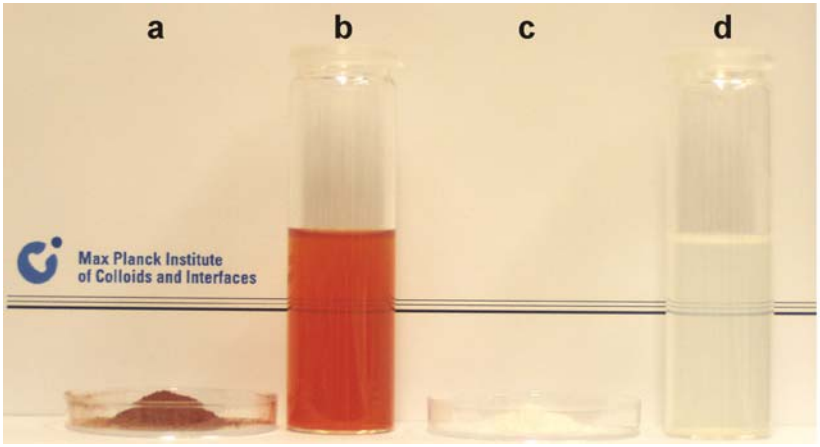

Figure 10.2. Photograph of dopamine-functionalized TiO_2 particles (**a**) and of glycine-capped partices (**c**), and their respective solutions in water (**b**, **d**).

The solubility properties and the crystallinity of the functionalized nanoparticles are mainly determined by two reaction parameters, namely by the titanium chloride-to-ligand ratio and by the reaction temperature. Well crystalline and water soluble titania nanoparticles were obtained with a molar Ti-to-dopamine ratio ranging from 12 to 16 at a reaction temperature of 80 °C. Higher amounts of dopamine, i.e., Ti-to-dopamine ratios smaller than 10, decreased the crystallinity of the nanoparticles considerably. For glycine and serinol, the molar Ti-to-ligand ratio could be decreased to 1.5 without observing a significant decrease in crystallinity. This is attributed to the smaller size of the ligands and their lower binding strength to titanium (see below). Even when using large amounts of Gly or serinol, though, no completely transparent

solutions were obtained, indicating that the particles were still present in some aggregated fashion. In the case of TBC, the amount of ligand had to be higher than for dopamine to provide good solubility. The initial molar Ti-to-TBC ratio was varied from 5 to 20. The best solubility in THF along with good crystallinity was obtained for ratios of 9 to 10 at a reaction temperature of 70 °C. At higher ratios, the particles also exhibited poor crystallinity. As crystallinity and solubility depend on the amount of ligand in an inverse fashion, an optimum had to be elaborated to ensure high crystallinity and solubility.

The XRD data of dopamine-functionalized TiO_2 particles obtained after reaction at 80 °C for 3 d, employing a Ti-to-dopamine ratio of 16 is shown in Figure 10.3, **a**. Very similar patterns were found for TBC-capped particles (**b**, obtained after reaction at 70 °C with a Ti-to-ligand ratio of 10) and serinol (**c**, 80 °C, Ti : serinol = 6) and glycine (**d**, 80 °C, Ti : Gly = 3) capped particles. All reflections can be assigned to anatase without any indication of other crystalline byproducts, except for the TBC system, where a small shoulder is visible on the higher angle side of the anatase (101) peak at $2\theta = 25.3°$, which may be assigned to a small amount of either amorphous intermediates or brookite[40] present in the sample. It is noteworthy that the particles exhibit such a good crystallinity despite the low reaction temperatures of 70-80 °C and the presence of the ligand. The mean crystallite size was determined for each system from the integral width of the (101) reflection using Scherrer's equation. For all systems, quite similar crystallite sizes were determined: for the dopamine system about 5.5 nm, for the TBC system 6.0 nm, whereas the serinol- and Gly-capped particles had slightly smaller crystallites being 4.2 nm and 5.3 nm in size, respectively.

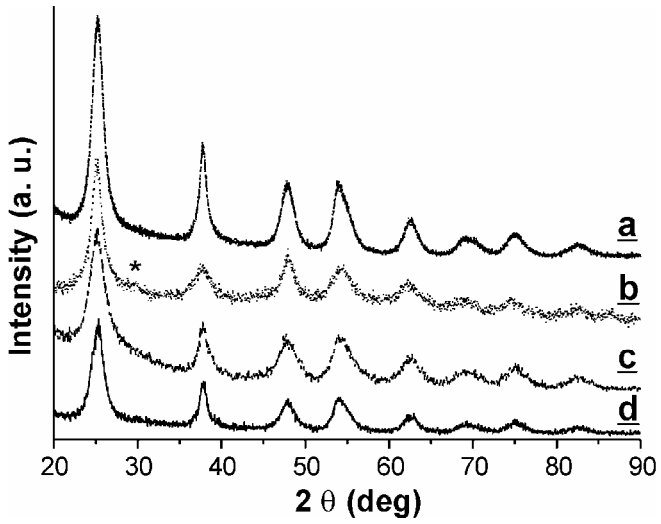

Figure 10.3. XRD patterns of the obtained titania particles functionalized with dopamine (**a**, short-dashed line), TBC (**b**, dotted line), serinol (**c**, dashed line), and glycine (**d**, solid line).

Figure 10.4 presents representative TEM images of functionalized titania nanoparticles. An overview image of the dopamine-capped particles (Fig. 10.4 **A**) at low magnification

illustrates that the sample entirely consists of nanosized titania particles arranged to a disordered thin film on the TEM grid, without the presence of larger particles or agglomerates. Crystallinity and phase are confirmed by electron diffraction analysis, revealing diffraction rings typical for anatase (Fig. 10.4 **A**, inset). HRTEM images of the same sample (Fig. 10.4 **B**, and **B** inset) shows sets of lattice fringes, giving additional evidence that the particles are highly crystalline. It can be stated that the particles are quite uniform in size and shape, although it is rather difficult to see distinct boundaries. Based on these images, the particle size can be estimated to about 5 nm, which is in good agreement with the data obtained from XRD peak broadening and from AUC (see below). Size and crystallinity of the titania particles functionalized with the other ligands are similar (Fig. 10.4 **C** shows TBC-capped particles as example).

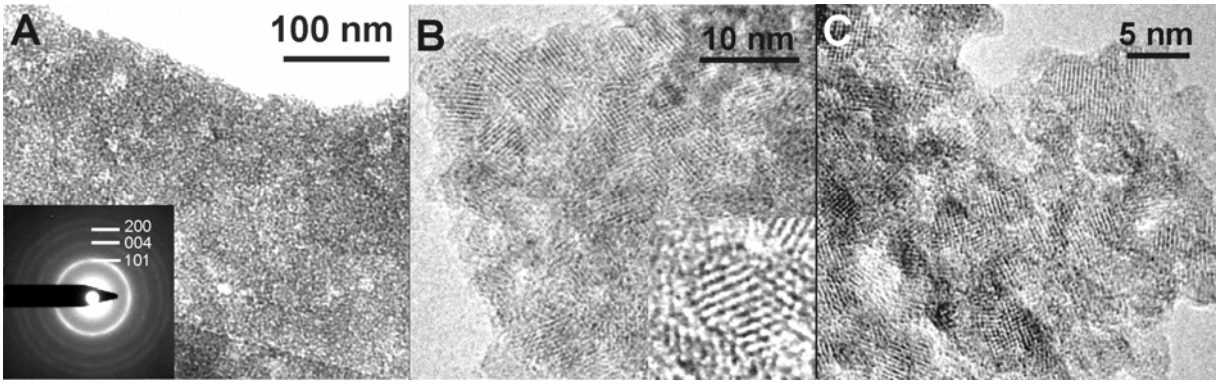

Figure 10.4. TEM pictures of dopamine-capped titania particles (**A**) and their electron diffraction pattern (**A**, inset) and high-resolution images (**B**); TBC-capped TiO_2 particles (**C**).

10.2.2 Investigations on the Nature and Stability of Ligand Binding

It is possible to estimate the surface coverage of the titania nanoparticles. Rajh et al.[39] reported that the formal molar concentration of the titania surface sites can be calculated according to

$$[Ti_{surf}] = [TiO_2] \cdot 12.5 / d \,, \qquad \text{(Eq. 10.1)}$$

$[TiO_2]$ being the molar concentration and d the diameter of the particles in Angström. With a mean particle diameter of 55 Å (see below), the mean fraction of surface TiO_2 is approximately 23 %, averaged over all crystal faces of the particles. Since the applied Ti-to-dopamine ratio is only 16, and assuming that all the $TiCl_4$ is transformed into TiO_2 and all the dopamine molecules are linked to titania nanoparticles, the coverage of the particles with dopamine is only about 27 %. Nevertheless, this is enough to provide good solubility of the particles in water. For glycine and serinol, much higher Ti-to-ligand ratios can be used,

leading to coverage in theory up to 100%. The resulting solubility in water, however, is not higher than for dopamine.

TGA measurements of dopamine- and Gly-modified TiO_2 nanoparticles are presented in Figure 10.5. The solid line represents the weight loss of Gly-capped particles (Ti-to-Gly ratio of 3) in the as-prepared state after overnight drying *in vacuo* at 100 °C (**a**). The other lines stem from dopamine-functionalized samples (Ti-to-dopamine ratio of 12) prepared at 80 °C, measured after thorough drying (**b**, dashed line) and after standing in air for a few days (**c**, dotted line). For all samples, a considerable weight loss of approx. 22-27 % is visible in the range from room temperature to about 500 °C. For the dopamine system, the weight decrease is a two-step process. The first step below 300 °C is due to the loss of adsorbed water and the residues of the organic solvent or washing medium.[41] Above 300 °C, the additional weight loss of about 13 % corresponds to the degradation of the dopamine ligand and the removal of –OH groups.[42,43] Considering the starting concentrations of $TiCl_4$ and dopamine and assuming that all the $TiCl_4$ is transformed to TiO_2 and all the dopamine is adsorbed on the surface of the nanoparticles, the theoretical value of dopamine attached to the nanoparticles is about 16 wt %. This is only slightly more than observed in the TGA, which means that almost all of the dopamine adsorbs on the particle surface during the synthesis procedure. Glycine, on the other hand, starts to decompose already at lower temperatures of 250 °C. Therefore, it is harder to evaluate the amount of bound Gly due to superposition with water/solvent desorption. Assuming similar amounts of water/solvent present as in the dopamine system, the Gly content can be estimated to about 14 wt %. Compared to the theoretical value of Gly attached to the particles of 23.9 wt %, this means that only 2/3 of the ligand present remains bound to the particles throughout the washing processes. This gives a strong indication that dopamine binds to the particles in a much more stable fashion than Gly.

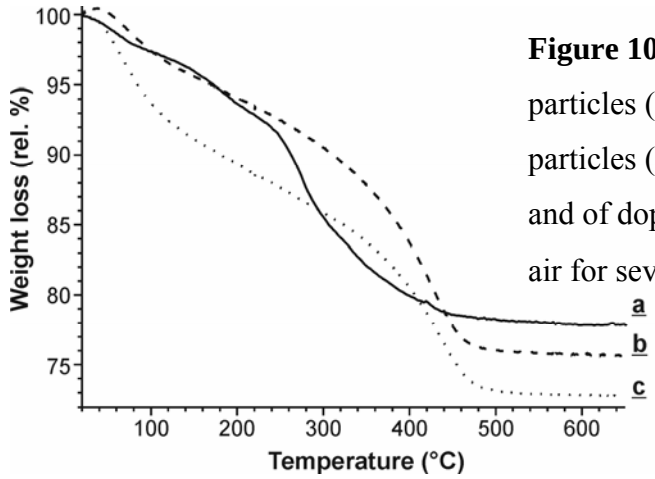

Figure 10.5. TGA plots of glycine-capped TiO_2 particles (solid line, **a**) and dopamine-capped particles (dashed line **b**), both after thorough drying, and of dopamine-capped particles after standing in air for several days (dotted line, **c**).

It was further found that especially the dopamine-functionalized particles are rather hygroscopic. Particles that were stored in air for several days (Fig. 10.5, dotted line **c**) show a weight loss of more than 12 % upon heating to 100 °C compared to a weight loss of 7 % of the dried product in the same temperature range (Fig. 10.5, dashed line **b**) due to additional desorption of water. The BET surface area increases with increasing Ti-to-ligand ratio, amounting to 122 m^2/g for dopamine-capped nanoparticles (Ti-to-dopamine ratio of 16), 210 m^2/g for TBC-functionalized nanoparticles (Ti-to-ligand ratio of 10), 240 m^2/g for serinol-capped particles (Ti-to-serinol of 6) and to 270 m^2/g for Gly-functionalized particles (at a Ti-to-Gly ratio of 3).

The binding properties of the ligand was investigated for all systems by NMR measurements of the functionalized particles in solution. Prior to most of these measurements, the concentration of surface-bound ligand was increased by a post-functionalization treatment. Post-functionalization allows increasing or altering the surface of nanoparticles simply by stirring in solution,[11,41,44] without any change in the crystallinity of the particles. The amount of ligand can hence be further increased easily, however, one must be careful to obtain indeed the targeted functionalization, as many species have the ability to bind to titania. For example, serinol-capped particles which were washed in EtOH several times to remove excess ligand featured almost no serinol after the washing but significant quantities of EtOH bound to the surface. Even more astonishing, serinol-particles that were dried in an oven (at 70 °C) where an atmosphere enriched in *n*-propanol was present, showed stronger *n*-propanol than serinol peaks in the subsequent NMR measurement (data not shown).

Alcohols, amines, mercaptanes and ethers are generally nucleophilic and thus possess the ability to bind to titania.[45] Therefore, they are not eligible to serve as the inert continuous medium for introducing additional functionalization onto the particles. In practice, chloroform and DCM have proven as suitable solvents for post-functionalization treatments, as they do not bind to the particles and can easily be removed in vacuo.

^1H NMR results obtained for dopamine particles are shown in Figure 10.6. The measurement of particles obtained directly after the synthesis (Ti-to-dopamine ratio of 12, 80 °C) proved difficult because of a low amount of organic material present in the sample, which resulted in very small, broad peaks, compared to the solvent signal. Useful spectra were only obtained when measuring in D_2O, ruling out the possibility to detect any hydroxyl or ammonium protons due to solvent exchange interactions. They however clearly suggested that substantial amounts of benzyl alcohol were present on the particle surface (data not shown).

Therefore, a post-functionalization treatment was performed by stirring the particles in an 0.1 M dopamine suspension in $CHCl_3$. The resulting powder was soluble enough in DMF (but not in $CHCl_3$) to obtain an acceptable spectrum. The obtained data (Fig. 10.6 **B**) is compared to pure dopamine hydrochloride (Fig. 10.6 **A**, also in DMF-d^7). It is clearly visible that after the post-functionalization, large amounts of dopamine are bound to the particles. No significant impurities are found on the particles other than adsorbed water which causes the large peak at 3.7 ppm. What is most interesting, the combined peak of –OH and $–NH_3^+$ functions of pure dopamine has vanished from its original position. It is assumed that the ammonium proton signal is now found at 8.6 ppm, only slightly shifted from its original position. The –OH signals, however, seem to be mostly disappeared, as the small signal at 9.1 ppm has an intensity of only about 1.2, compared to 2.0 in theory for the dopamine –OH groups. This is a good indication that dopamine is bound to the surface via the catechol functions, possibly in the deprotonated form, although the low intensity of the –OH signals might also be caused by the low mobility of the –OH groups when bound to the titania surface, resulting in slow relaxation and hence a decrease in signal intensity. Elemental analysis was performed both with as-prepared and post-functionalized dopamine-TiO_2 powders. Assuming no organic species present on the particles other than benzyl alcohol and dopamine, the content in these species can be calculated from the carbon-to-nitrogen ratio, as only dopamine contains nitrogen. After post-functionalization, a dopamine content of up to 40 wt % was obtained, whereas only 0.3 wt % benzyl alcohol are left. As-prepared samples were investigated after washing 3 × in $CHCl_3$ and drying under vacuum at room temperature. They contained, in average, about 8 wt % dopamine and 3.5 wt % benzyl alcohol, and significant moisture, amounting to up to 10 wt %. This proves a successful post-functionalization treatment, during which adsorbed benzyl alcohol is exchanged with dopamine.

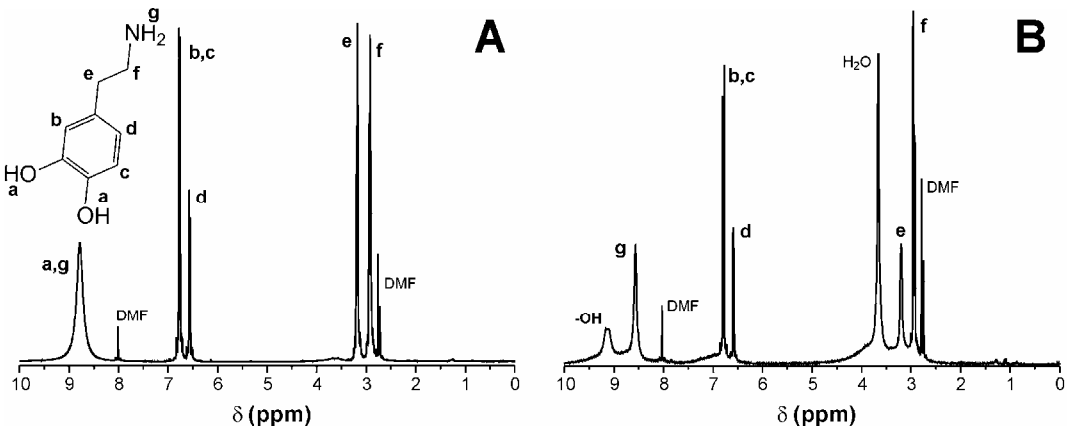

Figure 10.6. ^1H NMR spectrum of **A**: pure dopamine hydrochloride in DMF-d^7, **B**: dopamine-capped TiO_2 particles in DMF-d^7 after post-functionalization with dopamine.

TBC-functionalized particles are well soluble in DMF and therefore appear more suitable to study the binding manner of the ligand. The concentration of TBC was also increased by post-functionalization treatment in $CHCl_3$. This procedure had several effects. In addition to a higher intensity of the TBC signals in the NMR spectrum, which has also been observed for the dopamine system discussed above, the solubility of the titania particles in DMF and in chloroform itself was increased. Whilst stirring the particles in a solution of higher concentration (0.1 M TBC in chloroform) led to a homogeneous liquid, not even being separable by centrifugation, the use of lower concentrations (0.04 M) yielded a cloudy dispersion. The centrifuged precipitate, however, was well soluble in DMF. Figure 10.7 **A** shows a ^{1}H-NMR spectrum of TBC-functionalized titania nanoparticles obtained from the higher concentrated solution. After the evaporation of chloroform, the presence of titania nanoparticles functionalized with TBC as well as of the unreacted ligand can be expected. The precipitate was dissolved in DMF-d^7. This spectrum is compared with ^{1}H-NMR spectra obtained from measurements of the single components TBC and benzyl alcohol in DMF-d^7 (data not shown). Pure TBC gives rise to three signals at 1.4 ppm (*tert*-butyl group), 6.9-7.1 ppm (aromatic group) and 8.9 ppm (–OH groups). In contrast to the spectrum of TBC in $CDCl_3$, there is only one –OH peak visible when measuring in DMF-d^7. The integral ratio of the peaks is 9.0 : 3.0 : 2.0.

These signals are also present in the spectrum of the above described system containing functionalized nanoparticles as well as the unreacted ligand (the *tert*-butyl group and the C_6H_3 group corresponding to peaks **a** and **b** in Fig. 10.7 **A**). A decrease in intensity of the –OH signals was expected from particle-bound TBC due to the binding of the hydroxyl groups to the titanium sites. Indeed the integral ratio in this spectrum is 10.0 : 3.0 : 1.2, indicating that almost half of the TBC present in the system is coordinated to the titania particles (the slight intensity increase of the aliphatic peak probably originates from impurities). The presence of a remaining –OH peak, however, proves that the free hydroxyl protons are in principle detected in the system; also, H_2O adsorbed onto the surface of the particles is visible as a broad peak centered around 4.0 ppm. Smaller benzyl alcohol signals appear at 7.5 ppm (C_6H_5 group, peak **c**) and 4.8 ppm (CH_2 group, peak **d**) giving evidence that still a considerable amount of benzyl alcohol is adsorbed on the surface of the functionalized nanoparticles. To prove the presence of the ligand on the titania, the nanoparticles were stirred in a less concentrated solution of the ligand in $CHCl_3$. The particles could then be separated and were washed thoroughly. The resulting NMR spectrum is shown in Fig. 10.7 **B**. The –OH peak is completely absent, however the aromatic signals of TBC are clearly visible. Some $CHCl_3$ from the washing is

still present. According to the integral ratios, the ratio of surface-adsorbed benzyl alcohol to TBC is approximately 0.25, indicating that the coordination of TBC onto titania nanoparticles is strongly preferred compared to the coordination of benzyl alcohol. Unfortunately, elemental analysis cannot be used to verify these results, as TBC does not contain any nitrogen and hence the elemental analysis data cannot be deconvoluted.

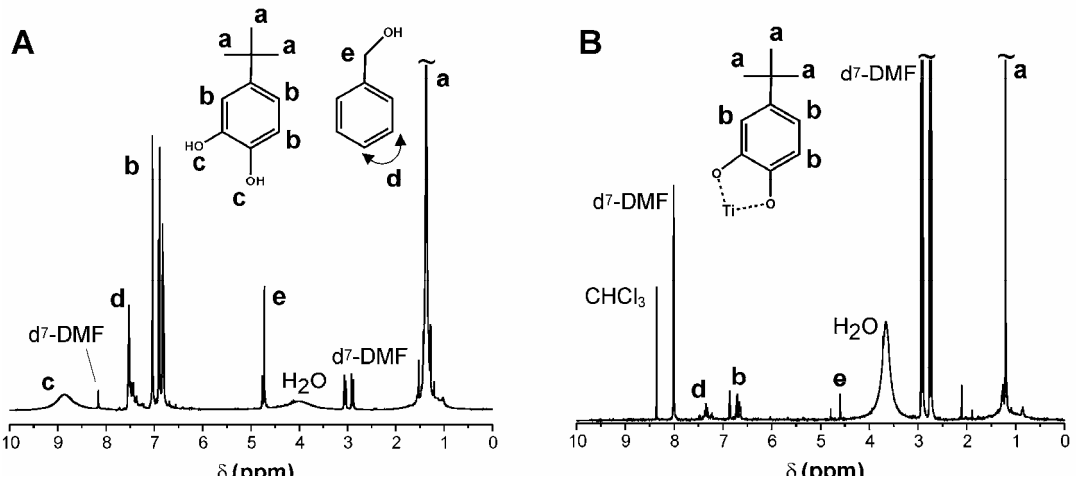

Figure 10.7. ^{1}H NMR spectrum of TBC-capped titania particles in DMF-d^7 after further post-functionalization with TBC, from a more concentrated solution (0.1 M), after simple solvent evaporation (**A**); and ^{1}H spectrum of TBC-capped particles after stirring in a less concentrated TBC-solution (0.04 M), after particle separation and washing (**B**).

In addition to TBC and benzyl alcohol, the titania nanoparticles also adsorbed water on the surface (broad peak at 3.9 ppm). However, by avoiding contact with air, the intensity of this peak can be diminished. It was found that upon further removal of benzyl alcohol, the concentration of adsorbed water increased considerably pointing to the hygroscopic character of the particles.

The ^{1}H and ^{13}C NMR spectra of serinol-capped particles are shown in Figure 10.8 **A** and **B** (both measurements were carried out in D_2O due to the low solubility of the particles in organic media). As the molar ratio for in situ functionalization can be greatly increased compared to dopamine and TBC, measurement of the particles is facilitated due to a much higher content in organic material. The particles were washed with hexane (2 ×) and DCM (3 ×) prior to the measurement. The spectra show a high amount of serinol present, and small amounts of benzyl alcohol (labeled BA) and hexane (hex). NMR spectra of particles further washed (DCM 3 ×) and dried (vacuum) showed only the serinol and H_2O peaks, proving that the surface of the particles can be purified via multiple washing and cleaning steps (data not

shown). Interestingly, the two serinol peaks were found at 58.6 and 54.1 ppm in all ^{13}C NMR spectra of the particles, whereas they appear at 62.3 and 54.1 ppm for pure serinol in solution. The C1 position (**a**) hence is shifted upfield by 3.7 ppm upon binding to TiO_2 whereas the C2 signal (**b**) remains unchanged. This suggests that serinol is bound to the titanium sites via the hydroxyl groups as reported in the literature.[39]

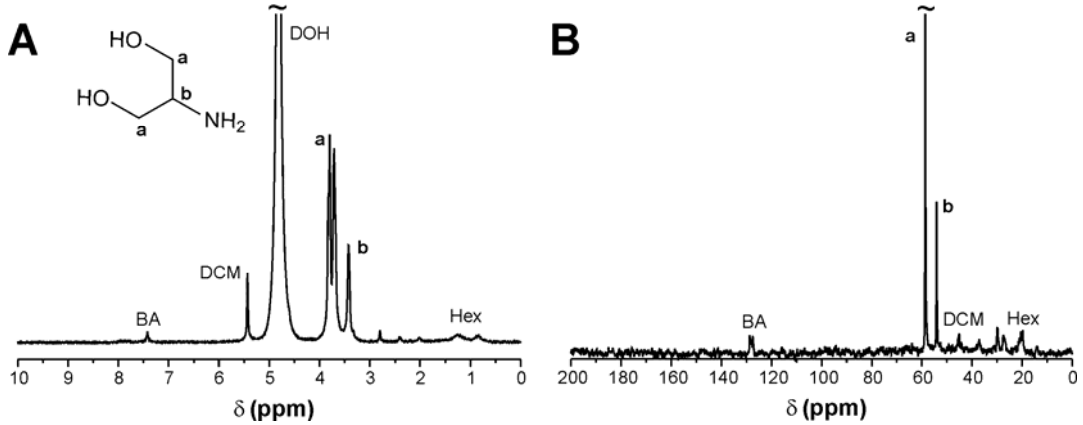

Figure 10.8. NMR spectra of serinol-capped TiO_2 particles in D_2O. **A**: ^1H spectrum after washing 3 × with hexane and 5 × DCM, **B**: ^{13}C $\{^1H\}$ NMR spectrum of a sample washed 3 × in hexane and 2 × in DCM.

10.2.3 Analytical Ultracentrifugation (AUC)

For many applications of nanoparticles, particle size distribution is a crucial parameter, but still its determination often remains a difficult task. Although TEM provides important information about the shape and size of individual nanoparticles, it can only give the data for a small subset, and there is no unambiguous statistics for particle size distribution of the whole sample. Analytical ultracentrifugation (AUC) has proven to be a versatile tool for the measurement of the particle size distribution of colloidal samples.[46] In contrast to TEM, AUC detects all particles even down to smallest sizes. The resolution of the particle size distribution for small nanoparticles lies in the Angström range.[46] Dopamine- and Gly-functionalized titania nanoparticles are a suitable model system for the particle size distribution measurement by AUC, because the particles exhibit good solubility in water, and low agglomeration tendency (at least in the dopamine system). Nanosized semiconductor titania furthermore shows a dependence of the bandgap on the particle size, which can be expected to be easily detected by the UV/Vis absorption optics of the centrifuge. The particle size distribution is calculated assuming a particle density of bulk anatase of 3.9 g cm^{-3}. This value is somewhat too high, since the ligands contribute considerably, but to an unkown extent, to the density of the functionalized particles. The results of AUC measurements of the TiO_2-dopamine system

are shown in Figure 10.9 **A**. The particle size distribution obtained ranges from about 3.5 nm to 8.0 nm, with a peak maximum at 5.5 nm. This proves that agglomeration of the particles in solution indeed is negligible. It has to be noted that this particle size distribution is widened by diffusive peak broadening which cannot be completely avoided during an AUC measurement. Therefore, the distribution is in reality even narrower than obtained here. The result is in accordance with the particle sizes obtained from TEM measurements, speaking for the fact that neglected density correction due to the ligands in AUC and the invisibility of the ligands in TEM are counterbalancing approximations. The obtained size distribution of Gly-capped particles is shown in Fig. 10.9 **B**. In contrast to the dopamine-fuctionalized particles, the distribution largely extents to higher particle diameter values up to 30 nm. The peak maximum, however, is below 10 nm, which indicates that the particles themselves possess comparable size as the dopamine-capped particles. The shoulder at higher particle size thus stems from particle aggregates – it is however visible that these aggregates are rather small, consisting of < 10 particles, which accounts for the good solublility of the sample in water.

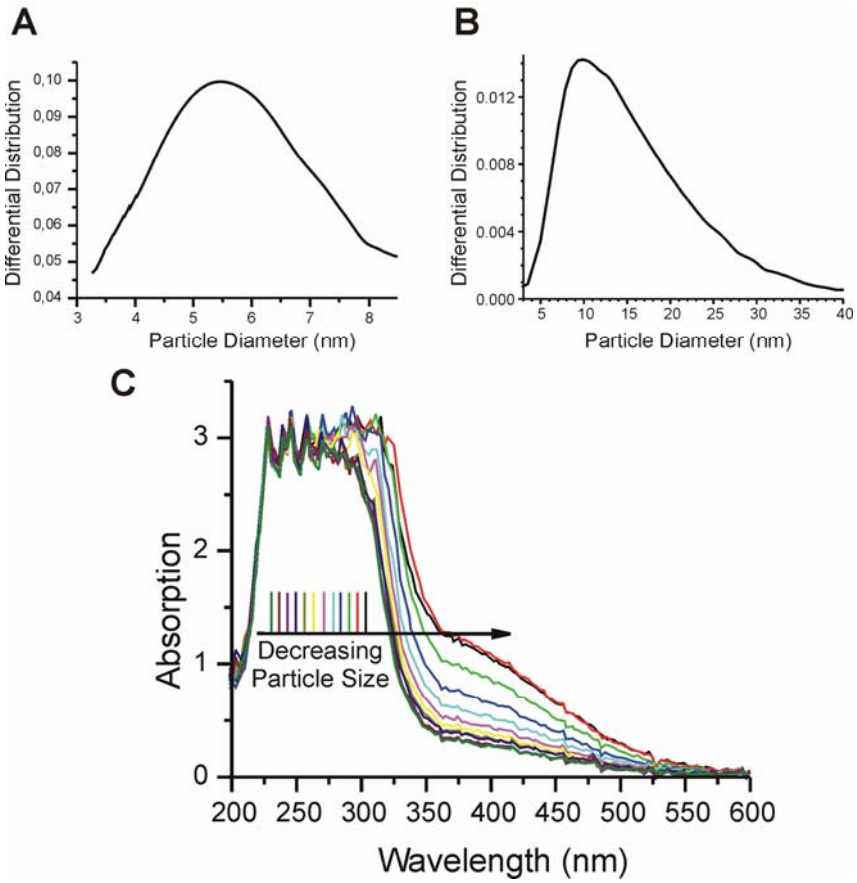

Figure 10.9. Results of the AUC measurements. Particle size distribution obtained for dopamine-capped TiO_2 particles (Ti : dopamine = 16, **A**), size distribution obtained for Gly-functionalized particles (Ti : Gly = 3, **B**). UV/Vis absorption spectra of dopamine-capped TiO_2 nanoparticles in dependence of the particle size fractions (**C**).

Nano-sized semiconductor titania particles with a diameter smaller than 3 nm show a dependence of the bandgap energy on the particle size due to the quantum size effect.[47,48] AUC equipped with a UV/Vis detector makes possible the measurement of the electronic absorption spectrum for each particle size fraction resulting in a direct measurement of the absorption threshold in dependence of the particle size (Fig. 10.9 **C**). Only dopamine-functionalized titania nanoparticles could be subjected to this measurement due to the partial aggregation in the Gly system. Interestingly, the nanoparticles show a red shift of the UV absorption band with decreasing particle size. This behavior is opposed to the quantum size effect induced by the electron and hole confinement, which shifts the band gap of nanosized semiconductors to higher energies with reduced size.[49] However, the measured red shift is in accordance to the results obtained by Rajh et al., where smaller dopamine-functionalized titania nanoparticles also showed a red shift upon changing the particle size from 15 to 4.5 nm.[16] The red shift of the absorption is in fact due to the surface complexation of the particles by enediol ligands. Light promotes electron transfer from the surface complexant to the conduction band of titania.[18] This effect is particularly pronounced in the present system, since the tail of the absorption band of dopamine-functionalized titania reaches far into the visible range with an onset at around 550 nm. It was reported that the red shift is proportional to the fraction of the surface Ti atoms and correlates with the number of surface sites in nanocrystalline titania.[16] For example, dopamine-functionalized titania nanoparticles with full surface coverage show a red shift compared to nanoparticles with a surface coverage of 70 %.[17] To conclude, it can be said that with decreasing particle size the number of surface atoms increases resulting in a red shift of the absorption band of the functionalized titania nanoparticles with decreasing particle size.

Although AUC generally allows the segregation of the sample into monodisperse fractions, it is not yet possible to assign every single absorption spectrum exclusively to a specific particle size. The reason for this problem lies in uncontrolled diffusion processes, concentration, and charge effects. However, to the best of our knowledge, this is the first time that it was possible to measure the UV/Vis spectra of semiconductor titania nanoparticles in dependence of the particle size by fractionation of a preformed powder. In contrast to measurements on growing particles, which usually exhibit a large polydispersity, the use of analytical ultracentrifugation allows the measurement of almost monodisperse particle fractions.

10.2.4 Conclusions

The functionalization experiments of anatase nanoparticles with organic ligands such as dopamine, TBC and Gly have shown that in situ functionalization is a facile means to obtain organically modified particles. Additionally, a post-synthesis treatment is possible, which allows a further increase of the amount of ligand bound to the particles and also introduce additional functionalities. In contrast to Gly and serinol, the ratio of Ti-to-dopamine or TBC for in situ functionalization must be relatively high, meaning that only a fraction of surface sites is covered with the ligand, to maintain high crystallinity of the particles. However, this low amount is sufficient to drastically improve the solubility in various solvents.

The functionalized particles were subjected to TGA and NMR measurements to gain further information about the binding of the ligand to the particles. TGA measurements revealed that practically all dopamine is consumed during in situ functionalization to bind to the particles, and remains on the particle surface throughout washing processes, whereas 1/3 of the used Gly was removed from the particles in the subsequent washing steps. This indicates the much lower binding stability of carboxylate functions compared to catechol ligands. NMR measurements further proved that the catechol ligands are bound to the titania surface in a stable fashion, and that their concentration on the particle surface can be enhanced by a post-functionalization treatment under removal of adsorbed benzyl alcohol. Solutions of dopamine- and Gly-modified nanoparticles were also characterized by means of AUC, showing that the dopamine-capped particles possess narrow size distribution. They are practically nonaggregated, whereas a significant fraction of Gly-capped particles was found to be present as small agglomerates.

10.3 Bioconjugation with Functional Oligopeptides

10.3.1 Introduction of the Synthesis Strategy

Based on the results discussed above, we decided to utilize a coupling agent featuring a catechol function to achieve stable linkage of the oligopeptide unit to the particle surface. In principle, sequential coupling of single amino acids to the particles would be conceivable. However, preliminary results indicated that adsorption of amino acids onto the particle surface is considerable, leading to low coupling efficiency and thus low purity of the peptide. Therefore, the targeted strategy was to first synthesize an oligopeptide unit in high purity, then link it to the coupling agent, featuring the catechol function, which after cleavage from the resin would be stirred with TiO_2 nanoparticles, pre-functionalized with the abovementioned

simple organic ligands for enhanced solubility, to selectively bind to the particle surface. All abbreviations used in this chapter are explained in the Appendix Section (Chapter 12.3).

Controlled synthesis of peptide chains up to dozens of amino acids is nowadays achieved in a convenient fashion through Solid-Phase Peptide Synthesis (SPPS).[50] As the N-terminus of the peptide segment functions as the free docking site, whereas the C-terminus is bound to the resin, it makes sense to utilize a coupling agent featuring a free carboxylic acid, as it can be bound to the peptide still remaining on the resin, which greatly simplifies the synthesis. The other function of the coupling agent needs to be a catechol group, whereas an amino function is not necessary unless one wants to bind a second peptide strand to the coupling agent in an inverse manner. 3,4-Dihydroxyhydrocinnamic acid (DHC, $C_9H_{10}O_4$) hence is a suitable coupling agent. The ethyl spacer leads to improved flexibility of the acid group, resulting in higher reactivity and, thus, better coupling efficiency compared to benzoic acids. Coupling of the acid to a peptide strand can be achieved conveniently following the (Benzotriazol-1-yloxy)tripyrrolidinophosphonium hexafluorophosphate (PyBOP) protocol, which involves addition of diisopropylethylamine (DIPEA) and, thus, a basic reaction milieu.[51] The free catechol system is however oxidized rapidly in basic solutions to form chinones, whilst the stability in acidic environment is much higher.[52,53] Therefore, a protecting group had to be introduced on the catechol function to prevent oxidation. Acetonide protecting groups are quite commonly used for *ortho*-dihydroxyphenyl systems,[54,55] however they can only be cleaved under rather harsh conditions at elevated temperatures, e.g. by refluxing in 6 N HCl or in acetic acid/H_2O.[56] Also methyl ethers were used frequently, but refluxing in a hydroiodic acid/acetic anhydride mixture or reaction with boron tribromide are required to cleave the protecting groups.[57-59] The *tert*-butyldimethylsilyl (TBDMS) protection group can be conveniently introduced using imidazole as catalyst and DMF as solvent, and, even more importantly, is cleaved rapidly at room temperature in solutions of tetrabutylammonium fluoride (TBAF) in THF.[60] Even cleavage in 50 vol % trifluoroacetic acid (TFA) solution is possible, which constitutes a particularly elegant pathway, as these conditions need to be applied anyhow to achieve cleavage of the peptide strand from the resin.

There is a significant number of reports on the synthesis of 3,4-dihydroxyphenyl-L-alanine (DOPA)-containing peptides, as these resemble natural mussel adhesive proteins, which are of high interest due to their tenacious bonding properties with such diverse materials as rocks, wood, metal and fiberglass.[61] Several described strategies to DOPA-containing peptides

involve protection of the catechol functions with TBDMS-Cl and subsequent deprotection occurring concomitantly to peptide cleavage from the resin.[62,63] Therefore, the following protocol was applied: after solid-phase synthesis of an elastin-like peptide chain, a coupling step of TBDMS-protected DHC to the peptide was performed, followed by cleavage of DHC-functionalized peptide from the resin, which was expected to concurrently bring about deprotection of the catechol groups. The final step was coupling of the catechol-functionalized peptide to anatase nanoparticles (the targeted binding of the ligand to the particles is illustrated in Figures 10.10 and 10.12).

We decided to utilize ligands featuring the VPGVG motif (V = valine, P = proline, G = glycine), which constitutes the hydrophobic backbone in elastin proteins.[64,65] Polymers of $(VPGVG)_n$ undergo a transition from random coil to β-spiral upon heating, leading to aggregation and precipitation, hence possessing a lower critical solution temperature (LCST).[66,67] Rees et al. have shown that even one single repeat unit of VPGVG shows this transition behavior.[68] Moreover, this unit can be incorporated into other structures whilst keeping its temperature-responsive properties. Polymer brushes featuring VPGVG-side chains and a methacrylic acid backbone show a remarkable increase in turbidity upon heating,[69] and block copolymers of VPGVG and poly(ethylene glycol) have an LCST behavior which can be tuned by varying the degree of polymerization, concentration or pH.[70] Elastin-mimetic block copolymers undergo reversible self-assembly into well-defined aggregates from aqueous solution under physiologically relevant conditions.[71] Therefore, binding of VPGVG units to nanoparticles was targeted to lead to elastin-functionalized particles also showing a temperature-responsive behavior. Below the LCST, isolated particles would be stable in aqueous solution, but upon heating they would aggregate, ideally in a reversible manner, which on the other hand would constitute a convenient means to both prove the presence of biological functions on the particle surface, and show that these groups retain their functionality.

10.3.2 Results and Discussion

In a first approach, a VPGVG trimer unit was used, featuring lysine branches to enhance coupling to the TiO_2 nanoparticles (Elastin I). The complete structure of the peptide and its targeted fashion of binding to the anatase surface is illustrated in Figure 10.10. The amino acids are shown in the one-letter code, except for the branching lysines.

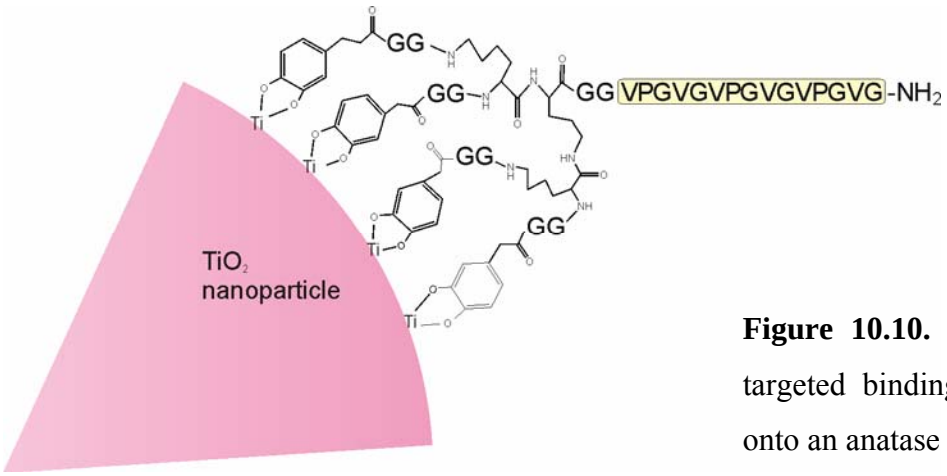

Figure 10.10. Sketch of the targeted binding of Elastin I onto an anatase nanoparticle.

The trimer of the VPGVG sequence (shown in yellow) was used to ensure significant functionality, whereas additional Gly was expected to serve as a spacer to provide sufficient flexibility of the terminal catechol functions to be able to bind to one particle in a chelating fashion, but not enough to allow any interparticle binding (bridging fashion). Four binding sites per peptide were designed in order to achieve not only stronger linkage but also to predetermine the steric orientation of the peptide strand as radial from the particle center and not to adsorb on the particle surface in a coiled fashion.

Synthesis of TBDMS-DHC (see Figure 10.11 for an illustration of its chemical structure) was achieved utilizing the aforementioned strategy of reacting DHC with TBDMSCl in the presence of imidazol as catalyst and DMF as solvent. The protected and purified coupling agent was then bound to the peptide by shaking in DMF following the PyBOP–HOBt (1-hydroxybenzotriazol) protocol. The Kaiser test was negative after only 1 h of coupling, therefore the reaction was stopped and the resin washed thoroughly. Separate deprotection was not performed. After cleavage and concentration, a white powder was precipitated in ether which after freeze-drying was stored in a glovebox.

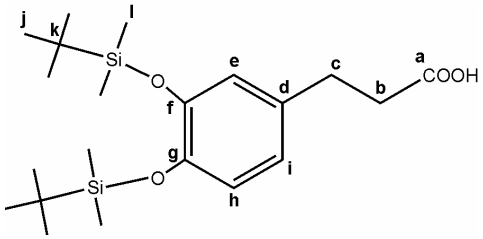

Figure 10.11. Chemical structure of TBDMS–DHC.

The obtained material was characterized by mass spectrometry (MS). As standard electron ionization MS produced a high number of signals due to the lack of charges on the peptide, MALDI-TOF MS was performed. Besides signals at lower molecular weight, caused by fraction of the peptide, two main peaks were found in the spectrum, equal in intensity, at 2894.42 and 3008.52 Da, which was higher than the calculated mass of 2857.13 Da. The

difference to the first peak, however, accounts to the weight difference caused by exchange of one proton to K^+, therefore the peak is likely caused by a potassium adduct. The weight difference between the two peaks, however, is 114.1 Da, which exactly corresponds to [TBDMS–H], indicating that a great portion of catechol functions is still protected. This is also confirmed by the main groups in the aforementioned conventional MS spectrum, where the largest m/z peaks are separated by 57 Da (for z = 2) and 38 Da (z = 3), respectively, all accounting for a mass difference of 114 in the sample. Moreover, a third peak can be found for z = 3, showing a mass increase by 38, indicating that even bis-protected species remain after the synthesis. The fact that not all catechol functions are deprotected was not expected to completely diminish its binding abilities to the nanoparticles but still to considerably decrease the stability of the resulting conjugates.

Solubility experiments of the DHC-functionalized Elastin I (DHC-Elastin I) showed good solubility in acetonitrile and acetonitrile/water mixtures, however it was not soluble in pure water, as was tested at various temperatures in the range of 5-80 °C. This was detrimental in view of its intended use as an agent soluble in cold and insoluble in warm water. Nevertheless, experiments were carried out to probe its ability to bind to the nanoparticles and to explore the properties of the resulting material. Addition of a diluted aqueous solution of DHC-Elastin I (0.2 μM) to Gly-functionalized particles resulted in a reddish suspension, proving binding of catechol units to the titania surface (cf. Chapter 10.2). TEM pictures of a dilute system show aggregated particles (data not shown), as was expected due to the poor solubility of DHC-Elastin I in water.

Therefore, a more hydrophilic oligopeptide was designed, featuring only one VPGVG repeat unit but attached to it three lysine units with free terminal amino groups on the side chains (Elastin II). The N-terminus of the oligopeptide is the same as in Elastin I, featuring two lysine branches and two G units for better flexibility. Figure 10.12 presents a sketch of the targeted binding of DHC-functionalized Elastin II to an anatase nanoparticle. Apart from the functional unit, again shown in yellow, the lysine units (blue) provide increased hydrophilicity to render the resulting peptide water-soluble. Indeed, the obtained material was well soluble in water and methanol. The obtained mass spectrum shows better intensity than the spectrum for DHC-Elastin I, which is due to the easily chargable free amine groups on the Lys side branches. The main peaks at m/z 1240 (z = 2) and 827 (z = 3) are in agreement with the targeted species, however there are strong peaks at higher molecular weight, corresponding to

[M+TBDMS–H] (m/z 1297) and even the bis-protected species (m/z 1354). When adding DHC-Elastin II to Gly-functionalized anatase nanoparticles (0.2 µM), again a red to brown color appeared within several seconds, proving binding of DHC-Elastin II onto the nanoparticles.

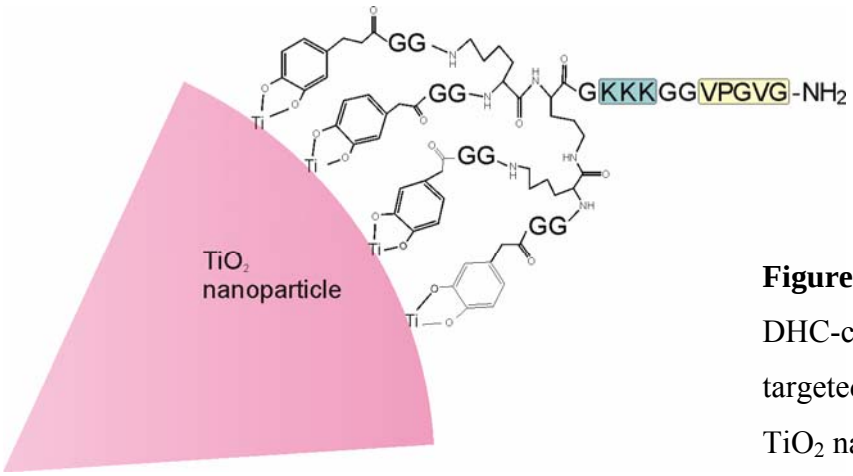

Figure 10.12. Sketch of DHC-capped Elastin II and its targeted way of binding onto a TiO_2 nanoparticle.

As DHC-Elastin II however possibly could not bind to the particles in the intended stabilized fashion because of a fraction of still protected catechol groups, it was decided to ensure deprotection by additionally performing a treatment with TBAF. As subsequent separation of TBAF and the TBDMS protecting group would be easily achieved whilst the peptide was still bound to the resin, the synthesis protocol was altered and carried out as follows: Another batch of Elastin II (termed Elastin IIa) was prepared by SPPS, then functionalized with DHC, treated with TBAF solution, cleaved from the resin and recovered as usual. In contrast to the samples described above, the material was not perfectly white but slightly brownish, which may indicate partial oxidation of the catechol groups but could also be caused by trace impurities.

The obtained mass spectrum is shown in Figure 10.13 **a**. The signals at 827 Da and 1240 Da are dominating, corresponding to the z = 2 and z = 3 signals of a molecular mass of 2480 Da. This is in excellent agreement with the calculated mass of 2479.7 Da. No indications were found in the spectrum for the presence of oxidized species, as partial oxidation would result in a mass loss of two protons per oxidation step, causing signals at 2478, 2476, 2474 and 2472 Da.

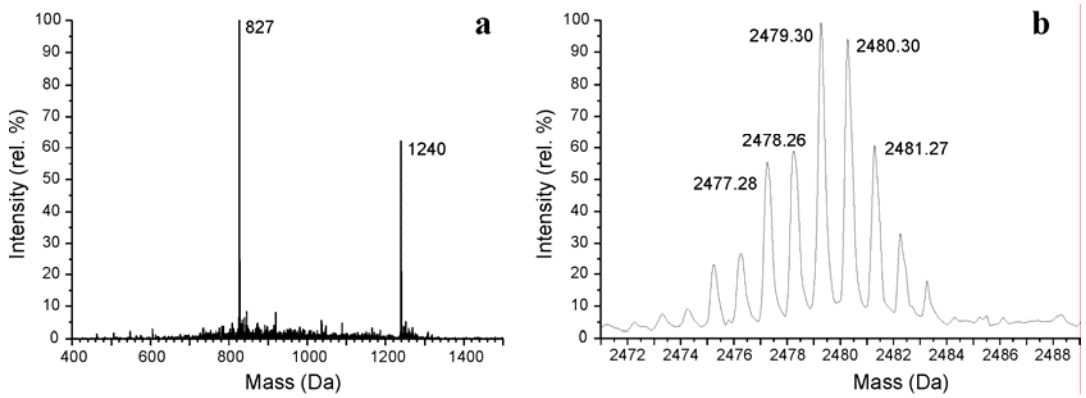

Figure 10.13. EI mass spectrum (**a**) and magnification of the MALDI-TOF spectrum (**b**) of DHC-capped Elastin IIa.

MALDI-TOF MS measurements were performed to unambiguously rule out the existence of any oxidized species. Only the main peak at 2479.30 Da is presented in high magnification (Fig. 10.13 **b**). Comparing these results with calculated data (cf. Section 10.4.3), there might be a small indication of oxidation of one catechol group, as the signal at 2477.28 Da has higher intensity than expected, but there is no more than one oxidized group per peptide (absence of stronger signals at lower mass). Compared to the main mass peak, the amount of oxidized product must lie below 20 mol %. Therefore, it is proven that all peptide ligands have at least three functional catechol groups for binding to the particles, more than 80 % having all four groups available for binding to the particles.

Also an aqueous solution of DHC-Elastin IIa (0.2 μM) reacted with Gly-functionalized TiO_2 nanoparticles to yield a red solution, indicating binding of the peptide function onto the nanoparticles via the catechol group. However, TEM images of such samples always indicated substantial aggregation of the particles. Therefore, dopamine-capped particles were used, featuring better initial stabilization in water. A possible mixed functionalization of the peptide units and dopamine would, through electrostatic particle-particle repulsion, possibly enhance the stabilization at low temperatures, whilst at higher temperatures, above the LCST of the oligopeptide, its hydrophobicity would lead to aggregation of the particles.

However, as a first step, binding of the oligopeptide units to the particle needed to be proven. Therefore, particles capped with both DHC-Elastin IIa and dopamine were prepared under removal of all excess peptide units. First, aqueous solutions of DHC-Elastin IIa and dopamine-capped TiO_2 nanoparticles were mixed. The particle-to-peptide ratio employed (cf. Section 10.4.2) was 1:10. A stable solution was obtained, therefore water was removed in vacuo. As DHC-Elastin IIa was soluble in water and MeOH, but the functionalized particles

were only slightly soluble in MeOH, the obtained precipitate was washed 5 × with MeOH. After thorough drying in vacuo at elevated temperatures, the IR spectrum was recorded (Figure 10.14, **a**). For comparison, the spectrum obtained for the dopamine-capped TiO_2 particles is also shown (**c**), as well as the spectrum of pure DHC-Elastin IIa (**b**).

Pure DHC-Elastin IIa results in strong, characteristic bands at 1641 and 1517 cm^{-1}, stemming from the amide bonds. The N–H stretching bands are found at 3275 and 3065 cm^{-1}. At 1176 and 1150 cm^{-1}, the C – N stretching vibrations are visible. The spectrum of the dopamine-capped titania on the other hand also has two strong bands at 1603 and 1488 cm^{-1}, which stem from the protonated terminal $–NH_3^+$ group of the dopamine ligands. At 1275 cm^{-1}, the aryl C–O stretching band is seen.[16] In the DHC-Elastin IIa modified dopamine-capped titania system, indeed the strongest vibrations are seen at 1631 and 1515 cm^{-1}, indicating the presence of the peptide. The shoulder on the low wavenumber side of the peak at 1631 cm^{-1} as well as the peak at 1487 cm^{-1} however prove that also the dopamine, and its terminal ammonium groups, are still present. The C–H and N–H bands above 2500 cm^{-1} are completely superimposed with strong, very broad –OH signals caused by moisture adsorbed on the particle surface. In the fingerprint region, the strongest signal of the spectrum is found at 650 cm^{-1}, caused by the Ti–O vibration of titania. Due to the long backbone of the peptide unit, any signals caused by the coupling agent, in particular any catechol signals which would change upon binding to the TiO_2 surface, are not visible, as superimposed. Therefore, the IR spectra prove that the peptide unit binds to the particles, but cannot give any indication for the manner of connection to the TiO_2 surface. The color change observed when coupling to Gly-functionalized particles however proves that binding takes place via the catechol functions, as intended.

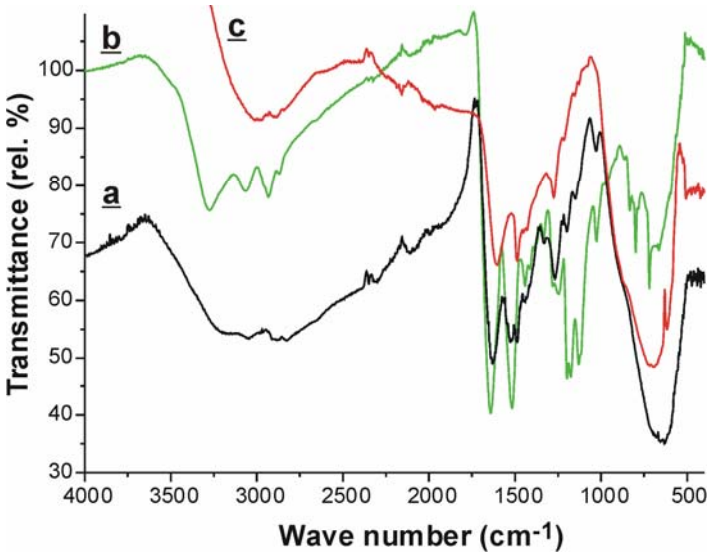

Figure 10.14. Obtained IR spectra of TiO_2 particles capped with DHC-Elastin IIa and dopamine (**a,** black line), and, as reference, the spectra of pure DHC-Elastin IIa (**b**, green line) and dopamine-capped TiO_2 (**c**, red line).

The obtained peptide–TiO_2 composites were further characterized by TGA. Figure 10.15 shows two TGA graphs, obtained by stirring TiO_2-dopamine particles in aqueous solutions of DHC-Elastin IIa, in molar ratios of 1:10 (**a**) and 1:25 (**b**), for 15 h. This treatment was followed by washing in MeOH and thorough drying as for the IR samples. In principle, it is not possible to determine the content of the peptide unit due to the additional presence of the dopamine ligand, which is replaced by DHC-Elastin IIa to an unknown extent.

The weight loss below 250 °C is attributed to adsorbed moisture and organic solvents from the washing, and amounts to less than 10 %. Above 250 °C, a clear step is visible for the lower peptide ratio (**a**), and the decomposition is complete at 450 °C. The decomposition proceeds much slower for the higher ratio of peptide (**b**), however this might be an effect of unsteady measuring conditions (higher flux of N_2 gas for sample **b**). The decrease in weight above 250 °C amounts to 19.0 % when using a particle-to-peptide ratio of 1:10, whereas it amounts to 30.9 % if a particle-to-peptide ratio of 1:25 is employed. These results therefore indicate that even a high surplus of 1:10 of peptide does not lead to saturation of the surface of the titania particles but obviously the dopamine ligands are exchanged in a slow fashion with the peptide unit. In comparison with the pure TiO_2-dopamine particles (cf. Figure 10.5), the content in organic material is slightly higher for sample **a** but substantially larger in the case of **b**.

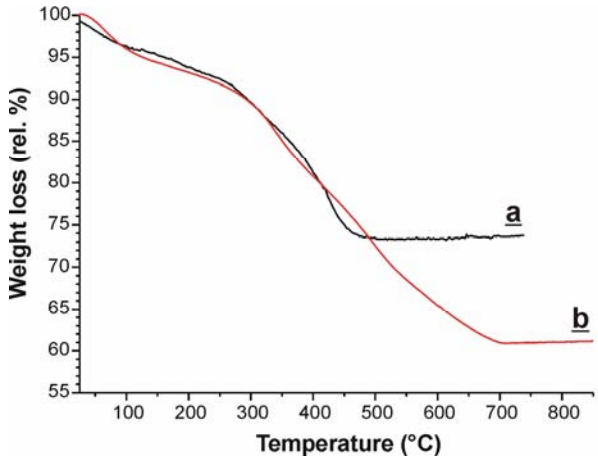

Figure 10.15. TGA plots of TiO_2-dopamine particles further functionalized with DHC-Elastin IIa in molar ratios of 1:10 (**a**, black line), and 1:25 (**b**, red line).

The influence of the organic ligand on particle assembly can be best illustrated by electron microscopy, even though one must take artifacts into account which are possibly caused by the drying step during sample preparation. In a first step, TiO_2-dopamine particles were stirred with DHC-Elastin IIa in dilute aqueous solution (0.1 nM) in a molar particle-to-peptide ratio of 1:1. In order to induce self-assembly, the solution was heated at 45 °C for 10 min and then instantly applied on a TEM grid. Figure 10.16 presents the obtained images. The overview picture (**A**) shows that small aggregates are present, about 100 nm in size. Most of these aggregates are worm-like or at least elongated. Such a structure is presented at higher

magnification (**B**). Worm-like substructures are clearly visible, being about 100 nm in length and 30 nm in thickness. For comparison, the dopamine-capped TiO_2 particles, in equal concentration, were also subjected to the heat treatment without adding the peptide ligand. In this case (**C**), large aggregates resulted, over 500 nm in length. Thus, an influence of the peptide ligand is clearly visible.

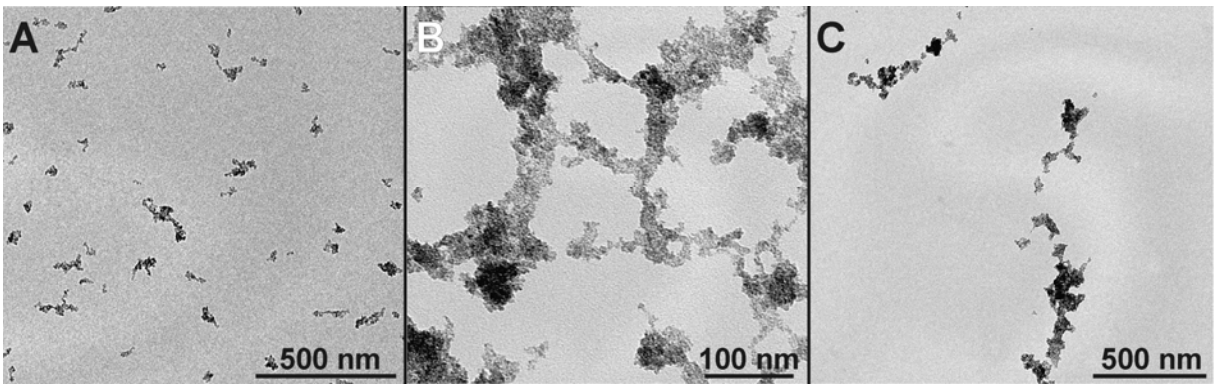

Figure 10.16. TEM images of DHC-Elastin IIa modified TiO_2-dopamine particles (**A**, **B**), and reference sample without the peptide ligand (**C**), all after heating at 45 °C for 10 min.

To achieve a more pronounced assembly behavior, a higher temperature of 60 °C was employed. Again using a particle-to-peptide ratio of 1:1, the mixture was first stirred for 1 h at room temperature to allow for equilibration. A portion of the solution was withdrawn and analyzed. The resulting TEM images are presented in Figure 10.17 **A** and **B**. Small aggregates of particles are visible in the overview image, about 80-120 nm in length. Interestingly, in the image at higher magnification it is visible that they mainly possess worm-like morphology, being < 10 nm thin. Therefore, they must be a chain-like arrangement of single particles.

In fact, such worm-like, highly anisotropic structures have been observed recently to form upon refluxing titania particles capped with agents such as serinol or trizma (2-amino-2-hydroxymethyl-1,3-propanediol) in water. The ligands were proposed to desorb selectively from the (001) crystal faces, leading to oriented attachment of the nanoparticles.[72,73] A similar mechanism is assumed to lead to the worm-like assemblies in the system discussed here. It is interesting to note that the anisotropy of these structures was much more pronounced in the presence of DHC-Elastin IIa than for pure dopamine-capped species, which were reported to form large, undefined aggregates upon refluxing in water.[73] This indicates that the peptide-featuring ligand indeed plays a role with respect to particle assembly even at room temperature.

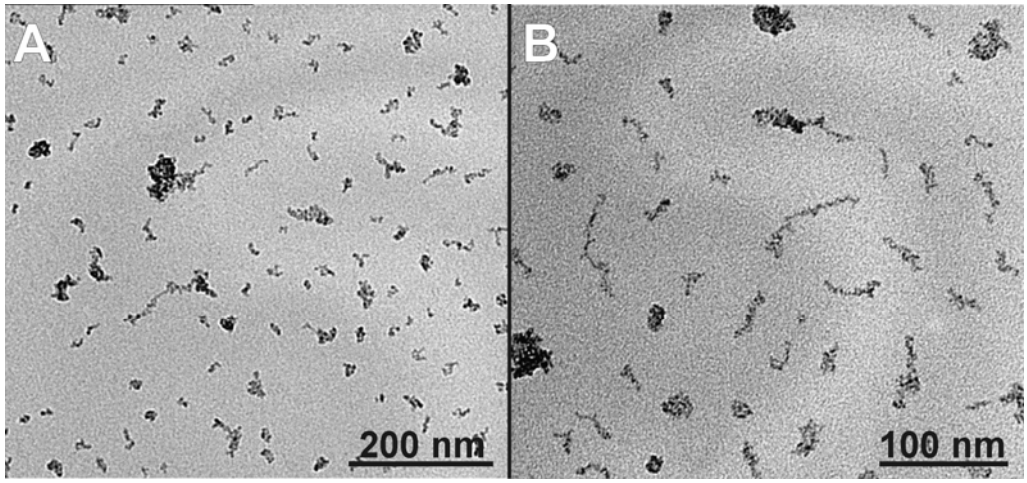

Figure 10.17. TEM images of DHC-Elastin IIa modified TiO_2-dopamine particles stirred for 2 h at room temperature, overview (**A**), and higher magnification (**B**).

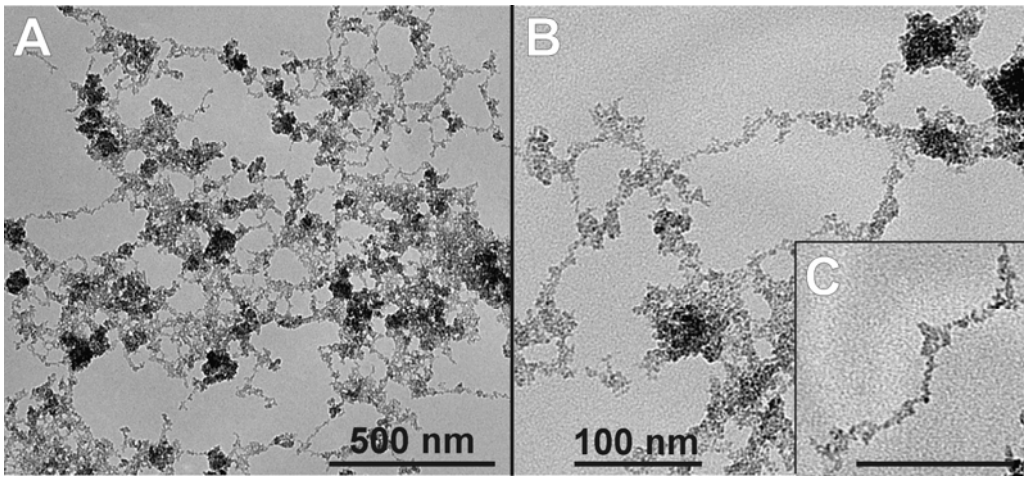

Figure 10.18. TEM images of DHC-Elastin IIa modified TiO_2-dopamine particles after 30 min at 60 °C, overview (**A**), and higher magnification (**B**, **C**, the scale bar corresponding to 100 nm).

After 30 min of heating at 60 °C, even optically visible reddish aggregates had formed. A portion of the supernatant was subjected to TEM (Figure 10.18). In the overview image (**A**), a substantial change in aggregation behavior is visible. A spider web-like structure had formed, being several micrometers in total size. This network featured some larger dense aggregates but mainly consisted of worm-like structures. These are shown in higher magnification in images **B** and **C**. The structures are again 100-150 nm in length, but less than 10 nm in width, again representing a chain-like arrangement of individual particles. Possibly, individual "nanoworms" assemble into the larger structures upon heating.

Interestingly, the large visible aggregates dissolved again upon further stirring at room temperature overnight. However, TEM analysis of these solutions reveals that the aggregation

is not completely reversible, as still larger, web-like aggregates were formed (data not shown as similar to Fig. 10.18).

10.3.3 Summary and Conclusions

In this chapter, surface modification of TiO_2 nanoparticles with functional oligopeptide ligands has been investigated. Using a coupling agent featuring a catechol group for binding to the titania surface, indeed a stable linkage of such ligands is possible. As the binding of the catechol group to surface Ti leads to a colored charge-transfer complex, the linkage via this group could even be observed visually. IR measurements proved the presence of peptide functions also after extensive washing. Additional stabilization of the particles is however necessary to prevent aggregation already at low temperatures. This is achieved by directly using dopamine-functionalized TiO_2 particles (cf. Chapter 10.2) which are simply stirred in aqueous solutions of the designed oligopeptide ligands to induce partial ligand exchange, resulting in mixed functionality with both dopamine ligands, featuring charged ammonium end groups causing electrostatic repulsion between the particles, as well as peptide units, being stable in aqueous solution at low temperatures but showing a tendency towards aggregation above a critical temperature.

Indeed, the particles were not completely isolated at room temperature but present in the form of small aggregates. Simple stirring for 1 h led to worm-like aggregates, which have been reported to form in very similar systems by selective desorption of surface-modifiers upon refluxing in water. Upon thermal treatment, these worm-like units combined to form a web-like structure. Particles only functionalized with dopamine but not with the peptide ligand also exhibited an aggregation tendency upon heating. They however formed larger aggregates and not worm-like structures, proving a strong influence of the peptide ligand on the assembly behavior of the particles.

10.4 Experimental Section

10.4.1 Particle Synthesis and Functionalization with Organic Ligands

The chemicals were used as received from Aldrich. Typically, 160 mg (0.84 mmol) dopamine hydrochloride, 250 mg (1.5 mmol) TBC, 341 mg (4.6 mmol) glycine or 207 mg (2.30 mmol) serinol, respectively, were dispersed in 30 mL benzyl alcohol in the glovebox. Dopamine, glycine and serinol formed cloudy suspensions whereas TBC was well soluble. The vial was sealed, removed from the box and stirred for 1 h before slowly adding 1.5 mL (13.6 mmol)

$TiCl_4$ under vigorous stirring. In the case of dopamine and TBC, the liquid turned dark red immediately whereas it stayed transparent to slightly greenish for Gly and serinol. Sometimes the liquid contained some fluffy precipitate that completely dissolved again upon further heat treatment. The vial was sealed and stirred at room temperature for about 2 hours. Subsequently, the sol was heated to 80 °C (70 °C for TBC), which was held for 3 days for aging. The resulting suspensions were centrifuged and the precipitate thoroughly washed with chloroform or methylene chloride (3-5 ×). After each washing step, the solvent was removed by centrifugation. The collected material was dried in air at 60 °C, yielding a dark red powder in the case of the dopamine-functionalized nanoparticles, a brittle brown solid in the case of the TBC-capped particles, or white powders for Gly and serinol-functionalized samples.

Wheras dopamine, serinol and Gly-capped nanoparticles could be easily redispersed after drying, the solubility of TBC-functionalized TiO_2 particles decreased substantially upon performing a drying step. Therefore, for the latter system only the solvent benzyl alcohol was removed by centrifugation but the particles were not washed and dried but stored in a "wet" state (note the high boiling point of benzyl alcohol of 205 °C preventing its evaporation). Post-functionalization treatments were generally performed as follows: about 100-200 mg of the particles were redispersed in a solution of the desired (additional) ligand in chloroform (20 mL of a 0.04-0.1 M solution or dispersion). The mixture was stirred for 2-6 h and the product retrieved by centrifugation at up to 9000 rpm. Excess organics were removed by washing 3 × with $CHCl_3$ or DCM, and the solvent removed by drying in vacuo for several hours. In cases where the particles did not sediment after the post-functionalization treatment, the solvent was removed by evaporation and the remaining precipitate dissolved directly in the NMR solvent.

10.4.2 Functionalization with Peptides.

Introduction of Protecting Group. The synthesis of 3',4'-(di-*tert*-butyldimethylsilyldioxy) hydrocinnamic acid (TBDMS-DHC) was carried out similarly as reported by Solladié et al.[74] In a dry argon atmosphere, 400 mg (2.2 mmol) 3,4-dihydroxyhydrocinnamic acid was dissolved in 6 mL dry DMF. Imidazol (1.35 g, 19.8 mmol) and *tert*-butyldimethylsilylchloride (1.49 g, 9.9 mmol) were added and the resulting clear, brownish solution stirred for 48 h (however, reduction of the reaction time to 24 h in subsequent experiments did not lead to a considerable decrease in yield). 40 mL diethyl ether and 10 mL distilled water were added and the mixture stirred until a phase separation occurred. In a separating funnel, the mixture was extracted with ether (4 × 50 mL), and the combined organic layers washed with sat. NH_4Cl (3 × 100 mL) and brine (sat. NaCl, 2 × 100 mL), dried over $MgSO_4$ and the solvents evaporated

to give crude (*tert*-butyldimethylsilyl)-3',4'-(*tert*-butyldimethylsilyldioxy)hydrocinnamate. The ester was dissolved in 10 mL THF and 28 mL methanol, to which a K_2CO_3 solution was added dropwise (9.4 mL of a 1 mM solution in water). The turbid liquid was stirred overnight and then the solvents evaporated. 28 mL brine was added to the residue and the pH carefully attached to 6 by adding a few drops of 0.1 N HCl. The aqueous solution was extracted with ether (4 × 60 mL), and the combined organic layers washed with brine (2 × 100 mL), dried over $MgSO_4$ and the solvent evaporated.

Oligopeptide Synthesis. In all cases, synthesis of the strands of native amino acids was performed on an Applied Biosystems ABI 433a Peptide Synthesizer using N-methyl-2-pyrrolidone (NMP) as solvent, and standard Fmoc protocols.[50] A TentaGel S RAM resin was used as support (showing a loading of 0.2-0.4 mmol/g). Double coupling was applied with a coupling time of 20 min for amino acids in the unbranched moiety, whereas the coupling time was extended to 60 min for Fmoc-Lys(Fmoc)-OH, used to introduce branching to the peptide, and for the subsequent amino acids in the branched subunits to ensure complete coupling. Fmoc-Lys(Boc)-OH was utilized for unbranched Lys sites. After the final coupling step, the terminal amine was deprotected and the resin-bound peptide transferred to a vial, washed 5 × with DMF and suspended in DMF.

Coupling of TBDMS-DHC to the Peptide. A PyBOP strategy was applied for the coupling reaction of the linker to the peptide.[52] TBDMS-DHC (5 equivalents), PyBOP (5 eq.) and HOBt (5 eq.) were each dissolved in small amounts of DMF and then combined to form the benzotriazolyl ester of DHC. After shaking for several minutes, the mixture was added to 0.25 eq. of the resin which had previously been filtered. The suspension was agitated for 30 min, and then DIPEA was added (10 eq.). After further shaking for 1-3 h, some beads were removed and the Kaiser test[75] performed. If the test was negative, the coupling solution was removed by filtration and the resin thoroughly washed with DMF.

Cleavage and Deprotection. Only for Elastin-IIa, a separate deprotection step was performed. An equimolar amount of TBAF was added to the resin using a 1 M solution of TBAF in THF previously further diluted with DMF. The resin changed its color instantly to green-black, nevertheless the mixture was shaken for 1 h before filtration. The fluoride reagent was removed by thorough washing with DMF. Cleavage of the peptide from the resin was achieved using a mixture of 49.5 %vol TFA, 49.5 %vol DCM, and 1 %vol triethylsilane. The solution was added to the dried resin, and the suspension was shaken for 1 h. After filtration,

the resin was again treated with the cleavage solution for ca. 15 min, filtered and thoroughly washed with TFA/DCM. The combined filtrates were concentrated to ca. half volume, and the peptide precipitated in cold ether. Freeze-drying in distilled water yielded the DHC-functionalized peptide.

Capping of the titania nanoparticles. For these experiments, a crucial parameter was the molar particle-to-ligand ratio used. In view of the high molecular mass of the peptide ligands, it appeared useful not to calculate the Ti-to-ligand ratio as for the simple organic ligands, but to estimate the molar quantity of particles, emanating from an average particle size of 8.0 nm, resulting in a molecular weight of $2.7 \cdot 10^5$ g mol^{-1} particles. However, it is clear that this value is an approximation, as the previous organic functionalization as well as the particle size distribution are not taken into account.

10.4.3 NMR and MS Data

Pure dopamine·HCl (Figure 10.6 **A**, 400 MHz, DMF-d^7; proton labels as illustrated in Fig. 10.6) δ [ppm]: 8.80 (s, >100 Hz broad, 6H, –OH and $-NH_3^+$), 6.80 (d, 1H, **b**, $J_{\mathbf{b-d}}$ = 2.0 Hz), 6.78 (d, 1H, **c**, $J_{\mathbf{c-d}}$ = 8.1 Hz), 6.59 (dd, 1H, **d**, $J_{\mathbf{d-c}}$ = 8.1 Hz, $J_{\mathbf{d-b}}$ = 1.8 Hz), 3.20 (t, 2H, **e**, $J_{\mathbf{e-f}}$ = 7.6 Hz), 2.94 (t, 2H, **f**, $J_{\mathbf{f-e}}$ = 7.7 Hz).

Pure TBC (400 MHz, DMF-d^7; labels as in Fig. 10.7): 8.75 (broad, 2H, **c**), 6.93 (d, 1H, $\mathbf{b}_{2'}$, $J_{2'\text{-}6'}$ = 2.5 Hz), 6.79 (d, 1H, $\mathbf{b}_{5'}$, $J_{5'\text{-}6'}$ = 8.4 Hz), 6.72 (dd, 1H, $\mathbf{b}_{6'}$, $J_{6'\text{-}5'}$ = 2.3 Hz, $J_{6'\text{-}2'}$ = 8.4 Hz), 1.27 (s, 9H, **a**).

Pure serinol (400 MHz, D_2O, labels as in Fig. 10.8): 3.34 (dd, 2H, **a**, $J_{\mathbf{a-a}}$ = 10.4 Hz, $J_{\mathbf{a-b}}$ = 5.4 Hz), 3.22 (dd, 2H, **a**, $J_{\mathbf{a-a}}$ = 10.4 Hz, $J_{\mathbf{a-b}}$ = 6.1 Hz), 2.66 (dd, 1H, **c**, $J_{\mathbf{c-a}}$ = 5.7 Hz).

TBDMS–DHC: ^{1}H NMR (400 MHz, $CDCl_3$, labels referring to Figure 10.11) δ [ppm]: 6.72 (d, 1H, **h**, $J_{\mathbf{h-i}}$ = 7.9 Hz), 6.66 (d, 1H, **e**, $J_{\mathbf{e-i}}$ = 2.0 Hz), 6.64 (dd, 1H, **i**, $J_{\mathbf{i-h}}$ = 8.2 Hz, $J_{\mathbf{i-e}}$ = 2.0 Hz), 2.83 (t, 2H, **c**, $J_{\mathbf{c-b}}$ = 7.6 Hz), 2.61 (t, 2H, **b**, $J_{\mathbf{b-c}}$ = 7.6 Hz), 0.97 (s, 18H, **j**), 0.18 (s, 12H, **l**).
^{13}C NMR (100 MHz, $CDCl_3$) δ [ppm]: 178.9 (**a**), 146.7, 145.3 (**f**, **g**), 133.3 (**d**), 121.0 (**e**, **h**, **i**), 35.8 (**c**), 29.9 (**b**), 25.9 (**j**), 18.5 (**k**), -4.1 (**l**).

Elastin I: $(GG)_4K^*{}_2K^*GGVPGVGVPGVGVPGVG–NH_2$
0.1 mmol of the peptide were prepared. MW_{th} = 2202.5.
MS of crude Elastin I: Peaks (rel. Intensity): 1101 (20), 734 (100), 710 (10).
MS of DHC-capped Elastin I: 1354 (20), 1297 (60), 1240 (70), 975 (36), 903 (40), 866 (65), 827 (100), variety of peaks with intensity 10-30.

Elastin II: $(GG)_4K^*{}_2K^*GKKKGGVPGVG–NH_2$
0.1 mmol of peptide were prepared. MW_{th} = 1823.1.

MS of crude Elastin II: 912 (100), 608 (72).
MS of DHC-capped Elastin II: 1354 (18), 1297 (59), 1240 (67), 975 (38), 903 (42), 866 (65), 827 (100), variety of peaks with intensity 10-35.

Elastin IIa: $(GG)_4K^*{}_2K^*GKKKGGVPGVG–NH_2$ (same as Elastin II)
0.25 mmol of peptide were prepared. MW_{th} = 1823.1.
MS of crude Elastin IIa: 912 (100), 608 (72).
MS of DHC-Elastin IIa: 1262 (10), 1251 (16), 1240 (76), 827 (100).
MALDI-TOF MS: Peaks (rel. Intensity): 2421.38 (5), 2479.30 (100), 2516.16 (10).
Isotopic signals of main peak: 2475.26 (22), 2476.27 (25), 2477.28 (53), 2478.26 (58), 2479.30 (100), 2480.28 (92), 2481.27 (60), 2482.25 (32), 2483.26 (17). Calculated data: 2479.26 (100), 2478.25 (80), 2480.26 (68), 2481.26 (38), 2482.27 (12).

10.5 References

[1] H. Weller, *Angew. Chem. Int. Ed.* **1996**, *35*, 1079.

[2] G. M. Whitesides, B. Grzybowski, *Science* **2002**, *295*, 2418.

[3] D. Philp, J. F. Stoddart, *Angew. Chem. Int. Ed.* **1996**, *35*, 1155.

[4] S. Svenson, *J. Dispersion Sci. Technol.* **2004**, *25*, 101.

[5] G. M. Whitesides, *Scientific American* **1995**, *273*, 146.

[6] J. M. Lehn, *Science* **2002**, *295*, 2400.

[7] M.-I. Baraton, *Encyclopedia of Nanoscience and Nanotechnology* **2004**, *10*, 267.

[8] R. Shenhar, V. M. Rotello, *Acc. Chem. Res.* **2003**, *36*, 549.

[9] A. K. Boal, K. Das, M. Gray, V. M. Rotello, *Chem. Mater.* **2002**, *14*, 2628.

[10] T. Rajh, O. V. Makarova, M. C. Thurnauer in *Synthesis, Functionalization and Surface Treatment of Nanoparticles* (Ed.: M.-I. Baraton), American Scientific Publishers, Stevenson Ranch, **2003**.

[11] G. Kickelbick, D. Holzinger, C. Brick, G. Trimmel, E. Moons, *Chem. Mater.* **2002**, *14*, 4382.

[12] G. Ramakrishna, H. N. Ghosh, *Langmuir* **2003**, *19*, 505.

[13] E. Scolan, C. Sanchez, *Chem. Mater.* **1998**, *10*, 3217.

[14] A. B. Bourlinos, A. Bakandritsos, V. Georgakilas, D. Petridis, *Chem. Mater.* **2002**, *14*, 3226.

[15] A. Rosenheim, O. Sorge, *Berichte* **1920**, *53*, 932.

[16] T. Rajh, L. X. Chen, K. Lukas, T. Liu, M. C. Thurnauer, D. M. Tiede, *J. Phys. Chem. B* **2002**, *106*, 10543.

[17] N. M. Dimitrijević, Z. V. Saponjić, D. M. Bartels, M. C. Thurnauer, D. M. Tiede, T. Rajh, *J. Phys. Chem. B* **2003**, *107*, 7368.

[18] J. Moser, S. Punchihewa, P. P. Infelta, M. Grätzel, *Langmuir* **1991**, *7*, 3012.

[19] P. C. Angelomé, S. Aldabe-Bilmes, M. E. Calvo, E. L. Crepaldi, D. Grosso, C. Sanchez, G. J. A. A. Soler-Illia, *New J. Chem.* **2005**, *29*, 59.

[20] C. Das, S. C. Shankaramma, P. Balaram, *Chem. Eur. J.* **2001**, *7*, 840.

[21] P. Pengo, Q. B. Broxterman, B. Kaptein, L. Pasquato, P. Scrimin, *Langmuir* **2003**, *19*, 2521.

[22] A. Verma, H. Nakade, J. M. Simard, V. M. Rotello, *J. Am. Chem. Soc.* **2004**, *126*, 10806.

[23] J. M. Nam, S.-J. Park, C. A. Mirkin, *J. Am. Chem. Soc.* **2002**, *124*, 3820.

[24] A. Schroedter, H. Weller, *Angew. Chem. Int. Ed.* **2002**, *41*, 3218.

[25] K. K. Caswell, J. N. Wilson, U. H. F. Bunz, C. J. Murphy, *J. Am. Chem. Soc.* **2003**, *125*, 13914.

[26] S. Connolly, S. Cobbe, D. Fitzmaurice, *J. Phys. Chem. B* **2001**, *105*, 2222.

[27] K. Aslan, C. C. Luhrs, V. H. Pérez-Luna, *J. Phys. Chem. B* **2004**, *108*, 15631.

[28] M. G. Ryadnov, B. Ceyhan, C. M. Niemeyer, D. N. Woolfson, *J. Am. Chem. Soc.* **2003**, *125*, 9388.

[29] P. Hazarika, B. Ceyhan, C. M. Niemeyer, *Angew. Chem. Int. Ed.* **2004**, *116*, 6631.

[30] S. Bareyt, S. Piligkos, B. Hasenknopf, P. Gouzerh, E. Lacôte, S. Thorimbert, M. Malacria, *Angew. Chem. Int. Ed.* **2003**, *42*, 3404.

[31] A. Frey, M. R. Neutra, F. A. Robey, *Bioconjugate Chem.* **1997**, *8*, 424.

[32] A. Nanci, J. D. Wuest, L. Peru, P. Brunet, V. Sharma, S. Zalzal, M. D. McKee, *J. Biomed. Mater. Res.* **1998**, *40*, 324.

[33] C. Wong, J. P. Burgess, A. E. Ostafin, *J. Young Investigators* **2002**, *6*.

[34] C. Xu, K. Xu, H. Gu, R. Zheng, H. Liu, X. Zhang, Z. Guo, B. Xu, *J. Am. Chem. Soc.* **2004**, *126*, 9938.

[35] T. Paunesku, T. Rajh, G. Wiederrecht, J. Maser, S. Vogt, N. Stojicevic, M. Protic, B. Lai, J. Oryhon, M. C. Thurnauer, G. Woloschak, *Nat. Mater.* **2003**, *2*, 343.

[36] N. M. Dimitrijević, Z. V. Saponjić, B. M. Rabatić, T. Rajh, *J. Am. Chem. Soc.* **2005**, *127*, 1344.

[37] M. Niederberger, M. H. Bartl, G. D. Stucky, *J. Am. Chem. Soc.* **2002**, *124*, 13642.

[38] M. Niederberger, M. H. Bartl, G. D. Stucky, *Chem. Mater.* **2002**, *14*, 4364.

[39] L. X. Chen, T. Rajh, Z. Y. Wang, M. C. Thurnauer, *J. Phys. Chem. B* **1997**, *101*, 10688.

[40] A. Pottier, S. Cassaignon, C. Chaneac, F. Villain, E. Tronca, J.-P. Jolivet, *J. Mater. Chem.* **2003**, *13*, 877.

[41] G. Guerrero, P. H. Mutin, A. Vioux, *Chem. Mater.* **2001**, *13*, 4367.

[42] M. Anpo, T. Shima, S. Kodama, Y. Kubokawa, *J. Phys. Chem.* **1987**, *91*, 4305.

[43] R. Mueller, H. K. Kammler, K. Wegner, S. E. Pratsinis, *Langmuir* **2003**, *19*, 160.

[44] S. Roux, G. J. A. A. Soler-Illia, S. Demoustier-Champagne, P. Audebert, C. Sanchez, *Adv. Mater.* **2003**, *15*, 217.

[45] I. Carrizosa, G. Munuera, *J. Catal.* **1977**, *49*, 174.

[46] H. Cölfen, T. Pauck, *Colloid Polym. Sci.* **1997**, *275*, 175.

[47] C. Kormann, D. W. Bahnemann, M. R. Hoffmann, *J. Phys. Chem.* **1988**, *92*, 5196.

[48] N. Serpone, D. Lawless, R. Khairutdinov, *J. Phys. Chem.* **1995**, *99*, 16646.

[49] A. P. Alivisatos, *J. Phys. Chem.* **1996**, *100*, 13226.

[50] W. C. Chan, P. D. White (Eds.), *Fmoc Solid Phase Peptide Synthesis - A Practical Approach*, Oxford University Press, New York, **2000**.

[51] J. Coste, D. Le-Nguyen, B. Castro, *Tetrahedron Lett.* **1990**, *31*, 205.

[52] A. E. Sánchez-Rivera, S. Corona-Avendaño, G. Alarcón-Angeles, A. Rojas-Hernández, M. T. Ramírez-Silva, M. A. Romero-Romo, *Spectrochim. Acta, Part A* **2003**, *59*, 3193.

[53] Y. Shen, M. Y. Ye, *J. Liq. Chromatogr.* **1994**, *17*, 1557.

[54] K. Ogura, G.-I. Tsuchihashi, *Tetrahedron Lett.* **1971**, *34*, 3151.

[55] E. J. Corey, S. D. Hurt, *Tetrahedron Lett.* **1977**, *45*, 3923.

[56] T. W. Greene, P. G. M. Wuts, *Protective Groups in Organic Synthesis*, J. Wiley & Sons, New York, **1999**.

[57] J. Z. Ginos, G. C. Cotzias, E. Tolosa, L. C. Tang, A. LoMonte, *J. Med. Chem.* **1975**, *18*, 1194.

[58] J. L. Neumeyer, B. R. Neustadt, K. K. Weinhardt, *J. Pharm. Sci.* **1970**, *59*, 1850.

[59] M. H. Gezginci, B. N. Timmermann, *Tetrahedron Lett.* **2001**, *42*, 6083.

[60] E. J. Corey, A. Venkateswarlu, *J. Am. Chem. Soc.* **1972**, *94*, 6190.

[61] J. L. Daisin, L. Lin, P. B. Messersmith, *Polymeric Mater. Sci. Eng.* **2004**, *90*, 247.

[62] M. J. Sever, J. J. Wilker, *Tetrahedron* **2001**, *57*, 6139.

[63] A. A. Ooka, R. L. Garrell, *Biopolymers* **1999**, *57*, 92.

[64] W. R. Gray, L. B. Sandberg, J. A. Foster, *Nature* **1973**, *246*, 461.

[65] B. Li, V. Daggett, *J. Muscle Res. Cell Motility* **2002**, *23*, 561.

[66] D. W. Urry, T. Hugel, M. Seitz, H. E. Gaub, L. Sheiba, J. Dea, J. Xu, T. Parker, *Philos. Trans. R. Soc. London, Ser. B* **2002**, *357*, 169.

[67] D. W. Urry, *J. Protein Chem.* **1988**, *7*, 1.

[68] H. Reiersen, A. R. Clarke, A. R. Rees, *J. Mol. Biol.* **1998**, *283*, 255.

[69] L. Ayres, M. R. J. Vos, P. J. H. M. Adams, I. O. Shklyarevskiy, J. C. M. van Hest, *Macromolecules* **2003**, *36*, 5967.

[70] L. Ayres, K. Koch, P. J. H. M. Adams, J. C. M. Van Hest, *Macromolecules* **2005**, *23*, 1699.

[71] E. R. Wright, V. P. Conticello, *Adv. Drug Delivery Rev.* **2002**, *54*, 1057.

[72] J. Polleux, N. Pinna, M. Antonietti, M. Niederberger, *Adv. Mater.* **2004**, *16*, 436.

[73] J. Polleux, N. Pinna, M. Antonietti, C. Hess, U. Wild, R. Schlögl, M. Niederberger, *Chem. Eur. J.* **2005**, Early View.

[74] G. Solladié, L. Gressot-Kempf, *Tetrahedron: Asymmetry* **1996**, *7*, 2371.

[75] E. Kaiser, R. L. Colescott, C. D. Bossinger, P. I. Cook, *Anal. Biochem.* **1970**, *34*, 595.

11 Summary and Conclusions

In this work, the nonaqueous synthesis of binary and ternary metal oxide nanoparticles has been reported for a number of technologically important materials. A strong focus was put on studying the reaction mechanism leading to particle formation upon solvothermal treatment of the precursors, as the formation processes of oxides in the absence of water are hardly known and their understanding is expected to result in better control of the systems, offering the possibility to tailor particle size and morphology.

The synthesis of $BaTiO_3$ was achieved by solvothermal treatment both in benzyl alcohol and in ketones such as acetone and acetophenone. Phase-pure, highly crystalline particles were obtained, spherical and about 6 nm in diameter when prepared in the alcohol, and ca. 10 nm in size for the acetophenone system. Surprisingly, not the expected ether elimination but a novel mechanism was found to lead to $BaTiO_3$ in benzyl alcohol, involving a C–C coupling step between the isopropoxide ligand and the benzylic carbon of the solvent. The resulting coupling product, 4-phenyl-2-butanol, is found in almost stoichiometric yield.

The possibilities and mechanisms of oxide formation by solvothermal reaction of alkoxide precursors in aprotic solvents were explored for TiO_2 as model system. Highly crystalline anatase was obtained when using ketones or aldehydes as solvents. It turned out that aldol condensation processes of the solvent occur during the solvothermal treatment, involving formal elimination of water which induces the formation of Ti–O–Ti bonds as building blocks of the oxide. The synthesis of anatase was even possible in benzamide and benzylamine, in the latter case the particles being arranged into lamellar superstructures.

The analogous treatment of yttrium isopropoxide in benzyl alcohol did not result in inorganic nanoparticles but in a highly ordered, lamellar nanocomposite of yttria and benzoic acid. The formation of the hybrid material involves an analogous C–C coupling mechanism as for the $BaTiO_3$ system. Benzoic acid is formed from benzyl alcohol via disproportionation processes.

Solvothermal synthesis however is not restricted to alkoxides as precursors but was also achieved when using metal acetylacetonates. The reaction in benzylamine as solvent proved particularly versatile, leading to nanocrystalline In_2O_3, Ga_2O_3, ZnO and iron oxide. On the other hand, phase pure magnetite particles were obtained in benzyl alcohol. During the synthesis, the acetylacetonate ligand undergoes a solvolysis under C–C cleavage, resulting in

metal-bound enolate ligands which, in analogy to the synthesis in ketones, induce ketimine and aldol condensation reactions.

The synthesis of lead zirconate titanate particles was not possible in benzyl alcohol due to the reducing character of the alcohol. With 2-butanone as solvent, amorphous powder precursors were obtained which could be transformed into highly crystalline PZT nanoparticles by calcination at moderate temperatures. Additionally, films were prepared by simply casting a suspension of the precursor powders followed by calcination. Highly homogeneous, crack-free PZT films were obtained with some larger spherical aggregates sitting on top of the film.

Sodium and potassium niobate nanoparticles were obtained by solvothermal treatment of the alkali metals and niobium ethoxide in benzyl alcohol. Whereas the $NaNbO_3$ particles were highly crystalline, potassium-containing systems had to be calcined at 700 °C to induce crystallization, however resulting in a mixture of phases. The mechanism leading to $NaNbO_3$ proceeds via the C–C coupling reaction as observed for $BaTiO_3$ and for the yttria system.

Therefore, it appeared worthwhile to study this mechanism in detail. Interestingly, solvothermal treatment of titanium alkoxides in benzyl alcohol resulted mainly in benzyl ether, whereas the presence of alkaline species led to the C–C coupling reaction. On the other hand, also other titanium alkoxides, like $Ti(O\textit{n}Bu)_4$, or $Ti(O–4\text{-heptyl})_4$, were shown to undergo the coupling. It is always the β position which undergoes deprotonation and nucleophilic attack. Other possible mechanisms leading to the C–C coupling, such as an elimination–addition reaction or radical mechanisms were discussed but found improbable.

In the last part of this work, surface functionalization of anatase nanoparticles is explored. The particles, prepared by a simple nonaqueous method, were first capped by various organic ligands via a facile in situ route. This results in altered properties, e.g. enhanced solubility in various solvents. Catechol ligands such as dopamine and TBC were found to strongly bind to the particle surface. In a second step, short functional oligopeptide segments were attached to the particles by means of a catechol linker. These segments were designed to provide an LCST-like behavior, leading to aggregation above a critical temperature. Peptide-modified dopamine particles indeed showed a significantly changed aggregation behavior, resulting in small worm-like assemblies at room temperature, arranging to spider web-like superstructures upon heating to 60 °C.

12 Appendix

12.1 Background to Solvothermal Reactions

Due to the generally low boiling points of ketones and aldehydes, the reactions could not be performed under ambient pressure but had to be carried out in a sealed autoclave. In addition, all syntheses presented in Chapters 3-9 were achieved only in autoclaves. Therefore, it appears worthwhile to shortly look at the specifications of such syntheses.

No additional pressure is applied but all syntheses are carried out under *autogenous pressure*, i.e. the pressure generated by the contents of the autoclave upon heating in an airtight vessel. One can assume the pressure to be caused primarily by the respective solvent, even though also the metal oxide precursors or reaction byproducts may contribute to this pressure, especially in samples where a high concentration of reactants was used.

Calculations were performed in order to determine the resulting pressure in the autoclave during the solvothermal treatment. It was not possible to measure the pressure, therefore these calculations are helpful to thoroughly describe the measurement conditions. Additionally, knowledge of the pressure building up upon heating is also necessary for safety reasons – the upper pressure limit of the used equipment is 1800 psig (124 bar). However, it turned out that the filling ratios of the autoclave were by far too low to get even close to the upper pressure limit of the autoclaves.

Basically, autogeneous pressures in solvothermal reactions can be calculated from cubic equations of state according to[1]

$$p = [RT/(V_m - b)] - [a/(V_m^2 + 2bV_m - b^2)] \qquad \text{(Eq. 12.1)},$$

with $a = 0.45724\ R^2\ T_C^2\ [1 + f_\omega\ (1 - \mathrm{sqrt}(T_r))]^2 / P_C$

and $b = 0.07780\ R\ T_C / P_C$

where $f_\omega = 0.37464 + 1.54226\ \omega - 0.26992\ \omega^2$

The values for T_C, P_C and ω of the individual solvents can be taken from the literature.[2]

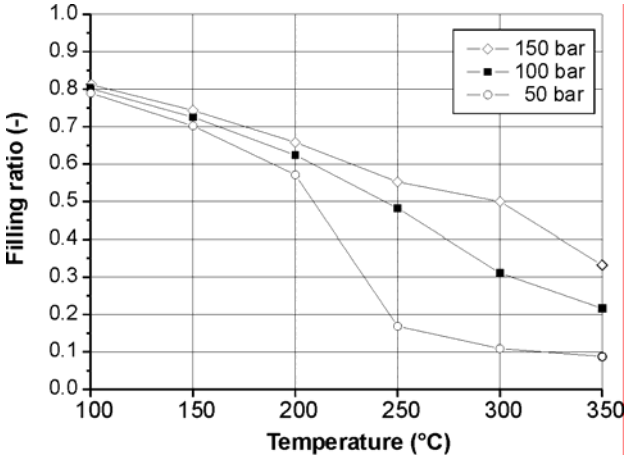

Figure 12.1. Calculated isobars of autogenous pressure illustrating the dependence of the usable filling ratio of pure acetone on the temperature.

In Figure 12.1, the isobars of autogenous pressure of acetone are shown for 50, 100 and 150 bar for various temperatures. The critical point temperature of acetone of 235.1 °C plays an important role here: below this temperature, the autogenous pressure is very low below a filling ratio of 0.55, then however increasing rapidly. At higher temperature, even a low filling ratio of 0.2 creates significant pressure. A pressure of 100 bar, which is important regarding the maximum allowable pressure in the autoclave, is however not reached below a filling ratio of 0.47. When even higher temperatures are used, the 100 bar isotherm decreases to a filling level of 0.3, which shows that the use of acetone for temperatures above 250 °C is not feasible.

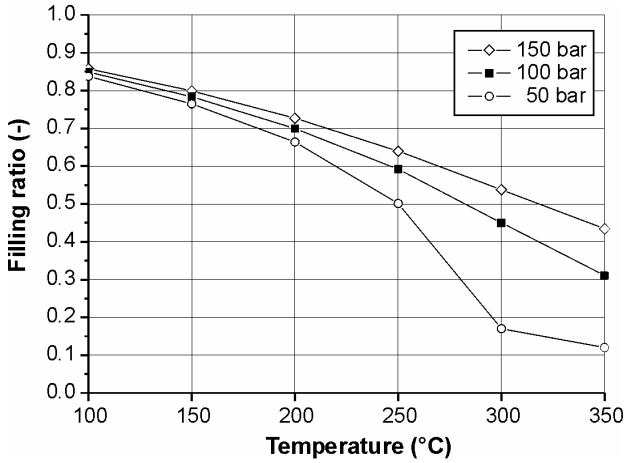

Figure 12.2. Calculated isobars of autogenous pressure illustrating the dependence of the usable filling ratio of pure 2-butanone on the temperature.

The calculated isobars for 2-butanone are shown in Figure 12.2. It shows a very similar pattern as obtained for acetone, however shifted towards higher temperatures by 50 °C, which is consistent with its higher critical point temperature of 261.9 °C.

The corresponding diagram for benzyl alcohol is not shown, as its high critical point temperature of 403.9 °C is well above the relevant temperature range (the maximum temperature for the standard autoclaves was 250 °C). Consequently, even high filling ratios around 0.8 did not lead to significant autogenous pressure.

Hence, it can be summarized that for the experiments described here, the autogenous pressure was calculated not to reach significant values, as the filling ratios used were always < 0.5.

12.2 Characterization

X-Ray Diffraction (XRD)

Crystallinity of the samples was checked on an Enraf-Nonius PDS-120 powder diffractometer in reflection mode, using an FR-590 generator as the source of Cu Kα radiation. A Nonius CPS-120 curved position sensitive detector, showing a resolution of 2θ = 0.018°, was employed to record the scattered radiation.

Alternatively, a Bruker D8 diffractometer equipped with a scintillation counter was used. The samples were measured in θ–θ reflection mode (under CuKα radiation), usually in the range 2θ = 10-100° by step-scanning with a step size of 0.01°.

The yttria nanocomposite was further characterized by small angle X-ray scattering (SAXS) using a Kratky camera assembly manufactured by Anton Paar, Germany. The samples were analyzed in transmission mode under vacuum with an X-ray source of Cu Kα radiation.

Transmission-Electron Microscopy (TEM)

Transmission electron microscopy (TEM) was performed on a Zeiss EM 912Ω instrument at an acceleration voltage of 120 kV. The samples usually were prepared by dispersing a small amount of powder in water or ethanol, followed by ultrasonication for 10 min. Next, one drop of the dispersion was put on a carbon-coated copper grid (400 mesh) and left to dry under ambient conditions before insertion into the device. Peptide-functionalized titania particles were analyzed by directly applying one drop of the sample solution/suspension on a copper grid. High-resolution TEM images were recorded on a Philips CM200 FEG microscope operated at 200 kV and equipped with a field emission gun. The coefficient of spherical aberration was C_s = 1.35 mm.

Scanning-Electron Microscopy (SEM)

Scanning-electron microscopy (SEM) was performed on the calcined PZT films after coating with gold, directly measuring on the Si substrate. A LEO 1550-Gemini instrument was used for the measurement.

Thermogravimetric Analysis (TGA)

The TGA measurements were carried out using a Netzsch thermoanalyzer TG 209, measuring under nitrogen from room temperature to 700 °C - 900 °C at a heating rate of 10 °C/min. Al_2O_3 crucibles were used as sample holders. The samples were pre-dried by evacuation or stored in a desiccator and then measured instantly. For one measurement, about 5-10 mg sample was used.

Nuclear Magnetic Resonance (NMR) Analysis

NMR analysis was performed on a Bruker DPX400 spectrometer at 400 MHz for ^{1}H and 100 MHz for ^{1}H-BB-decoupled ^{13}C measurements, at a sample spinning rate of 20 Hz, and a ZG30 pulse program. The obtained NMR data is listed in the experimental section of each chapter.

Atomic Force Microscopy (AFM)

Atomic force microscopy (AFM) was performed on a NanoScope IIIa device (Veeco Instruments, Santa Barbara, CA) in tapping mode. Commercial silicon tips (Type NCR-W) were used with a tip radius < 20 nm, employing a force constant of 42 N m^{-1} and a resonance frequency of 285 kHz. The image was recorded on a 10 × 10 µm e-scanner.

Fourier-Transform Infrared Spectroscopy (FTIR)

FTIR-ATR spectra were recorded on an FTS 6000 spectrometer (Bio-Rad Laboratories, Inc.) equipped with a horizontal ATR accessory (Zn-Se crystal) from Pike Technologies.

Elemental Analysis Techniques

Routinely, elemental analyses were carried out on a Vario EL Elementar instrument (Elementar Analysensysteme, Hanau, Germany). This combustion analysis revealed the amount of carbon, hydrogen and nitrogen present in the sample. The oxygen content could not be detected as it was present in the form of incombustible oxides.

For determination of the lead, titanium and zirconium content in PZT powders, and the yttrium content in the yttria nanocomposide, inductively coupled plasma optical emission spectrometry (ICP-OES) was performed on a Perkin Elmer Optima 3000 after digesting the samples in conc. nitric acid for Pb and Zr and a mixture of hydrochloric and hydrofluoric acid for Ti.

Coupled Gas Chromatography – Mass Spectrometry (GC–MS)

GC–MS analysis was carried out on a Varian Series 3400 gas chromatograph equipped with a fused-silica column (30 m × 0.25 mm i. d.) coated with a 0.25 μm film of DB5 poly(5% diphenyl- 95% dimethylsiloxane) from J&W Scientific. The samples were diluted with hexane or chloroform in a volume ratio of 1 : 2 before the measurement (ca. 1 μL was injected). The injector temperature was 270 °C. The oven temperature was maintained isothermal at 50 °C for 1 min and then increased to 250 °C at a rate of 20 °C min^{-1}. The final temperature was held for 10 min. For assignment of the individual signals, the gas chromatograph was directly coupled to a SSQ 710 quadrupole MS by Finnigan.

Mass Spectrometry (peptide analysis)

The synthesized oligopeptides were analyzed on a Shimadzu LCMS-QP8000α electrospray time-of-flight (ESI-TOF) instrument equipped with a standard electrospray ion source operating in positive mode (detector gain: 1.6 kV) with a nozzle temperature of 150 °C and a voltage of 4.5 kV. Prior to the measurement, the samples were dissolved in 50 μL of a 0.1 vol % solution of formic acid in MeOH (1 mg sample/mL).

Analytical Ultracentrifugation (AUC)

Analytical ultracentrifugation was performed on a Beckman Optima XL-I centrifuge (Beckman/ Coulter, Palo Alto, CA) with a scanning absorption optics and on-line Rayleigh interferometer. For the determination of the particle size distribution, the absorbance was measured at the two wavelengths of 400 nm and 450 nm at 10000 rpm at 25 °C in a band centrifugation experiment to allow for an optimum particle separation. 12 μL of the titania dispersion in water (ρ_{TiO_2} = 3.9 g/mL) were overlaid onto 300 μL D_2O in a self-made 12 mm synthetic boundary epon cell of the Vinograd type to avoid convection problems. The UV/Vis spectra were taken at radial positions where the local particle size was known from prior and subsequent radial scans.

Nitrogen Adsorption Experiments

Nitrogen adsorption and desorption isotherms of the functionalized titania particles were measured at 77 K with a Micromeritics Tristar 3000 system. Prior to the measurement, the sample was degassed at 150 °C overnight under vacuum. For the determination of the surface area, the BET method was used.

12.3 Symbols and Abbreviations

12.3.1 Analytical and Synthetic Methods

AFM ..... Atomic Force Microscopy
AUC..... Analytical Ultracentrifugation
FTIR ..... Fourier-Transform Infrared Spectroscopy
GC–MS..... Gas Chromatography – Mass Spectrometry
NMR..... Nuclear Magnetic Resonance Spectroscopy
SEM..... Scanning-Electron Microscopy
SPPS ..... Solid-Phase Peptide Synthesis
TEM..... Transmission-Electron Microscopy
TGA..... Thermogravimetric Analysis
XRD..... X-ray Diffraction

12.3.2 Chemicals and Materials

Acac..... Acetylacetonate
Boc..... *tert*-Butoxycarbonyl–
EtOH..... Ethanol
DCM..... Dichloromethane, Methylene chloride
DHC..... 3,4-Dihydroxyhydrocinnamic acid
DIPEA ..... Diisopropylethylamine
DMF ..... N,N-Dimethylformamide
Fmoc..... 9-Fluorenylmethoxycarbonyl–
HOBt ..... 1-Hydroxybenzotriazol monohydrate
NMP N-Methyl-2-pyrrolidone
PyBOP..... (Benzotriazol-1-yloxy)tripyrrolidinophosphonium hexafluorophosphate
PZT..... Lead Zirconate Titanate
TBAF..... Tetrabutylammonium fluoride
TBC ..... 4-*tert*-Butyl catechol
TBDMS ..... *tert*-Butyldimethylsilyl–
TFA ..... Trifluoroacetic acid
THF ..... Tetrahydrofuran

Peptides are abbreviated in the text using the standard three-character code (e. g., writing Gly for glycine). Only when stating the composition of longer segments, the one-character code (e.g., G for glycine, V for valine, P for proline) was used.

12.3.3 Physical and Mathematical Symbols

δ ..... chemical shift in ppm

$\mathscr{F}$ ..... Fourier transformation

k_B ..... Boltzmann constant, $k_B = 1.38 \cdot 10^{-23}$ J K^{-1}

R ..... Gas constant, R = 8.3145 J K^{-1} mol^{-1}

λ ..... wavelength

θ ..... scattering angle

$\vec{s}$ ..... scattering vector, $|\vec{s}| = \frac{2 \cdot \sin\theta}{\lambda}$ with λ = 1.5418 Å.

ω ..... acentric factor, general definition:[2] $\omega = -\log_{10}(P_r^0)_{(Tr=0.7)} - 1.000$

12.4 References

[1] M. Rajamathi, R. Seshadri, *Curr. Opin. Solid State Mater. Sci.* **2002**, *6*, 337.

[2] T. E. Daubert, R. P. Danner, H. M. Sibul, C. C. Stebbins, *Physical and Thermodynamic Properties of Pure Chemicals: Data Compilation*, Taylor & Francis, Washington, **1998**.

Acknowledgments

First of all, I would like to gratefully thank all the people who helped me to get this work together:

PROF. DR. MARKUS ANTONIETTI for giving me the opportunity to work at the MPI-KG, for his numerous ideas and for creating such a great atmosphere at the institute.

DR. MARKUS NIEDERBERGER, my direct supervisor, for his neverending support and help, and great patience with all of us as his group members.

DR. BERND SMARSLY, without whom I would not have found my way to the institute, and who continuously provided me with information about X-rays, film formation and many other issues a PhD student has to deal with.

DR. HANS BÖRNER for continuously supplying his ideas about peptides and peptide functionalization as well as standard organic chemistry.

DR. NICOLA PINNA for our great collaboration, leading to a steady supply of reaction mechanism data, which kept me busy pondering over organic reaction mechanisms, and for sharing his excellent computer skills and materials science knowledge with me.

Further, I would like to thank REGINA ROTHE for keeping the entropy in our lab at a comparably low level, and of course for her help in preparing and processing countless samples. I also thank my hard-working students JENS HENTSCHEL, CHRISTIAN MELCHERT and JONAS WIRTH for keeping our autoclaves busy.

I have to thank numerous people for carrying out measurements on my samples, or for helping me measure them:

JULIEN POLLEUX for spending countless sunny (?) Fridays in the dark basement measuring my TEM samples.

OLAF NIEMEYER for keeping the NMR instrument busy with my samples, measuring more than 300 spectra for me.

INGRID ZENKE for her patient help with the XRD devices.

DR. INES STARKE, Universität Potsdam, for the GC–MS measurements.

SILVIA PIROK for numerous elemental analysis measurements.

HELMUT CÖLFEN and especially ANTJE VÖLKEL for carrying out AUC measurements and helping us to interpret them.

ANNE HEILIG, for performing AFM Measurements.

PABLO BEATO, *Fritz Haber Institut der MPG, Berlin,* for RAMAN measurements of the Fe_2O_3 particles.

PROF. DR. ROBERT SCHLÖGL, *Fritz Haber Institut der MPG, Berlin*, for the use of the HRTEM device at the FHI, and KLAUS WEISS for his technical assistance

RONA PITSCHKE, DR. JÜRGEN HARTMANN, DR. NADINE NASSIF and HEIKE RUNGE for SEM measurements.

The lab team of the *Börner* group for their great help with peptide functionalization: KATHARINA OTTE for peptide synthesis, and JESSICA BRANDT for MS measurements of the synthesized peptides.

DR. EBERHARD KRAUSE from the *Institut für Molekulare Pharmakologie, Berlin,* for MALDI-TOF MS measurements of synthesized peptides.

Of course, I need to thank my group members, besides Nicola Pinna and Julien Polleux also JIANHUA BA and our short-term officemate STEPHANIE GRANT-GRANCHAROV, for a lot of interesting discussions and for spending such a nice and enjoyable time together.

Also, thanks to my former officemate DR. ATUL DESHPANDE for his help, for many discussions and for keeping me entertained throughout the day.

Thanks also to all my friends at the institute, especially my "Lunch Friends", the Börner group members, and the "*Polish Connection*", for giving me such a great time in Golm and making more out of the day than just work.

I deeply want to thank my parents for giving me the opportunity to go abroad and do what I enjoy most, and for their belief in me, their love and support. I would also like to thank my sister, DORIS, for giving me such a good time in the, unfortunately, few days per year that we manage to spend together, just as well as for helping me through bad days.

Last but not least, I need to thank all my friends, both in Potsdam/Berlin and in Austria, especially IRIS, VERENA, DANI, TANJA, DORIS, GREGOR, REGINA, MARCEL, CHRISTIAN, WILL, BERND, JENNY, DOREEN, HARTMUT, LAURA and BERNHARD for their continuous help and support, and for having so much fun together.

List of Publications

NOVEL SILOXANE-SILICA NANOCOMPOSITE AEROGELS AND XEROGELS
N. Husing, J. Bauer, G. Kalss, G. Garnweitner, G. Kickelbick, *J. Sol-Gel Sci. Technol.* **2003**, *26*, 73.

SELF-ASSEMBLY OF AN ENVIRONMENTALLY RESPONSIVE POLYMER/SILICA NANOCOMPOSITE
G. Garnweitner, B. Smarsly, R. Assink, W. Ruland, E. Bond, C. J. Brinker, *J. Am. Chem. Soc.* **2003**, *125*, 5626.

PREPARATION AND CHARACTERIZATION OF MESOSTRUCTURED POLYMER-FUNCTIONALIZED SOL-GEL-DERIVED THIN FILMS
B. Smarsly, G. Garnweitner, R. Assink, C. J. Brinker, *Prog. Org. Coat.* **2003**, *47*, 393.

CHARACTERIZATION OF SELF-ASSEMBLED LAMELLAR THERMORESPONSIVE SILICA-HYDROGEL NANOCOMPOSITE FILMS
G. Garnweitner, B. Smarsly, R. Assink, D. R. Dunphy, C. Scullin, C. J. Brinker, *Langmuir* **2004**, *20*, 9811.

TAILORING THE SURFACE AND SOLUBILITY PROPERTIES OF NANOCRYSTALLINE TITANIA BY A NONAQUEOUS IN SITU FUNCTIONALIZATION PROCESS
M. Niederberger, G. Garnweitner, F. Krumeich, R. Nesper, H. Cölfen, M. Antonietti, *Chem. Mater.* **2004**, *16*, 1202.

NONAQUEOUS AND HALIDE-FREE ROUTE TO CRYSTALLINE $BaTiO_3$, $SrTiO_3$, AND $(Ba,Sr)TiO_3$ NANOPARTICLES VIA A MECHANISM INVOLVING C–C BOND FORMATION
M. Niederberger, G. Garnweitner, N. Pinna, M. Antonietti, *J. Am. Chem. Soc.* **2004**, *126*, 9120.

NON-AQUEOUS SYNTHESIS OF HIGH-PURITY METAL OXIDE NANOPOWDERS USING AN ETHER-ELIMINATION PROCESS
N. Pinna, G. Garnweitner, M. Antonietti, M. Niederberger, *Adv. Mater.* **2004**, *16*, 2196.

NONAQUEOUS SYNTHESIS OF CRYSTALLINE ANATASE NANOPARTICLES IN SIMPLE KETONES AND ALDEHYDES AS OXYGEN-SUPPLYING AGENTS
G. Garnweitner, M. Antonietti, M. Niederberger, *Chem. Commun.* **2004**, 397.

SYNTHESIS OF YTTRIA-BASED CRYSTALLINE AND LAMELLAR NANOSTRUCTURES AND THEIR FORMATION MECHANISM
N. Pinna, G. Garnweitner, P. Beato, M. Niederberger, M. Antonietti, *Small* **2005**, *1*, 112.

A GENERAL NONAQUEOUS ROUTE TO BINARY METAL OXIDE NANOCRYSTALS INVOLVING A C–C BOND CLEAVAGE
N. Pinna, G. Garnweitner, M. Antonietti, M. Niederberger, *J. Am. Chem. Soc.* **2005**, *127*, 5608.

NONAQUEOUS SYNTHESIS OF BARIUM TITANATE NANOCRYSTALS IN ACETOPHENONE AS OXYGEN SUPPLYING AGENT
M. Niederberger, G. Garnweitner, *Mater. Res. Soc. Symp. Proc.* **2005**, *879E*, Z9.8.1.

NONAQUEOUS SYNTHESIS OF AMORPHOUS POWDER PRECURSORS FOR NANOCRYSTALLINE $PbTiO_3$, $Pb(Zr,Ti)O_3$, AND $PrZrO_3$
G. Garnweitner, J. Hentschel, M. Antonietti, M. Niederberger, *Chem. Mater.* **2005**, *17*, 4595.